

INFLUENCE OF MASONRY INFILL WALLS AND OTHER BUILDING  
CHARACTERISTICS ON SEISMIC COLLAPSE OF CONCRETE FRAME BUILDINGS

By

SIAMAK SATTAR

B.S., Azad University of Najafabad, Iran, 2004

M.S., Mazandaran University of Science and Technology, Iran, 2007

M.S., University of Colorado Boulder, 2010

A thesis submitted to the  
Faculty of Graduate School of the  
University of Colorado in partial fulfillment  
Of the requirement for the degree of  
Doctor of Philosophy  
Department of Civil, Environmental and Architectural Engineering

2013

This thesis entitled:

Influence of Masonry Infill Walls and Other Building Characteristics on Seismic Collapse of  
Concrete Frame Buildings

written by Siamak Sattar

has been approved for the Department of Civil, Environmental, and Architectural Engineering

---

(Abbie Liel)

---

(Guido Camata)

---

(Kenneth Elwood)

---

(Keith Porter)

---

(Yunping Xi)

Date\_\_\_\_\_

The final copy of this thesis has been examined by the signatories, and we  
find that both the content and the form meet acceptable presentation standards  
of scholarly work in the above mentioned discipline

## **Abstract**

Siamak Sattar (Ph.D., Civil, Environmental and Architectural Engineering)

Thesis title: Influence of Masonry Infill Walls and Other Building Characteristics on Seismic Collapse of Concrete Frame Buildings

Thesis directed by Assistant Professor Abbie Liel

Reinforced concrete frame buildings with masonry infill walls have been built all around the world, specifically in the high seismic regions in US. Observations from past earthquakes show that these buildings can endanger the life of their occupants and lead to significant damage and loss. Masonry infilled frames built before the development of new seismic regulations are more susceptible to collapse given an earthquake event. These vulnerable buildings are known as non-ductile concrete frames. Therefore, there is a need for a comprehensive collapse assessment of these buildings in order to limit the loss in regions with masonry infilled frame buildings.

The main component of this research involves assessing the collapse performance of masonry infilled, non-ductile, reinforced concrete frames in the Performance Based Earthquake Engineering (PBEE) framework. To pursue this goal, this study first develops a new multi-scale modeling approach to simulate the response of masonry infilled frames up to the point of collapse. In this approach, a macro (strut) model of the structure is developed from the response extracted from a micro (finite element) model specific to the infill and frame configuration of interest. The macro model takes advantage of the accuracy of the micro model, yet is computationally efficient for use in seismic performance assessments requiring repeated nonlinear dynamic analyses. The robustness of the proposed multi-scale modeling approach is examined through comparison with selected experimental results.

The proposed multi-scale modeling approach is implemented to assess the collapse performance of a set of archetypical buildings, representative of the 1920s era of construction in Los Angeles, California. The collapse performance assessment is conducted for buildings with varying height and infill configurations. Dynamic analyses are performed for the constructed nonlinear models. Results of this study capture the influence the infill panel has on the collapse performance of the frame. This assessment is also used to investigate the significant difference infill configurations have on the collapse performance of the frame. These results can be used to prioritize mitigation of the most vulnerable RC frames.

This research also examines the collapse performance of non-ductile RC frames without infill walls. One of the primary goals in the seismic assessment procedure used in this study is to identify the hazardous buildings that are in critical need of rehabilitation. These buildings are known as “killer buildings.” In order to reduce the seismic hazard risk, we need a simple evaluation methodology for existing buildings that can quickly identify the killer buildings. In this evaluation methodology, the collapse safety of the buildings is defined as a function of a set of parameters that are known to significantly affect the risk of building collapse. These parameters are known as “collapse indicators.” This research uses these collapse indicators to examine the trend between the collapse risk and variation of each indicator. In addition, this study investigates the relation between building collapse and the extent of deficiency. The extent of the deficiency is defined by the number or percentage of the deficient elements, for instance number of columns with wide transverse reinforcement spacing, in the story of interest. These results are used to investigate the appropriate definition of these collapse indicators in the evaluation methodology.

An important aspect of the seismic assessment procedure presented in this dissertation is to quantify the uncertainty embedded in the nonlinear model used in nonlinear dynamic analysis. In the last part of this study, a new methodology is proposed to quantify modeling uncertainty through a set of drift distributions derived from data submitted to a blind prediction contest conducted at UCSD (2007). In this contest, participants were asked to develop models for predicting the experimental seismic response of a building. After quantifying the modeling uncertainty, this source of uncertainty is combined with another source of uncertainty, known as record-to-record uncertainty, in order to measure the total uncertainty in the assessment procedure. This study is conducted on a concrete wall bearing system, to identify the extent of modeling uncertainty. This methodology can then be implemented to other structural systems if the corresponding blind prediction data are available.

*To:*

*My wife, Maryam*

*and my parents, Mohammadjavad and Badri*

## **Acknowledgment**

I am grateful to many individuals whom I worked with during my Ph.D. I would first like to thank my advisor, Professor Abbie Liel, for her guidance and support for this research and my overall graduate school career at University of Colorado at Boulder. I would also like to acknowledge my committee members Professors Ken Elwood, Guido Camata, Keith Porter, and Yunping Xi for serving on my research committee and providing thoughtful insight and comments on my research.

I am grateful for the opportunity to work on ATC-78 project during my Ph.D. In this project, I have had the opportunity to work with a group of knowledgeable and experienced people from industry and academia. I would like to thank all of them, including Mr. Bill Holmes, Prof. Jack Moehle, Drs. Mike Mehrain and Bob Hanson, and Mr. Panos Galanis and Peter Somers. Their suggestions and insights were very helpful in developing this work. This part of my research is funded by Applied Technology Council (through funding from FEMA), which is greatly appreciated.

I would also like to thank Drs. Maziar Partovi and Kesio Palacio from TNO DIANA for their valuable feedback on micro-modeling of masonry infilled frames, and Mr. Majid Baradaran-Shoraka from UBC, who graciously shared his code for triggering collapse. In addition, thank you to Prof. Paolo Martinelli from Politecnico di Milano for sharing the results of his nonlinear model used in quantifying modeling uncertainty.

I am grateful to all the people I worked with in my research group. I wish to thank my dear friends Holly Bonstrom, Meera Raghunandan, Cody Harrington, Jared DeBock, and Emily

Elwood for their support and insight through my graduate studies. They are always willing to provide feedback and encouragement, which has greatly motivated me throughout my work.

Above all, my special thanks to my wife, Maryam, for her support and patience during my studies, and to my parents Badri and Mohammadjavad for everything they have done for me.

## CONTENTS

1	Introduction .....	1
1.1	Motivation and Objectives .....	1
1.2	Organization .....	4
2	Behavior of Masonry Infilled Reinforced Concrete Frames .....	6
2.1	Overview .....	6
2.2	Failure Modes of Infilled RC Frames .....	6
2.3	Previous Research .....	10
2.3.1	Experimental Investigations.....	11
2.3.2	Analytical Investigations: Strut (Macro) Modeling of Masonry Infill Panel .....	17
2.3.3	Analytical Investigations: Finite Element (Micro) Modeling of Masonry Infilled Frames	27
3	Development of Micro-model of Masonry Infilled RC Frames for Use in Proposed Macro-Model .....	35
3.1	Introduction to the Proposed Macro-Model .....	35
3.2	Introduction to Micro-modeling of Masonry Infilled Frames.....	36
3.3	Development of Calibrated Finite Element Model for Masonry Infilled RC Frames ...	37
3.3.1	Selection of Software for Modeling of Masonry Infilled RC Frames .....	37
3.3.2	Overview of Micro-Model.....	38
3.4	Model Calibration and Validation through Finite Element Modeling of a Masonry Infilled Reinforced Concrete Frame Specimen .....	45
3.4.1	Overview.....	45
3.4.2	Experimental Tests.....	46
3.4.3	Proposed Finite Element Model for Experimental Specimen.....	47

3.4.4	Pushover Analysis of the Masonry Infilled Frame ( <i>Specimen 8</i> ) .....	59
3.4.5	Pushover Analysis of a Second Masonry Infilled Frame ( <i>Specimen 9</i> ).....	63
3.5	Conclusions .....	65
4	Proposed Macro-Modeling Approach for Masonry Infilled Reinforced Concrete Frames... 67	
4.1	Overview .....	67
4.2	Modeling of Masonry Infill Panel.....	67
4.2.1	Extraction of the Force-Displacement Relationship for the Infill Wall.....	70
4.2.2	Multi-Linear Representation of Strut Force-Displacement Response .....	74
4.2.3	Strut Configuration in the Proposed Macro-model.....	75
4.3	Frame Modeling .....	77
4.3.1	Frame Modeling Overview .....	77
4.3.2	Flexural Failure Modeling of RC Beams and Columns.....	79
4.3.3	Shear and Flexure-Shear Failure Modeling of Non-Ductile RC Columns.....	80
4.3.4	Axial Failure Modeling of Non-Ductile RC Columns.....	85
4.4	Comparison of Macro-Model with Experimental Results for Two Infilled Frame Specimens.....	86
4.5	Application of Proposed Macro-model .....	90
4.6	Conclusions .....	90
5	Collapse Assessment of Masonry Infilled RC Frames Using Multi-scale Modeling Approach 93	
5.1	Overview .....	93
5.2	Characteristics of RC Buildings in California for Case Study.....	94
5.2.1	Configuration of the Archetypical Buildings.....	96
5.3	Material Properties and Design of the Concrete Frames in Archetypical Buildings .....	98

5.4	Material Properties and Configurations of Masonry Panels in Archetypical Buildings	103
5.5	Overview of Modeling and Collapse Assessment Approach.....	105
5.5.1	Multi-scale Modeling Approach.....	105
5.5.2	Incremental Dynamic Analysis for Assessing Collapse Performance.....	106
5.5.2.1	Collapse Definition .....	107
5.6	Micro-Modeling of the Archetypical Buildings.....	108
5.6.1	Properties of the Infill and Frame in the Micro-Model.....	109
5.7	Micro-Modeling Analysis and Results for Archetypical Buildings.....	114
5.7.1	Effect of Vertical Load in the Micro-model for Archetype Buildings .....	115
5.7.2	Pushover Results from the Micro-Models for Archetypical Buildings .....	117
5.7.3	Extracted Infill Force-Displacement Responses for Archetypical Buildings .....	119
5.8	Out-of-Plane Behavior of the Archetypical Building .....	121
5.9	Macro-Modeling of the Archetypical Buildings .....	127
5.10	Seismic Response of the Archetypical Buildings from Macro-Models.....	130
5.10.1	Static Pushover Analysis Results.....	130
5.10.2	Incremental Dynamic Analysis Results .....	132
5.11	Conclusions .....	139
6	Collapse Indicators for Existing Nonductile Concrete Buildings with Varying Column and Frame Characteristics.....	141
6.1	Objectives.....	141
6.2	Overview of the ATC-78 Project .....	142
6.2.1	Collapse Indicators.....	143
6.2.2	Collapse Indicator Evaluation Methodology .....	143

6.2.3	Normalization to Isolate the Effect of Building Strength .....	145
6.3	Study of Collapse Indicators in Case Study Building .....	147
6.3.1	Case Study Building .....	148
6.3.1.1	Building Design.....	148
6.3.1.2	Modeling and Collapse Simulation.....	149
6.3.2	Variation of Column to Beam Strength Ratio, $M_c/M_b$ .....	150
6.3.2.1	Context and $M_c/M_b$ Parameter Definition .....	150
6.3.2.2	Variation $M_c/M_b$ in Uniform Building.....	151
6.3.2.3	Variation of $M_c/M_b$ with Non-Uniform $M_c/M_b$ Ratios .....	152
6.3.3	Variation of Adjacent Story Strength Ratio, $V_i/V_{i+1}$ .....	158
6.3.3.1	Context and $V_i/V_{i+1}$ Parameter Definition .....	158
6.3.3.2	Variation $V_i/V_{i+1}$ in Building with Non-Uniform Frame Lines .....	159
6.3.4	Variation of Column Flexural-Shear Strength Ratio, $V_p/V_n$ .....	161
6.3.4.1	Context and $V_p/V_n$ Parameter Definition.....	161
6.3.4.2	Variation of $V_p/V_n$ in Building with Non-Uniform Columns.....	162
6.4	Conclusions .....	168
7	Quantification of Modeling Uncertainties Based on the Blind Prediction Contest Submissions .....	171
7.1	Overview .....	171
7.2	Methodology of Study.....	172
7.3	Application of the Proposed Methodology .....	174
7.4	Combination of Modeling Uncertainty With RTR Uncertainty.....	181
7.5	Conclusions and Recommendations.....	186
8	Conclusion.....	188

8.1 Summary and Findings..... 188

8.2 Future Research..... 190

8.2.1 Modeling of Masonry Infilled RC Frames..... 190

8.2.2 Quantification of Modeling Uncertainty ..... 191

## TABLES

Table 2-1. Summary of strut models developed for infill panels. ....	26
Table 2-2. Chronological improvements on in-plane modeling the masonry wall/infill.....	34
Table 3-1. Modeling parameters and their definition for the interface model.....	44
Table 3-2. Model interface properties, illustrating the process of determining, first, tensile properties (row 1), second, monotonic shear properties (row 2), third, cyclic shear properties (row 3), fourth, dilatation (row 4), and fifth, prism sample (row 5). ....	49
Table 3-3. Properties of the total strain crack model to represent concrete behavior in the concrete frame and hollow bricks. ....	53
Table 3-4. Properties of total strain crack model used in model of bare frame. ....	58
Table 3-5. Steel material properties. ....	58
Table 3-6. Properties of the total strain crack model to represent the hollow concrete bricks in the FE model. ....	61
Table 3-7. Material properties of the head-joint and wall-to-frame joints. ....	61
Table 5-1. Steel and concrete material properties (reproduced from FEMA 356). ....	99
Table 5-2. Design loads for the archetypical buildings. ....	100
Table 5-3. Maximum allowable stress in concrete and steel based on the values recommended to UBC (1927).....	100
Table 5-4. Moment demands in the beams based on the values presented in UBC (1927). In these equations, $w$ is load per unit length of the beam and $l$ is length of the beam. ....	100
Table 5-5. Design of columns in the exterior frame of the 2-story building. ....	102
Table 5-6. Design of columns in the exterior frame of the 4-story building. ....	102
Table 5-7. Design of columns in the exterior frame of the 8-story building. ....	103
Table 5-8. Model interface (mortar) properties for the archetypical buildings. ....	112
Table 5-9. Model brick properties for the archetypical buildings. ....	113
Table 5-10. Model brick properties for the archetypical buildings. ....	114

Table 5-11. Model steel properties for the archetypical buildings. ....	114
Table 5-12. Ultimate out-of-plane strength and corresponding equivalent acceleration of the infill panel in the archetypical building. ....	124
Table 5-13. Characteristics of the archetypical buildings.....	129
Table 5-14. Summary of the results from pushover analysis and incremental dynamic analysis of the archetypical buildings. ....	132
Table 5-15. Failure modes of selected archetypical buildings.....	138
Table 7-1. Predicted (modeled) interstory drifts for the 7-story building for EQ.1.....	178
Table 7-2. Statistics of the predicted (modeled) drifts for different experimental drift values. .	181
Table 7-3. Median and standard deviation of the fragility curves representing uncertainty in RTR and modeling, obtained from histogram and distribution approaches.....	186

## FIGURES

Figure 1-1. Masonry infilled frame in India (Jaiswal et al., 2002). .....	2
Figure 2-1. Different failure mechanisms in: (a) Algeria (2003 Boumerdes Earthquake), masonry wall failure (photo: S. Brzev); (b) India (2001 Bhuj earthquake), (photo: EERI, 2001); (c) Taiwan, (1999 Chi-Chi earthquake) (photog: Charleson, 2008) .....	7
Figure 2-2. Failure mechanisms of the infilled frames observed in the experiments conducted by: (a) Al-Chaar et. al (2005);(b) Stavridis (2009); (c) Mehrabi (1994); (d) Blackard et. al (2009)....	8
Figure 2-3. Failure mechanisms of infilled frames (Mehrabi, 1994).....	9
Figure 2-4. Different failure modes of the infilled frames: (a) corner crushing; (b) sliding shear; (c) diagonal compression; (d) diagonal cracking; and (e) frame bending failure (El-Dakhakhni et al., 2003) .....	10
Figure 2-5. (a) Equivalent strut model, (b) Experimental results showing the formation of strut (Al-Chaar, 1998).....	12
Figure 2-6. Parameters relevant for equivalent strut modeling.....	19
Figure 2-7. Force-displacement response of the strut proposed by Klingner and Bertero (1976).	20
Figure 2-8. Schematic force-displacement response of the infill strut model proposed by Saneinejad and Hobbs (1995). .....	21
Figure 2-9. Schematic force-displacement response of the infill strut model proposed by Dolsek and Fajfar (2008).....	21
Figure 2-10. Alternative models with off-diagonal struts to model the frame infill interaction proposed by (a) Syrmakezis and Vratsanou (1986), (b) Zarnic and Tomazevic (1988), (c) Schmidt (1989), (d) Chrysostomou (1991). For clarity, struts in only one direction are shown..	22
Figure 2-11. Three-diagonal strut model proposed by (El-Dakhakhni et al., 2003).....	23
Figure 2-12. Schematic force-displacement response of the strut proposed by El-Dakhakhni et al. (2003).....	23
Figure 2-13. Multi-strut with shear spring model (Crisafulli 1997) .....	24
Figure 2-14. Comparison among different methods to compute the stiffness and strength of the infill panel in <i>Specimen 8</i> tested by Mehrabi (1994). Solid lines show the strength and dashed lines show the stiffness. Dashed lines are stopped at an arbitrary lateral displacement. For each method, the corresponding failure mechanism is reported in the legend. ....	25
Figure 2-15. Strut configuration proposed in ASCE-41 to compute (a) force in columns (b) force in beams. ....	25

Figure 2-16. Detailed micro-modeling approach for masonry or infill walls.....	29
Figure 2-17. Simplified micro-modeling (meso-modeling) approach for masonry or infill walls. .....	29
Figure 2-18. Homogenized modeling approach for masonry or infill walls.....	30
Figure 3-1. Nonlinear finite element (micro) model for masonry infilled RC frame. ....	39
Figure 3-2. Different types of tensile behavior in total strain crack model (DIANA, 2011).....	41
Figure 3-3. Different types of compressive behavior in total strain crack model (DIANA, 2011). .....	42
Figure 3-4. Two-dimensional interface model (adapted from Lourenço and Rots 1997). Notation defined in Equation (3-1). ....	43
Figure 3-5. Nonlinear compressive behavior of the cap model (Lourenco, 1996). ....	44
Figure 3-6. Details of the test specimen (Al-Chaar and Mehrabi, 2008).....	47
Figure 3-7. Geometry of hollow concrete bricks used as infill (dimensions are in inches). ....	47
Figure 3-8. 1D interface element between two shell elements (bricks).....	48
Figure 3-9. (a) Tensile test on an interface element (mortar joint) located between two bricks; (b) Shear test of the interface model for the mortar joint. ....	50
Figure 3-10. (a) Tensile stress vs. joint opening under monotonically applied vertical displacement and (b) Shear stress vs. shear displacement under monotonically applied horizontal displacement of the modeled interface element. ....	50
Figure 3-11. Shear stress versus shear displacement of the interface element in cyclic shear test, under 100 psi normal stress (modified from Mehrabi, 1994). ....	51
Figure 3-12. Normal versus shear displacement of the DIANA interface element under 150 psi normal stress compared with the experimental results (modified from Mehrabi, 1994).....	52
Figure 3-13. Concrete block under uniform compression. ....	53
Figure 3-14. Three block prism sample modeled in DIANA. ....	56
Figure 3-15. (a) Normal stress-strain response of the concrete material in a concrete block under compression ; (b) Normal stress-strain response of the three-block prism sample. Both responses are compared to the experimental reported values for peak stress and strain at peak stress for the corresponding sample configuration. ....	56
Figure 3-16. Nonlinear finite element model for the bare RC frame.....	57

Figure 3-17. Numerical and experimental results for the base shear vs. lateral displacement of the bare frame model. ....	59
Figure 3-18. Effect of modeling the bond-slip on the response of the bare frame using data from (Mehrabi, 1994). ....	59
Figure 3-19. Deformed shape of the modeled masonry infilled frame at 0.5 inch lateral top displacement (values shown represent lateral displacement in inches). ....	62
Figure 3-20. Base shear versus lateral displacement of the nonlinear finite element model compared with the experimental results of <i>Specimen 8</i> from Mebrabi (1994). ....	63
Figure 3-21. Base shear versus lateral displacement of the nonlinear finite element model compared with the experimental results of <i>Specimen 9</i> from Mebrabi (1994). ....	65
Figure 4-1. Schematic diagram of proposed macro-modeling approach based on the micro-model. ....	69
Figure 4-2. Force transfer mechanism in masonry infilled RC frame to be represented by proposed macro-modeling approach. ....	69
Figure 4-3. Stress in the wall to frame interface elements over height of the column. (Negative values of stress indicate compression). ....	71
Figure 4-4. Illustration of the sections at which the force is extracted from the infill wall in micro-model. ....	73
Figure 4-5. Force-displacement response for three sections $w_1$ , $w_2$ , and $w_3$ extracted for the strut from the micro-model for <i>Specimen 9</i> . ....	73
Figure 4-6. Average force-displacement and stress-strain response extracted for the strut from the micro-model for <i>Specimen 9</i> . ....	73
Figure 4-7. Multi-linear stress-strain macro-model representation of the nonlinear response of the infill wall extracted from micro-model for <i>Specimen 9</i> . ....	75
Figure 4-8. Typical moment and shear diagram for infilled frames (taken from (Crisafulli, 1997)). ....	76
Figure 4-9. Proposed double-strut configuration for macro-model. ....	77
Figure 4-10. Force distribution between frame and infill panel. ....	77
Figure 4-11. Schematic illustration of the (a) combined shear and flexure-shear model and (b) flexural model implemented in OpenSees for beam-columns. ....	79
Figure 4-12. Moment rotation backbone for Ibarra material model. ....	80

Figure 4-13. Schematic diagram of the shear model proposed by Elwood (2004) (taken from (Elwood, 2004)).	82
Figure 4-14. Schematic representation of limit state material model in shear failure (Elwood, 2004).	83
Figure 4-15. Schematic shear limits to define the shear limit curve.	85
Figure 4-16. Schematic axial limit curve (Elwood, 2004).	86
Figure 4-17. Macro-model, micro-model, and experimental results for <i>Specimen 8</i> . The experiment was carried out to a lateral displacement larger than 1.0 inches. Results are compared here until 1.0 inches, because the micro-model failed to converge before that point.	88
Figure 4-18. Macro-model, micro-model, and experimental results for <i>Specimen 9</i> . The experiment was carried out to a lateral displacement larger than 1.0 inches. Results are compared here until 1.0 inches, because the micro-model failed to converge before that point.	88
Figure 4-19. Macro-model and experimental results for the bare frame in <i>Specimen 8</i> and <i>9</i> . The experiment was carried out to a lateral displacement bigger than 2.0 inches. Results are compared here until 2.0 inches.	89
Figure 4-20. (a) Column bending and shear diagram from the macro-model and (b) Column shear diagram from the micro-model for <i>Specimen 9</i> at 0.4 in. displacement.	90
Figure 5-1. Distribution of built-year of non-ductile (pre-1980) concrete buildings in Los Angeles (Anagnos et al., 2010).	95
Figure 5-2. Distribution of the number of stories for non-ductile concrete frames in LA (Concrete Coalition, 2009).	95
Figure 5-3. Distribution of functionality of non-ductile concrete buildings in LA (Concrete Coalition, 2009).	96
Figure 5-4. (a) Plan view and (b) East-West elevation view of the archetypical building.	97
Figure 5-5. Different infill configurations: (a) fully infilled frame, (b) partially infilled frame, and (c) bare frame.	98
Figure 5-6. Two, four, and eight story buildings considered in the collapse assessment.	98
Figure 5-7. Design of exterior beams for (a) an arbitrary floor level and (b) the roof level.	101
Figure 5-8. Deformed shape of the eight micro-models at 0.6 inch lateral in different stories of the 8-story archetypical building. Colors represent the contour of the lateral displacement (in inches relative to the base of the model).	119

Figure 5-9. Force-displacement response extracted from the micro-model for the seventh story in the 8-story building. The deformed shape of the micro-model is shown at different displacement levels. Colors represent the contour of lateral displacement. ....	120
Figure 5-10. Force-displacement response of the infill extracted from the infill panel in eight different micro-models representing different stories of the archetypical buildings. ....	121
Figure 5-11. Schematic drawing shows the mass and equivalent ultimate force on the wall, where, $m$ is the mass of the wall, $a$ is the equivalent acceleration, and $F$ is the ultimate out-of-plane strength of the wall. ....	124
Figure 5-12. Interaction between in-plane strength and out-of-plane force of URM infill (taken from (Hashemi and Mosalam, 2007)).....	127
Figure 5-13. Fitted multi-linear force-displacement response to the response extracted from the micro-model of the 2-story models for (a) first story; (b) second story. ....	128
Figure 5-14. Plan view of the analyzed buildings for two cases: (a) Space frame (infill exists in all N-S frames), (b) Perimeter frame (infill exists in the perimeter frames only). ....	129
Figure 5-15. Pushover analysis results for Case (1) (a) 2-story, (b) 4-story, and (c) 8-story models. ....	131
Figure 5-16. IDA results for selected 2-story models: (a) bare frame (2BW0) and (b) fully infilled (2FC1W3) with three-wythe walls (case 1). ....	135
Figure 5-17. Collapse fragility functions for Case (1) 2-story models with different infill configurations. ....	135
Figure 5-18. Dynamic analysis results for the 2-story fully infilled frame with strong infill walls showing (a) roof displacement time history response when subjected to a selected ground motion time history (Imperial Valley-Delta station) at two different scale levels and (b) incremental dynamic analysis results for all 44 records. Results for the same time histories shown in (a) are presented with the same color in (b) for comparison. Experimental results from Stavridis et al. (2012) are superimposed on (b). ....	136
Figure 6-1. Schematic illustration of collapse performance as a function of a collapse indicator showing (a) fragility curves for variation of a collapse indicator in the same model; (b) variation of collapse performance, quantified by median collapse capacity, as a function of the collapse indicator, and (c) variation of collapse performance, quantified by the conditional probability of collapse on a specific hazard level, as a function of the collapse indicator. Note that (c) also shows two possible approaches to identify the critical collapse indicator with (1) shaded block showing the collapse indicator region of drastic change of slope and (2) the dashed-line showing the calculation of the critical collapse indicator based on a pre-defined acceptable probability of collapse. ....	145
Figure 6-2. (a) Plan view and (b) elevation view of the case study building. ....	149

Figure 6-3. Variation of collapse performance of the case study building with respect to the variation of the $M_c/M_b$ ratio in the entire building. ....	152
Figure 6-4. Schematic drawing of the gradual variation of $M_c/M_b$ ratio of joints in the first floor. ....	154
Figure 6-5. Variation of collapse performance of the case study building with respect to the variation of the average $M_c/M_b$ ratio in the first story. ....	154
Figure 6-6. Variation of collapse performance of the case study building with respect to the variation of the minimum $M_c/M_b$ ratio in the first floor. ....	154
Figure 6-7. Schematic drawing of cases for studying the effect of the extent and location of deficiency $M_c/M_b$ ratio in the first story with (a) average $M_c/M_b = 0.8$ , (b) average $M_c/M_b = 0.9$ , and (a) average $M_c/M_b = 1.1$ . ....	156
Figure 6-8. Comparison among three cases with the same average $M_c/M_b$ ratio in the first floor, but with different distributions of the deficiency. The lower values correspond to the dashed boxes in Figure 6-8a, b, and c, wherein all of the joints at the first floor have the same $M_c/M_b$ ratio. ....	156
Figure 6-9. Schematic drawing of three cases to study the effect of the number of piers and the extent of deficiency $M_c/M_b$ ratio in the first floor. ....	157
Figure 6-10. Comparison among three cases with the same average $M_c/M_b$ ratio in the first floor, <i>i.e.</i> 0.9, but with different number of piers with low (deficient) $M_c/M_b$ . ....	158
Figure 6-11. Schematic drawing for the variation of $V_1/V_2$ ratio. ....	160
Figure 6-12. Variation of collapse performance of the two frames in series with respect to the variation of the average $V_1/V_2$ ratio of the different frame lines. ....	160
Figure 6-13. Schematic drawing for two cases with different distribution of $V_1/V_2$ in order to study definition of deficiency $V_i/V_{i+1}$ . ....	161
Figure 6-14. Comparison between two cases with the same average $V_1/V_2$ ratio, <i>i.e.</i> 1.01, but with different distributions of the deficiency. ....	161
Figure 6-15. Schematic drawing for the variation of $V_p/V_n$ ratio in the first story. ....	163
Figure 6-16. Variation of collapse performance of the case study building with respect to the variation of the average $V_p/V_n$ ratio in the first story. ....	163
Figure 6-17. Variation of collapse performance of the case study building with respect to the variation of the maximum $V_p/V_n$ ratio in the first story. ....	164
Figure 6-18. Schematic drawing for two cases with different distribution of $V_p/V_n$ in order to study definition of deficiency $V_p/V_n$ . ....	165

Figure 6-19. Comparison between two cases with the same average $V_p/V_n$ ratio, i.e. 1.0, but with different distribution of deficiency. ....	165
Figure 6-20. Schematic drawing for three cases to study the effect of the number of piers and the extent of deficiency $V_p/V_n$ ratio in the first story. ....	166
Figure 6-21. Comparison among three cases with the same average $V_p/V_n$ ratio = 1.0, but with different distribution of deficiency and different pier numbers. ....	167
Figure 6-22. Schematic drawing for two pairs of models to study the effect of the location of deficiency $V_p/V_n$ ratio in the first story. ....	168
Figure 6-23. Comparison among four cases with the same number of deficient columns in the first story, but with different locations of the deficiency. ....	168
Figure 7-1. Schematic drawing illustrating the proposed methodology to consider (a) RTR uncertainty; (b) modeling uncertainty representing the blind prediction test data; and (c) IDA curves generated to represent the modeling uncertainty. ....	174
Figure 7-2. View of the building tested at UCSD (Moaveni et al., 2011). ....	175
Figure 7-3. Histograms and engineering distributions for the “original” prediction data corresponding to (a) $\Delta_{exp}=0.003$ and (b) $\Delta_{exp}=0.006$ . ....	180
Figure 7-4. IDA results from nonlinear simulation of the 7-story building, representing: (a) RTR uncertainty, and (b) RTR and modeling uncertainty. ....	183
Figure 7-5. Comparison between fragility curves computed considering RTR variability only (gray lines) and RTR and modeling variability (black lines) for the original data. The fragility curves computed represent the probability of drifts exceeding a) 0.003, b) 0.006, c) 0.009, and d) 0.02. ....	184
Figure 7-6. Comparison between fragility curves computed considering RTR variability only (gray lines) and RTR and modeling variability (black lines) for the unbiased data. The fragility curves computed represent the probability of drifts exceeding a) 0.006 and b) 0.009. ....	185

# **1 Introduction**

## **1.1 Motivation and Objectives**

Non-ductile reinforced concrete (RC) frame buildings with masonry infill walls have been widely constructed for commercial, industrial and multi-family residential uses in seismic-prone regions worldwide, as shown in Figure 1-1. For instance, there are approximately 1850 masonry infilled RC frames in the city of San Francisco (ATC, 2010). Non-ductile RC frames with masonry infill panels, built before new seismic codes were developed, may suffer from the poor frame detailing, such as widely spaced transverse reinforcement, short lap splices, weak columns relative to beams, and lack of transverse reinforcement in joints. Although the masonry panel is generally not considered in the design process, the existence of the masonry infill panels in a frame can increase structural strength and stiffness (relative to a bare frame), but, at the same time, can introduce brittle shear failure mechanisms associated with the wall failure and wall-frame interaction. In general, the presence of the masonry infill panel and interaction with the RC frame changes the failure mechanism of the infilled frame in comparison to the bare frame. The deficiencies in non-ductile RC frames, as well as the brittle failure mechanism induced by infill panels, may lead to the low seismic performance of these structures, but the life safety risks posed by such structures are unknown.



Figure 1-1. Masonry infilled frame in India (Jaiswal et al., 2002).

Most of the past research focuses on the behavior of the masonry panel and, more recently, on the improvement of the modeling techniques to capture the physical behavior of the relationship between the infill and frame. Due to the large number of structures and the potential fatalities and losses involved in high seismic regions, there is a need to develop the tools needed to assess the performance of these buildings more generally in a performance-based probabilistic framework.

The Pacific Earthquake Engineering Research (PEER) Center has developed a rigorous probabilistic framework for performance-based earthquake engineering (PBEE), which integrates seismic hazard and structural modeling with loss modeling to generate probabilistic predictions of building response, considering the inherent uncertainty in modeling and loading (Deierlein, 2004). The value in PBEE methods is in its ability to produce metrics that can be used to address the seismic assessment of existing buildings to permit more informed decision making on the seismic performance, vulnerability, and safety of the buildings considering various hazard levels (Krawinkler and Miranda, 2004).

The study of masonry infilled frames in the PBEE framework can help decision makers to improve their understanding of the risk posed by these types of buildings, which in turn could help them to prioritize mitigation of the most dangerous structures. Moreover, this thesis studies

the effect of several other building and modeling aspects that can significantly affect the assessed collapse performance of RC buildings with masonry infill in the PBEE framework. The main objectives of this study are as following:

- (1) Develop a multi-scale modeling technique to simulate the response of the masonry infilled frame in the PBEE framework. This multi-scale modeling technique includes:
  - a. a micro (finite element) model that accurately captures the complexities of the brick, mortar-brick interface and wall-frame interaction, which can be used to develop the force-displacement response of infill wall panel under a lateral load; and
  - b. a macro model with nonlinear struts representing the infill walls, the properties of which have been calibrated to the micro model and which are arranged in a configuration to capture the important aspects of the wall-frame interaction.

The model developed in this research aims to satisfy the simplicity and accuracy requirements to perform a suite of computationally intensive nonlinear dynamic analyses.

- (2) Implement the proposed multi-scale modeling technique to assess the seismic performance of the masonry infilled non-ductile RC frames in the PBEE framework to evaluate the seismic safety and collapse vulnerability of existing buildings. This assessment is performed for a set of archetypical buildings with different heights and infill configurations that are representative of 1920s era building studies.
- (3) Conduct a study to quantify indicators of collapse in RC buildings, accounting for the severity of that deficiency within the building and its influence on seismic collapse performance.

- (4) Develop a methodology to incorporate modeling uncertainty to the seismic assessment procedure, based on blind prediction test data.

## 1.2 Organization

**Chapter 2** serves as an overview on the past research conducted on the masonry infilled frames. First, experimental investigations on the masonry infilled frames are presented, followed by discussion of past analytical investigations and the different model approaches that have been used for masonry panels, including micro- and macro-modeling approaches. Chapter 2 also reports some of the failure modes of the masonry infilled frames to motivate the study of the seismic performance of these buildings.

**Chapter 3** presents the development of the micro-modeling approach which is used in the proposed multi-scale model. The proposed micro-modeling approach is implemented to simulate the pushover response of two masonry infilled RC frame specimens that have previously been tested experimentally and the numerical simulation results are compared with the experimental results.

**Chapter 4** presents the new macro-modeling approach developed in this study to simulate the response of the infill panel. The proposed macro-model has a double strut configuration to represent the infill response in two directions. To represent the frame, macro-model employs lumped plasticity, shear spring, and axial spring to capture the flexural, shear, and axial failure of beam-columns. An existing shear failure model for RC columns (Elwood, 2004) is modified in this chapter and implemented in the macro-modeling approach. The proposed double-strut model for the infill panel as well as the explained RC frame modeling are implemented to simulate the response of the same two experimental specimens, and the results are compared against the micro-modeling and experimental responses.

**Chapter 5** develops a set of building that are representative of masonry infilled RC frame buildings constructed in 1920's in the US, *i.e.* archetypical buildings. The configuration, material properties, and design process of these buildings are selected based on what was in practice in that era. The proposed multi-scale-modeling approach is applied to simulate the response of these archetypical buildings. The collapse performance of these buildings are compared for different infill configurations and building heights.

**Chapter 6** studies a set of building characteristics that are known to affect the collapse capacity of the building. This chapter examines how the severity of deficiency, in terms of amount and distribution of deficiency, affects the building's safety. The variation of the collapse performance of the building with respect to the variation of different indicators of collapse is studied in order to find a definition of each indicator and to evaluate the effect of the extent of each deficiency on the performance of the building.

**Chapter 7** quantifies the effect of modeling uncertainty on seismic fragility assessments, using results of the 7-story RC building blind prediction contest at University of California at San Diego. The modeling uncertainty is presented in terms of drift distributions based on the modeled drifts submitted by the contest participants. This chapter develops a methodology to propagate the modeling drift distributions through the results of the nonlinear time history analyses in order to develop a set of fragility curves which consider two sources of uncertainties including record-to-record (RTR) and modeling uncertainties.

**Chapter 8** presents the summary and conclusion of this study, as well as the needs for future research.

## **2 Behavior of Masonry Infilled Reinforced Concrete Frames**

### **2.1 Overview**

Masonry infilled RC frames have been constructed in regions with high seismicity around the world. These structures are still one of the common structural systems in some Mediterranean countries, as well as Asia (Stavridis, 2009). These structures also exist in California, and other places in the U.S. This chapter describes current knowledge about the behavior and different failure mechanisms of masonry-infilled RC frames, in Section 2.2. Then, Section 2.3 reviews the past experimental and analytical studies conducted on this category of buildings. Knowing different failure modes experienced by masonry infilled frames, mentioned in Section 2.2, helps us to understand the limitation and advantages of the each of the experimental and analytical investigations reported in Sections 2.3.1 to 2.3.3.

### **2.2 Failure Modes of Infilled RC Frames**

Observations from past earthquakes (including 1999 Kocaeli, Turkey earthquake, the 2008 Sichuan, China earthquake, and the 1999 Chi-Chi, Taiwan Earthquake) show severe damage to these types of structures, as illustrated in Figure 2-1. Damage patterns include partial or full failure of masonry panels, shear failure of columns, column plastic hinges, soft story mechanisms, short column shear failures, etc. (Li et al., 2008; Sezen et al., 2003).

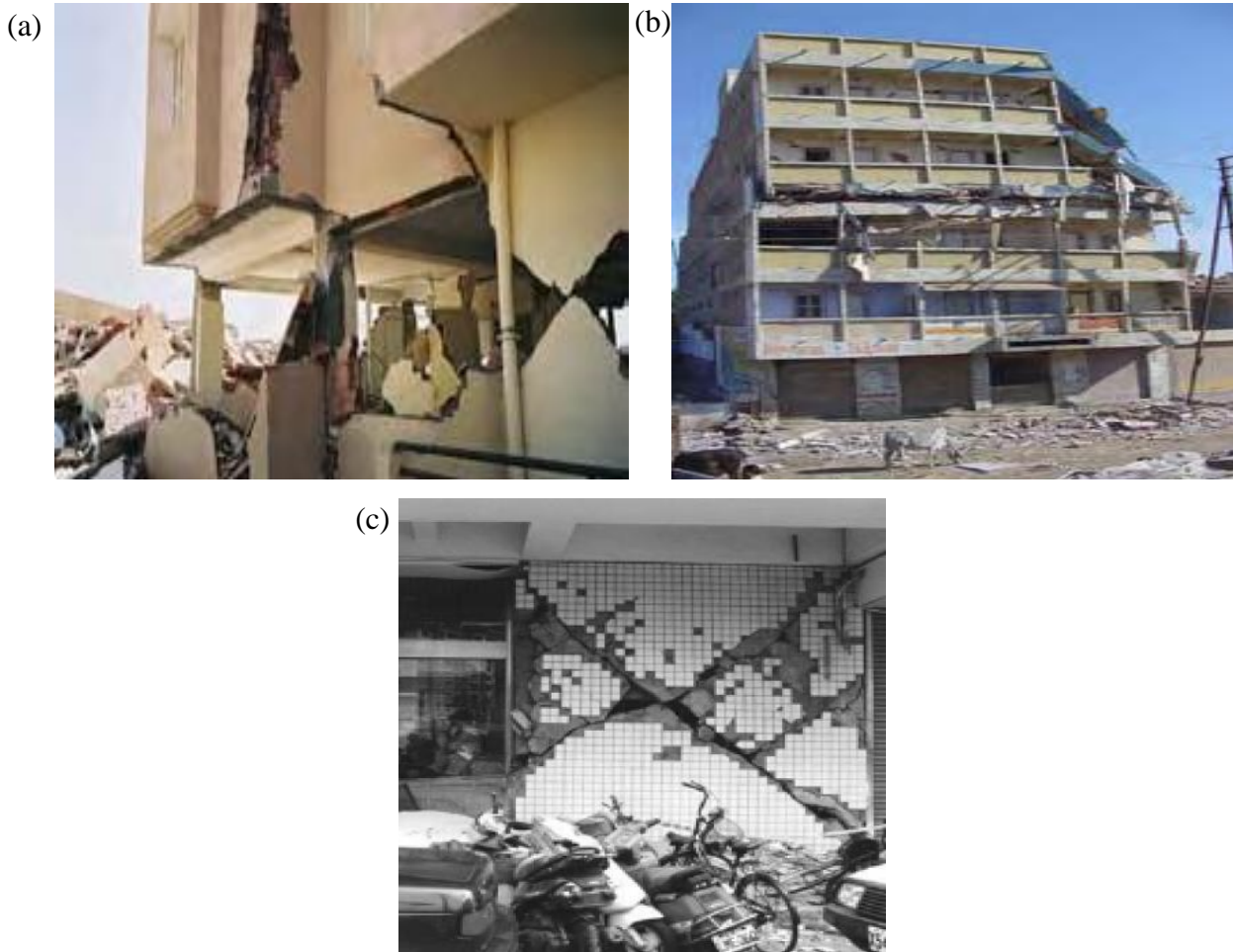


Figure 2-1. Different failure mechanisms in: (a) Algeria (2003 Boumerdes Earthquake), masonry wall failure (photo: S. Brzev); (b) India (2001 Bhuj earthquake), (photo: EERI, 2001); (c) Taiwan, (1999 Chi-Chi earthquake) (photog: Charleson, 2008)

The failure mechanisms of the masonry infilled frames are complex because of the high number of parameters involved in the seismic response of the structure such as the material property, configuration, relative stiffness of the frame to the infill, detailing, etc. Experimental results show that masonry infilled frames can experience a wide variety of the failure modes, as shown in Figure 2-2. Mehrabi (1994) defined 24 different in-plane failure mechanisms for infilled frames, based on the experiments on fourteen  $\frac{1}{2}$ -scale single-story frame specimens, which can be narrowed down to three main mechanisms as proposed by Stavridis (2009). These

three mechanisms have been defined such that they describe the full range of behavior exhibited in Mehrabi's tests, as shown in Figure 2-3:

(i) Diagonal cracking in the infill with column shear failure or, more rarely, plastic hinges in columns. This failure typically occurs in weak/non-ductile frames with strong infill;

(ii) Horizontal sliding of the masonry with flexural or shear failure of the columns. Infill crushing is sometimes observed in these tests. This failure mechanism was observed in the weak frames with weak panels and also in the strong and ductile frames with weak infill panels;

(iii) Infill corner crushing with flexural failure in the columns. This mechanism is most likely in strong and ductile frames with strong infill.

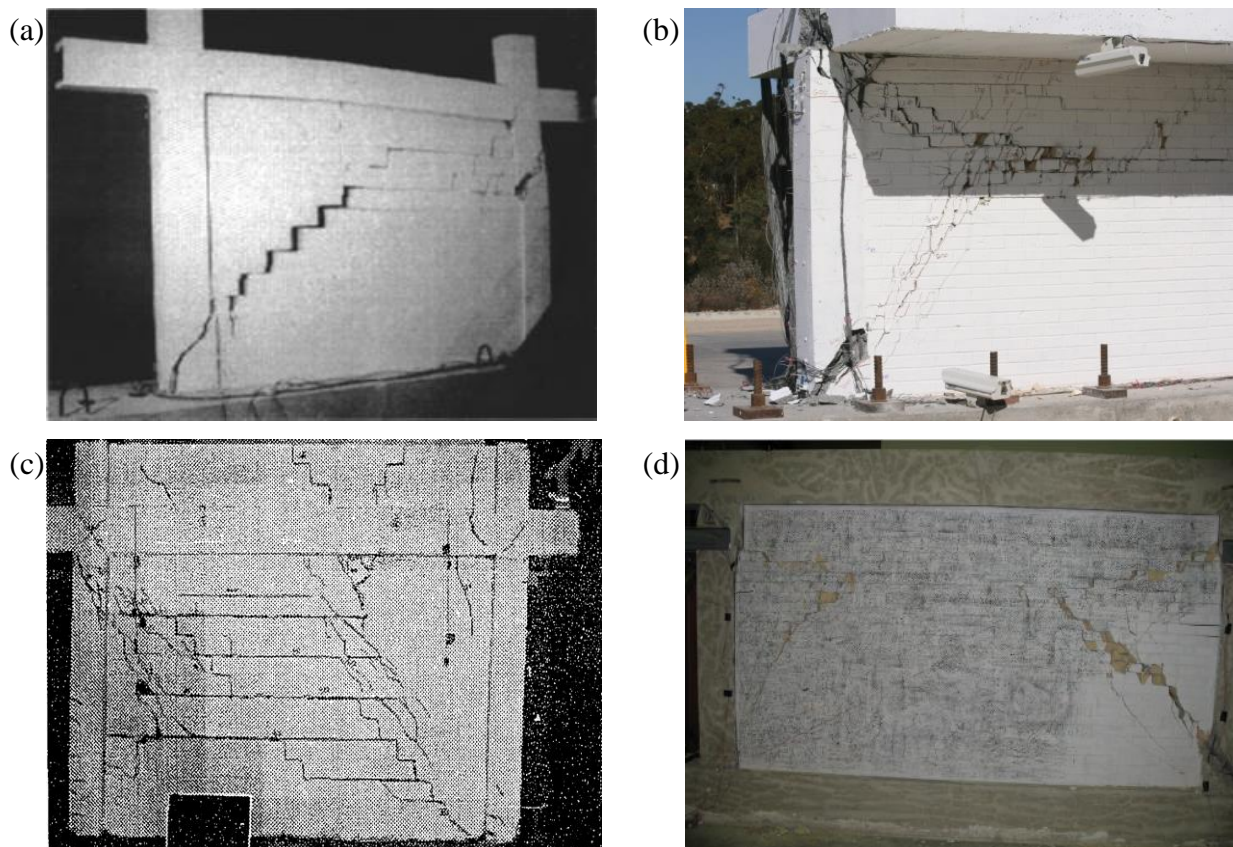


Figure 2-2. Failure mechanisms of the infilled frames observed in the experiments conducted by: (a) Al-Chaar et. al (2005); (b) Stavridis (2009); (c) Mehrabi (1994); (d) Blackard et. al (2009).

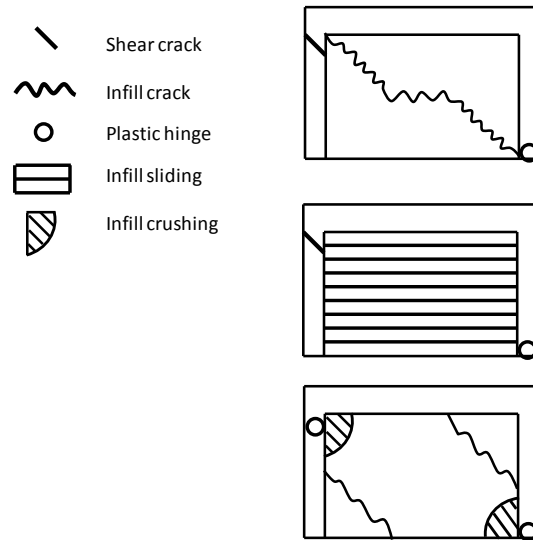


Figure 2-3. Failure mechanisms of infilled frames (Mehrabi, 1994)

Similarly, (El-Dakhkhni et al., 2003) categorized the failure mechanisms of masonry infilled frames into five distinct modes, illustrated in Figure 2-4: (a) corner crushing failure, which is associated with strong frame with weak infill (similar to failure mode (iii) above), (b) sliding shear failure, associated with weak mortar joint infill bounded with strong frame (same as failure mode (ii), above), (c) diagonal compression failure, associated with slender flexible infill walls, (d) diagonal cracking failure, associated with weak frame with relatively strong infill (similar to failure mode (i) above), and e) a frame bending failure mode which is associated with weak frame with weak infill. (Crisafulli, 1997) reported the most common failure mode of the masonry panel from his experimental data is the shear failure of the masonry panel by stepped debonding (mode (i) in Figure 2-3 or mode (d) in Figure 2-4).

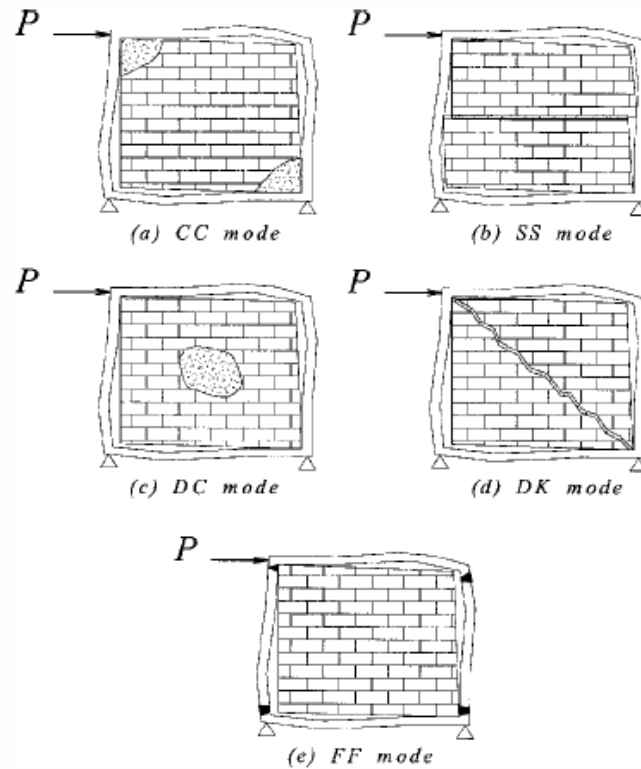


Figure 2-4. Different failure modes of the infilled frames: (a) corner crushing; (b) sliding shear; (c) diagonal compression; (d) diagonal cracking; and (e) frame bending failure (El-Dakhakhni et al., 2003)

An appropriate model for collapse simulation should be able to simulate the response of the structure to include different failure modes. Most of the previous studies, as well as this study, focus on in-plane failure of masonry infilled frames. There are a limited number of studies on the out-of-plane failure of this kind of structures, which will be discussed in Chapter 5. In order to have a better understanding of the behavior of the masonry infilled frame and also knowing the state of the art in this filed, section 2.3 reviews the past studies conducted on the masonry infilled frames.

### 2.3 Previous Research

Several attempts have been made to define the seismic behavior of the both concrete and steel frames with masonry panels and to develop methods for simulating the behavior of this

kind of structure in the past 60 years. Much of this work concentrated on evaluating the stiffness of the infilled frame (Al-Chaar et al., 2002). Infill-frame interaction is also addressed in many studies. The efforts conducted on the masonry infilled frames can be divided into three areas including experimental investigations and two types of analytical investigations, involving macro or micro-modeling approaches. Past research in each of these areas is reviewed in details in the following sections.

### **2.3.1 Experimental Investigations**

This section reviews experimental studies that have been conducted on masonry-infilled reinforced concrete (RC) and steel frames. All these studies focus on the in-plane response of infilled frames. The main difference between the case of RC and steel frames is the relative stiffness of the frame and infill wall. Considering experiments on steel as well as concrete can help us to have a better understanding of the behavior of masonry infilled frames more generally. In this section, past experimental investigations are described in chronological order.

An early study to understand infill-frame interactions was conducted by Polyakov (1960). Polyakov conducted experimental tests on masonry infilled steel frames, first proposing that the infill system works as a braced frame, with the wall forming compression “struts”, as shown in Figure 2-5. These struts are assumed to carry no tension load because of the very low tensile strength of the masonry infill material. In the same year, Sachanski (1960) conducted a set of static monotonic tests on full-scale infilled RC frames in order to check his theoretical approach to compute the stiffness of the combined frame-infill system and distribution of force between the frame and infill. His method is applied to an infilled frame with no separation between frame and wall with elastic, homogeneous, isotropic infill. However, these assumptions may not be realistic.

Later, Holmes (1961) carried out thirteen full-scale and small-scale tests on infilled steel frames subjected to rocking and shear loading. Holmes confirmed the formation of the strut mechanism in the specimen. On the basis of the experimental tests, he proposed that the width of the equivalent strut, denoted  $w$ , should be equal to the one-third of the panel length to compute the maximum strength of the infilled frame. Stafford-Smith (1962) conducted a set of experiments on three infilled steel frames. These observations extended the equivalent strut idea proposed by Polyakov (1960), but led to an alternate method for calculating the effective width of the diagonal strut. The new method for equivalent strut width was supported by test results from mortar panels to measure the stiffness of the panel.

In the light of the smaller number of full-scale tests as compared to reduced-scale tests, Mainstone (1971) and Mainstone and Week (1970) performed monotonic experiments on full-scale concrete-encased steel frames infilled with masonry panels. They also confirmed the strut formation in the masonry infilled frame and proposed an empirical equation to calculate the effective width of the strut as a function of the relative stiffness of the frame and infill and diagonal length of the infill. To develop this empirical equation, they assumed that the effective width of the strut is a function of the diagonal load on the infill at the first diagonal crack and thickness and crushing stress of the infill (both measured from the experiments).

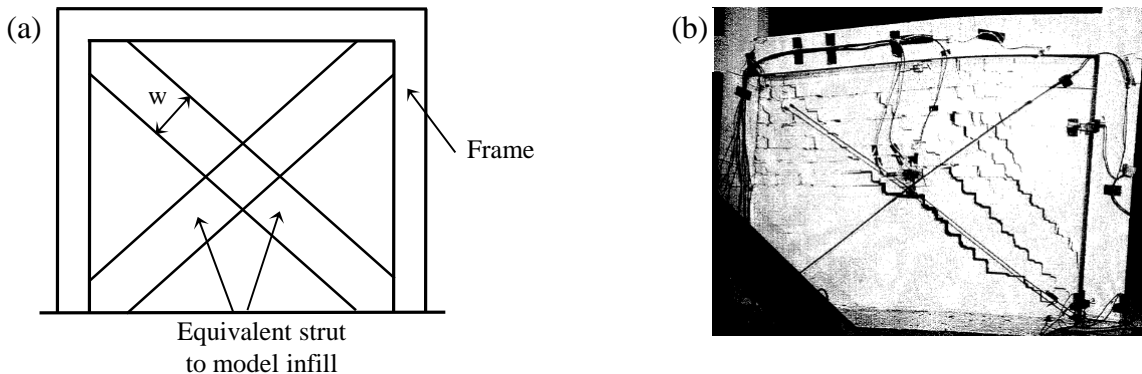


Figure 2-5. (a) Equivalent strut model, (b) Experimental results showing the formation of strut (Al-Chaar, 1998)

Fiorato et al. (1970) performed monotonic tests on 27 1/8-scale masonry brick infilled RC frames. The specimens were different in terms of the number of stories (one, two, and five stories), number of bays (one and two bays), and also in the reinforcement arrangement and quality in the frame, axial load on the columns and the existence of openings in the infill walls. They concluded that existence of the infill increases the stiffness and strength of the infilled frame, but decreases the ductility of the frame. In order to investigate the performance of infilled frame structures more broadly, Klingner and Bertero (1978) tested a 1/3-scale 3.5 story representation of an 11-story 1970s-era RC apartment building. Their study concluded that presence of the reinforced infill panels reduce the risk of incremental collapse, compared to a bare RC frame.

Ten years later, Zarnic and Tomazevic (1988) conducted cyclic tests of 28 specimens including bare and masonry infilled RC frames. These specimens varied in scale (1/2 and 1/3 scale), infill material (clay bricks and concrete blocks), unreinforced and reinforced wall, and the existence of openings (window, door, and no opening). They repaired nine of these specimens after the test using different repair techniques of the infill panel (epoxy grouted, and combination of epoxy-grouting and reinforced cement coating) to investigate the effect of different strengthening techniques. They found a significant increase in strength and stiffness as well as a significant reduction of the ductility of the infilled frame compared to the bare frame. They reported severe strength deterioration after the infilled systems reached their ultimate strength. The study also observed a severe reduction in stiffness of the infilled frame in the cyclic response, as compared to the previous cycles. Mehrabi et al. (1996) tested twelve 1/2-scale single-story single-bay bare and masonry infilled concrete frame specimens and two 1/2-scale

two-bay frames under monotonic and cyclic loading. They observed that the frames with infill showed higher strength and stiffness than the bare frames.

Mosalam et al. (1998) conducted pseudo-dynamic tests on two-bay, two-story masonry infilled steel frames to assess the seismic performance of the infilled frames. The global response and formation of crack patterns was shown to be similar to the results of the static tests conducted in the past. Likewise, Buonopane and White (1999) conducted pseudo dynamic tests on a two-bay, two-story, 1/2-scale masonry infilled non-ductile RC frame, with two openings in the second story. They observed the formation of compressive struts at low force levels. However, for higher force levels, the contribution of the diagonal strut decreased and the stress distribution changed due to bed joint sliding at several locations in the wall. This change in the stress path in the infill implies the use of other strut configuration than single diagonal strut in the modeling. These different strut configurations will be explained in Section 2.3.2. They also suggested using different strut configurations for modeling infill panel with openings.

Al-Chaar et al. (2002) tested four 1/2-scale, single-story, masonry infilled non-ductile concrete frames and one bare frame, under monotonic static loading. These specimens were different in terms of the number of spans (one, two, and three) and infill type (brick and concrete block). Their results showed a significant increase in stiffness, ultimate and residual strength of the infilled frame compared to the bare frame. They also reported that increase in the number of spans increases the maximum strength and stiffness of the infilled frame, but the effect is not linear. They observed that the rate of the strength and stiffness increase is less fast than the increase in the number of bays.

Lee and Woo (2002) performed dynamic and static monotonic tests on a 1/5-scale two-bay three-story masonry infilled non-ductile concrete frame. They reported a large increase in

stiffness, strength, and inertial force (due to added mass) of the infilled frame compared to the bare frame. They also observed that the deformation capacity of the infilled frame remains almost the same as the bare frame. However, they concluded that the increase in the inertial force due to the existence of the infill is less than the increase in the strength, explaining the improved seismic response of the infilled frame compared to the bare frame. They also observed shear failure of columns in the bottom story of the infilled frame. The corresponding bare frame experienced a soft-story mechanism due to the formation of plastic hinges in the columns. Hashemi and Mosalam (2006) conducted a shake-table test on a 3/4-scale one-bay masonry infilled concrete frame that represents a substructure of a five-story prototype. Observations showed the same results as previous tests in the behavior of the infilled frame, such as increase in the stiffness and strength, period shortening, and an increase the damping coefficient from 4 to 5-12% depending on the excitation level.

Anil and Altin (2007) conducted cyclic tests on nine 1/3-scale one-bay, one-story partially infilled ductile RC frames with different configurations and locations of the openings. They observed an increase in the strength and stiffness of the infilled frames compared to the bare frame. Their results also showed an increase in the strength of the infilled frame when the aspect ratio (infill length to the height ratio) increases. Furthermore, they observed a better performance, in terms of strength, for the frames with connections between frame and infill (such as shear keys and anchors). They reported that the fully infilled frame has seven times greater energy dissipation capacity than the bare frame. Blackard et al. (2009) conducted cyclic tests on six 2/3-scale masonry infilled non-ductile RC frames that are representative of a 1920's era building in California. The specimens were different in terms of the existence, configuration, and location of the openings. Moreover, the infill panels in two of the specimens were retrofitted

with an engineered cementitious composite (ECC) material applied to the face of the walls. For the case of small openings, they observed a small difference in stiffness and strength of the infilled frame with one opening compared to specimens without an opening. However, they observed lower stiffness and strength values for the specimen with a large window opening.

Stavridis et al. (2012) dynamically tested a 2/3-scale, two-bay, three-story masonry infilled non-ductile RC frame, as a representation of a 1920's building in California, under scaled historical ground motion records. This frame was fully infilled in one span and had window openings in the other span. They reported shear failure of concrete columns as well as considerable (but still repairable) damage of the structure, when the intensity of the spectra becomes 43% greater than maximum considered earthquake (MCE<sup>1</sup>) for Los-Angeles area. Stavridis et al. (2012) concluded that the selected archetypical infilled frame can behave safely under strong ground motions.

All these experimental studies conducted in the past decades demonstrate the increase in the strength and stiffness the infilled frame compared to the bare frame. Most of these studies reported the formation of the compression struts in the low force range. However, a change of the single diagonal strut mechanism to other mechanisms is also reported for some experiments at higher force levels (Buonopane and White, 1999). Previous studies also showed that the energy dissipation of infilled frame is much larger than the bare frame (Anil and Altin, 2007), while the ductility of the infilled frame is less than the bare frame (Fiorato et al., 1970, Zarnic and Tomazevic, 1988). However, Lee and Woo (2002) reported almost the same deformation capacity for the infilled frame and the bare frame.

---

<sup>1</sup> MCE is now calculated based on the risk targeted method (Luco et al., 2007). At most sites, it is close to the spectral acceleration that has 2% probability of exceedance in a 50-year period. The MCE in this study had spectral acceleration of  $S_s=1.5g$  and  $S_I=0.6g$ , where  $S_s$  and  $S_I$  are the spectral acceleration at 0.2 and one second period.

### 2.3.2 Analytical Investigations: Strut (Macro) Modeling of Masonry Infill Panel

Analytical methods to simulate seismic response of masonry infill panels have advanced alongside experimental research. Based on infill tests by Polyakov (1960) and others, Holmes (1961) proposed a linear equivalent compressive strut model, as shown in Figure 2-5a, for computing maximum strength, stiffness, and deflection at failure of the infill masonry walls. These struts represent the wall by carrying only compressive forces, having zero tensile strength. Holmes (1961) assumed a constant width for the equivalent strut based on results of the monotonic tests on masonry infilled steel frames. Failure was predicted from an assumed ultimate strain and compressive strength of the infill material in the strut.

For decades after this study, researchers have refined methods for computing the characteristics of the struts intended to represent the modeled infill. Stafford-Smith (1962), Mainstone and Weeks (1970), and Mainstone (1971), among others, proposed methods for calculating the effective width of the diagonal strut based on experimental results. The value of the effective width has bearing on both the stiffness and the strength of the strut representing the infill. Stafford-Smith (1962) reported the results of their experiments on mortar panels in terms of a curve, which relates the effective width of the strut model to the length over height ratio ( $L_w/h_w$ ) of the infill panel. Taking a slightly different approach, Stafford-Smith and Carter (1969) developed analytical techniques to calculate the effective width of the strut, and cracking and crushing loads, as a function of the contact length,  $\alpha$ , between frame and infill in its deformed configuration, as shown in (2-1). They expressed the contact length as a function of the non-dimensional parameter,  $\lambda h$ .  $\lambda h$  expresses the relative stiffness of the frame to the infill, as defined in Equation (2-2). Stafford-Smith and Carter considered a variable width for the equivalent strut that decreases as the loading increases, to account for variation of the Young's

modulus of the infill panel with increased cracking. Quantifying the cracking load in addition to the crushing load was one step forward in understanding the nonlinear response of the infill panel.

$$\frac{\alpha}{h} = \frac{\pi}{2\lambda h} \quad (2-1)$$

$$\lambda h = h \left( \frac{E_w t \sin(2\theta)}{4E I h_w} \right)^{0.25} \quad (2-2)$$

$E_w$ ,  $t$ , and  $h_w$  are the Young's modulus, thickness, and height of the infill, respectively. Properties of the frame's columns are  $E$  (Young's modulus) and  $I$  (moment of inertia).  $\theta$  is the angle between diagonal of the infill and the horizontal. Subsequently, Mainstone and Weeks (1970), and Mainstone (1971) proposed two equations (Equations (2-3) and (2-4)) defining the width of the equivalent strut as a function of  $\lambda h$ , based on the experiments conducted on masonry infilled frames.

$$\frac{w}{d} = 0.16\lambda h^{-0.3} \quad (2-3)$$

$$\frac{w}{d} = 0.175\lambda h^{-0.4} \quad (2-4)$$

Equations (2-2) and (2-4) have been adopted by FEMA-273, A SCE-41, and FEMA-306. Liauw and Kwan (1984) developed a semi-empirical equation, as shown in Equation (2-5), to compute the width of the strut as the function of  $\lambda h$ . This equation predicts a bigger equivalent width compared to Equation (2-4).

$$\frac{w}{h \cos \theta} = \frac{0.95}{\sqrt{\lambda h}} \quad (2-5)$$

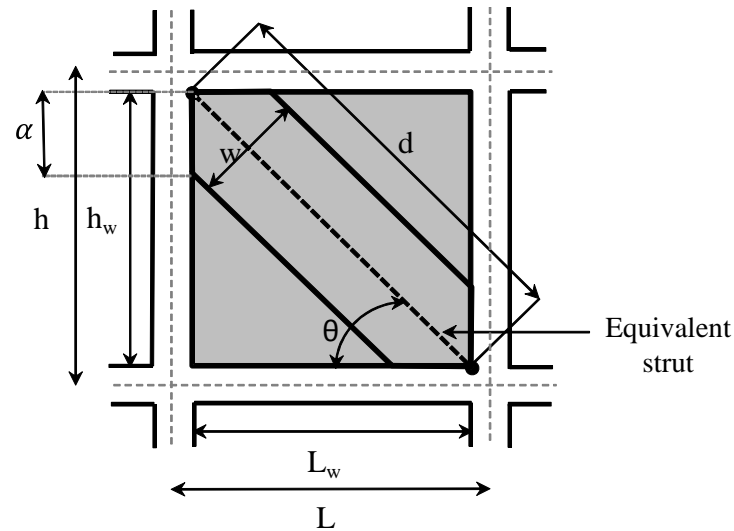


Figure 2-6. Parameters relevant for equivalent strut modeling.

All of these models define the effective width of the strut, which in turn is used to compute the stiffness and ultimate strength of the infill panel. However, they do not specifically define the force-displacement behavior of the strut. One of the early attempts to define the complete force-displacement behavior of the infill panel was conducted by Klingner and Bertero (1976). They proposed a nonlinear hysteretic response for the equivalent diagonal strut model based on the findings of the experiments conducted on masonry infilled RC frames. They considered the strength degradation and reloading stiffness deterioration in their cyclic model, as shown in Figure 2-7. After Klingner and Bertero (1976) considered the nonlinear behavior of the infill panel in the dynamic response, Saneinejad and Hobbs (1995) also tried to predict the nonlinear behavior of the infill panel. They modified the equivalent diagonal strut model to consider the nonlinear behavior of the infill, to account for its low ductility, cracking and crushing load as well varying response due to differences in the infill such as aspect ratio and beam to column strength/stiffness ratio. This bilinear model predicts the initial stiffness ( $k_e$ ), cracking load ( $F_{cr}$ ), crushing load ( $F_{max}$ ), stiffness and displacement ( $\delta_{cap}$ ) at the peak load, as shown in Figure 2-8. However, they did not define the post-peak response of the infill. This

bilinear model was developed based on the experimental and finite element analysis results on steel frames with concrete infill. Equations developed were proposed to be used in design and analysis of the steel infilled frames.

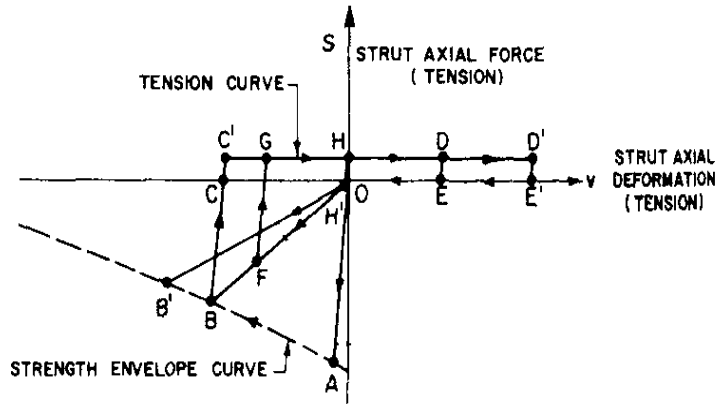


Figure 2-7. Force-displacement response of the strut proposed by Klingner and Bertero (1976).

Continuing to improve understanding of strength and nonlinear behavior of the infilled systems, Zarnic and Gostic (1997) proposed an empirical equation, which was later modified by Dolsek and Fajfar (2008), to compute the shear ultimate strength of the masonry infill panel, as shown in Equation (2-6):

$$F_{\max} = 0.818 \frac{L_{in} t_w f_{tp}}{C_I} \left( 1 + \sqrt{C_I^2 + 1} \right), C_I = 1.925 \frac{L_{in}}{H_{in}} \quad (2-6)$$

Specifically, Dolsek and Fajfar (2008) defined a tri-linear response of the single strut model including an elastic, hardening, and post-capping branch, as shown in Figure 2-9. They arbitrarily assumed a 1:5 ratio for post-capping slope of the infill response to the infill initial stiffness and assumed the cracking load as 60% of the ultimate strength from the Zarnic and Gostic (1997) predictions. They also assumed that the capping displacement occurs at 0.2% drift ratio. For the initial stiffness, they used an equation proposed in ECOEST-PREC 8 Report (1996). This equation predicts the stiffness of the infill as the function of shear modulus and configuration of the infill panel. Flanagan and Bennett (1999) used a piecewise-linear equivalent

strut to model infill and proposed an analytical procedure to calculate the strength of the infill, based on experimental results on steel frames with clay tile infill walls.

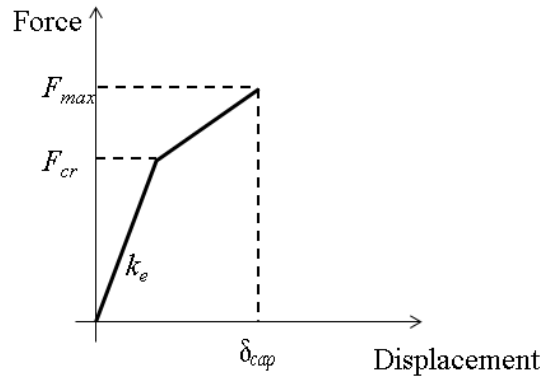


Figure 2-8. Schematic force-displacement response of the infill strut model proposed by Saneinejad and Hobbs (1995).

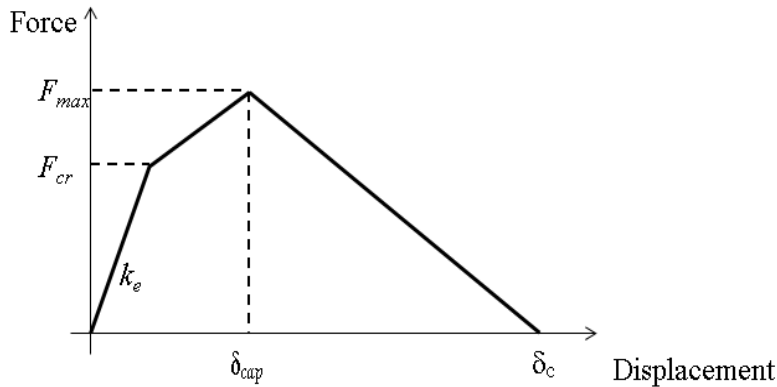


Figure 2-9. Schematic force-displacement response of the infill strut model proposed by Dolsek and Fajfar (2008).

The equivalent diagonal strut approach can model the global force-displacement behavior of the infilled frame, but it is not capable of modeling the masonry panel and frame interaction in local sense, specifically the change in the moment and shear diagram along the column length due to the presence of the panel (Crisafulli, 1997). Several researchers have tried to improve the infill-frame interaction by proposing models with different orientations and number of struts. Symakezis and Vratsanou (1986) initiated one of the early attempts to consider this infill-frame interaction by using five parallel compressive struts in each direction, as shown in Figure 2-10a, to study the effect of the contact length on the moment distribution of the frame. Zarnic and

Tomazevic (1988) attempted to consider this infill-frame interaction by changing the orientation of the struts. They developed an equivalent compressive strut model in which the strut is offset from the diagonal, as shown in Figure 2-10b. They developed this model based on the results of many cyclic tests conducted on infilled RC frames. Schmidt (1989) combined the idea of off-diagonal struts and increased the number of struts, proposing a strut model with offsets at both ends, as shown in Figure 2-10c. Chrysostomou (1991) further altered the orientation of the struts, in order to model the response of the infill panel with three parallel compressive struts (one diagonal and two off-diagonal) in each direction, as shown in Figure 2-10d. All of these models can represent the interaction between the infill and frame more accurately by increasing the number of the points connecting the infill panel to the columns or by changing the location at which the infill transfers load to the columns. However, the complexity and computational effort increase.

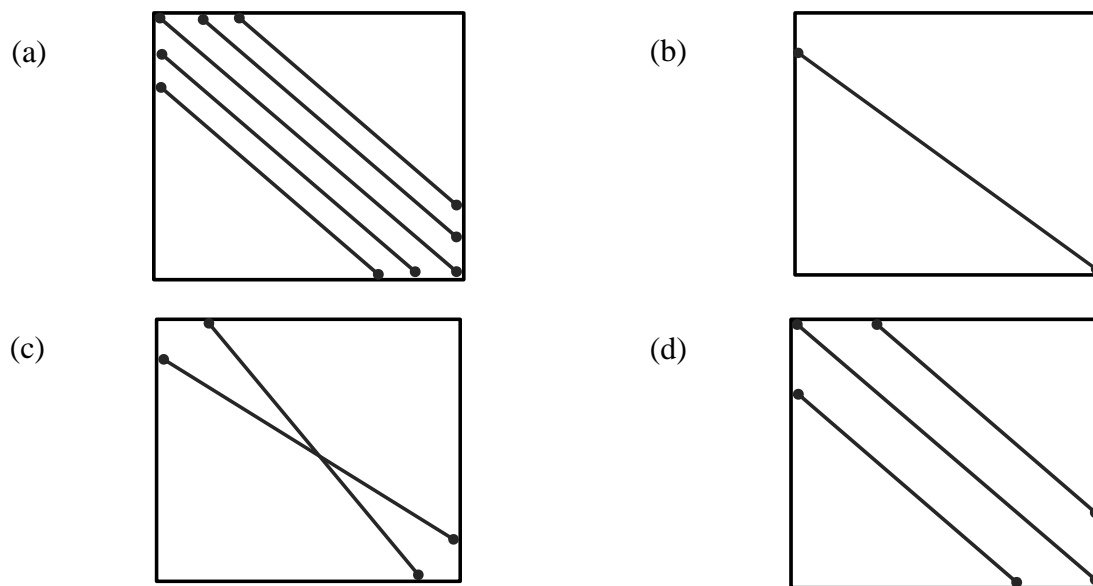


Figure 2-10. Alternative models with off-diagonal struts to model the frame infill interaction proposed by (a) Syrmakezis and Vratsanou (1986), (b) Zarnic and Tomazevic (1988), (c) Schmidt (1989), (d) Chrysostomou (1991). For clarity, struts in only one direction are shown.

More recently, El-Dakhakhni et al. (2003) developed a model with three non-parallel struts, as shown in Figure 2-11, to reproduce the proper moment diagram of the columns in an infilled frame due to the interaction between masonry and frame and also to adequately capture the corner crushing failure mechanism. They defined a tri-linear response including elastic, plastic (ultimate strength), and post-capping branch for the struts, as shown in Figure 2-12.

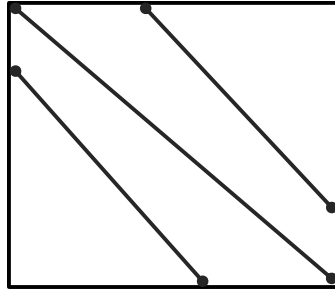


Figure 2-11. Three-diagonal strut model proposed by (El-Dakhakhni et al., 2003)

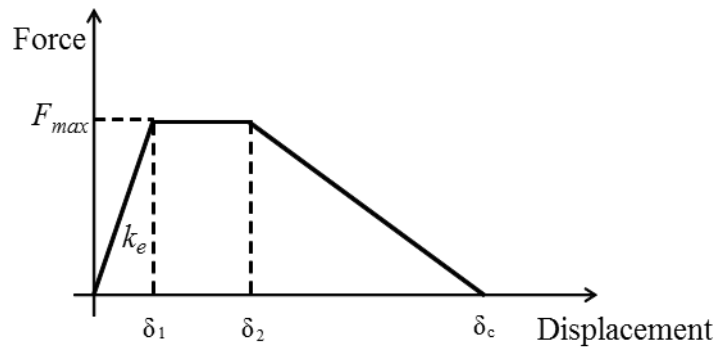


Figure 2-12. Schematic force-displacement response of the strut proposed by El-Dakhakhni et al. (2003).

To better represent the infill wall shear failure mechanism, Crisafulli (1997) proposed a different kind of multi spring model, which is implemented in a 4-node element. The model accounts for the compressive and shear behavior of the infill panel using a nonlinear double-strut and one elasto-plastic shear spring, as shown in Figure 2-13. The shear strength of the spring is evaluated based on the shear-friction mechanism that can represent the shear strength as a function of the maximum permissible shear stress, axial load, and length and thickness of the infill. The area of the struts in this model decreases as the axial strut displacement increases,

because of the reduction of the contact length between frame and infill and, also, due to cracking of the masonry infill. Crisafulli (1997) defined associated hysteretic rules.

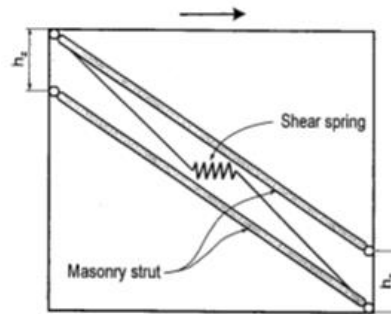


Figure 2-13. Multi-strut with shear spring model (Crisafulli 1997)

This literature review shows a large number of methods to compute different parameters of the strut model. These methods can predict very different values for the characteristics of the infill panel, such as strength and stiffness. Figure 2-14 compares different methods used to compute strength and stiffness of the infill panel for one of the specimens tested by Mehrabi (1994), known as *Specimen 8*. The solid and dashed lines in this figure show the strength and stiffness, respectively, computed based on various methods. A complete description of Mehrabi's test is provided in Chapter 3. This figure shows a large difference among the stiffness and strength predicted by various methods, which implies the need to have an accurate prediction of the properties of the infill panel in the macro-model approach. Table 2-1 summarizes different strut modeling approaches to simulate the infill panel.

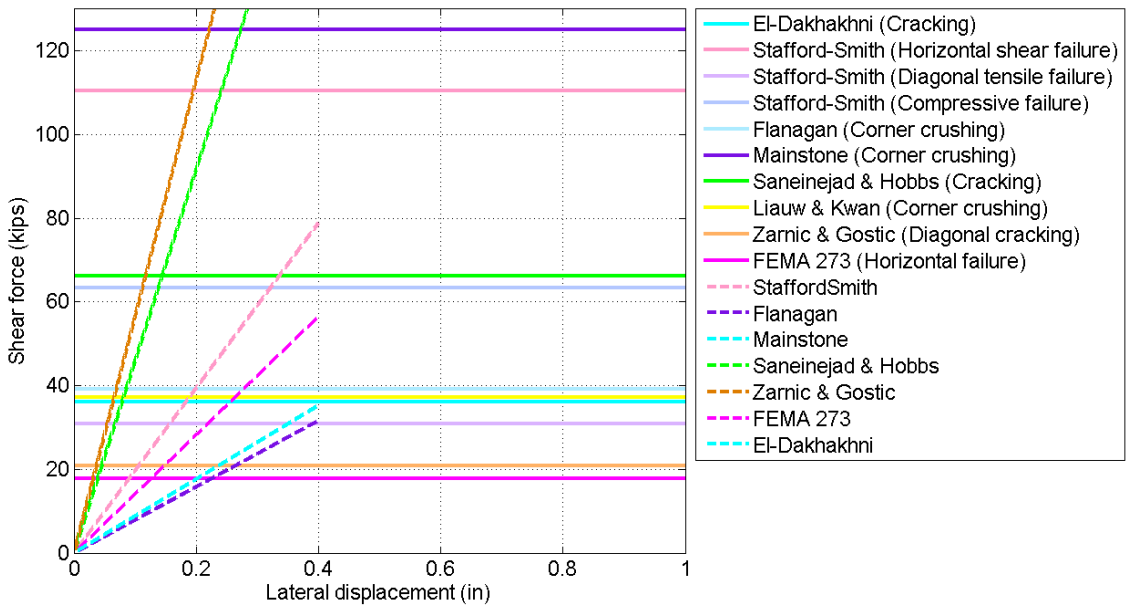


Figure 2-14. Comparison among different methods to compute the stiffness and strength of the infill panel in *Specimen 8* tested by Mehrabi (1994). Solid lines show the strength and dashed lines show the stiffness. Dashed lines are stopped at an arbitrary lateral displacement. For each method, the corresponding failure mechanism is reported in the legend.

Research on the masonry infilled frames is applied in ASCE-41 for evaluation of the existing buildings. ASCE-41 suggests the use of the diagonal inelastic strut modeling for the infilled frames for the purposes of global analysis (ASCE, 2006). However, to account for the effect of the infill on the beams and columns, this document suggests the eccentric struts as shown in Figure 2-15.

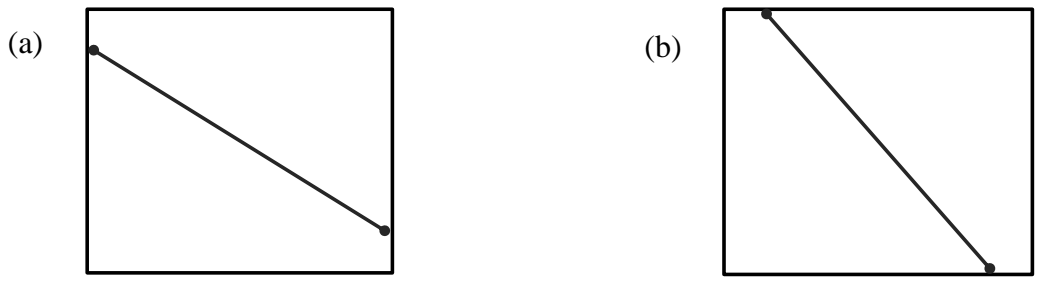


Figure 2-15. Strut configuration proposed in ASCE-41 to compute (a) force in columns (b) force in beams.

Table 2-1. Summary of strut models developed for infill panels.

<b>Authors</b>	<b>Year</b>	<b>Number of struts in each direction</b>	<b>Purpose of the model</b>
<b>Single-Strut Models</b>			
Holmes	1961	1	Modeling the ultimate strength, stiffness, and deflection at failure of the infill
Stafford-Smith	1962	1	Modeling effective width of the equivalent (linear) strut
Stafford-Smith and Carter	1969	1	Modeling stiffness, ultimate strength, cracking load of the infill
Mainstone & Weeks	1970	1	Modeling stiffness and strength of the infill
Mainstone	1971	1	Modeling stiffness and strength of the infill
Klingner & Bertero	1976	1	Modeling the hysteretic response of the infill, as well as strength and stiffness of the infill
Liau & Kwan	1984	1	Modeling stiffness and strength of the infill
Zarnic & Tomazevic	1988	1	Modeling the lateral strength and stiffness of the infill
Saneinejad & Hobbs	1995	1	Modeling nonlinear force-displacement response of infill up to the ultimate load
Flanagan & Bennett	1999	1	Modeling corner crushing strength and stiffness of the infill
Dolsek & Fajfar	2008	1	Modeling the force-displacement response of the infill by a tri-linear response, including post-peak response

<b>Multiple-Strut Models</b>			
Schmidt	1989	2	Modeling the frame-infill interaction as well as strength and stiffness of the infill
Syrmakezis & Vratsanou	1986	5	Considering the effect of the contact length on the moment distribution of the frame as well as strength and stiffness of the infill
Chrysostomou	1991	3	Modeling the frame-infill interaction as well as the hysteretic response of the infill frame under earthquake loading considering stiffness and strength degradation
Crisafulli	1997	2	Modeling the frame-infill interaction as well as accounting for compressive and shear strength of the infill
El-Dakhkhni	2003	3	Modeling the frame-infill interaction as well as corner crushing failure mechanism

### **2.3.3 Analytical Investigations: Finite Element (Micro) Modeling of Masonry Infilled Frames**

Experimental tests of masonry infilled RC frames provide a unique chance for researchers to investigate the complicated seismic behavior of this kind of buildings. However, the high cost of these tests has limited the number of experiments that have been conducted. Macro models, such as strut type models, represent the overall force-displacement relationship of these types of frames. However, the properties of these models can be difficult to validate based on experiments. This difficulty is due to different reasons such as the lack of exact material property of different components of the infilled frame, in an experiment. This lack of knowledge is due to the high material uncertainty involved in the sample. For instance, two prism samples made from the same brick and mortar may not give the same compressive strength of the

masonry. This fact may introduce some errors in the process of the calibration of macro models to the experimental results. These reasons motivated researchers to develop micro-models using finite-element analysis tools to represent complex aspects of masonry infilled frames, including different failure mechanisms observed in the experiments. The finite-element “micro” models require modeling of the frame elements (either steel or reinforced concrete), the masonry bricks, as well as interface between the bricks and at the joint between the wall and the frame. The highly nonlinear behavior of the masonry or infill wall due to the existence of very brittle material such as mortar makes the modeling of this part of the structure very challenging. For this reason, Sections 2.3.3.1 and 2.3.3.2 focus on modeling of the masonry panel/infill. Section 2.3.3.1 provides an overview of different methods for modeling of the masonry wall/infill. This section helps to have a better understanding of the studies conducted by previous researchers presented later in this chapter (Section 2.3.3.2).

### **2.3.3.1 Overview of Different Modeling Schemes for the Masonry Wall/Infill**

Masonry is a highly orthotropic material due to the existence of the mortar joint. In addition, the masonry or infill wall can experience different failure mechanisms, such as cracking, sliding, and compression failure. To simulate the behavior of the masonry wall, different types of models can be developed, depending on the level of accuracy needed, as follows:

#### 1) Micro-modeling:

Micro-modeling is a modeling technique which considers the effect of mortar joints as a discrete element in the model. Considering the fact that mortar joint is the weakest plane in a masonry wall, micro-modeling can be considered to be the most exact modeling approach for the masonry wall. Micro-modeling can be conducted in two levels (Lourenco, 2002):

- Detailed micro-modeling: In this approach, the brick and mortar joints are modeled as continuum elements and interface between the brick and mortar is modeled by an interface element, as shown in Figure 2-16. Both the continuum elements and interface elements may be defined by nonlinear stress-strain relations, as will be described in more detail later. Separate constitutive models are used to define 1) the bricks, 2) the mortar joint and 3) the interface between the mortar and bricks.

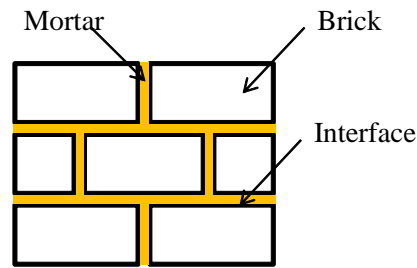


Figure 2-16. Detailed micro-modeling approach for masonry or infill walls

- Simplified micro-modeling or meso-modeling: In this approach, bricks are modeled by continuum elements, but the mortar joint and its interface with bricks is modeled together in an interface element, as shown in Figure 2-17.

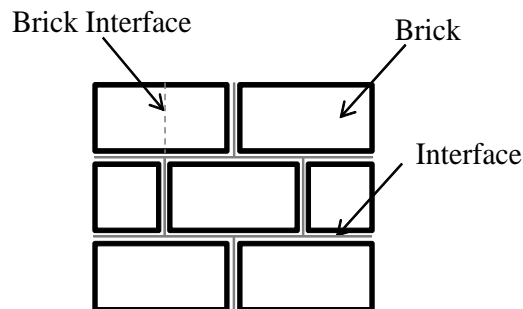


Figure 2-17. Simplified micro-modeling (meso-modeling) approach for masonry or infill walls.

There is another improvement possible for modeling the brick in either the micro-modeling or simplified micro-modeling approaches. Experimental results showed that the diagonal cracking of the infill panel usually goes through the bed joints and head joints. However, cracking sometimes occurs vertically through the middle of the bricks. This could be

due to the dilatation effect of the mortar joints. To capture this mechanism, a vertical interface can be added at the middle of each brick, as shown for one brick in Figure 2-18.

## 2) Macro-modeling

Macro-modeling can be considered in two levels, as following:

- Homogenized model: In this approach, the effect of the brick, mortar, and brick-mortar interface is modeled as one continuum element, as shown in Figure 2-18.

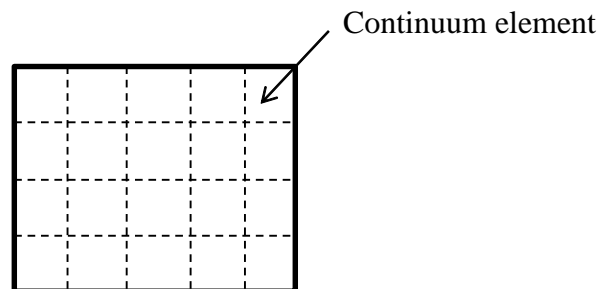


Figure 2-18. Homogenized modeling approach for masonry or infill walls.

- Strut model: In this approach the infill is modeled by one or more struts in each direction. Strut models have been discussed previously.

### 2.3.3.2 Past Research on Modeling of Masonry Infill Walls and Frames

This section reviews the background on finite element modeling of masonry infilled frames as well as masonry walls. Researchers have used the micro, meso and homogenous modeling approaches. Dhanasekar and Page (1986) conducted one of the earliest works in this field. The wall to frame joint was modeled with 1D joint element to model separation and shear failure of the joint and the wall modeled homogenously. They developed a nonlinear orthotropic failure surface to capture the failure of the brick masonry panel. The nonlinear material properties of the infill panel in their work were defined based on the results of biaxial tests on 186 half-scale square panels. They verified their model by comparison with the results of racking

tests of a masonry infilled steel frame and found that the tensile and shear strength of the masonry greatly influences the load-deflection behavior, ultimate strength, and failure mode of the infilled frame.

Lotfi and Shing (1991) studied the efficiency of a homogenous smeared-crack model to capture the response of a reinforced masonry wall. In the smeared-crack model, the uncracked material is considered as an isotropic material and the cracked material is modeled with a nonlinear orthotropic constitutive model. They showed the smeared-crack model can accurately capture the flexural failure of a reinforced masonry wall. However, they showed the brittle shear behavior of the wall coming from the diagonal cracking cannot be captured properly for lightly reinforced wall panels using this method. Instead of using a homogenous approach, Lotfi and Shing (1994) developed a nonlinear interface constitutive model to capture the combined normal and shear stress and also dilatancy observed in the experiments, in combination with their smeared crack model for masonry bricks. They evaluated the performance of their interface model by comparing their results with the available experimental data and showed the correct prediction of shear capacity and dilatancy. (Dilatancy is defined as the vertical displacement of the bricks due to the shear force, which occurs due to the wedging action of asperities (Mehrabi and Shing, 1997).) They also showed the capability of their model to predict the load capacity, failure mode, ductility, and crack pattern of a non-ductile concrete block masonry wall.

Mehrabi and Shing (1997) developed a constitutive model for the mortar joints in masonry infill panels. Their model considered the nonlinear hardening behavior of the interface, the reversal shear dilatancy in cyclic loading, and the contraction of the interface under shear sliding due to the loss of particles. For modeling the bricks, they used 4-node and 9-node smeared crack element to model the bricks in their finite element model for a masonry infilled

RC frame. They used the smeared –crack model to simulate the concrete frame. They showed that their model can simulate the cracking, crushing, and sliding of the masonry infill panel. They also compared their simulation results with the experimental results from cyclic and monotonic tests on half scale specimens of masonry infilled RC frame and found a good agreement in terms of the simulated and observed lateral strength. In the same year, Lourenco and Rots (1997) developed an elasto-plastic constitutive model for interface element. They showed the ability of their model to capture the peak load and post-peak behavior of the masonry shear wall by comparing their results with the experimental results on masonry walls.

Oliviera and Lourenco (2004) developed a constitutive model based on the earlier interface element to simulate the cyclic behavior of the interface element. They used 8-node continuum plane stress element to model the masonry units. They compared their simulation results with static cyclic experiments on three masonry walls (without frames) and showed the ability of their model to capture the stiffness degradation, energy dissipation, and deformed pattern of masonry walls. Most recently, Stavridis and Shing (2009) developed a complex nonlinear finite element model for RC frames with masonry infill, combining the smeared (for masonry units) and discrete crack (for mortar joints) approaches to compensate for the weaknesses of the smeared crack model to capture the brittle shear failure of the masonry mortar joints and RC frame. They used this new element to model the behavior of concrete, brick, and mortar. They used the 4-node smeared-crack element to model the masonry brick. They showed that their model can capture different failure modes observed in experiments such as diagonal cracking, sliding, and crushing of the infill and flexural and shear failure of the concrete columns. Following from Stavridis and Shing (2009)'s work, Koutromanos et al. (2011) used the cohesive crack interface model and an improved smeared crack model to capture the cyclic

behavior of a masonry infilled frame. They validated their results by comparing with the quasi-static and shake table tests and they found a good agreement between the numerical simulation and experimental results for both tests in terms of the hysteresis behavior and failure mechanism.

Table 2-2 summarizes the chronological improvements on modeling the masonry infilled frame and masonry wall. This background shows agreement among different researchers on modeling the brick units. However, modeling the mortar joint is more challenging than brick due to its highly nonlinear and brittle behavior. This motivated many researchers to work to improve the modeling of the mortar joint and interface between bricks.

Table 2-2. Chronological improvements on in-plane modeling the masonry wall/infill

<b>Author</b>	<b>Year</b>	<b>Model Capability</b>	<b>Structure System</b>	<b>Modeling Type</b>	<b>Brick Model</b>
Lotfi and Shing	1991	Captures the flexural response of masonry wall	Wall	Homogeneous	--
Lotfi and Shing	1991	Captures the flexural response of masonry wall	Wall	Simplified Micro-modeling	Smeared-crack
Mehrabi and Shing	1997	Simulates cracking, crushing, and sliding of masonry panel for cyclic and monotonic response	Infilled RC Frame	Simplified Micro-modeling	Smeared-crack
Lourenco and Rots	1997	Simulates cracking, crushing, sliding, and collapse load of the masonry wall for monotonic response	Wall	Simplified Micro-modeling	
Oliviera and Lourenco	2004	Improves the 1997 model to capture the cyclic behavior of masonry wall	Wall	Simplified Micro-modeling	Smeared-crack
Stavridis and Shing	2009	Combining the smeared and discrete crack approaches to compensate for the weaknesses of the smeared crack model to capture the brittle shear failure of masonry infill	Infilled RC Frame	Simplified Micro-modeling	Smeared-crack
Koutromanos et al.	2011	Enhance the 2009 model to capture the cyclic behavior of the masonry wall in dynamic tests	Infilled RC Frame	Simplified Micro-modeling	Smeared-crack

### **3 Development of Micro-model of Masonry Infilled RC Frames for Use in Proposed Macro-Model**

#### **3.1 Introduction to the Proposed Macro-Model**

Experimental tests of masonry infilled reinforced concrete (RC) frames provide a unique chance for researchers to investigate the complicated seismic behavior of this kind of building. However, the high cost of these tests has limited the number of experiments that have been conducted. Macro models, such as strut-type models, represent the overall force-displacement relationship of these types of frames in computationally efficient models (Crisafulli, 1997). However, the properties of such models can be difficult to validate based on experiments. This difficulty is due to different reasons, especially the uncertainties in the material properties of the different components of the infilled frame used in the experiment, which prevent a direct comparison between the experiment and macro-model in the calibration process. These reasons motivated researchers to develop micro-models using finite-element analysis tools to represent complex aspects of masonry infilled frames, including brittle failure mechanisms in the infill at mortar joints and the infill-frame interaction. Micro-models provide a chance to simulate the response of masonry infilled frames with different configurations with a lower cost compared to the experiment with no uncertainty in the material properties in the macro-model calibration process. Moreover, micro-model can potentially represent the multiple failure modes which can occur in the infill or frame. Although micro-models has been shown to accurately simulate the response of infilled frames (Stavridis et al., 2012), the approach is computationally intensive and is not practical to be implemented in the PBEE frame work where a nonlinear model needs to be run for a suite of ground motions scaled to different levels. The computational difficulty of micro-modeling shows the need for a more simplified modeling approach, such as strut-type

models, which, if appropriately developed, satisfies the both the needs of accuracy and efficiency.

The primary objective of this study is to propose a macro-modeling approach that relies on micro-modeling results to calibrate the parameters needed in a strut-type model for masonry infilled RC frames, which can be used in the PBEE framework to assess the seismic collapse performance of existing concrete buildings with masonry infill panels. For this purpose, we first need to develop a micro-modeling technique for this type of building. The micro-modeling approach is developed through the calibration of a model for an existing experimental case and comparing the numerical and experimental results. Then, the properties of the proposed macro-model including configuration, number, and force-displacement response of the struts, will be developed in Chapter 4 based on the results of the micro-modeling approach presented in this Chapter.

### **3.2 Introduction to Micro-modeling of Masonry Infilled Frames**

This study uses micro-models of masonry infilled RC frames to calibrate the seismic behavior of macro-models. Finite-element analysis of “micro-models” requires modeling of the frame elements (either steel or reinforced concrete), the masonry bricks, as well as interface between the bricks and at the joint between the wall and the frame. The highly nonlinear behavior of the masonry or infill wall due to the existence of very brittle material, including the bricks and mortar, makes the modeling of this part of the structure very challenging. This chapter describes the proposed micro-modeling approach for finite element analysis of RC frames with masonry infill. The micro-modeling approach is validated through comparison with results from experimental tests.

### **3.3 Development of Calibrated Finite Element Model for Masonry Infilled RC Frames**

Experimental results (Mehrabi, 1994) showed different in-plane collapse mechanisms experienced by masonry infilled RC frame. These mechanisms can involve the formation of diagonal cracks through the mortar joints or bricks, sliding along the bed joints, compression failure of the masonry, and flexural and/or shear failure in the columns. To make a good simulation of this kind of structure, the finite element model needs to be able to capture these different behaviors of the real structure. The micro-modeling of masonry infilled frame can be implemented in different software platforms, with different material models, etc. The goal of this section of study is to develop a micro-model for a masonry infilled frame tested previously with the available experimental results. The goal here is not the creation of new material models or modeling approaches, but the development of a validated modeling approach using an existing software package. The reliability of the modeling procedure is evaluated by comparing micro-model results with experimental results. This validated approach will be used later to simulate the response of the infilled frames for which no experimental results are available. After demonstrating the feasibility of micro-modeling procedure, the same procedure will be used to model archetypical buildings for which there are no corresponding available experimental results in Chapter 5.

#### **3.3.1 Selection of Software for Modeling of Masonry Infilled RC Frames**

There are different nonlinear finite element software packages available to simulate the behavior of the masonry infilled RC frames. Each of these software tools has some capabilities to model the nonlinear behavior of concrete, bricks or mortar interfaces. Al-Chaar and Mehrabi (2008) reviewed the capabilities of different software including ANSYS, ABAQUS, ADINA, and DIANA for modeling the discrete cracking behavior of the mortar joints and representing the

nonlinear behavior of concrete and bricks in the in-plane mode. The comparison focused on the capabilities of different software to model the cracking in the mortar joints, separation of the mortar joints, crushing of the infill, and shear degradation properties of the mortar joints, concluding that DIANA is the best available tool to model this kind of structure (DIANA, 2011). Based on their findings, this study uses DIANA to model the masonry infilled RC frame.

Different materials in the masonry infilled frames including concrete, bricks, and mortar can be modeled using material models available in DIANA. Section 3.3.2 introduces the material model selected to model the concrete frame, bricks, and mortar interface, reviewing the input parameters for each of these material models in DIANA. After defining these material properties, Section 3.4 goes through the validation of each of the material models as well as input parameters for the selected experimental specimen.

### **3.3.2 Overview of Micro-Model**

Figure 3-1 provides an illustration of the proposed finite element model for the masonry infilled RC frame for a one-bay frame. In this study, a smeared-crack continuum model will be used for bricks, employing two-dimensional plane stress 4-node quadrilateral elements with 2x2 Gauss points. A line interface element will be used to model the bed joint, head joint, wall to frame joint. The smeared crack model is adopted to model the concrete in the reinforced concrete frame. The concrete elements as well as brick elements are modeled with 4-node quadrilateral element. Reinforcement is modeled using the 1-D truss element with elastic-hardening-plastic material model. The constitutive model of smeared crack and interface models will be explained in detail in the Sections 3.3.2.1 and 3.3.2.2. The model is capable of capturing the most important characteristics of the masonry infill such as cyclic shear sliding along the mortar joints, tensile cracking of the mortar joints, tensile and compression cracking of the bricks. The

model aims to simulate the in-plane response of frames with different infill types, such as hollow or solid bricks.

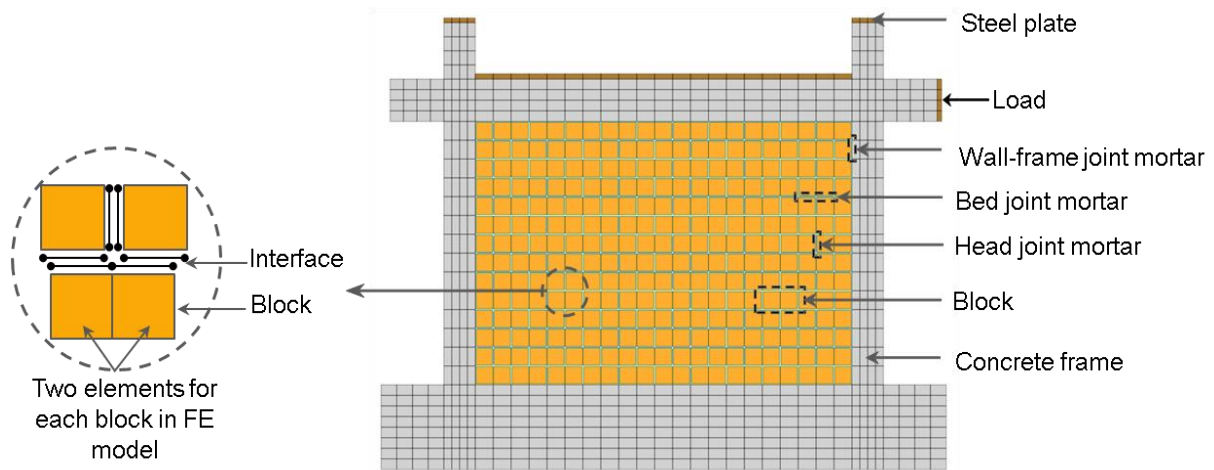


Figure 3-1. Nonlinear finite element (micro) model for masonry infilled RC frame.

### 3.3.2.1 Proposed Smeared-Crack Model for Concrete Frame and Bricks

In a smeared-crack model, cracks may develop throughout a continuum element without defining discrete elements at the crack locations. Lotfi and Shing (1991) showed the advantages of using this type of element to model masonry walls. Literature review also showed the general agreement among researchers on using this model for the masonry units and concrete in the frame (Mehrabi and Shing 1997, Stavridis and Shing 2009). The basic concept of the smeared crack model combines the failure surfaces in tension and compression to identify crack opening and define the crack orientation, considering material softening. Cracking occurs in a smeared crack model if the principal tensile stress is greater than the maximum tensile strength defined by the failure surface.

The total strain crack model is one type of smeared-crack model implemented in DIANA, which formulates the strain without decomposing it into different components, and is used in this study. This crack model has different types: including the fixed crack model, in which the crack angle remains the same after crack initiates, and the rotating crack model, in which the crack

direction updates in each analysis step following the direction of current principal stresses. This study uses the rotating crack model to model both the masonry units and concrete frame, due to the simplicity and good performance of this modeling approach for concrete frames (Li and Zimmerman, 1997).

In all of the different types of the total strain crack model, the material is considered isotropic before cracking occurs. In the rotating total strain crack model, the crack direction is normal to the principal stress and rotates during the analysis with the principal strain axes such that it always remains perpendicular to the direction of principal strain. Different types of tensile behavior can be defined for the total strain crack model, as shown in Figure 3-2. These models are mainly different in the tensile softening property. This study uses exponential tensile behavior, which is a widely used model for tensile behavior of concrete (Al-Chaar and Mehrabi, 2008; Mehrabi, 1994). To define this tensile behavior, three parameters need to be defined: the maximum tensile strength,  $f_t$ , the first mode fracture energy,  $G_f^I$ , and the crack bandwidth,  $h$ . The first mode fracture energy,  $G_f^I$ , is defined as the energy needed to create a crack opening with unit area (Lourenco, 1998). This energy is dissipated due to the irreversible damage associated with the cracking (Lourenco, 1996). One of the drawbacks of smeared crack model is that the fracture energy depends on the size of the elements defined in the model. To solve this issue, a length scale called the crack bandwidth, is defined, such that results are independent of mesh size. The crack bandwidth is defined as the square root of the twice of the element area,  $\sqrt{2A}$ , for 2D elements with linear shape functions, in DIANA.

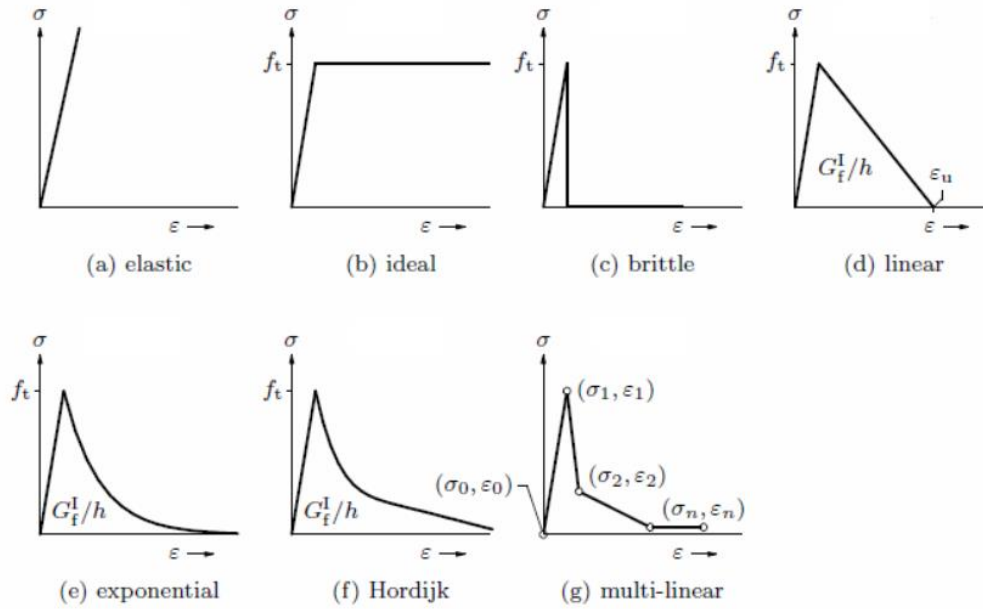


Figure 3-2. Different types of tensile behavior in total strain crack model (DIANA, 2011).

In addition to the tensile behavior, materials such as concrete or masonry may crush under excessive compressive stress. Different compressive behavior can be considered for smeared-crack model, as shown in Figure 3-3. Among these methods, those that consider compression softening, *i.e.* Thoren and Parabolic, are more popular for materials such as concrete, due to the fact that they can model the observed softening behavior the concrete. To define the Parabolic compression curve, which is used in this study, as well as similar studies (e.g. Al-Chaar and Mehrabi, 2008), three parameters including  $f_c$ ,  $G_c$ , and  $h$  need to be defined.  $f_c$  is the maximum compressive strength of the material.  $G_c$  is the compressive fracture energy defined as the area under the compressive stress-strain curve from strain at maximum stress to the ultimate strain, and  $h$  is, again, the crack bandwidth.

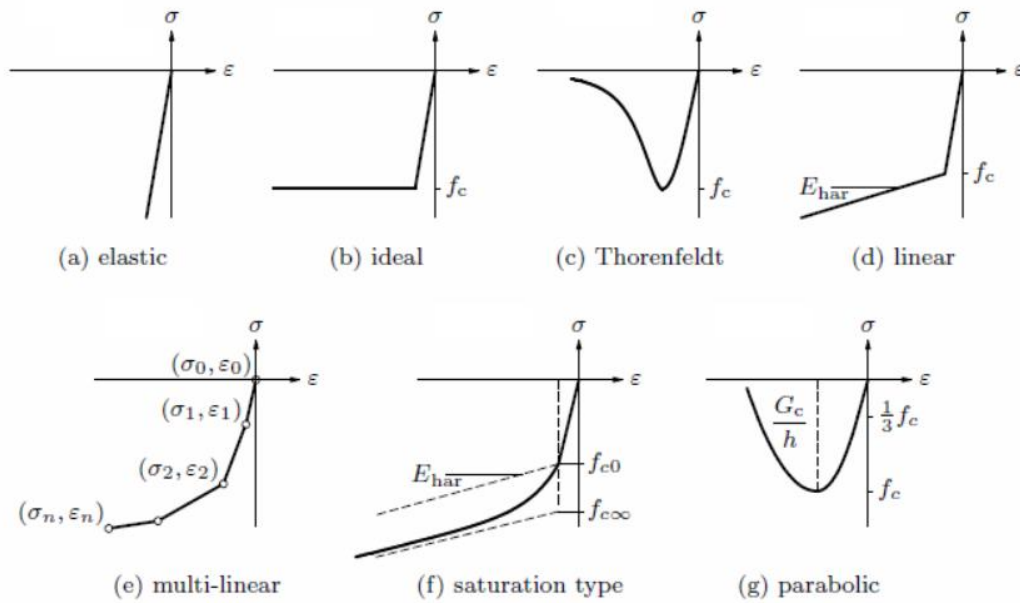


Figure 3-3. Different types of compressive behavior in total strain crack model (DIANA, 2011).

### 3.3.2.2 Proposed Interface Material Model

In the proposed micro-modeling approach, the discontinuous behavior between bricks and mortar is modeled using an interface element. The interface element is able to capture different possible failure mechanisms of the masonry joints such as sliding, tensile cracking, and crushing (Lourenco, 1996). DIANA's interface material model called "Combined Cracking-Shearing-Crushing" is used in this study. This model is able to model first-mode (tensile cracking) and second-mode (shear cracking) fracture failure, as well as compressive failure. These characteristics make this element suitable for modeling the brick-mortar interface. The model works by combining different yield surfaces, including tension, shear, and compression with softening in all three modes (Lourenco, 1996), as shown in Figure 3-4. In the following, each of these three yield surfaces is described in more detail.

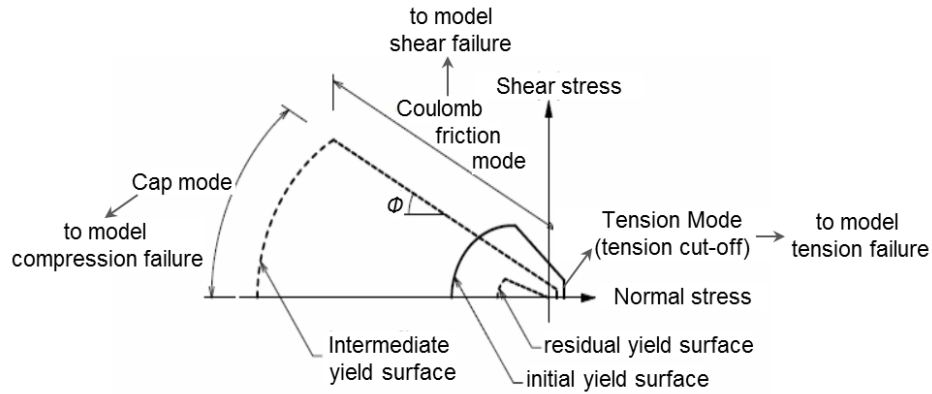


Figure 3-4. Two-dimensional interface model (adapted from Lourenço and Rots 1997). Notation defined in Equation (3-1).

### Tensile Behavior

The tensile cracking of the interface material is modeled with a tension cut-off with exponential softening. The tension cut-off is shown with a vertical line in the positive region of  $\sigma$  in Figure 3-4. This tension cut-off simulates the brittle failure of mortar joint under tensile force. The exponential softening behavior in tension is consistent with experimental results from Pluijm (1992) (Lourenco, 1994).

### Shear Behavior

The shear behavior of the interface element is modeled with the Coulomb friction yield surface, defined in Equation (3-1):

$$f = |\tau| + \sigma \tan(\phi) - c \quad (3-1)$$

Where  $\phi$  is the friction angle,  $c$  is the cohesion,  $\tau$  is shear stress, and  $\sigma$  is the normal stress. This interface material model considers exponential softening for both the cohesion and friction angle. The softening of the friction angle is assumed to be proportional to the softening of the cohesion (Lourenco, 1994). The dilatancy effect and strain softening behavior is also incorporated in this model. This interface model does not consider the cumulative damage due to the loss of mortar material (Al-Chaar and Mehrabi, 2008).

### Compressive Behavior

To model the compressive failure of the mortar joints in this model, a compression cap is added to this multi-surface plasticity model, as shown in Figure 3-4 by the label “cap mode”. This compressive cap enables the model to capture the crushing behavior of the mortar joint. This cap-model is representative of the maximum compression strength of the interface element. The softening or hardening of the compression cap follows the compressive stress-strain relationship of the material shown in Figure 3-5, where  $\kappa$  represent the amount of softening (Lourenço and Rots, 1997). Table 3-1 lists the parameters needed to define the interface model in DIANA.

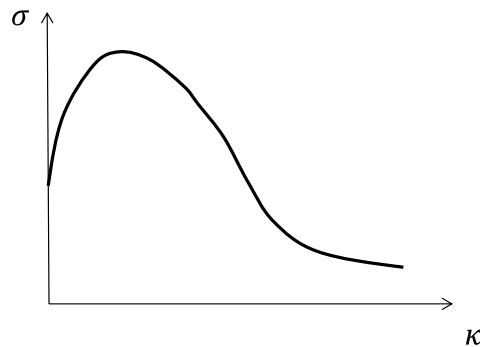


Figure 3-5. Nonlinear compressive behavior of the cap model (Lourenco, 1996).

Table 3-1. Modeling parameters and their definition for the interface model

<b>Parameters defined in interface model</b>	<b>Definition</b>
$K_{nn}$	Normal stiffness modulus (psi/in)
$K_{ss}$	Shear Stiffness modulus (psi/in)
$C$	Cohesion (psi)
$\phi$	Internal friction angle (radian)
$\psi$	Dilatancy angle (radian)
$\phi_r$	Residual friction angle
$\sigma_u$	Confining normal stress (psi)
$\delta$	Softening parameter (dilatancy degradation coefficient)
$f_t$	Tensile strength (psi)
$G_f^I$	Fracture Energy for Mode-I (lb/in)
$G_f^{II}$	Fracture energy for Mode-II (lb/in)

$f_c$	Compression strength (psi)
$C_s$	Shear traction contribution to the failure
$G_{fc}$	Compressive fracture energy (lb/in)
$\kappa_p$	Relative plastic displacement at peak compressive strength (in)

### 3.4 Model Calibration and Validation through Finite Element Modeling of a Masonry Infilled Reinforced Concrete Frame Specimen

#### 3.4.1 Overview

The objective of this part of the study is to create a finite element model of a masonry infilled non-ductile concrete frame that represents a frame that has been tested experimentally by Mehrabi (1994). The results of this section improve our understanding of the behavior of the masonry infilled frame, especially in terms of the wall-frame interaction, and provide verification of the finite element modeling approaches that will be used in the later sections to model other frames and to calibrate the strut model.

The characteristics of the experimental specimen being modeled are explained in Section 3.4.2. To construct the finite element model, the parameters defining various features of the model, such as brick and mortar, need to be calibrated to the experimental values. Sections 3.4.3.1 to 3.4.3.3 explain the calibration process for each of the different constituent components. In Section 3.4.3.4, the bare concrete frame is modeled and calibrated to the experimental results for the bare frame to ensure that the concrete frame is modeled properly. Finally, in Section 3.4.3.5, the finite element model for the masonry infilled frame is developed and results are compared with the experimental results.

### 3.4.2 Experimental Tests

Mehrabi (1994) conducted several monotonic and cyclic tests on half-scale bare and masonry infilled concrete frames with different infill and frame properties, as well as different geometric characteristics (*e.g.* varying aspect ratio and number of spans). This set of experiments is selected here due to the comprehensive data available for the tests, including data required for developing the micro-model, as well as the experimental explanation of failure mechanisms. This study selects one of these specimens, known as *Specimen 8* in Mehrabi's study, which represents an RC frame designed for gravity and wind loads (*i.e.* not seismic loads) with a hollow concrete brick infill panel. This specimen is representative of an interior bay of a six-story, three-bay RC frame (Mehrabi, 1994). This model is selected because no shear failure of concrete columns is reported in the experiment, which makes the modeling of this specimen easier and also helps us to focus more on the response of the infill panel by eliminating the complexity of capturing the shear failure of the concrete frame. Figure 3-6 shows the geometry of the selected specimen, as well as the member sizes and reinforcement detailing of the infilled frame. This specimen is subjected to a constant (downward) vertical force during the test shown by  $P_2$  and  $P_3$  in this figure, where  $P_2$  is 22 kips and  $P_3$  is 11 kips. The lateral load  $P_1$  is applied monotonically during the test. The infill panel is made of hollow concrete bricks with type S mortar. The configuration of the brick is shown in Figure 3-7. The shaded area in Figure 3-7 shows the mortar applied on the brick top surface. The thickness of the mortar (*e.g.*, in the  $z'$  direction in Figure 3-7) in both bed joints and head joints in this specimen is 3/8 inches.

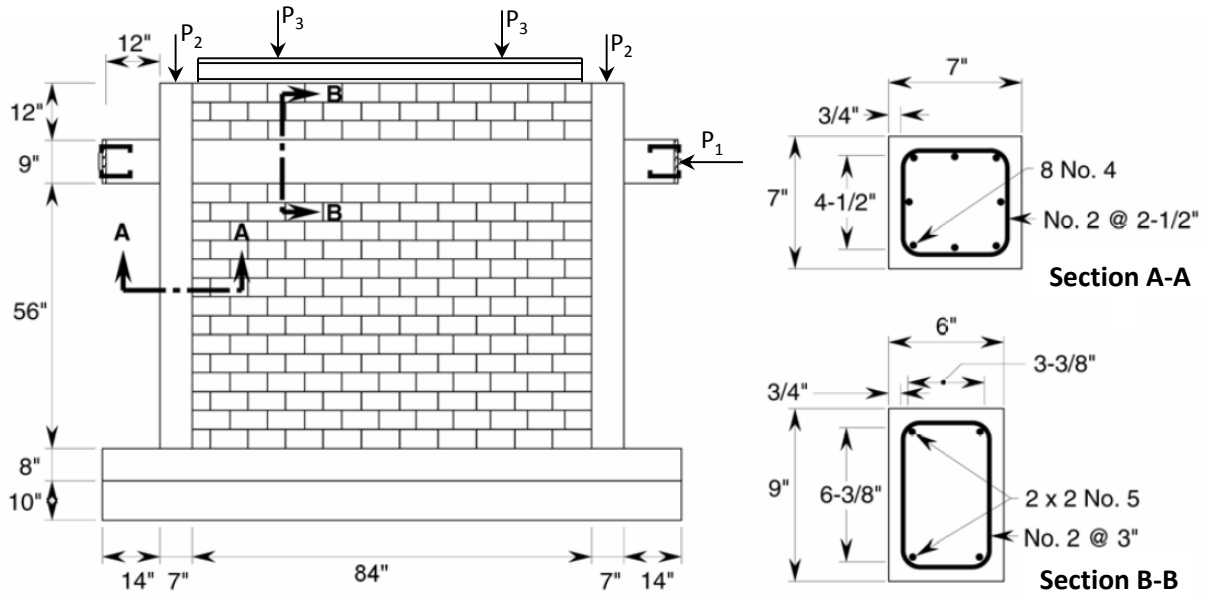


Figure 3-6. Details of the test specimen (Al-Chaar and Mehrabi, 2008).

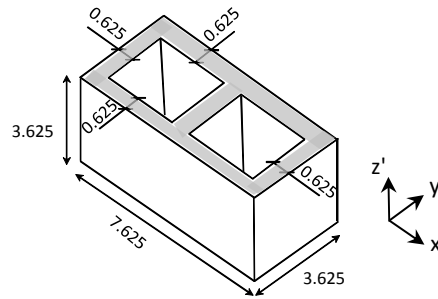


Figure 3-7. Geometry of hollow concrete bricks used as infill (dimensions are in inches).

### 3.4.3 Proposed Finite Element Model for Experimental Specimen

Figure 3-1 provided an overview of the finite element model for the masonry infilled RC frame that was tested experimentally. It is composed of nonlinear interface elements representing the mortar-brick interface, as well as the wall-frame interface. The element types adopted in this study to model the concrete, brick, mortar, and rebar were explained in Section 3.3.2. The process of calibrating the material properties is very similar to that presented by Al-Chaar and Mehrabi (2008) based on the same test. The calibration is described in detail here to provide confidence in the finite element modeling approach for later different models that will be based

on this first model. The sections that follow first discuss the calibration of the mortar-joint interface. Then, it goes through the validation and calibration of smeared-crack models for concrete frame and brick. Finally, the composite modeling of the bare frame and infilled frame will be presented.

### 3.4.3.1 Calibration of Model for Mortar Brick Interface

This section explains the calibration process of the interface element for modeling the mortar-brick interface in DIANA. A similar interface element is used for modeling the wall-frame interface. The interface element used in this study is a 1D interface element, as shown in Figure 3-8, and its properties were explained previously (Section 3.3.2.2). To calibrate the properties of the interface element, the experimental data from tensile and shear tests of mortar joints are desirable. However, only cyclic shear experimental data for one layer of mortar located between two bricks is available in this case.

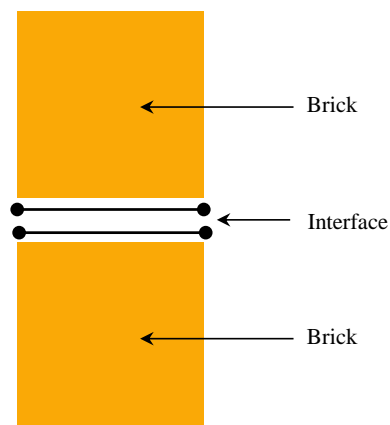


Figure 3-8. 1D interface element between two shell elements (bricks).

To examine the performance of the interface element in tension, the interface element is modeled between two elastic bricks and is analyzed under a tensile (normal) displacement, as shown in Figure 3-9a. The input parameters of the interface element are reported in row 1 of Table 3-2. These input parameters are identical to those recommended by Mehrabi (1994)

because there is no experimental data available for the tensile test. Figure 3-10a shows variation of the tensile stress of the interface element with respect to the vertical relative displacement of two bricks (joint opening), with a maximum tensile strength of the interface element as 38.3 psi. Model results also show the softening of the response after reaches to the maximum strength. This softening is due to the joint opening and matches with the experimentally observed shape of such softening noted by Al-Chaar et al. (2008).

Table 3-2. Model interface properties, illustrating the process of determining, first, tensile properties (row 1), second, monotonic shear properties (row 2), third, cyclic shear properties (row 3), fourth, dilatation (row 4), and fifth, prism sample (row 5).

Behavior	$K_{nn}$ (lb/in <sup>3</sup> )	$K_{ss}$ (lb/in <sup>3</sup> )	C (psi)	$\Phi_i$ (deg)	$\Psi$ (deg)	$\Phi_r$ (deg)	$\sigma_c$ (psi)	$\delta$	$f_t$ (psi)	$G_r^I$ (psi-in)	$G_r^{II}$ (psi-in)	$f_c$ (psi)	$C_s$	$G_{fc}$ (psi-in)	$\kappa_p$ (in)
(1) Tensile	28000	--	--	--	--	--	--	--	40	1.69	--	--	--	--	--
(2) Shear	28000	35000	40	45.3	--	37.3	--	--	40	1.69	16.1	--	--	--	--
(3) Cyclic Shear	28000	35000	26	47	--	42	--	--	40	1.69	16.1	--	--	--	--
(4) Dilatation	28000	35000	26	47	0.29	42	-150	2	40	1.69	16.1	1500	1	22	0.006
(5) Prism	280000	350000	26	47	0.29	42	-150	2	40	1.69	16.1	1500	1	55	0.006

In the next phase of the verification of the behavior of the interface element, the same model is analyzed for incremental shear displacement applied to the top brick (direct shear test) under no vertical load, as shown in Figure 3-9b. The input parameters corresponding to the shear behavior of the interface elements are reported in the row 2 of Table 3-2. Variation of the shear strength with respect to the applied shear (horizontal) displacement is shown in Figure 3-10b. This figure shows the softening behavior of the shear response after the maximum shear strength is reached. This general trend of the softening behavior is in agreement with the observation of the first cycle of the cyclic shear test conducted on the interface by Mehrabi (1994).

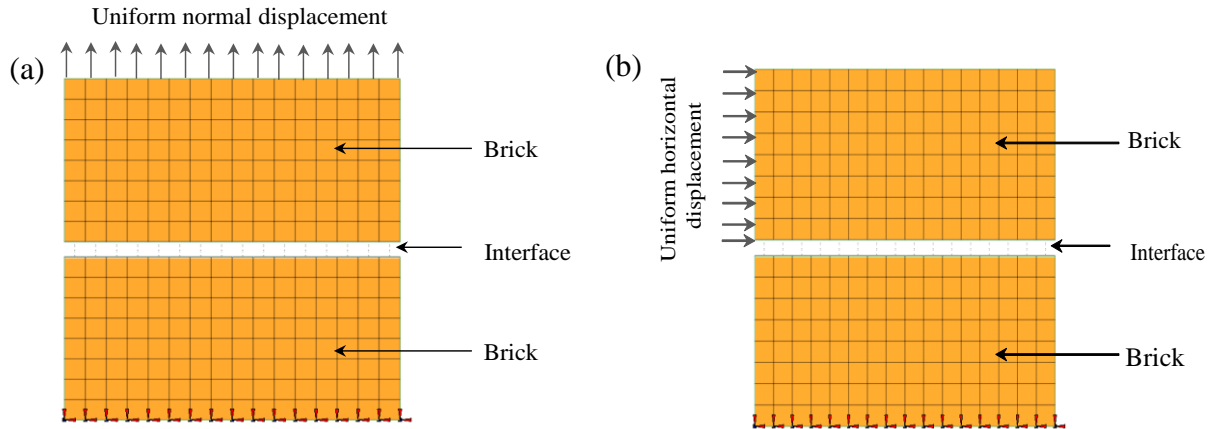


Figure 3-9. (a) Tensile test on an interface element (mortar joint) located between two bricks; (b) Shear test of the interface model for the mortar joint.

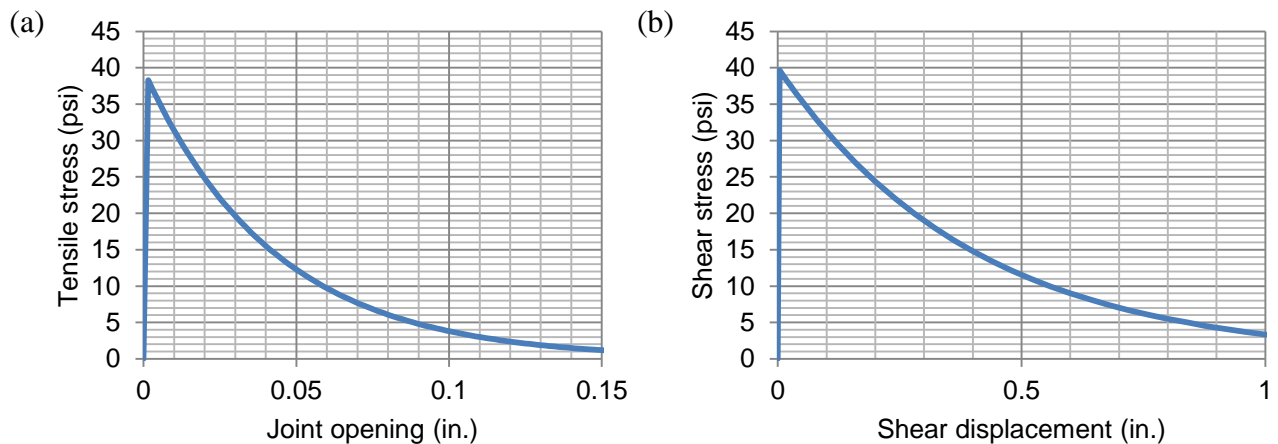


Figure 3-10. (a) Tensile stress vs. joint opening under monotonically applied vertical displacement and (b) Shear stress vs. shear displacement under monotonically applied horizontal displacement of the modeled interface element.

To validate the cyclic behavior of the DIANA interface element, the model is calibrated to the single set of available results of the cyclic test on the tested mortar joint. In the experiment, the shear cyclic displacement is applied to the mortar placed between two bricks, under constant normal pressure of 100 psi (Mehrabi, 1994). To simulate this experiment, the same DIANA model illustrated in Figure 3-9 is analyzed for cyclic displacement applied to the top brick. The input parameters of the interface element are then varied to achieve a good match between the numerical and experimental results.

Figure 3-11 shows the shear stress versus shear displacement of the DIANA model compared to the experimental results for the cyclic shear test of one layer of mortar located between two bricks, indicating a good agreement between the two responses. Figure 3-11 also shows that after the interface element reaches its maximum shear strength, *i.e.* initiation of shear mortar failure, the element softens and approaching a residual strength of 100 psi. This residual strength remains almost constant during the analysis to the displacements tested of 0.3 inches. The third row in Table 3-2 shows the calibrated input parameters of the interface element for the cyclic behavior.

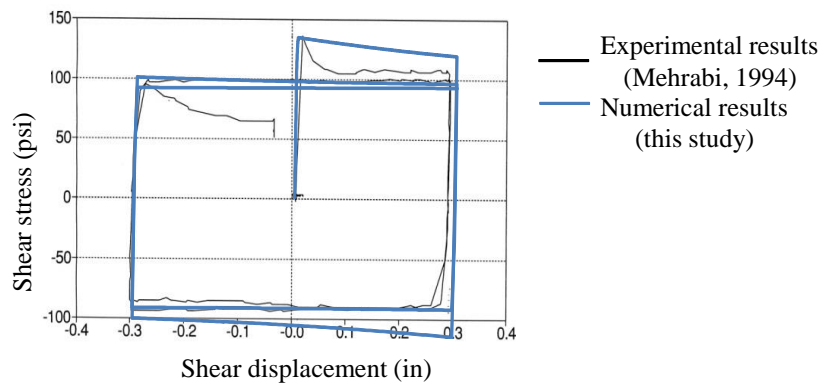


Figure 3-11. Shear stress versus shear displacement of the interface element in cyclic shear test, under 100 psi normal stress (modified from Mehrabi, 1994).

The last property of the interface element to be verified is dilatancy, defined as the vertical displacement of the mortar/brick due to the applied horizontal displacement. Mehrabi (1994) reported the vertical and shear displacements for a cyclic shear test under 150 psi normal stress, and these data are used here to investigate the model's capability of representing dilatancy. To determine the dilatancy input parameters, the same model used in the calibration of cyclic shear behavior is modified to have 150 psi normal stress. A parametric study was conducted on the dilatancy parameters of the interface element, *i.e.*  $\psi$ ,  $\sigma_w$ , and  $\delta$  to find the best match between the dilatancy response (vertical displacement versus shear displacement) of the

experimental and analytical model. The values suggested by Al-Chaar and Mehrabi (2008) are used as the initial guess in this process. Figure 3-12 illustrates the vertical (normal) versus shear displacement response of the final interface model, compared with the experimental results. The DIANA interface element is not capable of modeling of the loss of the material in the mortar joints, which is observed in the experimental direct shear test. This loss of material the reason for the larger negative measured in vertical displacements in the experimental tests (Al-Chaar and Mehrabi, 2008). The selected input parameters of the interface element in this study are presented in row 4 of Table 3-2. Parameters  $f_c$ ,  $C_s$ ,  $G_{fc}$ , and  $\kappa_p$  match those recommended by Al-Chaar and Mehrabi (2008). Some of these parameters will be modified later in the prism test calibration, in Section 3.4.3.3.

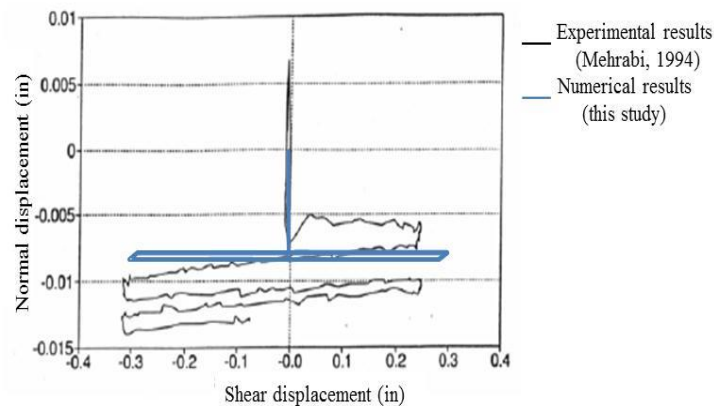


Figure 3-12. Normal versus shear displacement of the DIANA interface element under 150 psi normal stress compared with the experimental results (modified from Mehrabi, 1994).

### 3.4.3.2 Calibration of Total Strain Crack Model for Concrete

The total strain rotating crack model is used to model the concrete frame and concrete masonry bricks in the DIANA model. The compressive and tensile behavior of the material is modeled by parabolic and exponential response, respectively (as explained in Section 3.2.4). To verify the response of this material model, a 2D plane stress model for a single block of concrete (8" length x 4" width x 4" height) is created in DIANA and the compressive and tensile response

analyzed. The simple block model is fixed at the base and a uniform compressive displacement is applied to the top, as shown in Figure 3-13. The material properties of this model are varied to match the response with the experimental results reported by Mehrabi (1994) for compression test on 6-in diameter concrete cylinder, with compressive strength of 3 *ksi* and strain at peak stress of 0.0026. The compressive stress-strain relationship for the modeled block is presented in Figure 3-15a, which shows a good match between the numerical results and experimental results in modeling the stress and strain at the peak strength of the concrete block. The material parameters used in this model are presented in the first row of Table 3-3. There is no similar test reported by Mehrabi (1994) for the tensile behavior of concrete. The tension input parameters ( $f_t$  and  $G_f^I$ ) are taken from values reported by Mehrabi (1994) as used for modeling.

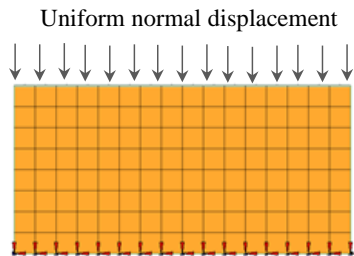


Figure 3-13. Concrete block under uniform compression.

Table 3-3. Properties of the total strain crack model to represent concrete behavior in the concrete frame and hollow bricks.

Element	$E^1$ (psi)	$\nu^2$	Density (lb/in <sup>3</sup> /g)	$f_t$ (psi)	$G_f^I$ (psi-in)	$f_c$ (psi)	$G_c^3$ (psi-in)	$C_s$
Concrete frame	$2.0 \times 10^6$	0.16	0.00022	230	0.09	3000	22	1
Hollow brick	$2.0 \times 10^6$	0.16	0.00022	240	0.09	2400	22	1

<sup>1</sup> $E$ : Young's modulus

<sup>2</sup> $\nu$ : Poisson ratio

### 3.4.3.3 Calibration of Prism Tests

The masonry infill panel is a composite section made of the concrete brick and the mortar. To represent the behavior of this composite section, it is not sufficient to model

separately the properties of the brick and mortar, as described above, but rather the whole section needs to be considered together. Mehrabi (1994) conducted compression tests on masonry prism sample composed of three bricks stacked with layers of mortar in between. The bricks are concrete hollow brick, as shown in Figure 3-7, and the mortar is applied in the experiment on the top face of the hollow brick (shown with the gray area in Figure 3-7). The equivalent width (in the y' direction in Figure 3-7) of the brick is 1.8 in computed as the ratio of net area (shaded area in Figure 3-7) to the gross cross section area of the brick multiplied by the width of the brick (Al-Chaar and Mehrabi, 2008). The width of the mortar joint (also in the y' direction in Figure 3-7) is considered as the summation of the thickness of the two face walls of a brick, 1.25 in.

The numerical model of the prism sample is built in DIANA, as shown in Figure 3-14. In this model, the concrete bricks are modeled with 4-node quadrilateral elements with 2x2 Gauss points; the mortar is modeled with linear interface element with 2 Gauss points. The bricks are constrained at the bottom and a uniform normal displacement is imposed at the top. These model properties used for the concrete block and the interface in the prism are taken from the separate calibrations of the response of the interface (Section 3.4.3.1) and the total strain model for concrete (Section 3.4.3.2), and then modified to provide the stress-strain response of the prism sample matches the experimental results. The final model properties are reported in the final row of Table 3-2 and the second row of Table 3-3. In particular, the values corresponding to the normal ( $K_{nn}$ ) and tangential ( $K_{ss}$ ) stiffness of the interface model are increased by a factor of 10 from the values reported in Section 3.4.3.1. Mehrabi (1994) also found that the relatively small stiffnesses observed in the direct shear tests are due to the deformation of the test machine and higher stiffness values need to be adopted. The normal stress/strain response of the model is shown in Figure 3-15b and compared with experimental results. In particular, experimental

results showed a compressive strength and strain at the peak stress value of 1380 psi and 0.0027, respectively (Mehrabi, 1994). These values are in a good agreement with the numerical (model) results. Remind that as explained in Section 3.3.2.1, the response of the smeared crack model is independent of the mesh size, which implies that we do not have to use the same mesh size as used in the calibration process to model the whole infilled frame.

Past research has shown that the compressive strength of a masonry wall can be evaluated from the compression test of a prism, as described above, or a wallette, *i.e.* a section of the wall. The results of the compression testing on a wallette represent the compression behavior of the masonry wall in a more reliable manner, since the wallette accounts for the response of the both bed joints and head joints in the compressive response of the wall (Gumaste et al., 2006). Gumaste et al. (2006) conducted a series of compression tests on different samples, including prism and wallettes samples with different bricks and masonry types, compared the resulting compressive strengths. They found that the compressive strength of wallettes vary from 0.65 to 1.45 times the strength found from the prism sample. For instance, for one of the Gumaste et al. (2006) samples, which had the closest compressive strength to the prism that Mehrabi tested, wallette test gave compressive strength 25% larger than the strength from the prism test. Since the difference between the wallette and prism test depends on brick and mortar properties, and there is no experiment conducted on the wallettes sample for the specimen that is simulated here, the compressive strength of the prism test is used to calibrate the numerical simulations for the entire wall.

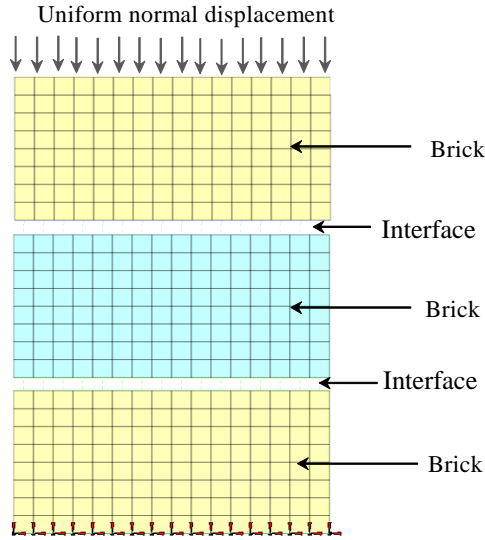


Figure 3-14. Three block prism sample modeled in DIANA.

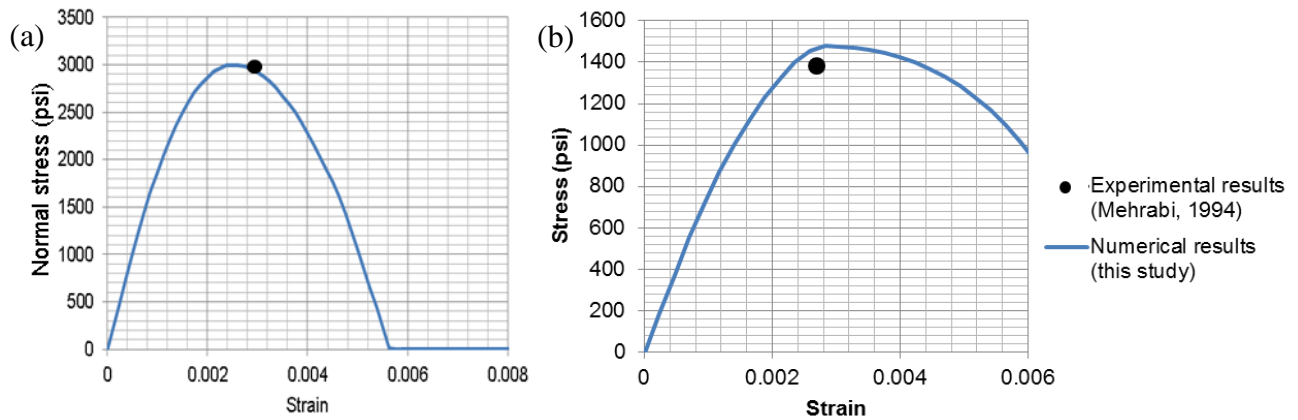


Figure 3-15. (a) Normal stress-strain response of the concrete material in a concrete block under compression ; (b) Normal stress-strain response of the three-block prism sample. Both responses are compared to the experimental reported values for peak stress and strain at peak stress for the corresponding sample configuration.

### 3.4.3.4 Modeling of the Reinforced Concrete Frame

Previous sections in this chapter focused on the calibration and modeling of the infill panel. The findings from these sections will be implemented in the nonlinear model of the infilled frame later in Section 3.4.4. In this section of the study, another specimen tested by Mehrabi (1994), known as *Specimen 1*, is modeled in DIANA. *Specimen 1* is a bare concrete frame with the same configuration and element dimensions as the frame presented in Figure 3-6.

Modeling of this frame alone is needed to ensure that our reinforced concrete frame model used in the finite element model is representative of what is tested in the experiment.

The model is a plane stress 2-D model with fixities in all direction at the base, as shown in Figure 3-16. The concrete is modeled with 4-node quadrilateral element with 2x2 Gauss points. The concrete material is modeled with rotating total strain crack model with parabolic compression and exponential tensile behavior. The input parameters of the concrete model are reported in Table 3-4. Mehrabi (1994) reported the concrete Young's modulus ( $E$ ) and compressive strength ( $f_c$ ) for 14 concrete cylinder samples. The mean values obtained from the 14 samples are used for compressive strength and Young's modulus of concrete in the model of the frame. The foundation is modeled with an elastic material with the same modulus as concrete. The steel is modeled with 1D strut element assigned the Von-Mises material model. The material properties of the steel are reported in Table 3-5, based on the tensile tests conducted by Mehrabi (1994).

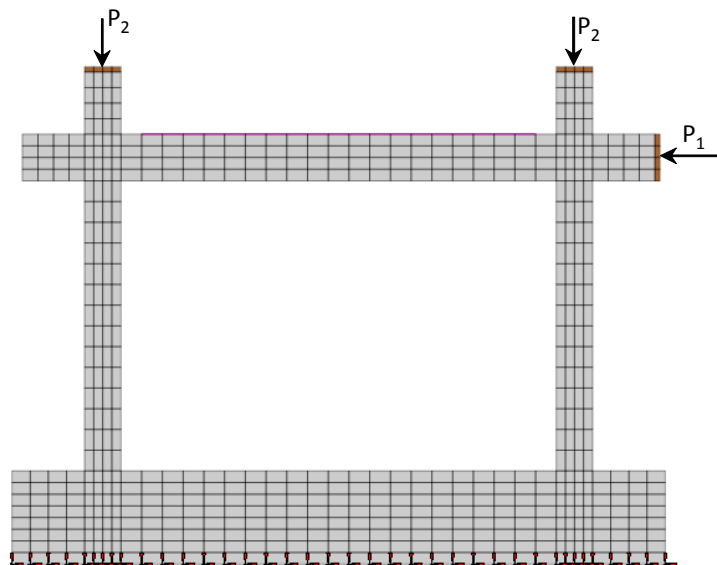


Figure 3-16. Nonlinear finite element model for the bare RC frame.

Table 3-4. Properties of total strain crack model used in model of bare frame.

<b>E(ksi)</b>	<b><math>\nu</math></b>	<b>Density (lb/in<sup>3</sup>/g)</b>	<b><math>f_t</math> (psi)</b>	<b><math>G_f^1</math> (psi-in)</b>	<b><math>f_c</math> (psi)</b>	<b><math>G_c</math> (psi-in)</b>	<b><math>C_s</math></b>
2.80E+06	0.16	0.00022	390	0.09	4000	110	1

Table 3-5. Steel material properties.

<b>Bar size</b>	<b>E (ksi)</b>	<b><math>f_y^1</math> (psi)</b>	<b><math>f_u^2</math> (psi)</b>
No. 2 (transverse)	224	53300	65200
No.4-5 (longitudinal)	224	70000	84100

<sup>1</sup> $f_y$ : Yielding stress  
<sup>2</sup> $f_u$ : Ultimate stress

The bare frame was tested under monotonic loading applied at top of the frame, with the same vertical load as that applied to the infilled frame. Figure 3-17 shows the base shear versus lateral displacement response of the finite element model of the bare frame compared to the experimental results. The results show good agreement in terms of the general trend of the response as well as the maximum strength. However, there are significant differences in stiffness, as well as the displacement corresponding to ultimate load. The difference between the experimental and numerical results is hypothesized to be due to the uncertainty in the material properties, such as the strength and stiffness of concrete, involved in the problem. The larger stiffness of the model as compared to the experimental results is also due to the bond-slip effect, which is not considered in the finite element model due to software limitations. Bond-slip would represent the slip between the rebar and the surrounding concrete, which can add flexibility to the concrete frame (Braga et al., 2012). Mehrabi (1994) compared the response of his bare frame model with and without considering bond slip.

Figure 3-18 shows these results, illustrating how the bond-slip effect reduces the model's stiffness. However, Mehrabi (1994) showed that modeling of the bond-slip does not affect the

response of the composite masonry infilled frame, because of the lower ductility of the infilled frames such that the system does not experience large slipping between bar and concrete before collapse.

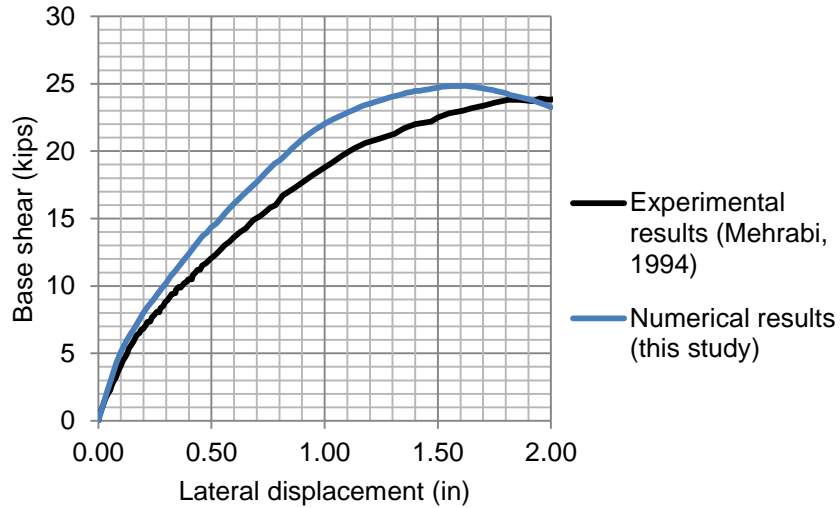


Figure 3-17. Numerical and experimental results for the base shear vs. lateral displacement of the bare frame model.

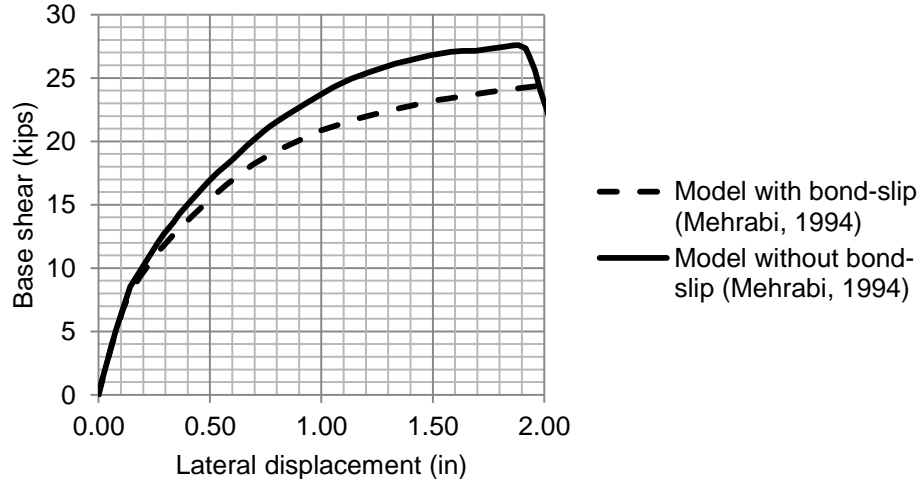


Figure 3-18. Effect of modeling the bond-slip on the response of the bare frame using data from (Mehrabi, 1994).

### 3.4.4 Pushover Analysis of the Masonry Infilled Frame (*Specimen 8*)

This section of the study explains the modeling of one of the masonry infilled frame *specimen 8* tested by Menrabi (1994). The configuration and details of this specimen are shown

in Figure 3-6 and Figure 3-7 and explained in Section 3.4.2. The 2D plane stress model is created for this specimen in DIANA and analyzed under monotonic lateral load, employing the calibration efforts described previously. As shown in Figure 3-7, the vertical load is applied on elastic steel plate modeled on top of the columns and beams in the finite element model. The vertical load is applied in the initial stage of the analysis and kept constant during the analysis. The lateral displacement is applied on the vertical steel plate modeled on the right side of the beam, shown in Figure 3.16, and increased monotonically. The base of the model is fixed in all directions.

The material properties of the concrete, steel, and brick in this model are reported in Table 3-4, Table 3-5, and Table 3-3. The element type used for each component in this model was explained in previous sections. The material properties of the bed joint are reported in row 5 of Table 3-2. The material properties of the head joints and wall-to-frame joints are taken from the values reported by Mehrabi (1994) and reported in Table 3-7. Among these parameters, normal and shear stiffnesses, cohesion parameter, and friction angle parameters reported in

Table 3-7 are different than the ones reported in Table 3-2, while the rest of parameters are the same. Due to the absence of experimental results on the head joint and the wall-to-frame joint, and also considering the fact that these two joints are usually weaker than the bed joints, Mehrabi (1994) proposed these different input properties. Mehrabi (1994) reported the average thickness (in the out-of-plane direction) of the bed joint, head joint, and wall-to frame joint as 1.25, 1.25, and 1.4 inches, respectively. These values are implemented in the finite element model.

Table 3-6. Properties of the total strain crack model to represent the hollow concrete bricks in the FE model.

Element	$E^1$ (psi)	$\nu^2$	Density (lb/in <sup>3</sup> /g)	$f_t$ (psi)	$G_r^I$ (psi-in)	$f_c$ (psi)	$G_c^3$ (psi-in)	$C_s$
Hollow brick	2.0 X 10 <sup>6</sup>	0.16	0.00022	240	0.09	1800	22	1

Table 3-7. Material properties of the head-joint and wall-to-frame joints.

Joint Type	$K_{nn}$ (lb/in <sup>3</sup> )	$K_{ss}$ (lb/in <sup>3</sup> )	C (psi)	$\Phi_i$ (deg)	$\Psi$ (deg)	$\Phi_r$ (deg)	$\sigma_c$ (psi)	$\delta$	$f_t$ (psi)	$G_r^I$ (psi-in)	$G_r^{II}$ (psi-in)	$f_c$ (psi)	$C_s$	$G_{fc}$ (psi-in)	$\kappa_p$ (in)
Head-joint	215300	269200	10	39	0.29	35	-150	2	10	1.11	11.1	150	1	55	0.01
Wall-to-frame joint	215300	269200	20	39	0.29	35	-150	2	20	1.31	13.1	150	1	55	0.01

The masonry infilled frame model based on the material and element properties explained above was created and statically analyzed in DIANA under monotonically increased applied displacement up to 0.8 inches at the top of the frame. The micro model does not consider P- $\Delta$  effects. The Newton solution algorithm based on the tangent stiffness method is used in the nonlinear analysis. An energy norm of 0.0001 and displacement norm of 0.001 are used as the convergence criteria. However, the results are governed by the energy norm. These convergence parameters are selected to impose the most restricted convergence criteria on the analysis for which we could get convergence up to the lateral displacement level close to what reported from the experiment.

Figure 3-19 shows the deformed shape of the modeled infilled frame, when the displacement at the top is equal to 0.5 inches. This deformed shape illustrates the sliding in the bed joints at the mid height of the infill panel, as well as diagonal cracking of the infill panel. These failure modes match the failure modes reported from the experiment (Mehrabi, 1994). The DIANA model also shows cracking of the concrete frame in the bottom-left and top-right side of the columns, which was also observed in the experiment.

Figure 3-20 shows the variation of the base shear versus lateral displacement of the frame, to the maximum lateral displacement under which the analysis converges, and compares it with the experimental results. The results show a pretty good agreement between the numerical and the experimental results, with about 10% difference in the maximum strength value. The discrepancies in ultimate strength come from different sources. Firstly, it is important to note that the concrete frame in this specimen was tested once previously, and repaired and infilled with the masonry panel. The initial tests could have decreased the strength and stiffness of the concrete frame, but there is no practical way to simulate the probable damage existing in the concrete frame prior to the test. Moreover, there is no available data on the tensile strength of the mortar, as mentioned in Section 3.4.3.1. This study uses the tensile properties suggested by Mehrabi (1994). Finally, the bond-slip between concrete and reinforcement is not considered in this model, due to the limitation of the FE platform, which can also affect the total strength of the infilled frame. All of these reasons can explain the difference between the numerical and experimental results.

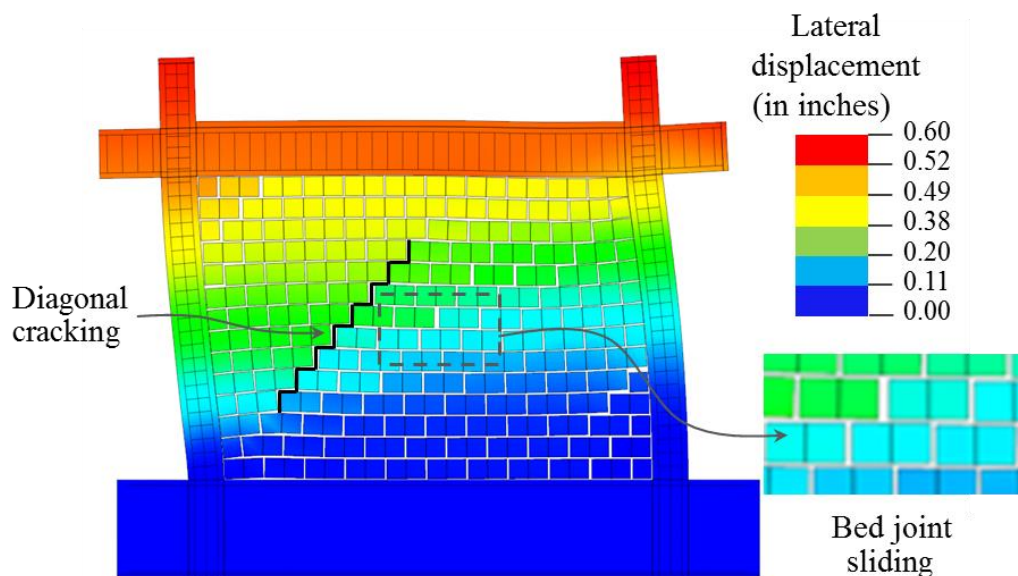


Figure 3-19. Deformed shape of the modeled masonry infilled frame at 0.5 inch lateral top displacement (values shown represent lateral displacement in inches).

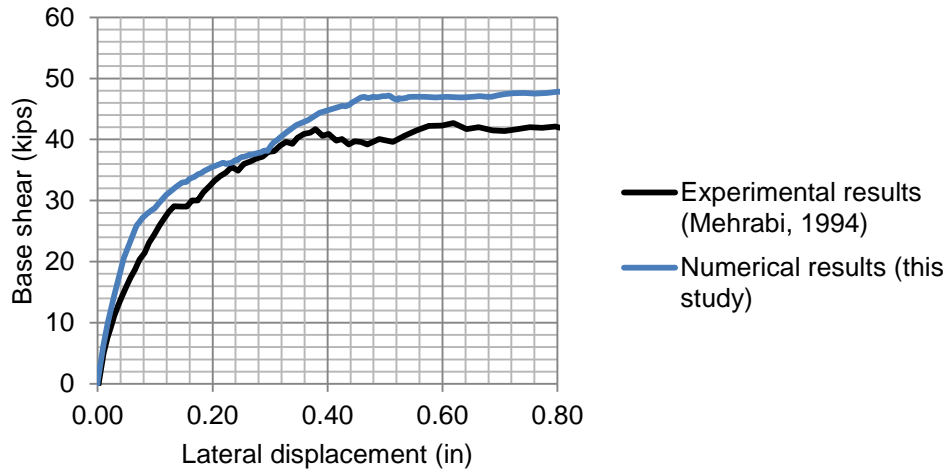


Figure 3-20. Base shear versus lateral displacement of the nonlinear finite element model compared with the experimental results of *Specimen 8* from Mehrabi (1994).

### 3.4.5 Pushover Analysis of a Second Masonry Infilled Frame (*Specimen 9*)

As mentioned in Section 3.1, the purpose of this study is to propose a new macro-modeling technique based on the results of micro-models. The proposed macro-model aims to be capable of capturing the most important failure modes of concrete frames such as shear failure of the columns, as well as the failure modes of the infill panel. For this purpose, it would be more appropriate to validate the micro-modeling results for an experimental study in which shear failure of columns is reported. Therefore, a second validation study is conducted here, considering a specimen that experienced shear failure of its concrete columns.

After testing *Specimen 8*, the same frame was repaired and infilled with one-wythe clay brick wall. This new specimen is known as *Specimen 9* in Mehrabi (1994). To develop the micro-model for *Specimen 9* here, the same model built for *Specimen 8* is used and the thickness of the bricks and mortar are increased to 3.625 inches, *i.e.* the thickness of the clay brick wall. No additional calibration was performed for this specimen, as the focus of this part of the study was to build a micro-model, which matches the experimental results and use it to calibrate the macro-model. The mortar and the frame of *Specimen 9* are the same as *Specimen 8*, but the

bricks are different. To make the micro-model of *Specimen 9* the same material properties of the brick as *Specimen 8* is used. The compressive strength of the infill is usually governed by the compressive strength of the mortar joint, which is the weakest part of the wall. The micro-model for the concrete frame cannot capture the shear failure of the columns. This limitation is deemed to be acceptable since the micro-model results are used to calibrate only the infill wall portion of the macro model, as will be described later in Chapter 5.

The base shear versus lateral displacement response of this new micro-model is plotted in Figure 3-21, up to the maximum lateral displacement at which analysis converges, and compared with the experimental results. This figure shows a good agreement between the developed micro-model and the experiment, especially up to lateral displacement of about 0.3 inches. Considering the fact that the concrete frame is the exactly the same as the one tested in *Specimen 8*, the numerical results imply that the infill panel modeled for *Specimen 9* (by increasing the thickness to 3.625") can adequately represent the behavior of the infill tested in the experiment. At a lateral displacement of about 0.3 inches, the column fails in shear in the experiment. We can conclude that the results of the model up to the shear failure of concrete the column have sufficient accuracy and after lateral displacement of 0.3 inches, the numerical results have a pretty good agreement with the experimental results, with the maximum 15% difference in the base shear, despite not representing the column shear failure. The reason of the difference between the micro-modeling and experimental results after the reported shear failure of concrete columns is that in the micro-modeling approach, the shear failure needs to be modeled with a discrete crack modeling Approach. To capture this effect in the micro-model, an interface element in the expected crack location (top of the columns) and expected shear failure direction (about 45

degree) need to be implemented to the model (Al-Chaar and Mehrabi, 2008), but these modeling features are not added here.

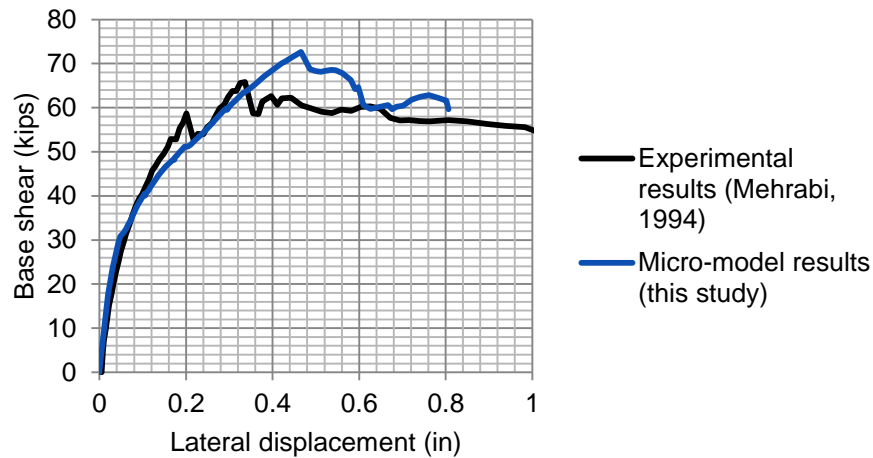


Figure 3-21. Base shear versus lateral displacement of the nonlinear finite element model compared with the experimental results of *Specimen 9* from Mehrabi (1994).

### 3.5 Conclusions

Findings of this section sufficiently demonstrate that the adopted modeling procedure including the element type, material models, etc. can adequately represent the behavior of the masonry infilled frame and can be used to simulate this category of buildings. This conclusion is reached based on the ability of the model to adequately capture the failure modes in the experiment, as well as the ultimate strength, and stiffness within a reasonable level of uncertainty. The modeling approach adopted here can simulate different failure mechanism in the infilled frame such as bedjoint sliding, tensile cracking and compressive crushing failure of the masonry panel as well as the flexural failure of the concrete frame. However, this modeling approach may not be able to capture the brittle shear failure can occur in concrete columns or discrete cracking that may occur through the bricks. Further improvements can be applied in this modeling approach to address these issues. This modeling approach will be implemented later in Chapter 5 to simulate the Archetypical masonry infilled frame as the representative of the

buildings built in California in 1920's. Material properties of the archetypical buildings will be defined based on a comprehensive literature review, as explained later in Chapter 5.

## **4 Proposed Macro-Modeling Approach for Masonry Infilled Reinforced Concrete Frames**

### **4.1 Overview**

The literature review in Chapter 2 presented different strut modeling techniques. The primary objective of this part of this study is to propose a macro strut-type modeling approach, the properties of which are based on the results of micro-modeling of the frame of interest. In the following sections, the procedure to develop the proposed macro-model is described. At the end of the chapter, the macro-model of two specimens tested by Mehrabi (1994) are built and the macro-model, micro-model and experimental results are compared.

### **4.2 Modeling of Masonry Infill Panel**

This study attempts to develop a robust nonlinear model of masonry infilled RC frames that can be used in the context of performance-based engineering and simulate response of the structure to engineering responses at a variety of intensity levels up to and including collapse. The key aspects of the proposed multi-scale model are:

(1) a micro (finite element) model that can be used to develop the force-displacement response of infill wall panel under an in-plane lateral load.

(2) a strut and beam-column based macro model that is calibrated to the micro model. By having a macro-model based on a micro-model, we would indirectly consider the effect of different failure modes which can occur in the masonry infill panel. The simplicity and accuracy of this type of model enables us to implement it in the PBEE framework and analyze it for a suite of ground motions, which in turn makes it an appealing modeling technique for collapse assessment procedure.

The proposed macro-modeling approach requires a detailed nonlinear finite element model of a single bay, single story subassembly of the building of interest, which is subjected to appropriate gravity loads and a monotonically increasing lateral load. For use in developing the macro-model, the micro-model should be capable of capturing the important failure mechanisms of the infill under lateral loading, such as bed-joint sliding, diagonal cracking and compression failure of the infill (as explained in Chapter 3). The micro-model is needed here to provide a backbone of the response of the infill, the results of which can be extracted to represent the infill with a strut-type model in the macro-model. The macro-model of the frame is developed based on the available modeling approaches for concrete frames (Baradaran Shoraka and Elwood, 2013; Elwood, 2004; Haselton et al., 2008).

The basic idea behind the macro (strut-based) models is that the force transfers from one corner, at which the load or displacement is imposed to the opposite corner, as shown in Figure 4-2. Accordingly, the proposed macro-modeling approach begins by extracting the response of the infill panel from the micro-model in the direction of interest, *i.e.* the diagonal direction. This thesis develops a set of rules to extract the response of the infill in the diagonal direction and to represent this response by a multi-linear relationship (Section 4.2.2). Then, using the extracted force-displacement behavior, a new double-strut model is proposed to represent the infill panel (Section 4.2.3). The proposed modeling of the frame elements to accompany the infill frame modeling is described in Section 4.3.

In the discussion that follows, when specificity is needed, we provide examples in terms of Mehrabi (1994)'s *Specimen 9*. As you will recall from Chapter 3, *Specimen 9* is a concrete frame infilled with clay bricks tested under monotonic loading, which experienced shear failure in the column, as well as the diagonal cracking of the infill. In the final section, Section 4.4, the

proposed strut model is tested in Section 4.4 for two specimens (*Specimen 9*, and *Specimen 8*) tested by Mehrabi (1994) for which a macro-model is implemented in *OpenSees*. The robustness of the proposed macro-model is examined through quantitative and qualitative evaluation of how accurately the proposed macro-model can predict the following properties of the experiment:

- 1) Infilled frame stiffness and strength
- 2) Drift ratio at shear failure of columns
- 3) Bending and shear diagram of the columns

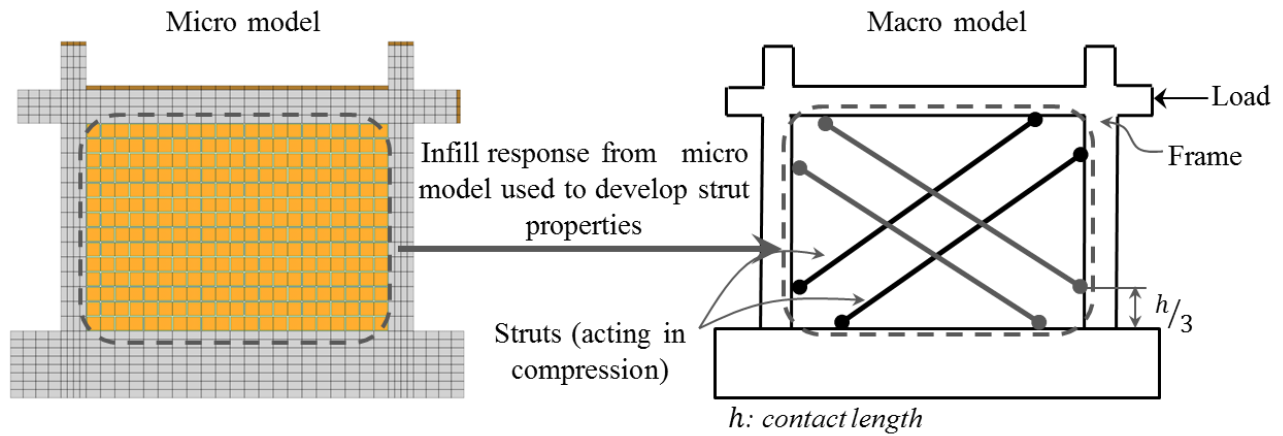


Figure 4-1. Schematic diagram of proposed macro-modeling approach based on the micro-model.

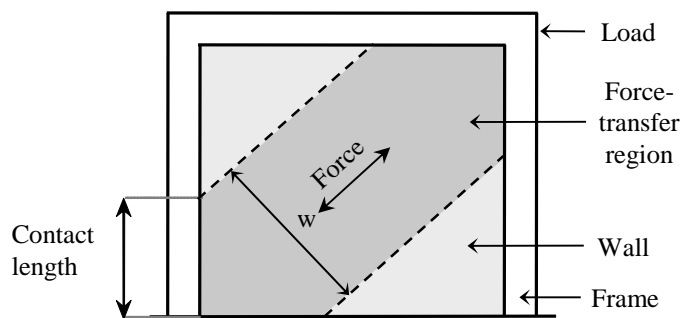


Figure 4-2. Force transfer mechanism in masonry infilled RC frame to be represented by proposed macro-modeling approach.

#### 4.2.1 Extraction of the Force-Displacement Relationship for the Infill Wall

In the macro-model the entire force transfer region is represented by a set of diagonal struts. The first step in developing the model is to extract the force transferring through this region in the micro-model. To accomplish this extraction, this region is defined by the equivalent strut width ( $w$ ), as shown in Figure 4-2. Conceptually, this strut width defines the wall area over which the majority of the lateral action is resisted. To compute the equivalent width of the strut, the contact length (between the infill wall and columns) in the micro-model is defined as the region in which the interface between the walls and columns is in compression in the micro-model. For *Specimen 9*, this contact length is measured as 24 in. at the analysis step corresponding to the peak load, as shown in Figure 4-3. After finding the contact length between the infill and columns the shaded region in Figure 4-4 is defined by drawing two lines starting from the end of the contact length on the each column (denoted by  $h$  on the diagram) and running parallel to the diagonal of the infill panel, as shown by dashed lines in Figure 4-4. This region is termed the force transfer strut and the response of this region is represented in the macro-model. For *Specimen 9*, the equivalent width is found to be 43 inches. However, a limitation of the approach is that there may be some force resisted by the other part of the infill that is not included in this strut region.

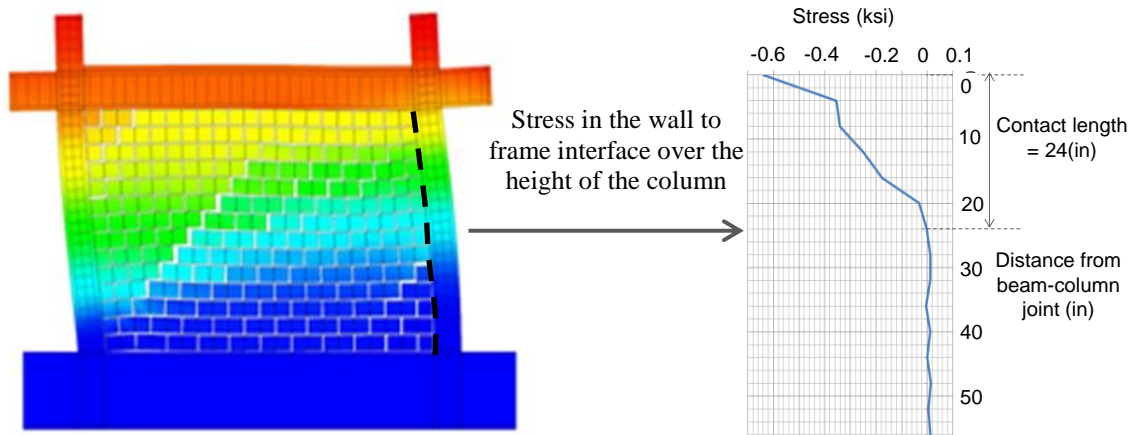


Figure 4-3. Stress in the wall to frame interface elements over height of the column. (Negative values of stress indicate compression).

Next, the force-displacement relationship for the strut defined in the previous step is computed. Due to non-uniform stress in this strut, this study proposes to compute the force in the diagonal direction at three different sections within the identified region, as shown in Figure 4-4. One of these three sections is defined exactly through the middle of the infill panel and is perpendicular to the diagonal of the panel. The other two sections, *i.e.* end sections  $w_2$  and  $w_3$ , are parallel to the middle section ( $w_1$ ) and located on either side of it. The positions of the end sections are limited by the size of the force transfer region, such that (1) each of the end sections coincides with the intersection of the force transfer region and the frame and (2) each of the end sections has the equivalent width of  $w_1$ , as shown in Figure 4-4. There are slight differences in the extracted force-displacement response at these different sections because the crack formation and as a result the stress distribution is not exactly the same at these sections.

Figure 4-5 shows the extracted force-displacement response for each of these three sections for the example specimen, as well as the force-displacement response averaged among all three sections. The force is averaged among three sections at each increment of displacement (as shown in Figures 4-5 and 4-6a) to develop a generalized force-displacement relationship that is appropriate for the whole wall, as will be represented in the macro-model, smoothing out

possible localized failures. The results shown in both figures continue until the last displacement at which the micro-model converged. The force in the wall observed at a lateral displacement of zero in the force displacement responses plotted in Figure 4-5 is due to the pre-application of the vertical load in the model.

For the purpose of macro-modeling, this force-displacement response needs to be assigned to the strut element(s) that are defined in terms of the force-displacement or stress-strain relationship in the axial direction. In the process of developing the proposed macro-model we need to investigate various struts with different locations and cross sectional area, as described in the following section. In order to simplify this process, the force displacement is extracted for a single equivalent strut, as shown in Figure 4-6a, and transformed to units of stress and strain, as shown in Figure 4-6b. This stress-strain relation can be considered as the material property of the struts in the macro-model and can be assigned to struts with different length or width in the multi-strut model. The stress is computed by dividing the force by the cross-sectional area of the force transfer region, computed as equivalent width,  $w$ , times the thickness of the wall,  $t$ , which is 3.625 in. for *Specimen 9*. The strain is computed from the projection of the lateral displacement on the diagonal of the frame (*i.e.* the diagonal deformation of the frame) divided by the diagonal length of the frame.

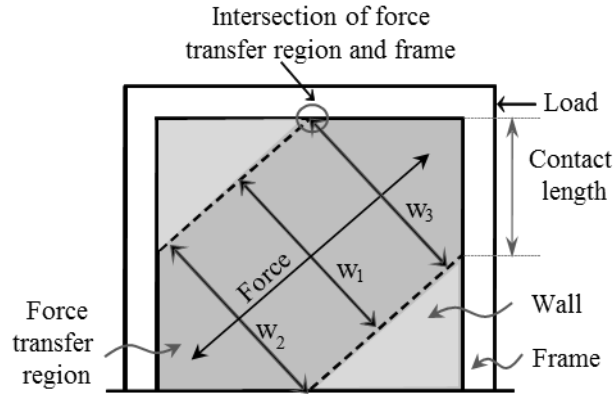


Figure 4-4. Illustration of the sections at which the force is extracted from the infill wall in micro-model.

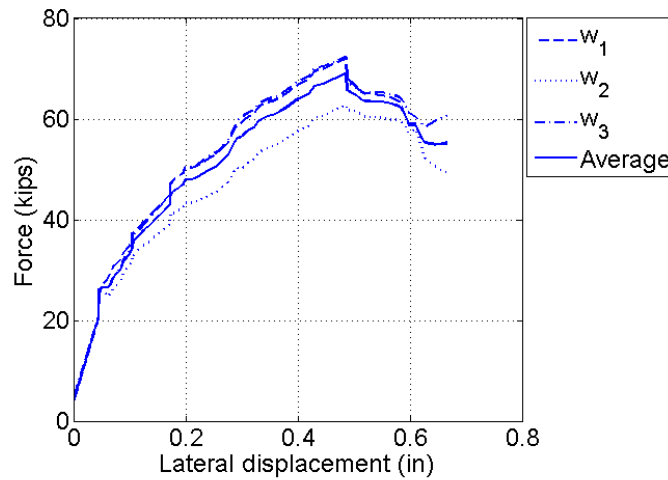


Figure 4-5. Force-displacement response for three sections  $w_1$ ,  $w_2$ , and  $w_3$  extracted for the strut from the micro-model for *Specimen 9*.

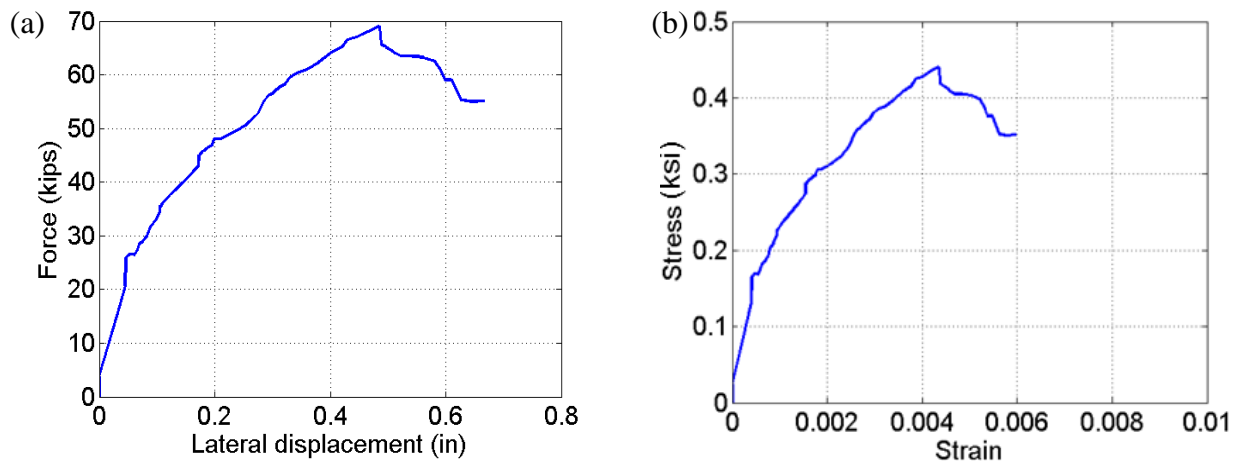


Figure 4-6. Average force-displacement and stress-strain response extracted for the strut from the micro-model for *Specimen 9*.

#### 4.2.2 Multi-Linear Representation of Strut Force-Displacement Response

The nonlinear response of the infill extracted from the micro-model is represented by a multi-linear force displacement relationship for implementation in the macro-model. The fitted multi-linear response needs to be capable of representing the key characteristics of extracted force-displacement response, including initial stiffness, maximum strength, and post peak response. The proposed idealized multi-linear response is composed of an elastic branch, “yielding” point, which is corresponding to cracking of the infill wall, hardening region, maximum strength, which is corresponding to the widening of the crack in the wall, post-capping slope, and residual strength, as presented in Figure 4-7. In order to fit the multi-linear response to the complex extracted response, first, the maximum strength of the multi-linear curve is determined to match the nonlinear response extracted from the micro-model. Then, the initial stiffness is defined such that the stiffness is equal to the initial tangent stiffness of the results from the micro-model. The “yielding” strength is computed such that the area under the multi-linear response (red line) matches the area under the nonlinear response (blue line) up to the strain corresponding to the maximum strength. In the other words, the area between the red and blue curves are matched such there are equal areas above and below the fitted response. The post-capping slope of the multi-linear response is visually matched to the one from the nonlinear response while maintaining (approximately) the same area above/below condition. In the micro-model, we may not always be able to push the model far enough to get to the residual strength of the infill. For this reason, this study models the infill with a residual strength equal to the 50% of the maximum strength, based on the recommendation from Stavridis (2009). Figure 4-7 illustrates an example calibration of the multi-linear response fitted to the extracted micro-model response of the infill for *Specimen 9*.

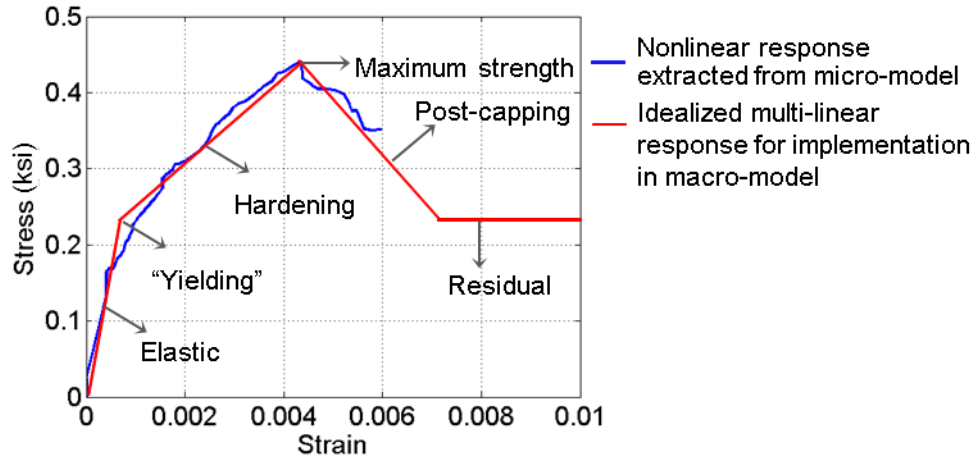


Figure 4-7. Multi-linear stress-strain macro-model representation of the nonlinear response of the infill wall extracted from micro-model for *Specimen 9*.

#### 4.2.3 Strut Configuration in the Proposed Macro-model

The multi-linear response represents the aggregate response of the equivalent strut as extracted from the infill. In the macro-model, the idealized multi-linear response needs to be assigned to one or more struts. The background research, described in Chapter 2, showed that a model with single strut (in each direction) is not capable of capturing the infill-frame interaction and the correct shear and bending diagram in the frame members. Crisafulli (1997) reported the typical shapes of the bending and shear diagram of columns in an infilled frame, as presented in Figure 4-8, which are noticeably different from those observed in a bare frame and from what could be obtained with a single strut model. Here, we varied the number and orientation of struts to find the best strut geometry for the proposed macro-model.

During the first attempt to develop the macro-model, the infill panel was modeled with three struts, including one diagonal and two off-diagonal struts, wherein one-half of the equivalent strut width was assigned to the diagonal strut and one-quarter of the width to each of the off-diagonal struts. Then, gradually the width of the off-diagonal strut was increased while the area of the diagonal strut was decreased. Moreover, the location of the strut-column

connection (*i.e.* the location of intersection between the off-diagonal struts and the frame), was varied over the infill-frame contact length.

For each variation, the configuration's capability of satisfying the properties listed in Section 4.2 was considered. These studies showed that the strut configuration shown in Figure 4-9, in which the infill is replaced with two compression struts in each direction, successfully satisfies all of these requirements, as will be shown by the examples in Section 4.4. Each strut has half of the equivalent width computed in the previous section and is assigned the idealized stress-strain curve fitted in the previous step.

As shown in Figure 4-10, the distribution of force applied from the infill to the column is approximately triangular. This study uses the simple theory from statics in which the triangular stress/force distribution can be replaced by a single force located at the centroid of the triangle. Accordingly, each strut is connected to the columns at the distance equal to one-third of the contact length from the end of the column, as shown in Figure 4-9.

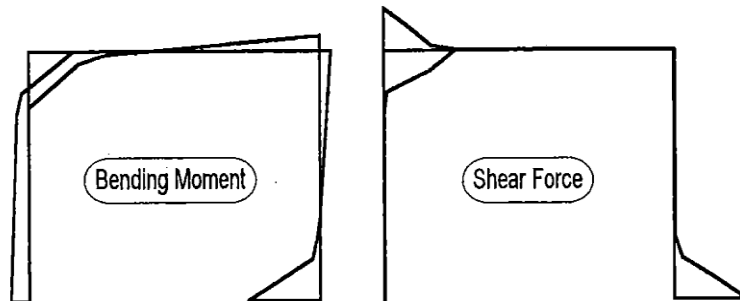


Figure 4-8. Typical moment and shear diagram for infilled frames (taken from (Crisafulli, 1997)).

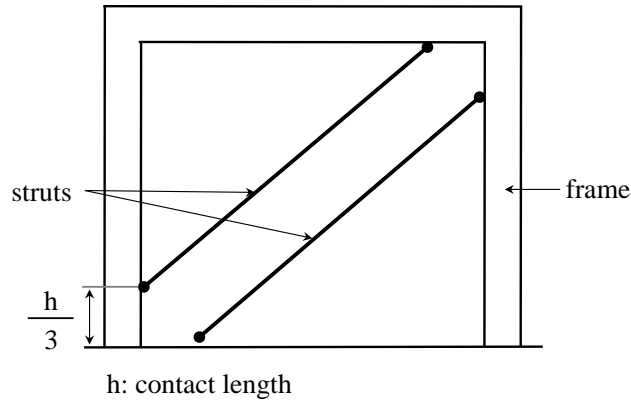


Figure 4-9. Proposed double-strut configuration for macro-model.

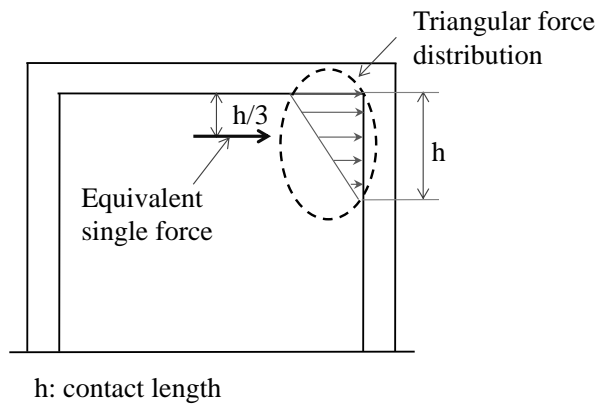


Figure 4-10. Force distribution between frame and infill panel.

## 4.3 Frame Modeling

### 4.3.1 Frame Modeling Overview

To create a nonlinear model for masonry infilled frames, both components of the model, including the frame and infill should be capable of capturing their most important response characteristics. Section 4.2 presented the modeling approach proposed in this study for the infill. This section explains the modeling approach adopted here to model the reinforced concrete frame. The nonlinear model of the frame aims to capture different failure mechanisms of each element, including those coming from flexural, shear, and axial response.

A reinforced concrete beam or column can experience different failure modes such as flexural, shear, and axial failure. The dominant failure mode depends on different parameters

such as axial load, reinforcement detailing, aspect ratio, etc. To model a bare concrete frame, *i.e.* a frame without infill, this study uses the criteria defined in ATC-78 (2012) and ASCE/SEI 41 (2006) to decide whether columns should be simulated as a purely flexural element, or shear or flexure-shear element. In this criterion, the ratio of the  $V_p/V_n$  is computed first, where  $V_p$  is the shear corresponding to the development of the flexural strength at two end of the columns and  $V_n$  is the shear strength computed using Equation (4-2). Then elements with  $V_p/V_n \leq 0.6$  are simulated with the purely flexural element and elements with  $V_p/V_n \geq 0.8$  are modeled with the combined shear and flexure-shear model. Figure 4-11a shows four types of elements which have been modeled in series to pursue the goal of capturing the right failure mode of concrete columns with  $V_p/V_n \geq 0.8$ , *i.e.* the shear and flexure-shear columns. Figure 4-11b shows the modeling scheme adopted here to simulate the response of concrete columns with  $V_p/V_n \leq 0.6$ , *i.e.* purely flexural columns, as well as concrete beams. Each part of these elements will be considered in detail in the following sections. Observations from past earthquakes, as well as experiments, show that concrete columns in masonry infilled frames are susceptible to shear failure. This study proposes to model the concrete columns in masonry infilled frames with the shear based approach regardless of the  $V_p/V_n$  ratio, as shown in Figure 4-11a.

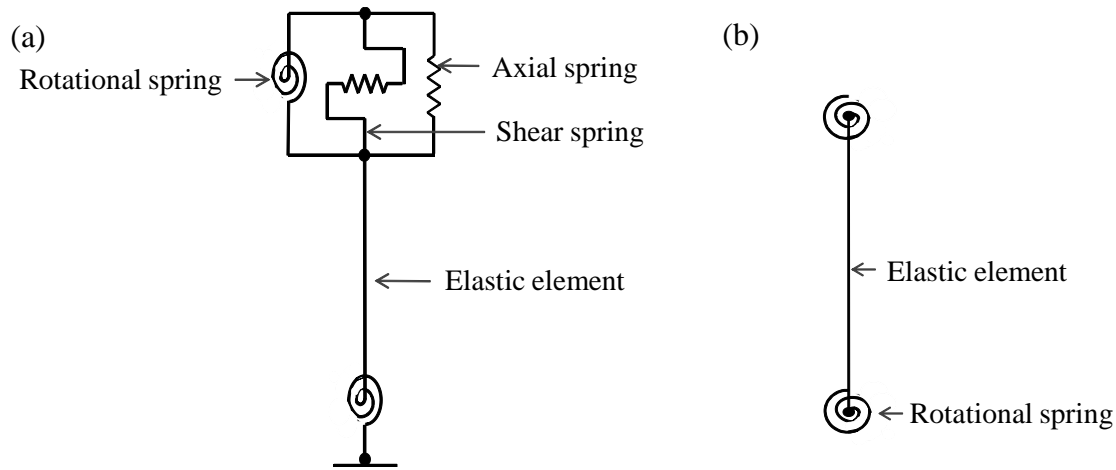


Figure 4-11. Schematic illustration of the (a) combined shear and flexure-shear model and (b) flexural model implemented in OpenSees for beam-columns.

### 4.3.2 Flexural Failure Modeling of RC Beams and Columns

The flexural response of beams and columns in this study is modeled based on lumped plasticity element model developed by Ibarra and Krawinkler (2005). In this modeling method, the nonlinear properties of the element are lumped at the end of the element in two plastic hinges in series with an elastic element. The backbone response curve in this model is able to capture the important element flexural characteristics such as initial stiffness ( $K_e$ ), yield strength ( $M_y$ ), ultimate strength ( $M_c$ ), hardening ( $K_s$ ), and softening ( $K_c$ ) response, in addition to the hysteretic and deterioration properties of the element, as illustrated in Figure 4-12. An important aspect of this model, which makes it more suitable for modeling flexurally dominated components than fiber-type models, is the post-peak branch of the response which enables the modeling of strain softening of concrete beam-columns, which is due to the rebar buckling, concrete crushing, and bond failure. The Ibarra and Krawinkler (2005) model also captures four kinds of cyclic deterioration including stiffness deterioration, strength deterioration due to the hardening and post-peak strain softening, and accelerated unloading stiffness deterioration. The parameters used to model beam-column elements in this study are computed using a set of equation proposed by

Haselton et al. (2007), based on calibration of the Ibarra *et al.* element model to 255 reinforced concrete column tests. These equations also consider the bond-slip effect. For columns, the model parameters depend on the expected gravity load during the analysis, and cannot account for changes in axial load associated with overturning.

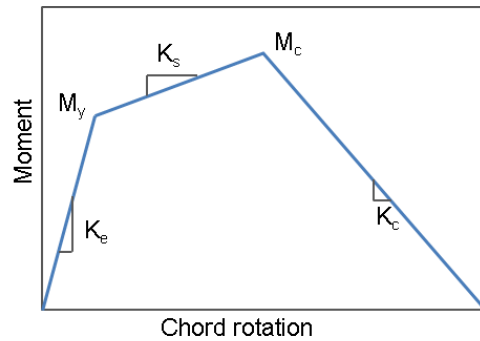


Figure 4-12. Moment rotation backbone for Ibarra material model.

### 4.3.3 Shear and Flexure-Shear Failure Modeling of Non-Ductile RC Columns

#### 4.3.3.1 Overview

The behavior of non-ductile reinforced concrete columns under seismic loading shows the high vulnerability of this category of columns to shear failure. Experimental and analytical research has been conducted by researchers in the past decades to develop models for shear failure behavior of concrete columns. Experimental studies indicated that the column shear strength is dependent on a number of different parameters, including column aspect ratio, axial load, effective cross-sectional area, and material properties (Elwood, 2004). Moreover, observations from cyclic and dynamic tests on the infilled frames indicate that columns in masonry infilled frames may be more susceptible to shear failure, which implies the need to consider the column shear failure in infilled frames in detail.

#### 4.3.3.2 Existing Models for Column Shear Failure

Most of the available shear strength models calculate the maximum shear strength of a column as a summation of shear strength contribution from concrete and transverse reinforcement (Aschheim and Moehle, 1992; Pincheira et al., 1999; Priestley et al., 1994). A few researchers also tried to calculate the shear response for the entire range of shear-deformation behavior (Lehman and Moehle, 1998; Sezen, 2002; Vecchio and Collins, 1986). These models consider shear failure as a function of shear strength of the element and are termed as “force-controlled” models, in this study.

Elwood (2004) used a database of 50 experimental tests to show that above-mentioned shear models cannot capture the behavior of columns that yield in flexure prior to failing in shear. For these columns, Elwood proposed an empirical equation, Equation (4-1), defining a force-deformation-controlled failure surface:

$$\frac{\Delta_s}{L} = \frac{3}{100} + 4\rho'' - \frac{1}{500} \frac{v}{\sqrt{f'_c}} - \frac{1}{40} \frac{P}{A_g f'_c} \geq \frac{1}{100} \text{ (psi units)} \quad (4-1)$$

Where  $\frac{\Delta_s}{L}$  is drift ratio at shear failure,  $\rho''$  is the transverse reinforcement ratio,  $v$  is the shear stress,  $f'_c$  is the concrete compressive strength, and  $A_g$  is the gross cross-sectional area. Elwood’s relationship indicates that the displacement at which shear failure occurs depends on the transverse reinforcement ratio, axial load, shear stress in the column, concrete compressive strength, and area of the column. The coefficients in Equation (4-1) were calculated based on the least square-fit to the data. Figure 4-13 shows the schematic diagram of this model, illustrating that drift ratio at which shear failure occurs increases when the shear force in the column is lower for a given transverse reinforcement ratio, axial load, column compressive strength and area. The shear model proposed by Elwood can only capture the shear failure occurs in drift ratio greater than one percent, as indicated by the inequality in Equation (4-1). Baradaran Shoraka and

Elwood (2013) have recently developed an updated model for the shear limit curve, but this study uses the formulation proposed by Elwood (2004).

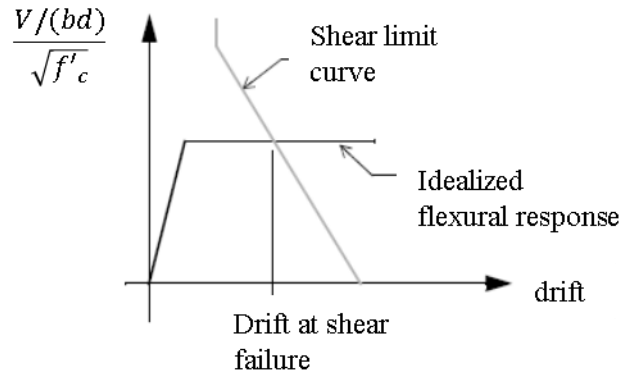


Figure 4-13. Schematic diagram of the shear model proposed by Elwood (2004) (taken from (Elwood, 2004)).

Elwood implemented this shear model in OpenSees in the limit state uniaxial material class. The limit state material model traces the response of the beam-column element and updates the stiffness of the shear spring by reducing it to a negative value once the response hits the shear limit curve. Since the shear spring is in series with the components of columns, as shown in Figure 4-11a, updating the stiffness of the shear spring updates the stiffness of the whole column response, as shown in Figure 4-14. This stiffness update aims to simulate stiffness degradation occurs in a concrete column after shear failure occurs. The limit state material is defined in series with the column, as illustrated in Figure 4-11a, such that it does not affect the response of the column before shear failure starts. The response of the column before shear failure can be represented by a fiber element or a bilinear lumped plasticity based representation of structural response.

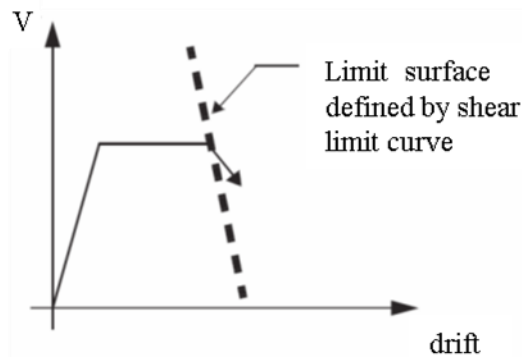


Figure 4-14. Schematic representation of limit state material model in shear failure (Elwood, 2004).

#### 4.3.3.3 Proposed Modified Shear Failure Model

The Elwood (2004) model was developed for columns in a bare (non-infilled) frame that bend and then fail in shear (so-called “flexure-shear” columns). As shown in past experimental studies such as Mehrabi (1994), in infilled frames, the infill panel prevents the columns from developing large bending deformations, thereby inducing shear failure in the columns at lower drift ratios and before yielding occurs. More precisely, the infill-frame interaction also changes force distribution in the column, preventing flexure and leading to a direct shear failure of the column. In this case, the response of the column is governed by the shear strength at low deformations and can be considered as a force-controlled response. These differences in the behavior of a concrete column in an infilled frame versus bare frame implies the need to modify the existing shear failure model (Elwood, 2004) to properly simulate the column shear failure in infilled frames.

To capture these force-controlled shear failures, considering the shear failure of columns in an infilled frame as a force-control response, this study adds another shear limit line to the existing shear limit curve developed by Elwood. Figure 4-15 shows the schematic plot for shear limit curve used in this study, where  $VF$  is the force-controlled shear strength based on the shear

strength equation proposed by Sezen (2002) for reinforced concrete members, Equation (4-2), and  $VFD$  is the shear limit curve (force-displacement controlled) proposed by Elwood (2004):

$$VF = \left( \frac{6\sqrt{f'_c}}{a/d} \sqrt{1 + \frac{P}{6\sqrt{f'_c}A_g}} \right) 0.8A_g + \frac{A_s f_y d}{s} \quad (4-2)$$

In Equation (4-2),  $VF$  is the shear strength of concrete column in the force-controlled region of Figure 4-15,  $f'_c$  is the compressive strength of concrete,  $a$  is the shear span of the concrete column, which is one half of the clear length of the column for columns tested in double curvature,  $d$  is the column effective depth,  $P$  is the column axial load,  $A_g$  is the column gross cross sectional area,  $A_s$  is the area of the transverse reinforcement,  $f_y$  is the yielding stress of the transverse reinforcement, and  $s$  is the spacing between transverse reinforcement.  $a$  is defined as the column length between the maximum and zero bending moment. This length is usually considered as 0.5 times height of the column for columns in bare frames, assuming double curvature of the column. However, for columns in infilled frames, this length is usually smaller (Crisafulli, 1997), due to the existence of the infill panel, which changes the bending moment diagram of the column. The size of  $a$  in infilled frames depends on the contact length and relative stiffness of the frame to the infill. For simplicity, this study considers  $a$  as the 40% of the length of the column. The minimum of the VF and VFD curves at any drift ratio represents the shear strength of the beam-column element.

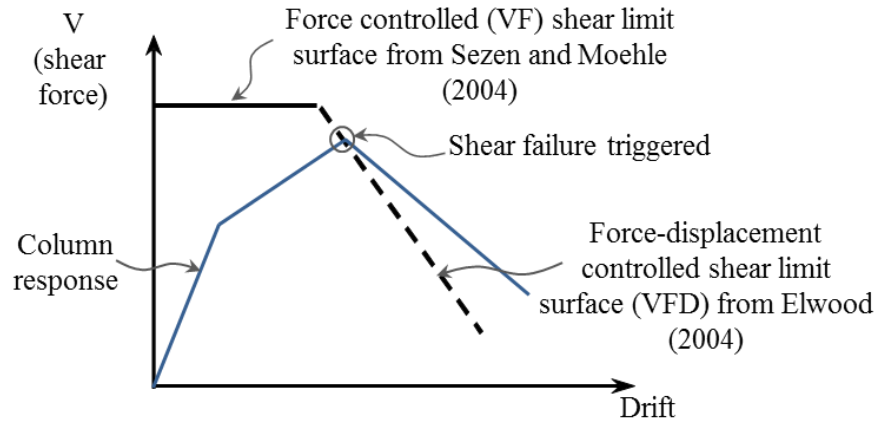


Figure 4-15. Schematic shear limits to define the shear limit curve.

#### 4.3.4 Axial Failure Modeling of Non-Ductile RC Columns

In non-ductile reinforced concrete frames, as described previously, columns sometimes have small amounts of transverse reinforcement, typically with 90° hook, and small concrete cover. These deficiencies can make the columns susceptible to the axial failure after they fail in shear due to the lack of confinement and poor protection against spalling and rebar buckling. This is followed by concrete falling out of the rebar cage.

This study uses the axial failure model developed by Elwood and Moehle (2004), shown in Figure 4-16. They used the limit state material model concept to capture the axial failure in the column and update the axial stiffness of the column after the failure occurs. This model assumes that axial failure always occurs after shear failure occurs. The axial limit curve is defined in Equation (4-3):

$$\left(\frac{\Delta}{L}\right)_{axial} = \frac{4}{100} \frac{1 + \tan(\theta)^2}{\tan(\theta) + P/(s/A_{st} f_{yt} d_c \tan(\theta))} \quad (4-3)$$

Where  $\left(\frac{\Delta}{L}\right)_{axial}$  is drift at axial failure,  $\theta$  is the critical crack angle,  $d_c$  is depth of the column core from center line to center line of the ties,  $A_{st}$  and  $f_{yt}$  are the area and yield strength of the transverse reinforcement respectively,  $s$  is the transverse reinforcement spacing, and  $P$  is the column axial load. This limit state material is defined in a stiff zero-length element, which is in

series with the column shown in Figure 4-11, such that it does not affect the initial axial stiffness of the column. After axial failure is triggered, the axial stiffness of the spring-column system is degraded and updated such that the axial response of the column follows the axial limit curve shown in Figure 4-16.

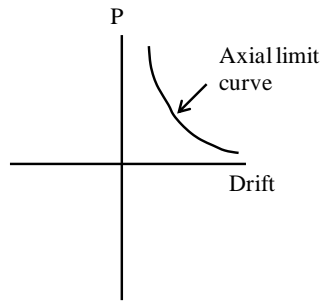


Figure 4-16. Schematic axial limit curve (Elwood, 2004).

#### 4.4 Comparison of Macro-Model with Experimental Results for Two Infilled Frame

##### Specimens

Two of the specimens tested by Mehrabi (1994) are modeled using the approaches explained in the previous sections for modeling the infill and the frame. Two different failure mechanisms were observed in the experiments; Specimen 8 failed due to the formation the plastic hinges at the end of the columns, *i.e.* a flexurally dominated column response, and *Specimen 9* experienced shear failure at top of one of the concrete columns. These two specimens are selected to represent two extremes of the frame response observed in the experiment, *i.e.* flexural failure versus brittle shear failure of the frame, to verify the feasibility of the proposed modeling scheme to simulate the response of the infilled frames and the interaction between the frame and infill. The specimens were tested under monotonically increasing lateral load with a constant vertical load of 66 *kips*.

Recall that the proposed macro-modeling approach attempts to ensure that (1) the infilled frame stiffness and strength, (2) the drift ratio at which column shear failure occurs, and (3)

bending and shear diagram of columns are accurately represented by the proposed macro-model. Figure 4-17 and Figure 4-18 show the comparison among the experimental, micro-model, and macro-model results for Specimens 8 and 9, showing good agreement among these results. To illustrate the discrepancies between the frame model and experiment, with the additional complication of the infill, Figure 4-19 reports the frame responses from a bare frame experience by itself.

With regard to criterion (1), we observe a maximum of 8% difference between the maximum strength of the experiment and the macro-model results for the two specimens. The lower strength of the macro-model as compared to the micro-model and experiments is due to the fact that the load transferring through the entire infill in an infilled frame is larger than the load that transfers through the identified strut region used in developing the macro-model. In addition, some of the difference in the responses of the macro-model and experiment is due to the response of the frame by itself, the components of which are represented by an idealized multi-linear response that does not match perfectly with the nonlinear response of the frame elements in the experiment, as shown in Figure 4-19. The equations used in the first macro-modeling attempt defined the frame elements' elastic stiffness as the slope of the line connecting the origin to the point with 40% of strength based on component experiments. This stiffness is about 35-40% of the stiffness of the uncracked members. For a non-ductile infilled frame, in which the frame may fail while its columns before the columns yield or flexure or early after yielding, we need to have a better estimation of the stiffness of the frame elements. The results of this study showed that using the uncracked stiffness lead to a better match of the macro-model with the micro-model, as well as the experimental results.

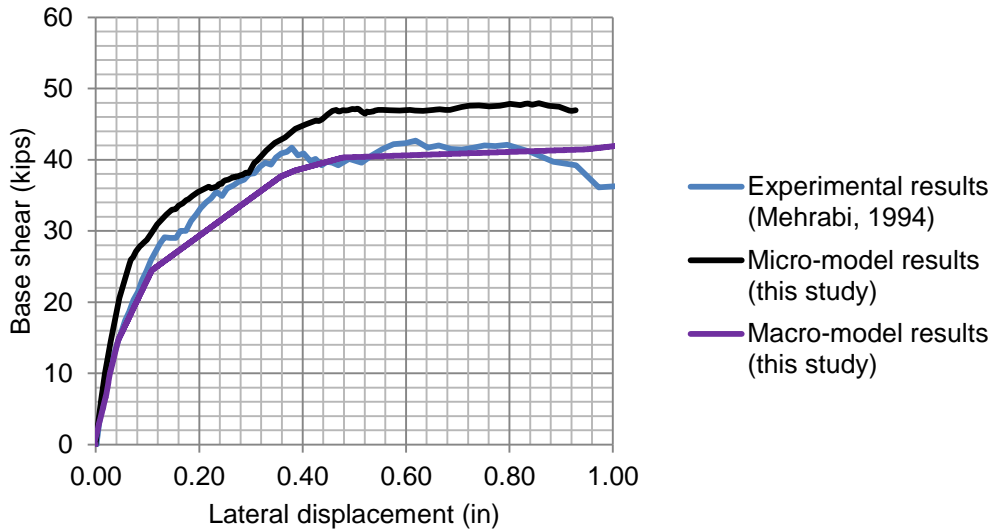


Figure 4-17. Macro-model, micro-model, and experimental results for *Specimen 8*. The experiment was carried out to a lateral displacement larger than 1.0 inches. Results are compared here until 1.0 inches, because the micro-model failed to converge before that point.

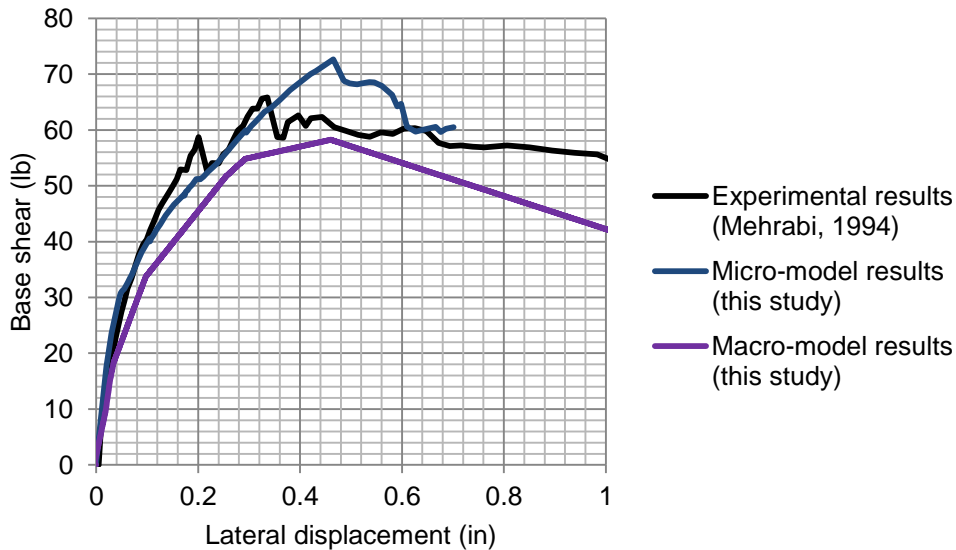


Figure 4-18. Macro-model, micro-model, and experimental results for *Specimen 9*. The experiment was carried out to a lateral displacement larger than 1.0 inches. Results are compared here until 1.0 inches, because the micro-model failed to converge before that point.

Since column shear failure is one of the dominant failure modes in older concrete frames with masonry infill panels, capturing the right drift ratio at shear failure is an important aspect of simulating the response of this category of structures (criterion 3). In *Specimen 9*, experimental results reported shear failure of the concrete frame at 0.5% drift ratio. This value is very close to

the drift at the shear failure of the frame observed in the macro-model of 0.4%. (The micro-model is not intended to represent column brittle shear failure.) The macro-model for Specimen 8 does not experience column shear failure even though the flexure-shear model is employed.

To verify the satisfaction of the third requirement, the results of the micro-model analysis (Figure 4-10) showed that the stress distribution along the infill-frame interface is approximately triangular. In the macro-model, this triangular force/stress pattern representing the infill force on the column is replaced with a single force applied on the column from the strut. The bending and shear diagram of the columns in macro-model based on the proposed approach in this study for *Specimen 9* as well as the shear diagram of the columns in the micro-model are presented in Figure 4-20. This figure shows good agreement of the macro-model results with the typical shapes proposed by Crisafulli (1997).

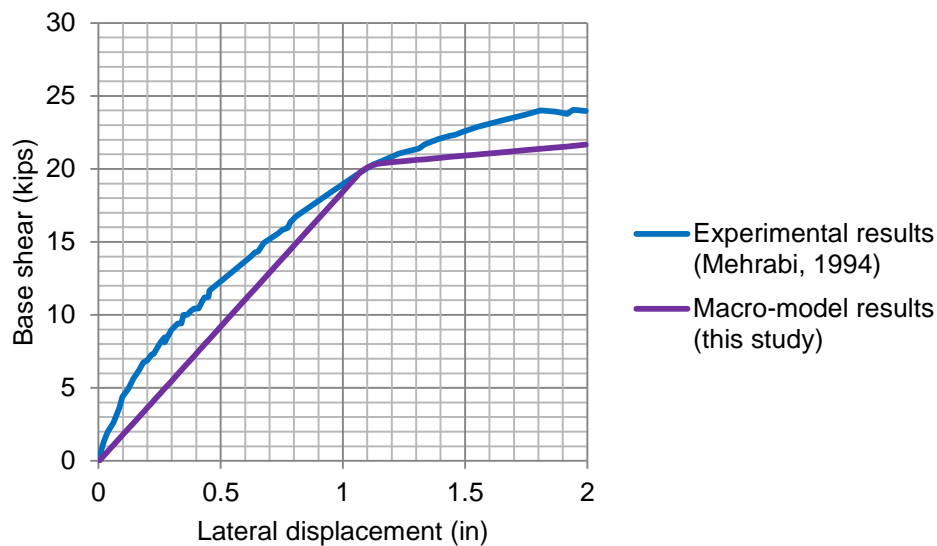


Figure 4-19. Macro-model and experimental results for the bare frame in *Specimen 8* and *9*. The experiment was carried out to a lateral displacement bigger than 2.0 inches. Results are compared here until 2.0 inches.

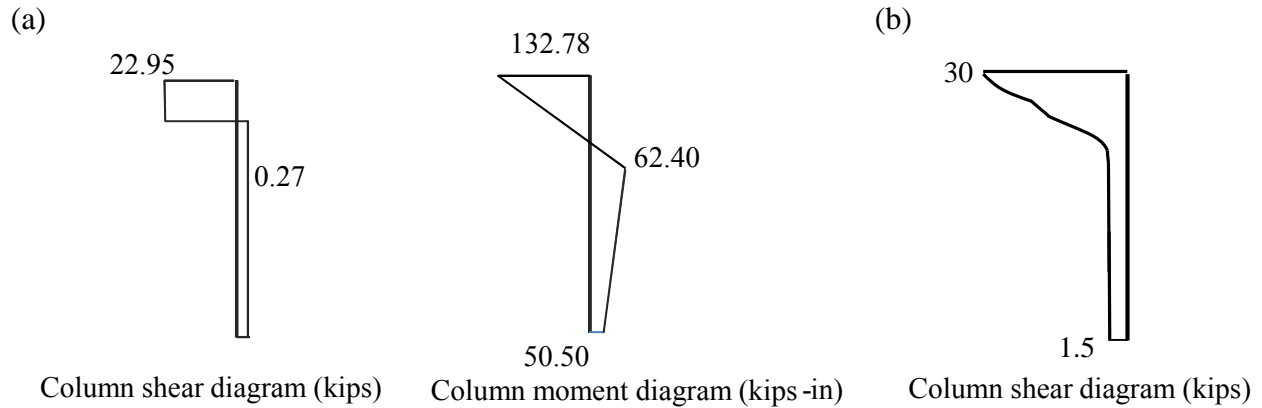


Figure 4-20. (a) Column bending and shear diagram from the macro-model and (b) Column shear diagram from the micro-model for *Specimen 9* at 0.4 in. displacement.

#### 4.5 Application of Proposed Macro-model

In Chapter 5, the multi-scale micro-model/macro-model approach will be used to develop models for infill frame buildings for use in nonlinear dynamic time history. The extrapolation of the proposed modeling approach from single-bay single-story frames to buildings presents a number of additional challenges. In particular, each bay and story of a multi-story building must be represented in a micro-model that has the appropriate gravity load and these micro-model results used to develop the strut properties for each infill wall panel. The computation and application of the gravity load in the micro-model to represent a frame with more than one story is explained in Chapter 5.

#### 4.6 Conclusions

This chapter proposed a new multi-scale modeling technique to simulate the response of the infill panel in masonry infilled frames. In this multi-scale modeling technique, a macro-model is built based on the results of the micro-model. The proposed macro-model is capable to capture appropriately the stiffness and strength of the infilled frame, drift at which the shear failure of columns occurs, and bending and shear diagram of the columns. The simplicity and

accuracy of the proposed macro-model makes it desirable to be implemented in the PBEE framework in order to evaluate the collapse performance of masonry infilled frames.

Although the multi-scale modeling approach has a number of advantages, there are limitations that should be addressed in future research. First, the micro model cannot capture the fracture of the brick, some features of dilatation or certain 3D geometric effects (such as the spaces within the hollow bricks). In addition, the micro model is analyzed under static monotonic loading. Under dynamic loads, the infill may respond differently, including experiencing different failure modes under different ground motions, which is not captured by the infill response extracted in the current approach. The macro model also does not account for cyclic deterioration of strength and stiffness the struts or plastic hinging at mid-height of the columns. Moreover, the 2D modeling approach adopted here neglects the possible out-of-plane failure of the infill walls, which may be important for buildings with single-wythe or hollow clay tile walls. Shing (2013) suggests that out-of-plane response could be represented using a fiber-section beam-column to represent the arching action of the strut out-of-plane, but there are currently insufficient data on the effect of out-of-plane excitation on the in-plane strength of the infill wall (Hashemi and Mosalam 2007).

Modification on an existing shear failure model for concrete columns is proposed in this chapter in order to capture the brittle shear failure may occur in the concrete columns of the masonry infilled frames at very low drift ratios. More research is needed in order to have a better understanding of shear failure of concrete columns in an infilled frame and to examine the feasibility of available equations (and the respective input parameters, such as the shear span or shear drift ratio) to predict the shear failure of concrete columns in this type of buildings.

The proposed macro model is examined for two specimens tested experimentally and a good agreement between the experimental and numerical results was observed. The proposed macro-modeling technique is aimed to be served for any infilled frame regardless of the configuration or material properties of the infill as well as the frame. Because the proposed macro-model is developed based on the basic knowledge from the response of the masonry infilled frames, such as formation of diagonal strut in the infill panel, developing the contact length, etc., and no other calibration or over fitting related to the considered specimens in used in this process. However, limited numbers of specimens are used for validation. Finally, the proposed macro-model would require some modification in strut orientation in order to represent infill walls with openings or partial height infills.

## **5 Collapse Assessment of Masonry Infilled RC Frames Using Multi-scale Modeling**

### **Approach**

#### **5.1 Overview**

This Chapter introduces the “archetypical” buildings that are intended to be representative of existing non-ductile reinforced concrete frames with unreinforced masonry infill panels in high seismic regions of the U.S., such as California. For this purpose, findings of a comprehensive literature review on existing non-ductile concrete buildings in the city of Los Angeles is presented in Section 5.2 and has been used to define the configuration of the archetypical buildings. The material properties as well as the configuration of the infill and frame are defined based on the data found for the existing buildings in the time period of interest. The design geometry and detailing of the archetypical concrete frames are based on the design criteria that were in practice during this era and explained in Section 5.3. Section 5.4 overviews the material properties and configuration of masonry panel in the archetypical buildings. Section 5.5 overviews of the implementation of multi-scale modeling technique for the archetypical buildings as well as definition of collapse used in the seismic assessment procedure. Then, the designed infilled frames are modeled based on the micro-modeling approach explained in Chapter 3. Section 5.6 reviews the micro-modeling of the archetypical buildings and Section 5.7 presents the results of the micro-modeling approach. Out-of-plane behavior of the infill panel in the archetypical buildings is studied in Section 5.8. In the next step, a macro-model corresponding to each micro-model is developed based on the proposed multi-scale modeling approach in Chapter 4, as described in Section 5.9. Finally, the seismic collapse performance of these buildings is assessed in the performance-based earthquake engineering framework and is compared with the corresponding bare frame (Section 5.10).

## 5.2 Characteristics of RC Buildings in California for Case Study

Reinforced concrete buildings started to become a popular form of construction in high seismic zones of US, such as Los Angeles, in the beginning of the 20<sup>th</sup> century (Linares, 2007). The poor performance of some structures in the 1906 San Francisco earthquake showed the need to change the dominant construction type from masonry buildings to engineered reinforced concrete and steel buildings and, as a result, concrete structures became popular in California after that event (FEMA, 2006). In addition, construction of five-to-thirteen story buildings grew in downtown area of the city of Los Angeles in the 1920s and 1930s to satisfy the growing need for new government, banking, and commercial offices (Linares, 2007). During that time, many of the framed buildings that were constructed were infilled with masonry panels (Stavridis, 2009). Most of these buildings have not been retrofitted yet (Holmes et al, 2013). The use of unreinforced masonry walls, has been prohibited in California since Long Beach Earthquake in 1933 (Stavridis, 2009).

Many of these buildings are still in use. Anagnos et al. (2010) conducted a comprehensive survey of reinforced concrete buildings constructed in Los Angeles before the development of seismic detailing requirements for concrete buildings in the 1980s. They found 1600 non-ductile concrete frames in Los Angeles. Figure 5-1 illustrates the distribution of these buildings by year built, showing that most of these buildings (about 25% of the 1600) were constructed in the 1920s. Furthermore, Stavridis (2009) reported that a very small portion of these buildings has been retrofitted. Figure 5-2 shows the height distribution of these buildings varies from 1 to 14 stories. This figure shows that more than 85% of the buildings have 8 stories or less. These buildings have different functionality, as shown in Figure 5-3. Most of these buildings are used for offices, industrial, commercial, and residential purposes.

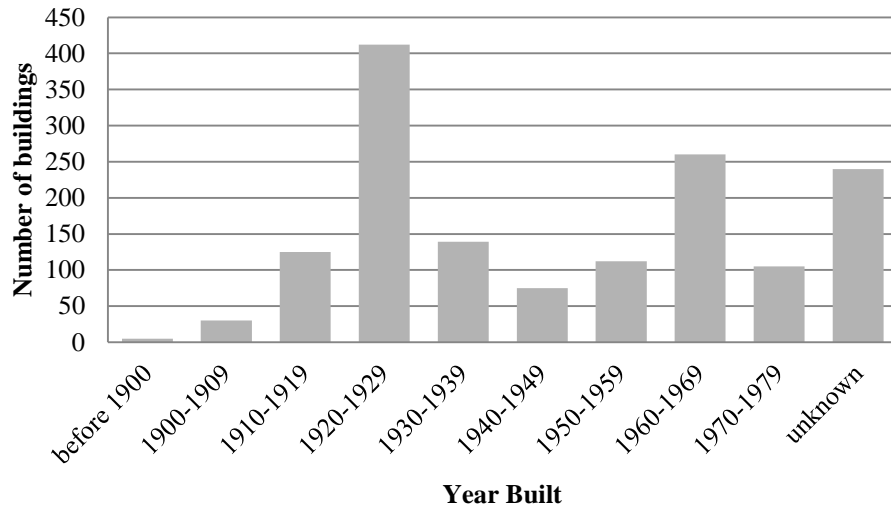


Figure 5-1. Distribution of built-year of non-ductile (pre-1980) concrete buildings in Los Angeles (Anagnos et al., 2010).

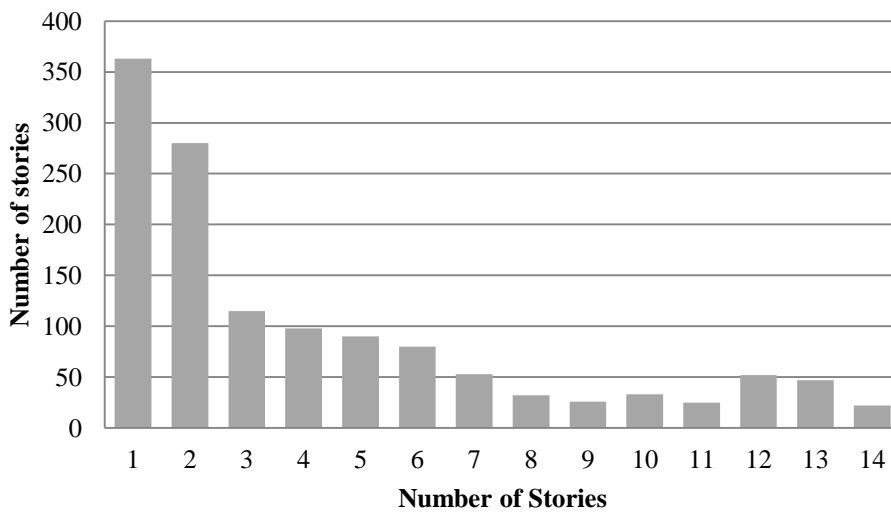


Figure 5-2. Distribution of the number of stories for non-ductile concrete frames in LA (Concrete Coalition, 2009).

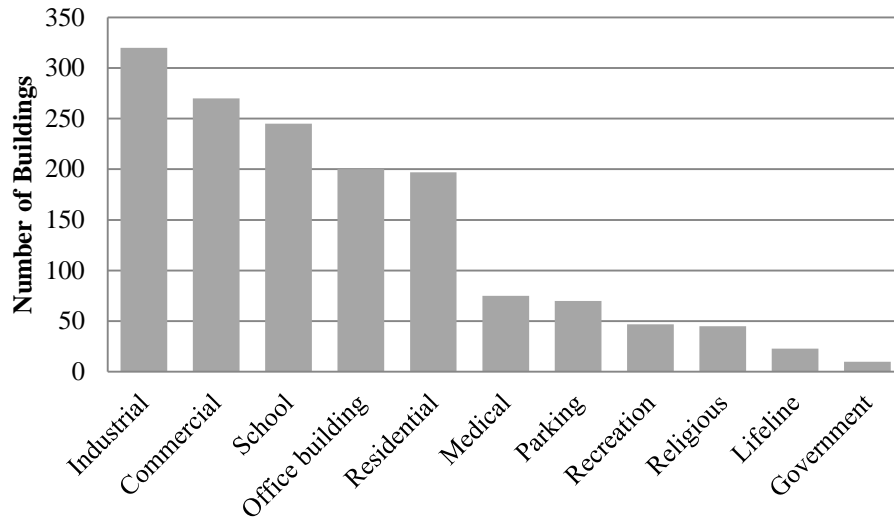


Figure 5-3. Distribution of functionality of non-ductile concrete buildings in LA (Concrete Coalition, 2009).

### 5.2.1 Configuration of the Archetypical Buildings

In this section, a set of archetypical concrete frame office buildings with unreinforced masonry infill panels built in 1920s is introduced. These structures aim to represent 1920s-era engineering practice. The following paragraphs describe the definition of the buildings' configuration, plan, elevation, material properties, and design.

The dimensions of the archetypical building in this study are selected as 120 ft. by 72 ft., with 12 ft. story heights. This geometry is consistent with Faison *et al.* (2004)'s study of non-ductile reinforced concrete frames in the U.S., which found that the long dimension of these buildings varies between 98 and 147 ft. and the short dimension varies between 49 and 98 ft. Faison et al. (2004) also reported the typical beam span length and story height of the buildings as 13-26 ft. and 10 ft., respectively. Stavridis (2009) selected the span and story height for a prototype building from 1920 era as 18-22 ft. and 11.ft., respectively, based on personal communication with practicing engineers familiar with this form of construction. Bennett et al.

(1996) reported the span and height of intermediate floors for an office building in Los Angeles built in 1913 as 18 ft. and 12 ft., respectively.

The elevation and plan view of the archetypical buildings in this study are represented in Figure 5-4. For these buildings, it is assumed that the infill panels of the interior frames have probably been removed or replaced with movable partitions due to the remodeling, so the infill walls are assumed to be present only on the perimeter. Observations from existing buildings constructed in the era of interest approves that the interior infills can be considered as “highly punched” components which show that neglecting the interior infill panels can be a reasonable assumption (Holmes et al., 2013). In Figure 5-4a, the frame lines with infill panels are hatched. The floor system is assumed to be a 2.5 in. slab supported by joist system along the longer direction of each span, as shown in Figure 5-4 for one span. Three different infill configurations, as shown in Figure 5-5, for an example 4-story building, are considered for each case study building. For simplicity, although it is not realistic, infill panels with openings are not considered in this study. Considering the distribution of number of stories presented in Figure 5-2, three different heights of 2, 4 and 8 stories are studied for the archetype buildings, as shown in Figure 5-6.

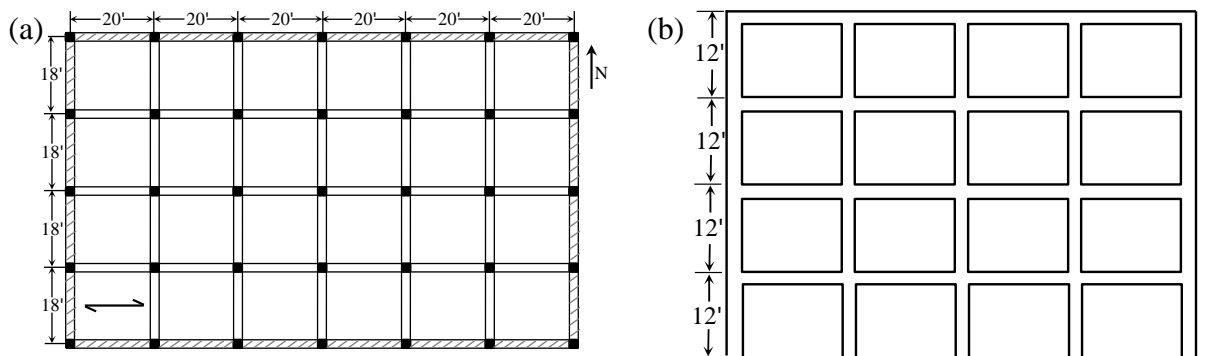


Figure 5-4. (a) Plan view and (b) East-West elevation view of the archetypical building.

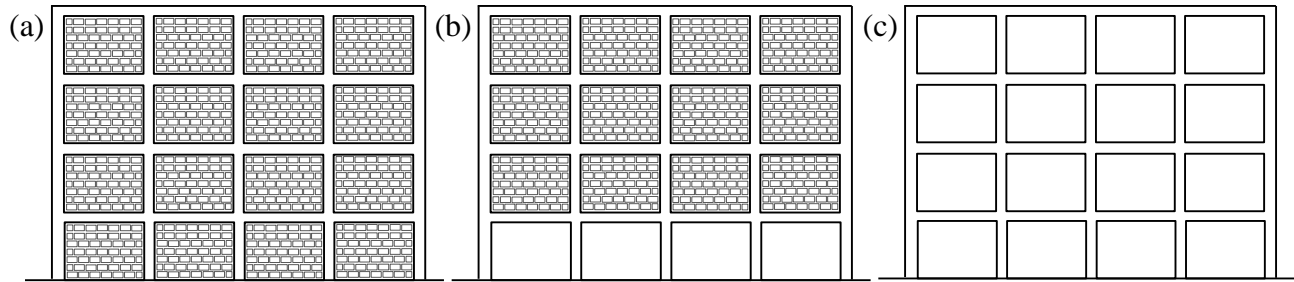


Figure 5-5. Different infill configurations: (a) fully infilled frame, (b) partially infilled frame, and (c) bare frame.

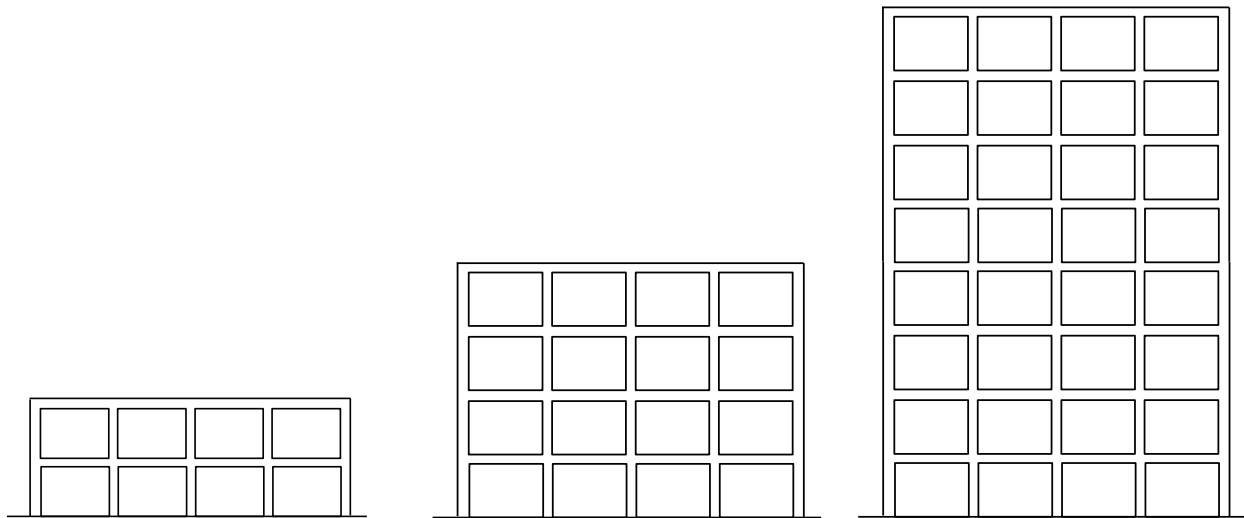


Figure 5-6. Two, four, and eight story buildings considered in the collapse assessment.

### 5.3 Material Properties and Design of the Concrete Frames in Archetypical Buildings

Concrete and steel material properties have changed substantially since the 1920s. A good approximation of the common material properties in the time of interest is needed for a good prediction of the structure response as well as having a realistic design for buildings built in that era. Table 5-1 defines the characteristic properties of steel and concrete in the time period of interest based on FEMA 356 (2000). The compressive strength of concrete in this study is assumed 3000 psi for both columns and beams. Three grades of steel were in use in the construction industry between 1911-1959: structural steel (yield stress of 33 ksi), intermediate steel (yield stress of 40 ksi) and hard steel (yield stress of 50 ksi), as shown in Table 5-1. This

study uses steel grade 33 for reinforcement in beams and ties and grade 50 for longitudinal reinforcement in columns, based on recommendations from Stavridis (2009).

Table 5-1. Steel and concrete material properties (reproduced from FEMA 356).

<b>Steel</b>	<b>Year</b>	1911-1959	<b>Grade</b>	<b>33</b>	<b>40</b>	<b>50</b>
			Minimum Yield (ksi)	33	40	50
			Minimum Tensile (ksi)	55	70	80
<b>Concrete</b>	<b>Year</b>	1920-1949	<b>Lower-Bound Concrete Compressive Strength (ksi)</b>			
			Footing	Beams	Slab	Columns
			1.5-3	2-3	2-3	2-4

The archetypical reinforced concrete frames are designed based on the working stress design methodology presented in the 1927 Uniform Building Code (ICBO, 1927) and reinforced concrete design books published in that era (Turneure and Maurer, 1935, 1914). In working stress design procedure, elements are designed such that the maximum stress under the service loads does not exceed the allowable stress levels defined by the building code. Table 5-2 shows the loads considered in the design of the archetypical buildings. Earthquake forces were not considered in the design process in that era. Wind forces were considered in the design process in this study based on the requirements from the UBC (ICBO, 1927), but the design was governed under combination of dead and live load. The allowable stress limits are defined such that the elements stay in the elastic limits. Allowable stress limits for different element in the concrete frames based on the values proposed in UBC (ICBO, 1927) are presented in Table 5-3.

To follow the common design practice in the era of interest, approximate equations are used to determine design moments in beams and columns, rather than computer analysis. Table 5-4 shows the moment demand in the beams and columns considered in the design procedure based on the recommended values in UBC (ICBO, 1927).

Table 5-2. Design loads for the archetypical buildings.

Load Type	Value (Units)	Source
Live Load	50 (psf)	UBC (1927)
Dead Load: Masonry	130 (pcf)	Calc. from wall geometry
Dead Load: Ceiling	12 (psf)	Haselton (2006)
Dead Load: slab and joist system	80 (psf)	Calc. from floor geometry
Dead Load: Parapet	390 (lb/ft)	Calc. from wall geometry

Table 5-3. Maximum allowable stress in concrete and steel based on the values recommended to UBC (1927).

Concrete	
Compression due to positive bending in extreme fiber	$0.4f'_c$
Compression due to negative bending in extreme fiber	$0.45f'_c$
Shear in beams with stirrups and or bent bars	$0.06f'_c$
Steel	
Hard grade	20000 (psi)
Intermediate grade	18000 (psi)
Structural grade	16000 (psi)

Table 5-4. Moment demands in the beams based on the values presented in UBC (1927). In these equations,  $w$  is load per unit length of the beam and  $l$  is length of the beam.

Interior spans	
Negative moment at interior supports except the first	$\frac{wl^2}{12}$
Maximum positive moment near center of the interior spans	$\frac{wl^2}{16}$
Exterior spans	
Maximum positive moment near center of span and negative moment at first interior support	$\frac{wl^2}{12}$
Negative moment at the exterior support	$\frac{wl^2}{12}$

Figure 7 shows the design of beams at the floor and roof level of the exterior frame, for all of the archetypical buildings. The reinforcement arrangement shown in Figure 7 is the most common reinforcement arrangement in that period of interest (Turneure and Maurer, 1935).

Turneure and Maurer (1914), who wrote one of the first texts about designing concrete buildings, recommend that the portion of the lower reinforcement in beams should continue to the columns or over the support and overlap in order to provide good anchorage. The minimum lap-splice length is 24 and 30 times the diameter of longitudinal reinforcement for structural and hard steel, respectively (Stavridis, 2009). The minimum clear concrete cover should be diameter of the round bars or the diagonal of square bars (UBC, 1927).

Table 5-5, Table 5-6, and Table 5-7 show the design of exterior frame columns for the two-story, 4-story, and 8-story buildings, respectively. The column design differs with building height depending on the level of axial load. Available drawings for old concrete buildings with masonry infill panels built in 1920's and later also approve the reinforcement configuration used in this study for the frame, in terms of having bent bars in the beams and wide transverse reinforcement in the columns. Moreover, some of the drawings show that in beams both bent bars as well as the vertical transverse reinforcement were used (Holmes et al., 2013).

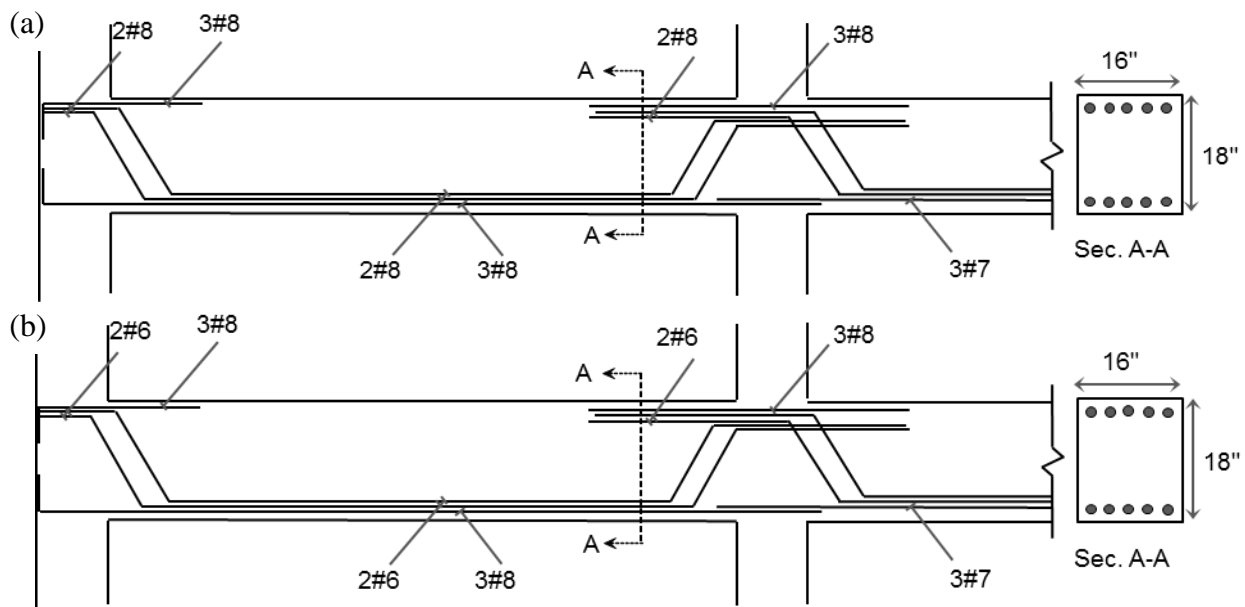


Figure 5-7. Design of exterior beams for (a) an arbitrary floor level and (b) the roof level.

Table 5-5. Design of columns in the exterior frame of the 2-story building.

<b>Column</b>	<b>Story</b>	<b>Dimension</b>	<b>Longitudinal Reinforcement</b>	<b>Tie</b>
Corner	1 <sup>st</sup>	16"x16"	6#8	#3@8"
Interior	1 <sup>st</sup>	14"x14"	4#8	#3@8"
Corner	2 <sup>nd</sup>	16"x16"	6#8	#3@8"
Interior	2 <sup>nd</sup>	14"x14"	4#8	#3@8"

Table 5-6. Design of columns in the exterior frame of the 4-story building.

<b>Column</b>	<b>Story</b>	<b>Dimension</b>	<b>Longitudinal Reinforcement</b>	<b>Tie</b>
Corner	1 <sup>st</sup>	16"x16"	6#8	#3@8"
Interior	1 <sup>st</sup>	18"x18"	6#8	#3@8"
Corner	2 <sup>nd</sup>	16"x16"	6#8	#3@8"
Interior	2 <sup>nd</sup>	16"x16"	4#8	#3@8"
Corner	3 <sup>rd</sup>	16"x16"	6#8	#3@8"
Interior	3 <sup>rd</sup>	14"x14"	4#8	#3@8"
Corner	4 <sup>th</sup>	16"x16"	6#8	#3@8"
Interior	4 <sup>th</sup>	14"x14"	4#8	#3@8"

Table 5-7. Design of columns in the exterior frame of the 8-story building.

Column	Story	Dimension	Longitudinal Reinforcement	Tie
Corner	1 <sup>st</sup>	24"x24"	8#8	#3@8"
Interior	1 <sup>st</sup>	26"x26"	8#8	#3@8"
Corner	2 <sup>nd</sup>	22"x22"	6#8	#3@8"
Interior	2 <sup>nd</sup>	26"x26"	8#8	#3@8"
Corner	3 <sup>rd</sup>	20"x20"	6#8	#3@8"
Interior	3 <sup>rd</sup>	24"x24"	8#8	#3@8"
Corner	4 <sup>th</sup>	18"x18"	6#8	#3@8"
Interior	4 <sup>th</sup>	22"x22"	8#8	#3@8"
Corner	5 <sup>th</sup>	16"x16"	6#8	#3@8"
Interior	5 <sup>th</sup>	18"x18"	6#8	#3@8"
Corner	6 <sup>th</sup>	16"x16"	6#8	#3@8"
Interior	6 <sup>th</sup>	16"x16"	4#8	#3@8"
Corner	7 <sup>th</sup>	16"x16"	6#8	#3@8"
Interior	7 <sup>th</sup>	14"x14"	4#8	#3@8"
Corner	8 <sup>th</sup>	16"x16"	6#8	#3@8"
Interior	8 <sup>th</sup>	14"x14"	4#8	#3@8"

#### 5.4 Material Properties and Configurations of Masonry Panels in Archetypical Buildings

This section of the study explains the material properties and configuration of the masonry infill panels corresponding to the archetypical building considered here. The configuration and material properties of the masonry infill panels depend on different parameters, including the construction era.

With regard to the type of masonry used in construction during the 1920s, Hamburger and Meyer (2006) reported that clay brick masonry was the most common type of masonry in 1906 San Francisco earthquake. FEMA 306 (1998) also mentioned clay brick as the common type of infill panel. Based on this information, clay brick masonry is also adopted in this study. Clay bricks have been produced in different sizes during the past century. Stang et al. (1929)

measured the compressive strength of 168 brick walls and 129 wallethes. The brick sizes used in that study can be considered as a representative of the brick sizes that were in common in the 1920s, and had average sizes of 8" x 3.7" x 2.6" (length x depth x height). The average mortar thickness was reported as 0.5". A separate study by Atkinson-Noland & Associates (1995), measured the compressive modulus of masonry for two infilled frame buildings built in the era of interest in Los Angeles. This report mentions the common brick sizes as the 8.5" x 3.75" x 2.75" (length x depth x height) and the common mortar thickness as 0.5", which are adopted in this study. Cement-lime-sand mortar was common during that era (Mack and Speweik, 1998).

Tests on these older unreinforced masonry walls can be used to quantify the shear strength and compressive strength of the masonry walls, depending on the properties of the wall and the vertical stress. In 1978, the Los Angeles City Council commissioned a study of the unreinforced masonry buildings built before 1934 in the city. The work included a survey to identify all pre-1934 unreinforced masonry buildings. In the absence of data about this construction type in Los Angeles area, a comprehensive testing program was conducted by researchers, the Smith-Emery testing laboratory and the city of Los Angeles (Schmid et al., 1978). The testing consisted of the sampling for four masonry buildings with clay bricks including three one-story building and one three-story building. The results of their tests are adopted in this study as the representative properties of masonry wall that were in common in the era of interest, based on the assumption assuming that infill panel properties are the same as the unreinforced masonry walls built at the same time. Based on data presented in (Schmid et al., 1978), the shear strength of the masonry,  $V$ , panel depends on vertical load applied to the panel. The minimum shear strength (psi) of the masonry panel is defined in Equation (5-1):

$$V(\text{psi}) = 30 + \text{axial stress}(\text{psi}) \quad (5-1)$$

This shear strength corresponds to the first movement in the shear test, based on the in-situ shear tests. This value gives the 80 percent confidence level for the shear strength of the masonry specimens. The data also show that the ultimate shear strength is 1.2 times greater than the shear strength at first movement. Based on this information, in this study, the ultimate shear strength of the masonry panel is considered as:

$$V(\text{psi}) = 1.2(30 + \text{axial stress}(\text{psi})) \quad (5-2)$$

Schmid et al. (1978)'s compression tests revealed ultimate strengths of the 400-500 psi. The present study uses 500 psi as the compressive strength of the masonry.

Infill panels may consist of one or more wythes. In old infilled concrete buildings, the exterior frames are usually infilled with two or more wythe walls (ATC, 2010). Hamburger and Meyer (2006) reported four-wythe walls as a common infill panel for steel frames at the time of the 1906 San Francisco earthquake. Stavridis (2009) reported that exterior frames in that era have three-wythe wall. This study considers three-wythe walls for the exterior frames. In some countries a gap between the infill and frame are in common, however, in the U.S., the frame is tightly infilled with infill panel on all sides (FEMA, 2010; ATC, 2010).

## **5.5 Overview of Modeling and Collapse Assessment Approach**

### **5.5.1 Multi-scale Modeling Approach**

The collapse assessment of the archetypical buildings utilizes the multi-scale modeling approach developed in this thesis. First, the appropriate micro-models are developed for the archetypical buildings, using the findings of Chapter 3, and the results of the micro-models used to create macro-models for each archetypical building, based on the procedure developed in Chapter 4. The final macro-models are implemented in the performance-based earthquake

engineering framework and analyzed using Incremental Dynamic Analysis (IDA) approach, in order to develop the fragility curves for archetypical buildings.

### **5.5.2 Incremental Dynamic Analysis for Assessing Collapse Performance**

The procedure for assessing seismic performance applies the methodology for performance-based earthquake engineering developed by the Pacific Earthquake Engineering Research Center, which provides a probabilistic framework for relating ground motion intensity to structural response and building performance through nonlinear time-history simulation. Incremental Dynamic Analysis (IDA) is used to assess collapse (Vamvatsikos and Cornell, 2002). In IDA, a nonlinear structural model is subjected to a recorded ground motion, and dynamically analyzed to predict the structure's response. The time-history analysis is repeated, each time increasing the scale factor on the input ground motion, until that record causes structural collapse. The definition of collapse used is discussed in Section 5.5.2.1. This process is repeated for a large set of ground motion records, in order to quantify record-to-record variation in nonlinear structural response. This study uses 44 recorded ground motions (22 pairs) selected to represent large earthquakes with moderate fault-rupture distances (i.e., not near-fault conditions) (FEMA, 2009).

The outcome of IDA is a fragility function, which is a cumulative probability distribution that defines the probability of experiencing a specific damage state, *i.e.* structural collapse, as a function of the ground motion intensity (given by the spectral acceleration at the first mode period of the building [ $Sa(T_1)$ ]). The fragility functions account for uncertainties due to record-to-record variation in ground motions ( $\sigma_{ln,RTR}$ ).

### 5.5.2.1 Collapse Definition

Two collapse mechanisms are defined here accounting for shear and axial column failure mechanisms to capture collapse in a building in the macro model. The definition of collapse in this study is similar to that defined by Baradaran Shoraka et al. (2013). In this approach, shear failure is defined when the shear capacity of a story degrades to become smaller than 40% of that story's maximum capacity. The shear capacity of each story is composed of shear capacity of all elements in that story including columns and struts (for infilled frames). The maximum capacity is computed from pushover analysis. The dynamically varying capacity of the story is monitored throughout the time history analysis. For the columns, the method of computing the capacity depends on whether shear failure has been triggered in the column. Prior to the triggering of shear failure (i.e. when the response hits the limit state surface), the shear capacity of each column is taken as the minimum of Elwood (2004) and Sezen (2002) limit curves, as explained in Chapter 4. After triggering the shear failure in each column, the capacity of the column is assumed to be equal to the shear demand in that column. The initial capacity of the struts is based on the peak strut capacity, determined from the micro-model. For drifts exceeding the drift at the peak strength of the wall, the capacity of the struts is assumed to follow the negative post-peak response. The post-peak response of the frame system is governed with the degradation response of the column as well as the response of the struts after failure of the column. Once shear failure has occurred in one of the columns on either side of the strut of interest, the struts will unload rather than follow its prescribed force-displacement response. If this occurs, the capacity of the strut is assumed to be equal to the demand in the strut. The cut-off identifying when collapse occurs indicates the strength of the story is less than 40% of its

original capacity. 40% is selected as an arbitrary value which is smaller than half of the maximum strength; however, results are not very sensitive to the selected value.

Axial failure is triggered when the axial capacity in any story becomes smaller than axial demand (Baradaran Shoraka et al., 2013). For columns in which shear failure has not started, the axial capacity is computed as the elastic axial capacity of a column. The axial capacity for a column in which shear failure is initiated is calculated based on the Elwood axial limit curve, and depends on the drift ratio in the column (Elwood, 2004). This study assumes no axial capacity for the infill, as a conservative approximation, but this approximation is not critical since the analysis results showed that axial failure never governs the response for the infilled frame since they fail consistently in shear. The axial demand in each story is computed as the summation of the axial forces in the columns in that story. The axial demand is considered constant in each floor during the analysis. The collapse identification procedure checks the shear and axial collapse criteria for each story in the building at each time step during the analysis, until one or more stories is identified as being collapsed.

## **5.6 Micro-Modeling of the Archetypical Buildings**

The general properties of the infill panel such as compressive and shear strength as well the compressive strength of concrete and tensile strength of steel were presented in Section 5.4. In order to develop the micro-model, there is a need to define properties and configuration of the brick and mortar separately such that the properties of the wall in the micro-model lead to the values found in the literature and presented in this previous section. As explained in Chapter 3, in order to simulate the infill panel in a micro –model we need to quantify 17 material parameters for the mortar interface and 7 parameters for clay bricks and concrete. An additional 7 parameters are used to define the concrete and steel properties in the micro-model. This section

of study explains how the input parameters for the purpose of micro-modeling are derived based on the available data from literature.

### **5.6.1 Properties of the Infill and Frame in the Micro-Model**

The literature presented in Section 5.4, provided the more important parameters defining the infill and concrete frame, such as compressive, shear and tensile strength. The rest of parameters need to be derived from the available data. This section defines the model parameters for mortar, clay brick, concrete, and steel. These parameters are derived from four sources:

- (1) Parameters that are defined directly in the literature and described in Section 5.4, such as compressive strength of concrete. These parameters are identified by a superscript <sup>\*</sup> in the following sections.
- (2) Parameters that are defined indirectly based on the parameters in group 1 by conducting a calibration process in DIANA. These parameters are shown with superscript <sup>\*\*</sup>.
- (3) Parameters that can be computed based on the first group of parameters using the available equations relating different material parameters of a material together. Some of these parameters are calibrated using the FE models. These parameters are shown with superscript <sup>\*\*\*</sup>.
- (4) Parameters with no available data, identified with superscript <sup>\*\*\*\*</sup>. This group of parameters defines the dilatation properties of the interface. For the fourth group of parameters we use the corresponding values defined in Chapter 3 for the Mehrabi's specimens.

The input parameters computed for each of the constituent materials, *i.e.* mortar, brick, concrete, and steel are presented in following.

### 5.6.1.1 Model Properties for the Mortar Interface

Table 5-8 presents the mortar interface model properties implemented in the micro-modeling process of the archetypical buildings. As explained in Section 5.6.1, parameters are shown with different superscripts based on the method that they are defined. The normal stiffness modulus of the interface,  $K_{nn}^{**}$ , is computed based on calibration. To determine  $K_{nn}$ , a wallette model is made in DIANA with an arbitrary elastic brick properties and  $K_{nn}$  is varied such that the elastic slope of the compressive stress-strain response becomes equal to the expected Young's modulus value of the masonry,  $E^{**}$ , which is equal to  $750f'_m$  as proposed by (ICBO, 1997), where  $f'_m$  is the compressive strength of the masonry wall. The shear stiffness modulus,  $K_{ss}^{***}$ , is a parameter of type (3) and is related to  $K_{nn}$  using Equation (5-3), (Stavridis, 2009), where the Poisson ratio,  $\nu$ , is chosen as 0.16 based on the literature for masonry infill walls (Mehrabi, 1994).

$$K_{ss} = K_{nn}/2(1 + \nu) \quad (5-3)$$

The cohesion parameter  $C^{**}$ , which is the shear strength of mortar under zero axial load (Terzaghi, 1996), is defined based on a simple calibration in DIANA. To define the cohesion parameter, a model composed of two elastic bricks and one layer of mortar is made in DIANA where a uniform increasing displacement under zero axial load is imposed on the top brick, similar to the process explained in Chapter 3 to calibrate the interface of Mehrabi's Specimen 8. Then value of  $C$  is defined such that the shear strength of this specimen becomes equal to  $1.2(30\text{psi} + 0(\text{axial stress}))$ , which is the shear strength of the infill in psi based on the literature presented in Section 5.4 in Equation (5-2). The internal friction angle,  $\Phi_i^*$ , is defined as the angle between the line relating the shear to the axial stress in the yield surface in the Mohr-Coulomb model (Terzaghi, 1996). We use the relationship defined in Section 5.4, *i.e.* shear stress

=  $1.2(30 + \text{axial stress})$ . The residual friction angle,  $\Phi_r^{****}$ , is assumed as  $0.9\Phi_i$ , based on the same values reported in Mehrabi (1994).

As mentioned in Chapter 3, the compressive strength of the infill wall is usually governed by the compressive strength of its weakest part, which is the mortar joint. The literature review in Section 5.4 reported the compressive strength of the masonry wall as 500 psi. To obtain the compressive strength of the mortar joint,  $f_c^{**}$ , a wallette specimen is developed in DIANA with elastic bricks and subjected to a compressive displacement. The value of the mortar  $f_c'$  is varied until the compressive strength of the wallette becomes 500 psi, the value predicted from literature review. The tensile strength of the mortar,  $f_t^{***}$  is considered as 6% of the  $f_c$ , (Rao, 2001). The first mode fracture energy,  $G_f^{I**}$ , of the mortar is interpolated from the splitting test data conducted by Wittmann (2002). These data reported the first mode fracture energy of 0.7-0.9 psi/in for concrete with the tensile strength of 28-55 psi. The second-mode fracture energy,  $G_f^{II***}$ , is computed based on an equation proposed by Lotfi (1994) which related the first and second mode fracture energy:  $G_f^{II} = 10 G_f^I$ . Compressive fracture energy,  $G_{fc}$ , is computed using Equation (5-4) proposed by (Nakamura and Higai, 2001):

$$G_{fc} = 8.8\sqrt{f_c(MPa)} \quad (5-4)$$

Due to lack of available data for parameters dilatancy angle,  $\Psi^{****}$ , confining normal stress,  $\sigma_c^{****}$ , softening parameter,  $\delta^{****}$ , and relative plastic displacement at peak compressive strength,  $\kappa_p^{****}$ , the value of these parameters were adopted from the values presented in Chapter 3 for Mehrabi's Specimen 8.

The modeling properties presented in Table 5-8, are used for the bed-joints in the archetypical building. As mentioned in Chapter 3, usually the head-joints and wall to frame joints are weaker than the bed-joints. In this study, the same ratio between the stiffness of the

head-joint to the bed joint used in Chapter 3 is used to define normal and shear stiffnesses, strength, cohesion parameter, and friction angle parameters of the head-joint and wall to frame joint properties based on the bedjoint properties.

Stavridis (2009) conducted a sensitivity study on the response of the infilled frame for two specimens tested by Mehrabi (1994). Stavridis (2009) measured the variation in the response of the infilled frames including stiffness, maximum strength, drift at maximum strength, and drift at which the strength becomes 90% of the maximum strength, when each parameter in the model is varied. His results showed that among the parameters for the interface element,  $f_t$ ,  $C$ ,  $\Phi$ ,  $\delta$ , are the most important. However, they reported that the range of variation of  $\delta$  in their study was very large. Among these parameters, we have the most confidence in defining  $f_t$ ,  $C$ , and  $\Phi$ .

Table 5-8. Model interface (mortar) properties for the archetypical buildings.

$K_{nn}^{**}$ (lb/in <sup>3</sup> )	$K_{ss}^{***}$ (lb/in <sup>3</sup> )	$C^{**}$ (psi)	$\Phi_i^*$ (deg)	$\Psi^{****}$ (deg)	$\Phi_r^{****}$ (deg)	$\sigma_c^{****}$ (psi)	$\delta^{****}$	$f_t^{**}$ (psi)	$G_f^{I**}$ (psi-in)	$G_f^{II****}$ (psi-in)	$f_c^{**}$ (psi)	$C_s^{****}$	$G_{fc}^{***}$ (psi-in)	$\kappa_p^{****}$ (in)
100000	43103	36	50	0.29	45	-150	2	31	0.72	7.2	515	1	93	0.005

### 5.6.1.2 Model Properties for the Bricks

Table 5-9 presents the modeling parameters for the bricks in the micro-model. Recall that the bricks are modeled with the total strain rotating crack material model. Density\* and compressive strength,  $f_c^*$ , of the bricks are computed as the average values reported by Stang et al. (1929) from testing on the bricks from 1920s. The compressive strength of the bricks is computed as 3280 psi. However, in this study we assumed that the compressive strength of bricks as 3000 psi, in order to ensure that bricks are weaker than the concrete in the frame. The tensile strength,  $f_t^{***}$ , of the clay bricks is assumed as 10% of the compressive strength of the bricks (Drysdale et al., 1999). The first mode fracture energy,  $G_f^{I*}$ , is interpolated from the experimental data reported for bricks with different tensile strength (Van der and Pluijm, 1992).

Van der and Pluijm (1992) reported for bricks with tensile strength varying from 220-510 psi, the first model fracture energy varies from 0.34-0.74 psi/in. (Rao, 2001) also conducted several tests on different types of bricks including solid bricks and hollow bricks. Linear interpolation from his results gives a tensile fracture energy of 0.43psi/in, which is very close to the value reported by Van der and Pluijm (1992), *i.e.* 0.45psi/in. This study uses the average of these values. Finally, the compressive fracture energy,  $G_c^{**}$ , of the bricks is computed using Equation (5-4). The author is aware that this relationship is developed for the concrete material. However, due to the lack of a similar relation for the bricks, we decided to use this relation. Young's modulus and Poisson's ratio of the bricks are adopted from those found for modeling the Mehrabi's Specimen.

Table 5-9. Model brick properties for the archetypical buildings.

Young's Modulus $E^{**}$ (psi)	$\nu^{****}$	Density* (lb/in <sup>3</sup> /g)	$f_t^{***}$ (psi)	$G_f^{I*}$ (psi-in)	$f_c^*$ (psi)	$G_c^{**}$ (psi-in)
2000000	0.16	0.000162	300	0.44	3000	224

### 5.6.1.3 Model Properties for Concrete

Table 5-10 presents the modeling parameters for the concrete in the frame in the micro-model. The concrete is modeled with the total strain rotating crack material model. Young modulus,  $E^{**}$ , and  $f_t^{**}$  of concrete are computed using Equations (5-5) and (5-6), respectively, from ACI 318 (2002).  $\nu$  is selected as 0.16 which is a common Poisson ratio for concrete. The compressive strength,  $f_c^*$ , is selected based on the literature review presented in Section 5.3.  $G_c^{***}$  is computed using Equation (5-4).  $G_f^{I***}$  is computed based on a linear relation between  $G_f^I$  and  $G_c$ ,  $G_c=250$ .  $G_f^I$ , found by Nakamura and Higai (2001).

$$E_c = 57000\sqrt{f_c} \quad (5-5)$$

$$f_t = 6\sqrt{f_c} \quad (5-6)$$

Table 5-10. Model brick properties for the archetypical buildings.

<b>Young Modulus (psi)</b>	<b><math>\nu</math><sup>***</sup></b>	<b>Density<sup>*</sup> (lb/in<sup>3</sup>/g)</b>	<b><math>f_t</math><sup>***</sup> (psi)</b>	<b><math>G_r^I</math><sup>***</sup> (psi- in)</b>	<b><math>f_c</math><sup>*</sup> (psi)</b>	<b><math>G_c</math><sup>***</sup> (psi-in)</b>
3122019	0.16	0.000225	329	0.89	3000	223.6326

#### 5.6.1.4 Model Properties for Steel

Table 5-11 shows the modeling parameters for the steel in the concrete frame. In the micro-model Steel is modeled with elastic-hardening-plastic material model. As mentioned in Section 5.3 two grades of steel has been used in the modeling and properties for both are shown in Table 5-11. The yield stress,  $f_y^*$ , of the steel is selected from the literature in Section 5.3. The ultimate stress,  $f_u^*$ , of the steel is assumed to be 1.1 times the yield stress based on (ATC, 2011).

Table 5-11. Model steel properties for the archetypical buildings.

<b>Steel types</b>	<b>Density<sup>*</sup> (lb/in<sup>3</sup>/g)</b>	<b>Yield stress(<math>f_y^*</math>) (psi)</b>	<b>Ultimate stress(<math>f_u^*</math>) (psi)</b>
Structural	0.00073	33000	36300
Hard	0.00073	50000	55000

### 5.7 Micro-Modeling Analysis and Results for Archetypical Buildings

The modeling parameters of different components of the archetypical building are explained in Section 5.6. These modeling parameters are implemented in DIANA using the same elements types as explained in Chapter 3 for brick, interface, concrete, and steel, to develop micro-models for the archetypical buildings introduced in Section 5.2. As explained in Section 5.2, archetypical buildings are defined in three different heights of two, four, and eight stories. For each story each archetypical building, one of the interior spans is modeled and analyzed in DIANA, accounting for the member sizes and reinforcement, etc. of each distinct story. However, since the top two stories of the 8-story model are the same as the top two stories of the 4-story building, which is the same as the two-story building, in total the analysis requires 8 micro-model representations. However, one primary difference between the modeling of the

archetypical building and the experimental specimens presented in Chapter 3 is the application of the vertical load. The sequence of the application of the vertical load on the masonry infilled frame needs to be simulated as close as what happens in construction, in order to ensure that the simulated model capable of predicting an accurate prediction of the response. Section 5.7.1 explains the effect of the vertical load and how it has been simulated in this study for archetypical buildings, accounting for the different properties of each story. Section 5.7.2 presents the pushover results for the micro-models of the archetypical buildings and Section 5.7.3 shows the extracted response of the infill panel from the micro-model.

### **5.7.1 Effect of Vertical Load in the Micro-model for Archetype Buildings**

The masonry infill panel is a composite section made of bricks and mortar. Experimental results also showed the response of the mortar joint depends on the level of vertical stress in the mortar joint (Mehrabi, 1996), where the higher vertical stress leads to the higher shear strength of mortar. This interaction between shear and compression response of the mortar joint implies the need to accurately simulate the vertical stress in the infill panel in the micro-model simulation and the calibrated strut model. During the past years, several, but not many, studies tried to investigate the effect of the vertical load on the response of the infilled frame.

Stafford-Smith (1968) conducted a series of monotonic tests on single-bay, single-story, infilled steel frame and found that the amount of the vertical load on the beam affects the stiffness and strength of the infilled frame, such that higher vertical load lead to an increase in the stiffness and strength of the infilled frame. However, they did not consider the effect of the vertical load in their proposed strut modeling approach. Abrams (1994) stated that the effect of vertical load on the developing the strut model should be considered and identified the need of more research in this field. Cavaleri et al. (2004) conducted a set of numerical and experimental

investigations on single-story, single-bay infilled frames and showed that higher vertical load on the frame increases the masonry-frame contact length. More recently, (Amato et al., 2008) proposed an equation to compute the initial stiffness of the single strut model as a function of the vertical load, based on the FE simulation of a single-bay single-story infilled frame with different levels of vertical load. They found that the equivalent width of the strut increases proportionally with the amount of the vertical load.

This literature shows the importance of considering the appropriate level of vertical load in order to capture the realistic behavior of the infilled frame in the micro-model. In order to evaluate the response of the infill panel, the vertical load in the model need to be applied in the same sequence as in the construction. In U.S. construction practice, the frame and floor are typically built first and, subsequently, the infill panel is inserted into the frame (Cavaleri et al., 2004). Since the beam has already deflected under the dead load of the floor and frame system before the infill is installed, the infill carries only the vertical forces from loads applied after it is inserted, such as load of the ceiling and live load, and the weight of the infill panel of the floor immediately above (Cavaleri et al., 2004). It is worth mentioning again that in the U.S. it is not common to leave a gap between the beam and infill, so the infill is in contact with the beam.

In this study, the vertical load applied on columns and beams in the single-bay single-story micro-model is considered as follows:

#### *Vertical loads on columns*

The vertical load imposed on each column in the micro-model is computed from the vertical load coming from all of the stories above the stories of interest. The vertical load on the columns is computed based on the area tributary to that column. The load of upper stories is computed as the sum of the dead load of the frame, 25% of the live load, and the dead load of the

masonry infill panels. 25% of Live Load is considered as the expected live load in the structure based on (Ellingwood et al., 1980).

#### *Vertical loads on beams*

The vertical load on the beams is more critical and is applied in two phases in the micro-model to mimic the construction process. In the first phase, before the infill panel is added to the model, the distributed load corresponding to the dead load of slab is applied on the beam, simultaneous to the application of the column vertical load. In the next phase, the infill panel is inserted in the model and subsequently, the vertical load corresponding to the summation of 1) the remaining dead load (due to ceiling and other fixtures), 2) 25% of live load, and 3) the dead load of the infill panel in the story immediately above is applied.

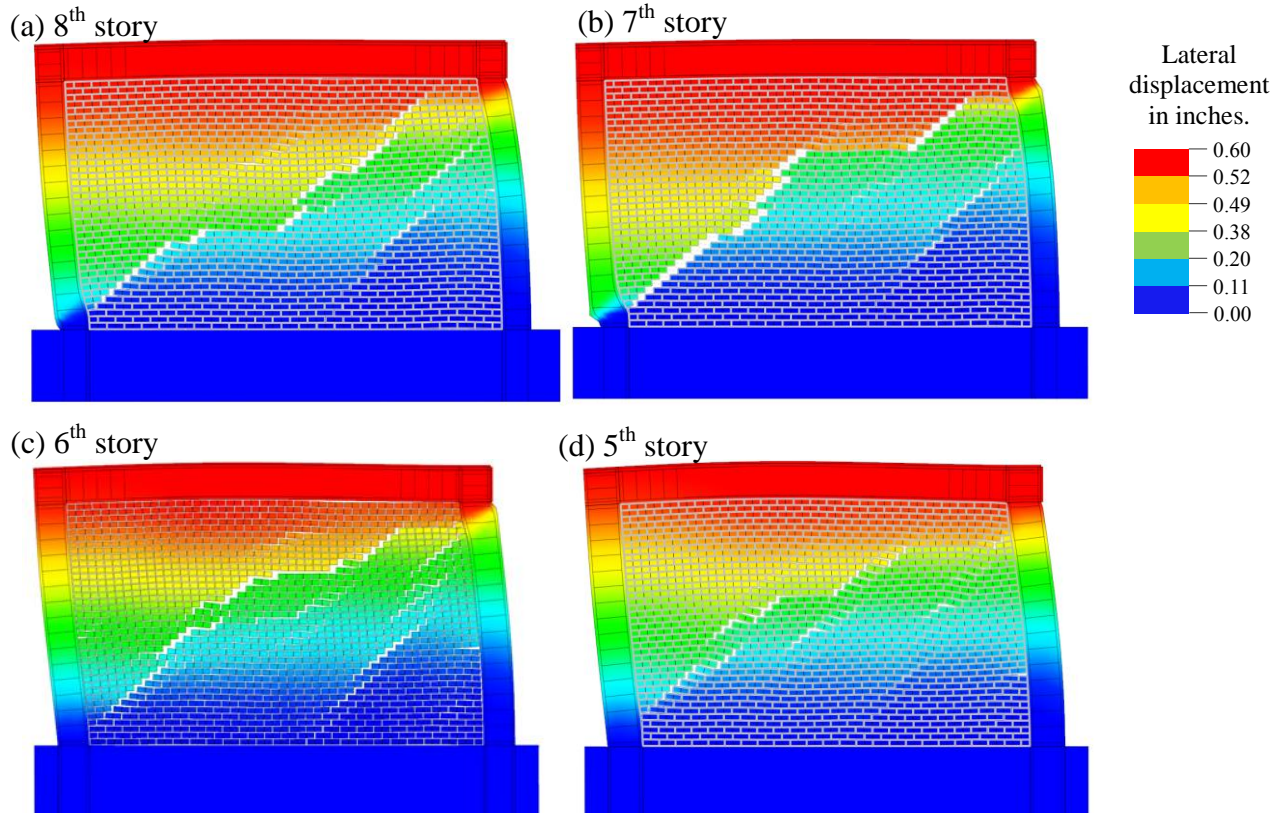
This sequence of the vertical load application can be considered as analogous to what happens in construction. This modeling technique leads to the realistic simulation of the vertical forces existing in the infill panel, which in turn results in the accurate simulation of the infill panel response.

### **5.7.2 Pushover Results from the Micro-Models for Archetypical Buildings**

Eight micro-models are analyzed to develop the multi-scale models for the archetypical buildings. Recall that each of these models can be representative of the infill panel response of different stories in the archetypical buildings, as long as those stories have the same frame and vertical loading. The micro-models are analyzed for gradually increasing lateral displacement applied at top of the frame. Three different convergence norms, including energy norm of 0.0001, displacement norm of 0.001, and force norm of 0.01, are defined in order to have restricted convergence criteria (DIANA, 2011). All of these norms need to be satisfied to obtain

a converged solution at each time step. The models were pushed as far as possible with the defined convergence algorithms.

Figure 5-8 shows the deformed shape of eight models made in this study at 0.6 inch top displacement. The analyses results show that failure mechanism of the upper four stories in the 8-story building, which also represent the 4-story and 2-story buildings, experience diagonal cracking. However, the four lower stories in the 8-story model experience more of bedjoint sliding and some step-cracking pattern in the infill. The variation observed in the failure modes of different frames might be expected from the change in the vertical load and the surrounding frame.



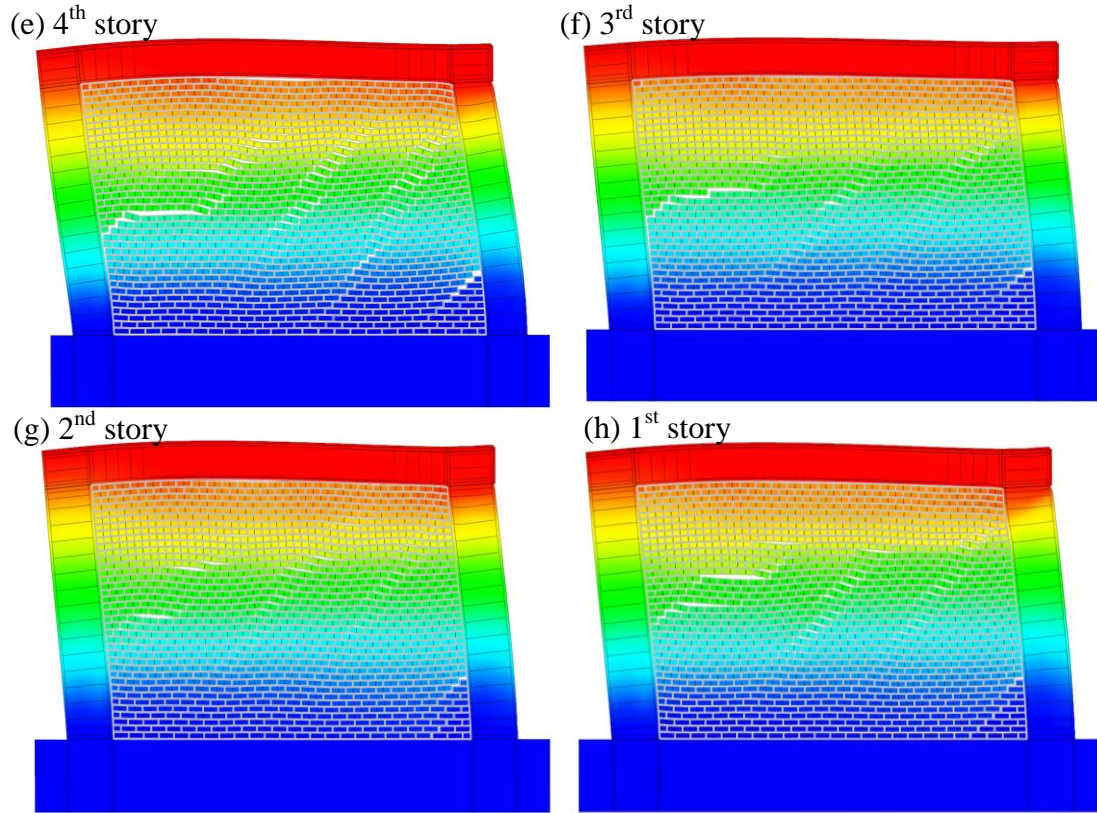


Figure 5-8. Deformed shape of the eight micro-models at 0.6 inch lateral in different stories of the 8-story archetypical building. Colors represent the contour of the lateral displacement (in inches relative to the base of the model).

Once the micro model results are obtained, the response of the infill is extracted for each model, as explained in Section 4.2.1. The extracted force-displacement responses for different stories are presented in Section 5.7.3.

### 5.7.3 Extracted Infill Force-Displacement Responses for Archetypical Buildings

The properties defining the struts in the macro-models are obtained by extracting the results from the micro-models. The first step in extracting the infill response is to compute the infill-frame contact length. The infill-frame contact length is computed for each frame, using the procedure explained in Section 4.2.1, as 49 in. for the eighth story, 65 in. for the seventh story and 90 in. for the rest of the stories. These contact lengths show that increasing the vertical load and columns sizes increases the infill-frame contact length when we move from the eighth story

to the sixth story. Recall that this contact length is used to define the subsection of the micro-model that will provide the basis for the strut in the macro-model.

In the next step, the force-deformation of the infill panel is extracted in diagonal direction, based on the rules explained in Section 4.2.2. Figure 5-9 shows the force-displacement extracted for the seventh story in the eighth-story building, which is also representative of the 1<sup>st</sup> story in the 2-story building or the 3<sup>rd</sup> story in the 4-story building. The force in this figure is extracted in the diagonal direction, as explained in Section 4.2.2. The deformed shape of the model at different stages is shown in Figure 5-9 to represent the gradual formation of diagonal crack in the infill panel.

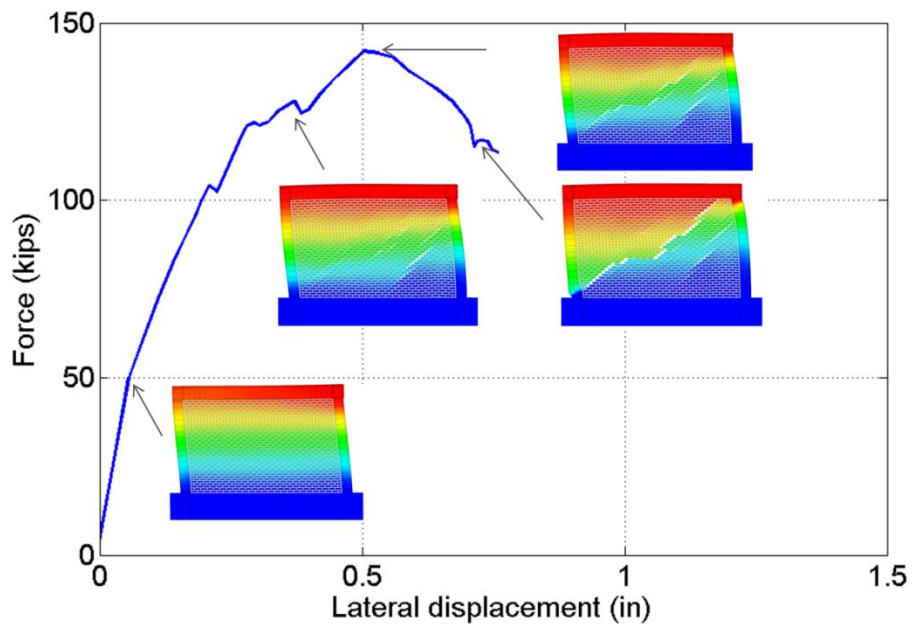


Figure 5-9. Force-displacement response extracted from the micro-model for the seventh story in the 8-story building. The deformed shape of the micro-model is shown at different displacement levels. Colors represent the contour of lateral displacement.

Similarly, the force-displacement responses of the infill in the other models are extracted and results are shown in Figure 5-10 for the eight micro-model representations. This figure shows that increasing the vertical load on the micro-model frame, to represent the lower stories in the taller buildings, leads to an increase in the stiffness and maximum strength of the infill

response, which will produce to higher stiffness and strength of the equivalent struts in the macro-model. Recall that part of this increase in the strength and stiffness is due to the increase in the stiffness, *i.e.* column sizes, and strength of the surrounding frames. The results presented in Figure 5-10 also shows that, as a general trend, increasing the vertical load on the frame can lead to a decrease in the ductility of the response. However, this trend may not be observable between any two selected stories, due to other changes in the model such as variation of the frame dimensions and reinforcement and also the failure mechanism experienced by the different micro-models.

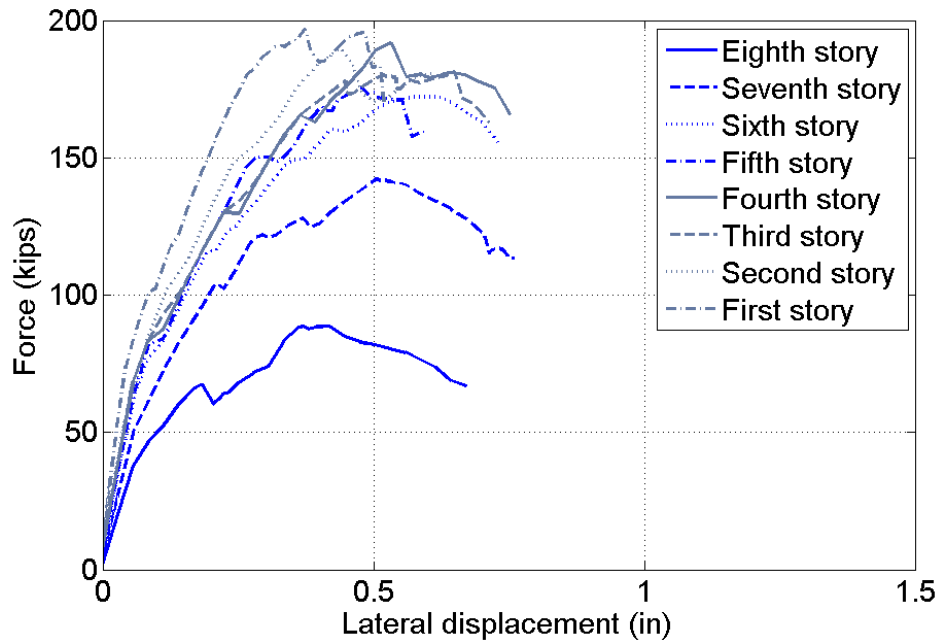


Figure 5-10. Force-displacement response of the infill extracted from the infill panel in eight different micro-models representing different stories of the archetypical buildings.

### 5.8 Out-of-Plane Behavior of the Archetypical Building

A masonry infill panel encased in a concrete frame is subjected to two perpendicular forces, *i.e.* in-plane and out-of-plane, during an earthquake. The work discussed this far focuses exclusively on the in-plane response. However, out-of-plane behavior may be important and few

studies have been conducted on the evaluation of the out-of-plane strength of infill panels. These efforts can be classified as analytical and experimental studies, as will be explained in the following.

Analytical models have been developed based on an empirical approach (Dawe and Seah, 1989) or a purely theoretical approach (Klingner et al., 1996; Angel and Abrams, 1994). Dawe and Seah (1989) developed an empirical equation based on data from testing of several full-scale concrete masonry infilled steel frames subjected to uniform out-of-plane pressure applied to the wall. They conducted a parametric study of how different parameters such as infill thickness and aspect ratio, frame rigidity, and bed-joint reinforcement affect out-of-plane failure strength. On the basis of this study, they proposed an equation for out-of-plane strength of the infill. The equation is valid for hollow concrete block panel infills in the frames pinned at the bottom. However, Dawe and Seah (1989) hypothesize that their equation gives a conservative estimation for other infill or frame types. Angel and Abrams (1994) developed an analytical model to consider the infill as several unit width strips supported at two ends and cracked at the mid-span. They proposed that each strip rotates as two rigid bodies around the ends and forming an arch, known as arching action. Each strip experiences internal compression forces. They computed the out-of-plane strength of the strip from the equilibrium equation between the external load and the internal force of the arch strips. Klingner et al. (1996) adopted the idea of arching action and computed the out-of-plane strength of the infill panel as the integration of the strength of horizontal and vertical strips in the wall. Flanagan and Bennett (1999) compared these three studies with the existing experimental data and determined that the Dawe and Seah approach gives the best prediction of the out-of-plane strength. Flanagan and Bennett (1999), using the

available data, proposed a similar equation to the one proposed by Dawe and Seah (1989) with a correction factor of 0.93.

The analytical studies are used to estimate the possible role of out-of-plane failure for the archetype building models developed in this study. The out-of-plane strength of the masonry infill panel depends on the material properties of the infill such as compressive strength of the masonry, as well as the configuration of the panel, *i.e.* height to thickness ratio ( $h/t$ ). The decision of whether we need to consider the out-of-plane failure of the infill panel in the seismic assessment procedure depends on the type and configuration of the infill. To investigate the need to consider the out-of-plane failure of the infill walls in the analysis, the ultimate out-of-plane strength of the infill panel in the archetypical building of this study is calculated and presented in Table 5-12, using the three different analytical approaches. In Table 5-12,  $f'_m$  is the compressive strength,  $E$  is the Young's modulus, and  $h$  and  $t$  are height and thickness of the masonry panel, respectively. This table also presents the corresponding acceleration needed to reach to the ultimate out-of-plane strength. This acceleration is computed as the acceleration that needs to be applied on the mass of the infill panel to induce an inertial force equal to the ultimate out-of-plane strength of the infill, as shown schematically in Figure 5-11. Table 5-12 shows that the computed equivalent acceleration is large and thus is highly unlikely to occur under reasonable levels of ground shaking. As a result, this study does not consider the out-of-plane behavior of masonry infill panel because of the high corresponding equivalent acceleration.

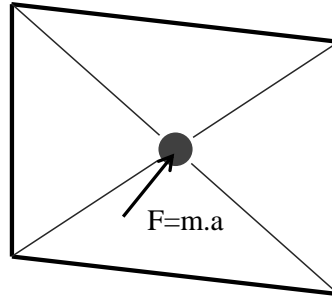


Figure 5-11. Schematic drawing shows the mass and equivalent ultimate force on the wall, where,  $m$  is the mass of the wall,  $a$  is the equivalent acceleration, and  $F$  is the ultimate out-of-plane strength of the wall.

Table 5-12. Ultimate out-of-plane strength and corresponding equivalent acceleration of the infill panel in the archetypical building.

Approach	$f'_m$ (psi)	$E$ (ksi)	$t$ (in)	$h/t$	Ultimate Strength (psi)	Equivalent Acceleration (g)
Dawe & Seah (1989)	450	337.5	12.4	10.6	2.78	3.10
Angel & Abrams (1994)					4.45	4.95
Klingner et al. (1996)					5.40	6.02

Along with the analytical approaches developed to evaluate the ultimate out-of-plane strength of the infill panel, a number of experimental studies have been quantified out-of-plane strength, which are used to verify the above described modeling assumptions. The experimental results can be separated into three different categories (Hashemi and Mosalam, 2007) as: (i) unreinforced masonry infills subjected to uniform or concentrated load perpendicular to the wall applied by the airbags or hydraulic actuators (Dawe and Seah, 1989), (ii) unreinforced masonry infills subjected to the out-of-plane acceleration generated by shake table test (Klingner et al., 1996), and (iii) unreinforced masonry infills subjected to the air pressure in a wind tunnel (Gabrielsen and Kaplan, 1997). Most of the experimental studies have been conducted on one-way clay tile wall, which is more susceptible to out-of-plane failure than brick masonry walls and only a few sets of experiments conducted on brick masonry walls like those considered in the archetype buildings. Gabrielsen and Kaplan (1997) conducted a set of wind tunnel tests on an

8 in. brick wall. They reported the ultimate and cracking stress of 19 and 13 psi, respectively. Both of these two values are substantially higher even than the ultimate strength values in Table 5-12. They also showed that the ultimate strength of the tightly infilled panel in a frame is six to eight times that of the infill panels with gaps between the frame and the infill. Thomas (1953) conducted a set of out-of-plane tests on brick masonry wall surrounded by a concrete cased steel frame. He used several point loads applied perpendicular to the wall to represent a uniform out-of-plane force distribution. Thomas (1953) reported the ultimate out-of-plane strength of the wall as 7.8 psi and 26.5 psi for 9 in. and 13 in. wall. Again, these experimental results show a higher ultimate strength than the values presented in Table 5-12. Negro and Taylor (1996) reported a set of shaking table tests, to investigate the strength of the unreinforced masonry frames under combined in-plane and out-of-plane excitation. In these experiments, four infilled frames with the infill thickness of 4" with compressive strength of 333.0 psi and infill height to the thickness ratio of 16 were tested for various excitations including sine waves and earthquake records. They did not report any out-of-plane failure even for out-of-plane accelerations of 2g. These high ultimate strengths or equivalent accelerations from experimental tests confirm the idea of neglecting the out-of-plane failure of the masonry infill panel in this study.

This conclusion is made for the archetypical infill panels considered in this study. However, for other infill panels with different configurations and material properties, the equivalent acceleration corresponding to the ultimate out-of-plane strength can be computed and compared to the exciting acceleration at each time step. At the time step in which the exciting acceleration becomes equal to the equivalent acceleration representing the out-of-plane strength, the equivalent struts (representing the infill panel in the macro-model) need to be removed from the model or their properties significantly degraded. This strut removal is needed because

reaching to the equivalent acceleration means that the infill panel fails in the out-of-plane direction and no longer contributes to carrying in-plane forces. This procedure assumes that the exciting accelerations in the two orthogonal directions are the same.

In studying the out-of-plane behavior of the masonry infill panel, two issues can be considered. The first one is the possible out-of-plane failure of the infill panel, which was discussed in detail above. The second issue relates to the interaction between the in-plane and out-of-plane behavior of the masonry infill panel. In other words, how much can the out-of-plane force affect the in-plane response of the infill panel. Hashemi and Mosalam (2007) studied the interaction between in-plane and out-of-plane strength of an unreinforced masonry infill panel. They conducted a set of in-plane pushover tests for various out-of-plane forces, using a finite element model which is calibrated based on experimental tests on single-wythe hollow clay brick panels in a concrete frame. Figure 5-12 shows the interaction diagram between the in-plane strength and out-of-plane force in the masonry infill panel. This figure shows that by increasing the out-of-plane forces, the in-plane strength of the masonry infill panel reduces. Hashemi and Mosalam noted that their results are valid for the specific configuration, geometry, and material properties of their study and do not serve as a generalized relationship, although their study is the only one addresses this issue. To investigate the interaction between the out-of-plane and in-plane behavior, a similar study needs to be conducted for each case study. The micro-model developed in this study is a 2D plane-stress model, which is not capable of modeling the effect of the out-of-plane force on the infill. As a result, this study does not consider the reducing effect of in-plane strength due to the existence of the out-of-plane forces.

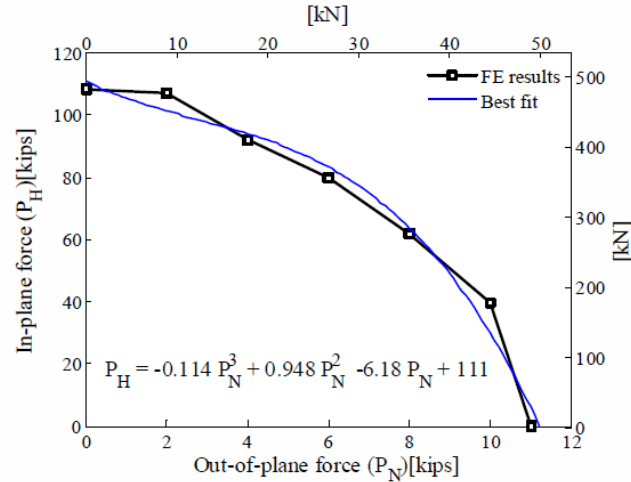


Figure 5-12. Interaction between in-plane strength and out-of-plane force of URM infill (taken from (Hashemi and Mosalam, 2007))

### 5.9 Macro-Modeling of the Archetypical Buildings

In this section, the force-displacement response extracted in Section 5.7.3 is used to define the multi-linear force-displacement response of the struts that will be used in the macro-models. The multi-linear response is fitted to the nonlinear response extracted from the micro-model, based on the rules developed in Section 4.2.2. Figure 5-13 shows the fitted multi-linear response of the infill panel for the 2-story archetypical building. Similarly, the multi-linear responses are developed for other stories in the archetypical buildings. Recall that the flexural behavior of columns and beams are modeled using the lumped plasticity approach, as explained in Section 4.3. The shear behavior of columns is modeled using the shear spring developed by Elwood and modified in this study, as explained in Section 4.3.3.3.

Analysis of the archetypical building is performed for two cases. In Case (1), we assume that all the frames in the N-S direction have the same infill, as shown in Figure 5-14a. In this case, all frames in the N-S direction are modeled as the space frame, which carries the same amount (1/6) of seismic mass. The vertical load on each frame corresponds to the gravity load tributary to that frame and there is no additional P- $\Delta$  load. In the second case, known as Case (2),

the infill frame is assumed to exist only in the exterior frames, as shown in Figure 5-14b. This case corresponds to buildings in which the interior infills have been removed in remodeling, as explained in Section 5.2.1. In this case, the exterior frames are modeled as the perimeter frames, due to their much higher strength and stiffness compared to the punched interior frames. Infill panels with openings are not considered here, for simplification purposes, as mentioned in Section 5.2.1. The effect of bi-axial bending is not considered here. For each of these cases, two infill configurations, including, fully infilled, and partially infilled are considered, as explained in Section 5.2.1, and results are compared with respect to each other and the bare frame. The bare frame is always modeled as a space frame since all of the frame lines in the building are the same. Results of the Case (1) models provide a direct comparison between the bare, fully and partially infilled frames regardless of the changes which may occur in the P- $\Delta$  load or effective mass because all our treated as space frames. However, results of Case (2) buildings represent how the predicted trend for Case (1) buildings may change if the interior frames are not infilled. Table 5-13 summarizes the characteristics of the buildings analyzed. Section 5.10 present analysis results for each of the considered cases in this study.

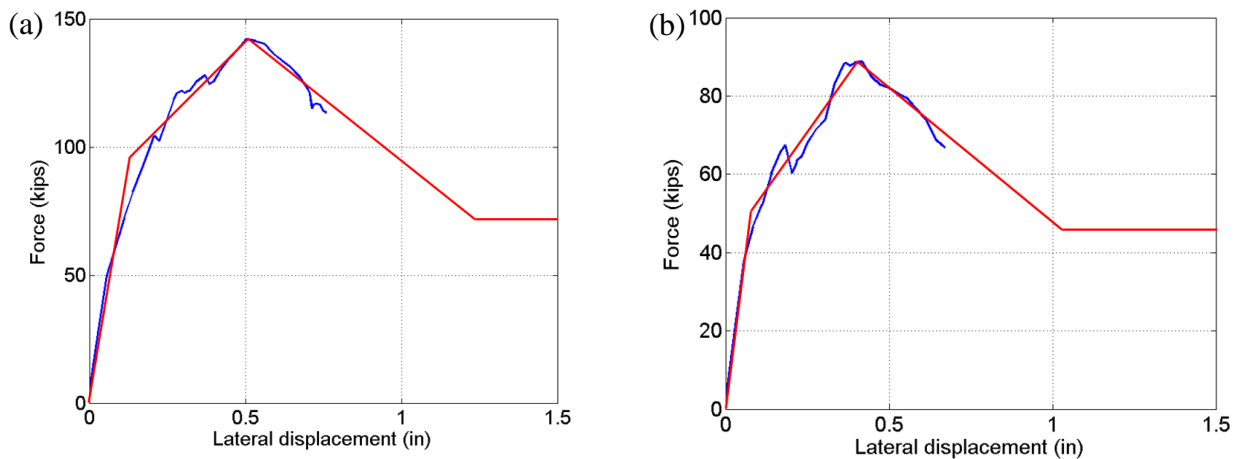


Figure 5-13. Fitted multi-linear force-displacement response to the response extracted from the micro-model of the 2-story models for (a) first story; (b) second story.

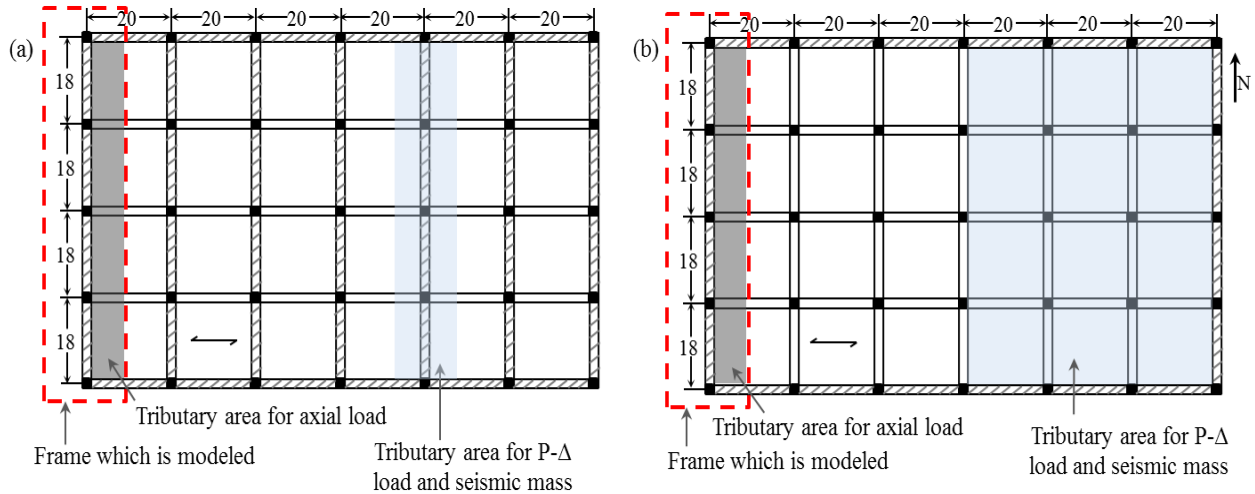


Figure 5-14. Plan view of the analyzed buildings for two cases: (a) Space frame (infill exists in all N-S frames), (b) Perimeter frame (infill exists in the perimeter frames only).

Table 5-13. Characteristics of the archetypical buildings.

Building identifier*	No. of stories	Infill	Infill configuration in plan (case)	No. of wythes of masonry infill
Bare Frames				
2BW0	2	No	1	n/a ("Bare")
4BW0	4	No	1	n/a
8BW0	8	No	1	n/a
Infilled frames				
2FC1W3	2	Full	1	3
2PC1W3	2	Partial	1	3
4FC1W3	4	Full	1	3
4PC1W3	4	Partial	1	3
8FC1W3	8	Full	1	3
8PC1W3	8	Partial	1	3
2FC2W3	2	Full	2	3
2PC2W3	2	Partial	2	3
4FC2W3	4	Full	2	3
4PC2W3	4	Partial	2	3
8FC2W3	8	Full	2	3
8PC2W3	8	Partial	2	3

\*The building identifier reports number of stories, followed by a letter indicating the infill configuration (B-bare; F-fully infilled; P- partially infilled), followed by a code indicating the configuration of the infill in plan (C1 – case 1, C2- case 2), followed by W and the number of wythes in each wall.

There is a lack of information about the damping ratio of the masonry-infilled frames.

The level of damping clearly depends on the extent of damage incurred in the structure (Hashemi

and Mosalam, 2006; Kodur et al., 1995). Hashemi and Mosalam (2006) performed  $\frac{3}{4}$ -scale shake table tests on a RC frame with clay brick infill wall at different excitation levels for two earthquakes, showing that the presence of the infill can increase the damping ratio from 4% to 5-12%, depending on the level of shaking. Based on these data, the infilled frame models here are assigned 8% Rayleigh damping in the first and the third modes. Bare frame models are assigned 5% damping.

## **5.10 Seismic Response of the Archetypical Buildings from Macro-Models**

### **5.10.1 Static Pushover Analysis Results**

Pushover analysis is conducted for all of the archetype buildings. The ASCE 7-10 equivalent seismic load distribution is applied in the analysis. Pushover results are presented in Table 5-14 including: (1) the first-mode period (from eigenvalue analysis); (2) the maximum base shear strength of the structure; and (3) the roof drift ratio at which 20% of the lateral strength of the structure has been lost. The roof drift ratio is computed as the roof displacement divided by the total height of the building.

Figure 5-15 illustrates the effect of infill on the pushover response, showing the base shear versus roof drift response for the 2-story case 1 buildings with “strong” infill. Although all of these buildings fail in the first story, the addition of infill to the frame increases both stiffness and strength. Indeed, the fully-infilled frame shown in Figure 5-15 has approximately 22 times larger stiffness and 3.2 times greater peak strength than the bare frame. The response of the partially-infilled frame is between the fully-infilled and bare frame case, such that, the partially-infilled frame has about double the stiffness and slightly greater peak strength than the bare frame. However, the presence of infill decreases the structures’ deformation capacities. As reported in Table 5-14, the first-mode periods of the archetypical buildings vary between 0.12

and 1.1 sec, with smaller periods computed for the shorter structures with more infill walls/wythes. Table 5-14 also shows that the trends of the responses exhibited in Figure 5-15 are similar for structures of different heights and infill configurations. The maximum pushover strength of the case 1 and 2 buildings are similar; case 2 buildings have higher P- $\Delta$  forces, but these forces do not have a big influence on the response of these very stiff structures. In addition, the results show that the response of the partially-infilled frame is highly dependent on the failure mode of the structure. If the structure fails in the same location as the bare frame, the response is close to that of the bare frame (as in the 2-story structures in Figure 5-15); if the partially-infilled frame experiences more distributed damage (as in the 8-story “strong” wall, case 1, structures) the response of the partially-infilled frame is closer to that of the fully-infilled frame.

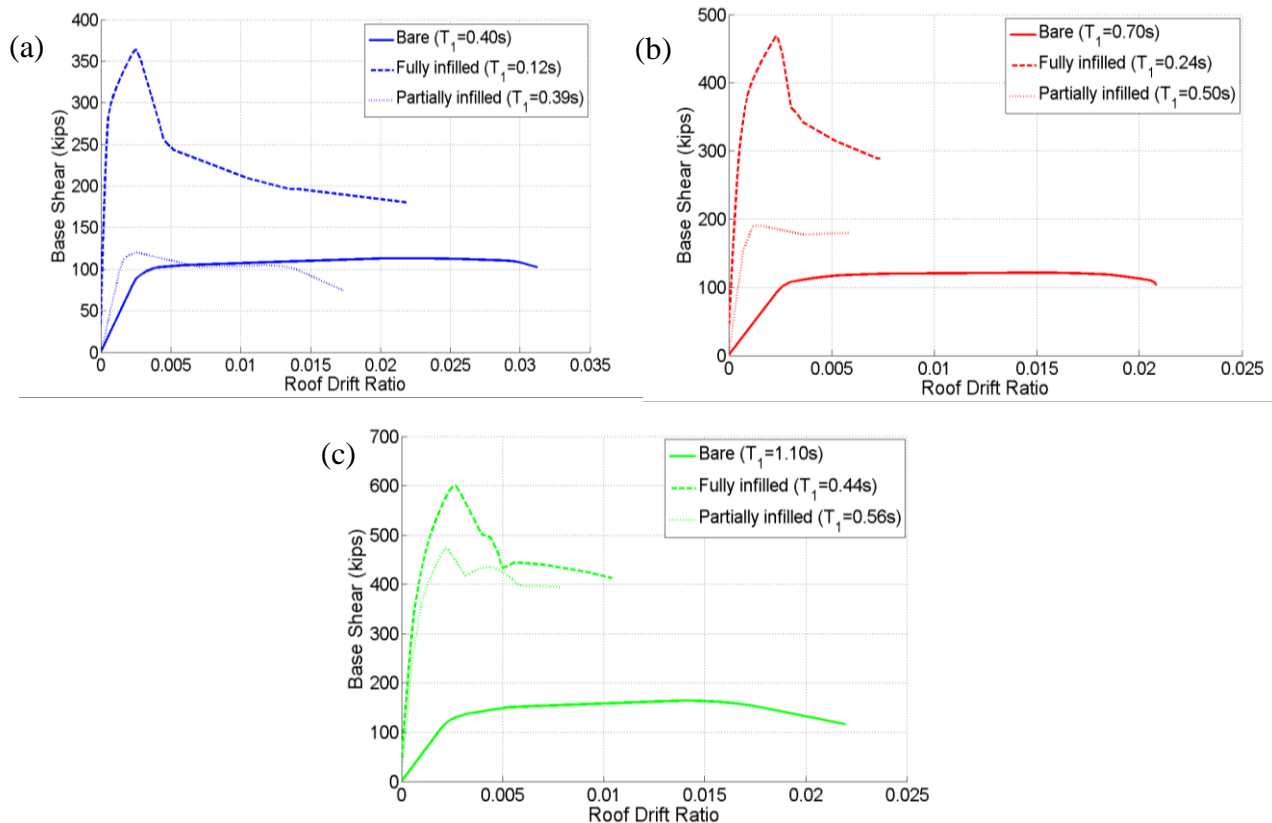


Figure 5-15. Pushover analysis results for Case (1) (a) 2-story, (b) 4-story, and (c) 8-story models.

Table 5-14. Summary of the results from pushover analysis and incremental dynamic analysis of the archetypical buildings.

Building identifier	Pushover analysis results			Incremental dynamic analysis results	
	$T_1$ (sec)	Pushover strength (kips)	RDR at 20% loss of strength	Median collapse capacity $S_{di}$ (in.)	% change in median $S_{di}$ w.r.t the bare frame with the same height
<i>Bare Frames</i>					
2BW0	0.40	113	3.3	3.8	0
4BW0	0.70	122	2.1*	3.6	0
8BW0	1.10	164	2.0	4.7	0
<i>Infilled frames</i>					
2FC1W3	0.12	366	0.4	3.1	-18
2PC1W3	0.39	120	1.5	2.1	-44
4FC1W3	0.24	469	0.3	1.9	-47
4PC1W3	0.50	191	0.6**	2.1	-42
8FC1W3	0.44	610	0.5	3.5	-26
8PC1W3	0.56	473	0.6*	2.7	-42
2FC2W3	0.17	363	0.4	1.8	-54
2PC2W3	0.53	119	0.7	1.6	-58
4FC2W3	0.31	469	0.3	1.4	-62
4PC2W3	0.65	189	0.6**	1.7	-54
8FC2W3	0.57	599	0.5	1.5	-68
8PC2W3	0.72	471	0.6	2.2	-53

\* RDR at 15% loss of strength (last converged step).

\*\* RDR at 5% loss of strength (last converged step).

### 5.10.2 Incremental Dynamic Analysis Results

This study uses 44 recorded ground motions, which have been selected to represent large earthquakes recorded at moderate fault-rupture distances (*i.e.*, not near-fault conditions) (FEMA, 2009). Ground motion intensity is quantified by inelastic spectral displacement,  $S_{di}$ .  $S_{di}$  is calculated as the maximum displacement of a single-degree-of-freedom oscillator with bilinear material properties subjected to the ground motion of interest (Tothong and Luco, 2007). These computations depend on the oscillator's fundamental period,  $T_1$ , and the yield displacement,  $d_y$ , generally assuming 5% damping, and a 5% post-yielding hardening stiffness ratio. The primary

advantage of quantifying ground motion intensity with  $S_{di}$ , rather than spectral acceleration or any of a number of commonly used intensity measures, is that it is effective in representing both ground motion intensity and spectral shape, or rather, it represents a composite measure of ground motion intensity over a range of periods (Tothong and Luco, 2007).  $S_{di}$  implicitly captures the shape of the response spectra for periods greater than the oscillator's fundamental period, due to oscillator yielding and elongation of the fundamental period. This advantage is important here because it is well known that the spectral shape of records used in nonlinear time history analyses can substantially impact results (Baker and Allin Cornell, 2006; Haselton et al., 2011), yet it was infeasible to select ground motions that had realistic spectral shape, since that process is inherently site and structure specific (Liel et al., 2013). For the purpose of computing  $S_{di}$ ,  $T_1$  and  $d_y$  can be quantified from nonlinear pushover analysis of the structure of interest. In this study, an oscillator with properties representing the average  $T_1$  and  $d_y$  of the buildings of interest is used to quantify an intensity measure that can be used to compare results across buildings.

The outcome of IDA is illustrated in Figure 5-16 for the 2-story bare and fully-infilled frames (case 1), showing the relationship between ground motion intensity ( $S_{di}$ ) and peak interstory drift ratio for the suite of ground motions. The collapse risk of each of the RC frames can be represented by a collapse fragility curve. Example collapse fragility, shown in Figure 5-17 for the 2-story bare, fully, and partially-infilled frames (case 1), indicate that the bare frame has the highest collapse safety; the collapse capacities of the fully and partially-infilled frames are 18% and 44% lower than the bare frame, respectively.

To illustrate the model results, Figure 5-18a presents the dynamic response of the 2-story fully infilled frame for one ground motion at two different scale levels, showing the progression

of damage over time. At the higher scale level, the record causes collapse. Figure 5-18b illustrates the results obtained for the macro model of the 2-story fully infilled frame using the 44 recorded ground motions from FEMA (2009). The same collapse mechanism described above for this building, characterized by sequential shear failure of the columns initiating in the first story, is observed in all of the ground motion records. There are insufficient data to validate the modeled response of this building. However, for comparison, shake table results for a 2/3-scale, three-story, two-bay masonry-infilled RC frame (Stavridis et al., 2012), which was designed and constructed to represent 1920s era California buildings, are presented in Figure 5-18b. Although the buildings are different, they have similar design detailing and period, and this comparison shows a good match with the results of the current study in terms of the general trend between variation of intensity measure and the interstory drift ratio in the structure. However, the experiment seems stiffer at lower levels of deformation.

Table 5-14 summarizes the statistics of the collapse fragility curves for all of the archetypical buildings in terms of the median collapse capacity (quantified by  $S_{di}$ ). The average logarithmic standard deviation of archetypical buildings is 0.45. The median collapse capacities of the different buildings are also shown graphically in Figure 5-17. Trends are discussed in subsequent sections.

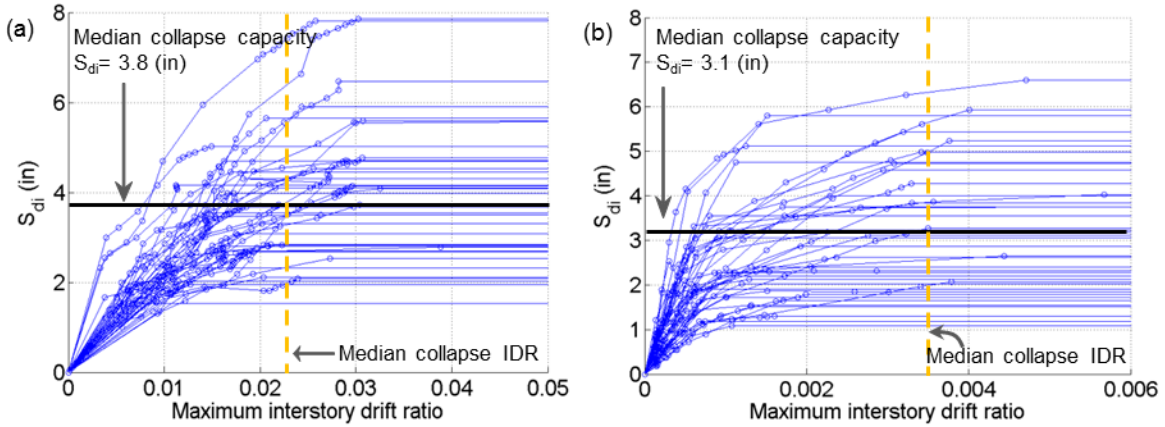


Figure 5-16. IDA results for selected 2-story models: (a) bare frame (2BW0) and (b) fully infilled (2FC1W3) with three-wythe walls (case 1).

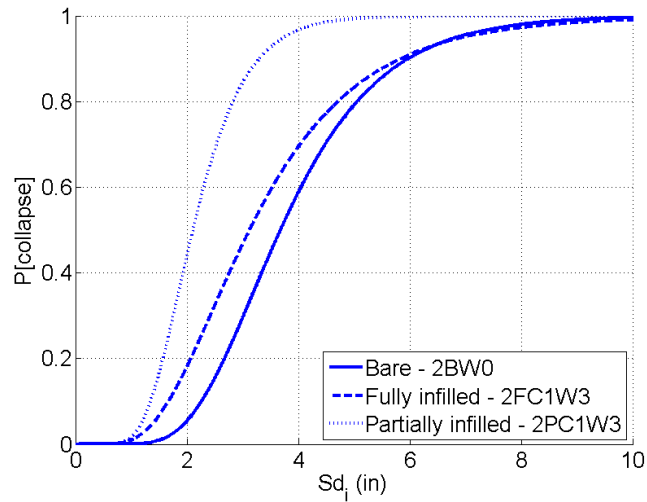


Figure 5-17. Collapse fragility functions for Case (1) 2-story models with different infill configurations.

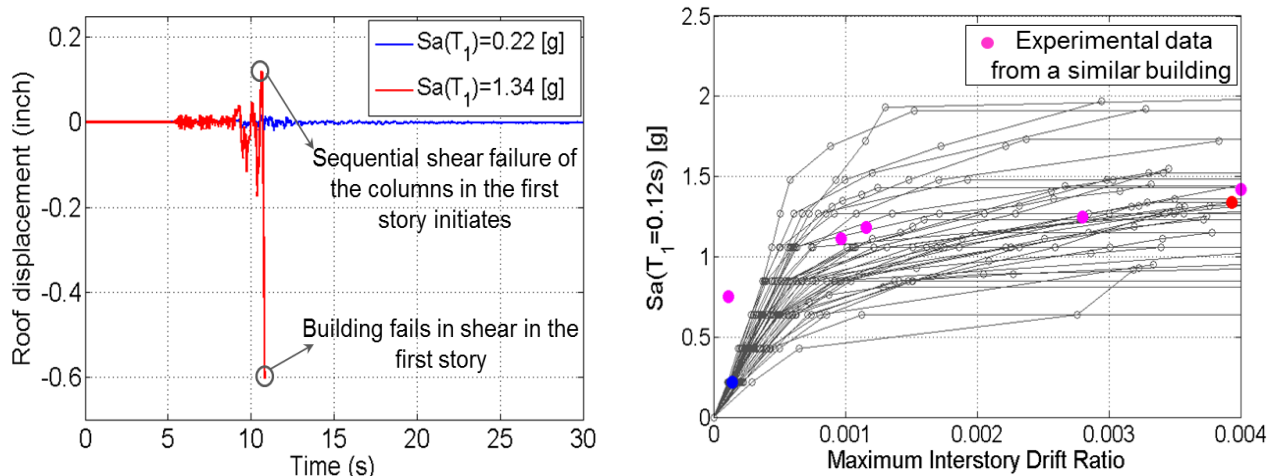


Figure 5-18. Dynamic analysis results for the 2-story fully infilled frame with strong infill walls showing (a) roof displacement time history response when subjected to a selected ground motion time history (Imperial Valley-Delta station) at two different scale levels and (b) incremental dynamic analysis results for all 44 records. Results for the same time histories shown in (a) are presented with the same color in (b) for comparison. Experimental results from Stavridis et al. (2012) are superimposed on (b).

Effect of Infill Configuration: Results in Table VI show that the bare frames consistently have better collapse performance, *i.e.* higher median collapse  $S_{di}$ , than the infilled frames for all building heights. If bare and infilled frames are examined at the same excitation level, the bare frames absorb less seismic force compared to the infilled frames, due to their lower stiffness and mass. In addition, the greater deformation capacity of the infill-free frames means the bare frames experience higher drifts before collapse occurs (compare Figure 5-16a and b).

These differences are reflected in the collapse mechanisms exhibited in the different archetypical buildings, as reported in Table 5-15. In the fully-infilled frames the strong and stiff infill induces large shear forces first in the interior, then, exterior columns. The frame failure prevents the walls from reaching their maximum capacities and the first story loses its ability to carry further lateral loads. This loss of lateral load capacity occurs at lower ground motion intensity levels compared to the bare frames. The story is slightly more complicated comparing the partially-infilled and bare frames since, in fact, these structures are identical at the first story

where collapse concentrates. However, the shear demand induced by the earthquake is higher in the partially-infilled frame due to the larger seismic mass coming from the heavy infill.

The fully-infilled frames may have better or worse collapse performance than the partially-infilled frames. These patterns are a function of the relative stiffness and mass of the different frames since the introduction of additional infill increases both mass and stiffness. In the case of the 4-story case 1 frames, the median collapse capacity of the partially-infilled frame is larger than the fully-infilled frame. Similar trends are observed between partially and infilled frames in the 8-story building. However, for 2 and 8-story case 1 frames, the fully-infilled frames have higher median collapse capacities than the partially-infilled frames. The relative performance of the fully and partially-infilled frames depends on the shear demand induced in the columns. For instance, for the 2-story buildings case 1, higher shear demand is experienced by the columns in the first story of the partially-infilled frame compared to the fully-infilled frame, at the same excitation levels. However, in the 4-story buildings, the opposite is true.

Effect of Infill Configuration in Plan: The case 1 and case 2 results can be thought of as bracketing the response of the infilled frame, depending on how highly perforated the interior infill walls are in the building. Table 5-14 shows that the median collapse  $S_{di}$  of the case 2 buildings are on the order of 20-57% smaller than the corresponding case 1 buildings. The smaller collapse capacities of the case 2 buildings are due to their plan configuration, which produces larger seismic mass and P- $\Delta$  load to be carried by these frames (Figure 5-14). This result suggests that buildings with some frame lines having infill and some frames with removed infill may be especially vulnerable.

Effect of Building Height: Results in Table 5-14 indicate that the median collapse capacity of the 8-story bare frame is 24-31% higher than the 2 and 4-story bare frames. The 8-

story building experiences distributed failure modes over different stories, which is different than the concentrated failure occurring in the first story of the 4 and 2-story buildings. The 8-story infilled frames also have greater collapse capacities than the 2 and 4-story buildings. However, the order of magnitude of the difference varies depending on the pairs of buildings being compared.

Table 5-15. Failure modes of selected archetypical buildings.

Building identifier	Stories where collapse mechanism occurs	Mechanism
Bare frames		
2BW0	1 <sup>st</sup> story	Column shear failure, leading to loss of story lateral load carrying capacity
4BW0	1 <sup>st</sup> (40% of records) or 2 <sup>nd</sup> (60% of records) stories	
8BW0	Fails in a single story between the 2 <sup>nd</sup> and the 6 <sup>th</sup> story	
Frames with "Strong" infill		
Fully infilled		
2FC1W3	1 <sup>st</sup> story	Shear failure in columns, as well as cracking in the walls, leading to loss of story lateral load carrying capacity
4FC1W3	1 <sup>st</sup> story	
8FC1W3	Fails in a single story between the 5 <sup>th</sup> and the 7 <sup>th</sup> story	
Partially infilled		
2PC1W3	1 <sup>st</sup> story	Column shear failure, leading to loss of story lateral load carrying capacity
4PC1W3	1 <sup>st</sup> story	
8PC1W3	1 <sup>st</sup> story	Column shear or axial failure, leading to loss of story lateral load or axial carrying capacity

## 5.11 Conclusions

In order to evaluate the collapse performance of the masonry infilled frames, a set of buildings that are representative of masonry infilled RC frames built in 1920s are considered in this chapter as the archetypical buildings. The material properties, infill and frame configuration, and design of the concrete frame are based on the engineering practice in that era. The buildings are considered in different heights of two, four and eight story with three different infill configurations including, bare frame, fully and partially infilled frames. The infilled frames are modeled using the modeling procedure explained in Chapter 4. The infill panels are modeled based on multi-scale simulation methodology developed in this thesis. Recall that multi-scale modeling technique requires micro-modeling of the masonry infilled frame followed by the calibration of the proposed two double-strut model to the results of the micro-model. The out-of-plane failure mode can be ignored for the selected archetypical building.

The macro-models of the infilled frames are built and analyzed statically, *i.e.* pushover analysis, and dynamically, *i.e.* IDA, in *OpenSees*. The IDA results showed that the bare frame has the better collapse performance compared to the partially and fully infilled frames. Fully infilled archetypical buildings are considered for two cases including space and perimeter frames. Results of this study showed that the fully infilled space frame has the higher median collapse capacity compared to the perimeter frame due to having less seismic mass and P- $\Delta$  load. The same trend is expected for the partially infilled frames. Results of this study also showed that the fully infilled frame can perform either better (in case of 2-story building) or worse (in case of 4-story building) than the partially infilled frames, depending on height of the building which affects the shear demand in the first (critical) story.

This study focused on the collapse performance of the masonry infilled frames. However, the developed multi-scale modeling approach can be used in order to identify the performance of the buildings at other damage states. The presence of infill walls, which take some of the gravity loads, prevents a collapse triggered by axial failure in columns. Infill walls are assumed not to fail out-of-plane because they are quite thick. Possible improvements can be considered for the modeling and triggering collapse procedure, such as considering the vertical capacity of the infill panel and modeling the cyclic deterioration in the strut response.

Moreover, more studies are required to be conducted on the interaction between the in-plane and out-of-plane strength. The trends observed here among the collapse performance of the bare, fully and partially infilled frames are valid for the selected archetypical buildings. These trends may change in case of considering different concrete frames and more especially different infill types. We expect to see an improvement in the collapse performance of the infilled frames with weaker infills. In this type of infilled frame, the frame may benefit from the added stiffness and strength from the infill, while the infill does not induce an excessive amount of shear force into the columns which causes the shear failure of the columns at low intensity levels.

## **6 Collapse Indicators for Existing Nonductile Concrete Buildings with Varying Column and Frame Characteristics**

### **6.1 Objectives**

One of the critical goals in the seismic assessment of existing buildings is to identify buildings that are so hazardous they are in critical need of retrofit. Identifying these unsafe buildings, known also as “killer” buildings, can help decision-makers to mitigate hazardous buildings in order of priority. The definition of an unsafe (critical) building depends, of course, on judgment and acceptable risk. For instance, one may consider an unsafe building as a building with greater than 50% probability of collapse at a given excitation level of interest. However, another decision-maker may consider 70% probability of collapse as the threshold of unacceptable risk. Regardless of the definition of criticality, procedures for identifying “killer” buildings need to be formulated such that an engineer can define the performance of a building based on a systematic and simple methodology to classify it as unsafe or not. In order to be useful for policy makers and building owners to quickly identify “killer” buildings, the procedures cannot require detailed analysis of any individual building.

In this methodology, we consider the building’s collapse performance as a function of a set of building characteristics that are known to affect the collapse capacity. These characteristics are termed “collapse indicators” (NIST, 2010). In concept, if the values of certain collapse indicators are too severe, the building can be classified as unsafe. This chapter studies collapse indicators related to column and story strength characteristics to examine how the severity of the deficiency, related to the number of columns or frame lines exhibiting the negative trait or the severity of the characteristics of any individual column or frame line, affects the building’s safety. This relationship is presented in terms of the variation in the collapse performance of the

building as the collapse indicator values changes at different locations of the building. The relationship between the collapse performance and collapse indicator yields valuable information about the trend of variation, including the sensitivity of collapse performance to the collapse indicator and the identification of critical values of the collapse indicator. These assessments also provide insights into the best metrics for measuring collapse indicators in buildings that have widely varying column and frame line characteristics. An efficient collapse indicator measure should give a reasonable trend based on engineering judgment from the physical behavior of the structure and effectively summarize information about the severity and location of that particular deficiency in the building to serve as good predictor of collapse risk.

## **6.2 Overview of the ATC-78 Project**

This effort is part of the ATC-78 project “Identification & Mitigation of Non-ductile Reinforced Concrete Buildings”, which is funded by FEMA. ATC-78 aims to identify the most important deficiencies in the old concrete buildings and to develop a methodology to evaluate the existing concrete buildings in order to identify a subset of the most collapse prone “killer” buildings (ATC, 2011). This methodology is intended to be simple and relatively cost-effective, such that, in concept, every older non-ductile concrete building in a jurisdiction could be evaluated using such an approach. Developing an evaluation methodology involves several subtasks that have been conducted in a multi-year effort in a collaborative effort carried out by ATC, the University of Colorado-Boulder, the University of California-Berkeley and a group of practicing engineers. This section provides an overview of the project and some of the terminologies and challenges involved. The analyses conducted to explore collapse indicators for buildings with varying column and frame characteristics are described in Section 6.3.

### 6.2.1 Collapse Indicators

Collapse indicators are defined as design and response parameters that may be correlated with the collapse probability of non-ductile concrete buildings (NEHRP Consultants Joint Venture, 2010). These collapse indicators may be defined at the element or system level. NIST (2010) defined a number of such potential indicators, including those that can be determined by Rapid Assessment (RA), Engineering Calculation (EC), and Building Analysis (BA). The present study focuses on a subset of the engineering calculation type of collapse indicators. Engineering calculation indicators are quantities that require calculation of the demand and capacities using the drawings of the building, but not nonlinear building analyses (NIST, 2010).

### 6.2.2 Collapse Indicator Evaluation Methodology

After identifying the collapse indicators of interest, as explained in Section 6.2.1, nonlinear dynamic analysis is used to investigate the relation between collapse indicators and collapse performance level for a given building of interest or suite of buildings. The Incremental Dynamic Analysis (IDA) technique, which was explained in Chapter 5, is used to organize the nonlinear dynamic analyses (Vamvatsikos and Cornell, 2002). Recall that the outcome of IDA is a fragility function, which is a cumulative probability distribution, that defines the probability of structural collapse as a function of the ground motion intensity (given by the spectral acceleration at the first mode period of the building [ $Sa(T_1)$ ]).

Different metrics may be used to quantify collapse performance on the basis of the IDA-derived fragilities. One metric of collapse that may be considered corresponds to the ground motion intensity at which  $x\%$  of the ground motions cause collapse, denoted  $Sa_{col,x\%}(T_1)$ , where  $x$  can be selected as different percentiles. Commonly,  $x = 50\%$  is considered, such that  $Sa_{col,50\%}(T_1)$

represents the median ground motion intensity at which collapse occurs. Another important metric is the probability of collapse at a specified excitation level.

After finding the relation between the collapse performance and a building with the particular value of a collapse indicator of interest, the same process is repeated for different values of the same collapse indicator to explore the trend between the collapse indicator value and collapse performance. Figure 6-1a shows the schematic fragility curves obtained by repeating IDA for multiple versions of a building model with different values of the collapse indicator of interest. Figure 6-1b shows how the median collapse capacity, computed based on Figure 6-1a, varies with the value of the collapse indicator. Similar results in Figure 6-1c illustrate the variation of the probability of collapse conditioned on a specific hazard level varies with the value of the collapse indicator. Note that Figures 6-1b and c are developed from the same data, but represented using different metrics.

These trends can be used to quantify critical values for each collapse indicator. These critical values serve as a line in the sand to distinguish between buildings that are most at risk of earthquake-induced collapse from those that have a smaller risk. One approach for identifying critical collapse indicator values, which is based on (NIST, 2010), defines the critical collapse indicator value where a drastic change is observed in the probability of collapse for a small change in the collapse indicator, known as the kink point. The highlighted region in Figure 6-1c shows the range of the identified collapse indicator in which a rapid change in the gradient of collapse performance with variation in the collapse indicator is observed. Alternatively, the critical collapse indicator could be defined at some pre-defined acceptable probability of collapse. For illustration, a 30% probability of collapse is arbitrarily chosen as the acceptable collapse level, as shown in Figure 6-1c.

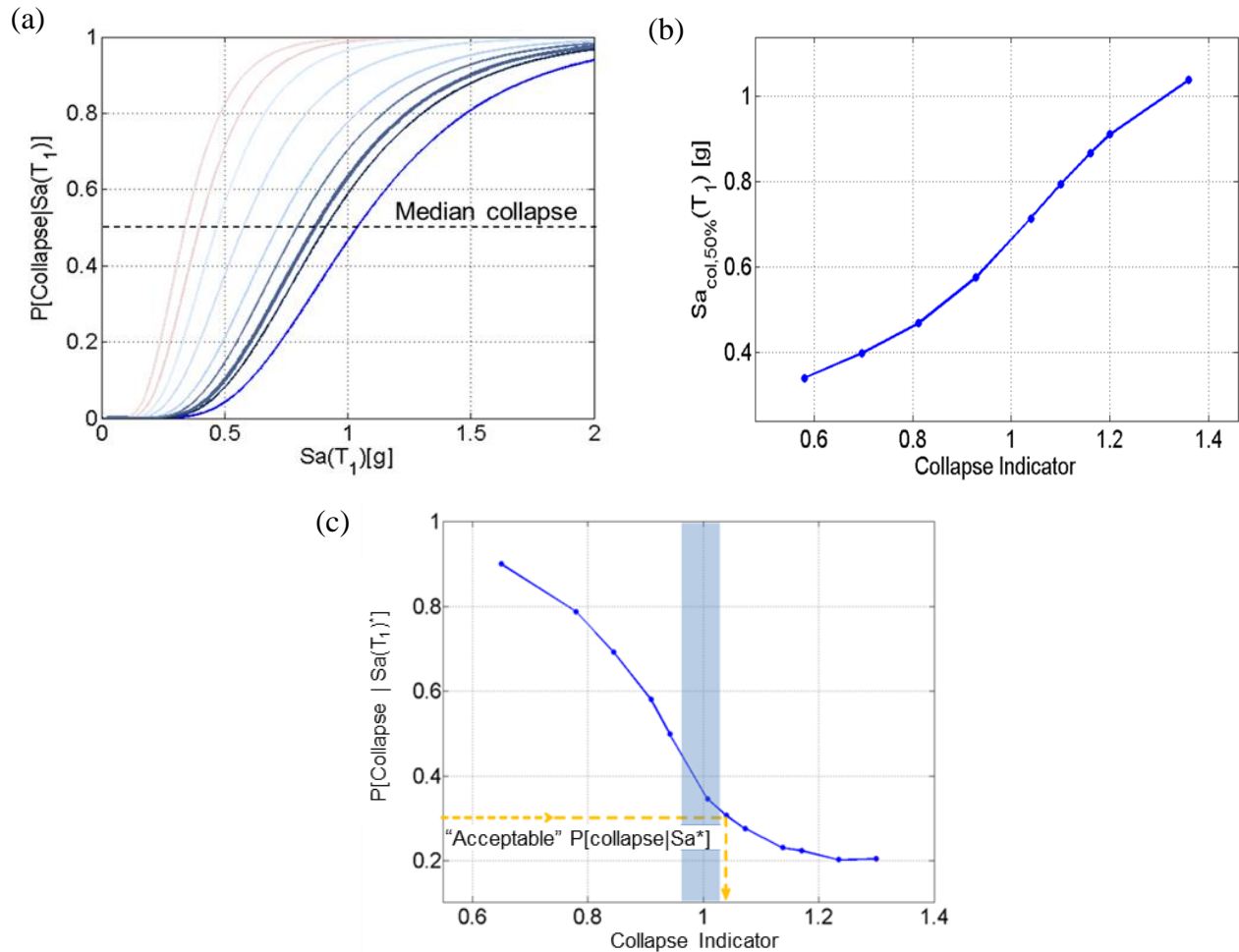


Figure 6-1. Schematic illustration of collapse performance as a function of a collapse indicator showing (a) fragility curves for variation of a collapse indicator in the same model; (b) variation of collapse performance, quantified by median collapse capacity, as a function of the collapse indicator, and (c) variation of collapse performance, quantified by the conditional probability of collapse on a specific hazard level, as a function of the collapse indicator. Note that (c) also shows two possible approaches to identify the critical collapse indicator with (1) shaded block showing the collapse indicator region of drastic change of slope and (2) the dashed-line showing the calculation of the critical collapse indicator based on a pre-defined acceptable probability of collapse.

### 6.2.3 Normalization to Isolate the Effect of Building Strength

As explained in Section 6.2.2, this study examines the effect of a collapse indicator in a model by varying that collapse indicator and re-evaluating the collapse performance of the building. It is important to acknowledge that variation of the collapse indicators in different models may be accompanied by a change in the strength of the building. Since the effect of the

buildings strength on the collapse performance is not the primary goal of this study, the results should preferably presented without regard for building strength.

For this purpose, ground motion intensities are normalized with respect to the maximum shear strength of the frame,  $V_{max}$ .  $V_{max}$  can be computed either from the peak value of pushover analysis results or from simplified method developed in the ATC-78 project. The simplified method enables the computation of building strength without the need to perform nonlinear modeling of the building and is only based on hand calculations (ATC, 2012). To obtain the normalized value of the collapse performance of the structure, the median collapse spectral acceleration,  $Sa_{col,50\%}(T_1)$ , is divided by the ratio of  $V_{max}$  to the weight of the structure,  $W$ , as shown in Equation (6-1). This normalization modifies the x-axis of the fragility curve to an  $M$  value that represents the ratio of ground motion intensity to building strength.

$$M_{col,50\%} = \frac{Sa_{col,50\%} \times W}{V_{max}} \quad (6-1)$$

To compute  $V_{max}$  by the simplified approach, the base shear capacity is determined based on the shear capacity of each story, where story shear strength is computed as the summation of the column shear strengths in that story. Column shear strength is computed as the minimum of column strength in shear and flexure. The shear strength of the column is computed uses the equation proposed in ASCE 41 (ASCE, 2006). The flexural strength of the column is computed as the summation of end (top and bottom) moments divided by the height of the column. The column end moments are computed as the minimum of the summation of the column or beam strengths (computed according to (ACI, 2008)), distributed relative to the height of the column above or below the joint. Detailed explanation about this method is provided in another document (ATC, 2012). The simplified method and pushover analysis provide relatively consistent values of  $V_{max}$  (within 10-15% of each other).

### 6.3 Study of Collapse Indicators in Case Study Building

In this study, we focus on developing the trends between the collapse indicators and metrics of collapse performance, examining especially the trends between various collapse indicators and the median normalized collapse capacity. Variations of collapse indicators that are non-uniform across a story are considered, in order to investigate the effect of the extent of deficiency on the collapse performance of a building.

This chapter studies three collapse indicators:

- (1) the ratio of column to beam strength ( $M_c/M_b$ )
- (2) the ratio of story shear strength for two adjacent stories ( $V_i/V_{i+1}$ )
- (3) the ratio of column flexural to shear strength ( $V_p/V_n$ )

The first collapse indicator, (1), is important because it affects the distribution of damage over the height of the building and, particularly, whether damage concentrates in beams or columns. Collapse indicator (2) can indicate a large discontinuity in story shear strength between two adjacent stories. This deficiency can trigger a weak-story mechanism. The third collapse indicator, (3), may be critical because it identifies whether columns are likely to fail in shear, flexure or a combination. These three collapse indicators are selected for this study because they have a critical influence on collapse performance and are very common in old concrete buildings.

To quantify the influence of a collapse indicator on the collapse vulnerability of non-ductile concrete buildings, we develop a case study uniform building, and develop a building model in OpenSees (Section 6.3.1). Then, each of the three collapse indicators is perturbed separately and the variation in collapse performance evaluated (Sections 6.3.2 – 6.3.5).

### 6.3.1 Case Study Building

The case study building considered in this study is a six-story reinforced concrete building designed as a space frame system. Figure 6-2 shows the plan and elevation views of the case study building, which are loosely based on drawings of a building built in the 1960s in Seattle, Washington. The building has no infill walls. The design base shear strength was selected by the practicing engineers on the ATC-78 team as  $0.1W$ , where  $W$  is the effective seismic weight of the building. This value is thought to be typical of early seismic designs.

#### 6.3.1.1 Building Design

The case study building was designed by Galanis and Moehle (2012) using an idealized approach that leads to uniform frame stiffness over the height of the building, uniform column to beam moment capacity ratios at every joint, and uniform ratios of column flexural to shear strength ratio at every column. In this design procedure, the design moment strength capacity is computed as the moment demand from the design load combinations multiplied by a set of correction factors. These correction factors account for the increase in the strength of the sections due to oversizing of the members in the design process and material overstrength while maintaining the uniformity of column and joint characteristics over the building.

The originally designed building has  $M_c/M_b$  equal to 1.0, which is smaller than suggested value in new design codes (ACI, 2008), and  $V_p/V_n$  equal to 1.0 in all joints and columns, respectively. Column dimensions are 18 in. by 18 in. with #8 bars for longitudinal reinforcement and #4 reinforcement at 3 inches on center for transverse reinforcement. Beam dimensions are 18 in. by 28 in. with #8 bars and transverse reinforcement consisting of #4 bars at 10 inches on center. The number of longitudinal bars is chosen for each beam and column to satisfy the

desired  $M_c/M_b$  and  $V_p/V_n$  ratios. Due to its uniform characteristics, the building is suitable for the parametric study that is the focus of this project.

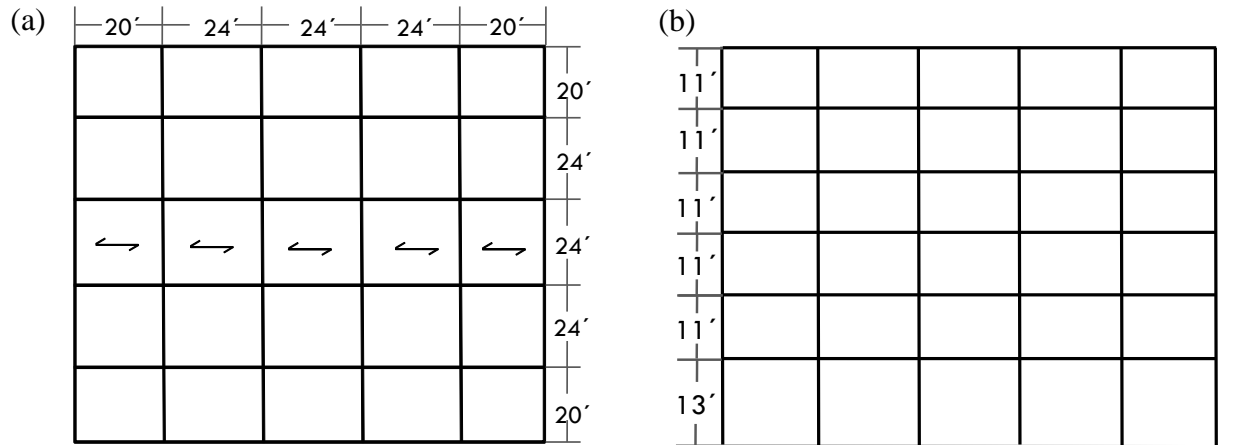


Figure 6-2. (a) Plan view and (b) elevation view of the case study building.

### 6.3.1.2 Modeling and Collapse Simulation

This building is modeled in *OpenSees* using a similar approach to that explained in Chapter 4. In this approach, columns with  $V_p/V_n \leq 0.6$  are considered to be flexurally dominated and modeled with an elastic element with two plastic hinges at the end, *i.e.* a lumped plasticity approach. Columns with  $V_p/V_n \geq 0.8$  are considered to be shear dominated and are modeled with shear, axial, and rotational springs in series with an elastic element. The properties of these springs are developed in the same way discussed in Chapter 4. In so-called “shear” buildings, all the columns have  $V_p/V_n \geq 0.8$ , while in “flexural” buildings all the columns have the  $V_p/V_n \leq 0.6$ , but the specific properties of different columns in each building may vary.

Different criteria have been proposed to define the occurrence of collapse in a building on the basis of nonlinear analysis results (Baradaran-Shoraka and Elwood, 2013). To the author’s knowledge, all of the collapse criteria define criteria identifying collapse in a story, since story collapse implies global building collapse. However, the quantitative criteria used to identify collapse in a particular story vary. For instance, the collapse criteria may be defined as the

without bound increase in the drift in a particular story (FEMA, 2009), or the decrease of the capacity of a story below a prescribed value (Baradaran-Shoraka and Elwood, 2013). Two different collapse criteria are adopted in this study. For the “flexural” models, collapse is identified if interstory drifts in any story increase without bounds (*i.e.* dynamic instability). For the “shear” models, collapse is defined as when at least half of the columns in a particular story have failed in shear or axially. Shear failure in a column occurs when the column shear strength has been reduced to its residual value. Axial failure in a column occurs when the axial strength of the column reaches to its residual value, which corresponds to experiencing a big axial deformation in the column.

The story-based nature of the collapse criteria means that it is the properties of the critical story, or that story in which collapse occurs, that should be represented by the collapse indicator. Imagine, for example, a building which always fails in the first story; the fifth story could have terrible characteristics, but these characteristics will not impact the building response unless they cause the collapse mode to change to the fifth story. In this study, the case study building always fails in the first story. Therefore, collapse indicators are defined at the first story level.

## **6.3.2 Variation of Column to Beam Strength Ratio, $M_c/M_b$**

### **6.3.2.1 Context and $M_c/M_b$ Parameter Definition**

When a flexurally-dominated frame structure is subjected to an earthquake, plastic hinges in columns and beams form. The number and the amount of the nonlinearity in these hinges increase as the intensity of the ground motion increases, until the building collapses in a sidesway mechanism. Column hinging may lead to deformations concentrated in one story, a so-called weak-story mechanism. However, formation of the hinges in the beams rather than

columns lets the building experience a more distributed damage over the height of the structure before collapse. As a result, modern seismic design requires stronger columns than beams through the strong column-weak beam requirement. In the current ACI 318 design code for reinforced concrete in the U.S., the summation of moment capacity of columns shall not be less than 1.2 times the summation of moment capacity of beams at each joint (ACI, 2008). However, this requirement is likely not satisfied in many older concrete buildings. We expect that as the column to beam strength decreases, the chance of experiencing a story mechanism increases.

To study the effect of the column to beam moment strength ratio in a building, a collapse indicator denoted as  $M_c/M_b$  is defined in this study. The  $M_c/M_b$  ratio at each joint is defined as the summation of the moment strengths of the columns framing into the joint, divided by the summation of the moment strengths of the beams framing into the same joint. The goal of this section is to study how a building's column to beam strength ratio affects its collapse capacity, paying special attention to buildings with different ratios at different locations in the building. For buildings in which different joints have different  $M_c/M_b$  ratios, the collapse indicator  $M_c/M_b$  can be computed in various methods: taking the average, maximum or minimum value of the  $M_c/M_b$  for the joints at each floor level, or considering, for example, the average  $M_c/M_b$  over the entire whole building. Examination of the efficiency of the definition of this collapse indicator is one of the focuses of this section.

### **6.3.2.2 Variation $M_c/M_b$ in Uniform Building**

The study of variation of  $M_c/M_b$  can be conducted by varying simultaneously the  $M_c/M_b$  ratio of all joints in the building model, or only in one floor level, or only at one joint location. The variation of the  $M_c/M_b$  in the entire building uniformly explores cases of buildings in which all joints have the same level of deficiency. To perform this variation, the moment strength of the

beams in the uniform building with  $V_p/V_n = 0.6$ , *i.e.* “flexural” buildings, is varied without changing any other modeling parameters. As a result, all the buildings have the same first mode period ( $Sa(T_1)$ ).

Figure 6-3 shows the variation of collapse performance of the case study building with respect to the variation of  $M_c/M_b$  collapse indicator, where all joints in the building have the same collapse indicator value. This figure shows how increasing the  $M_c/M_b$  ratio in the building improves (increases) the collapse performance of the building. Moreover,

Figure 6-3 shows the kink point on this curve around  $M_c/M_b=1.0$ , at which a drastic change in the collapse performance of the building is observed due to a small change in  $M_c/M_b$ .

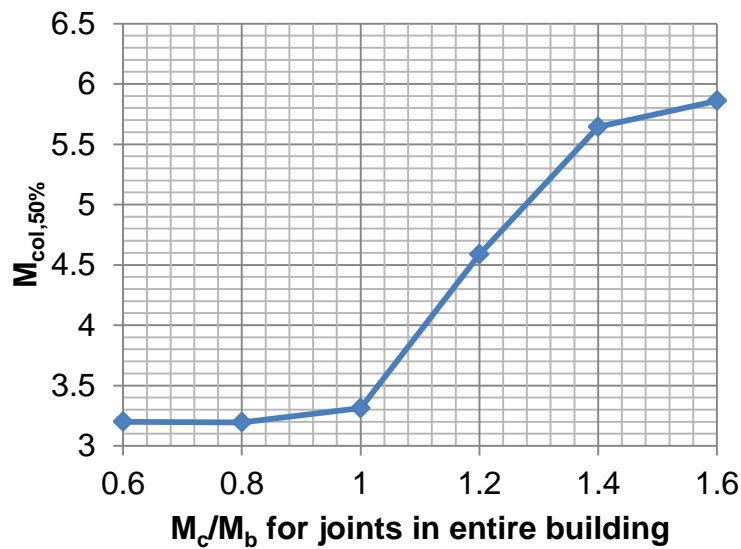


Figure 6-3. Variation of collapse performance of the case study building with respect to the variation of the  $M_c/M_b$  ratio in the entire building.

### 6.3.2.3 Variation of $M_c/M_b$ with Non-Uniform $M_c/M_b$ Ratios

These results clearly show that buildings with lower  $M_c/M_b$  ratios are at higher risk of collapse, particularly if  $M_c/M_b < 1.0$ . However, what if one column has a very small  $M_c/M_b$  ratio and the rest of the columns are substantially better? On what basis should such a building be evaluated? To study how the effect of the deficiency in  $M_c/M_b$ , both in terms of spatial and local

severity, the  $M_c/M_b$  ratio in the first floor is gradually changed from the building in which all the joints have the  $M_c/M_b = 1.2$ , to a building in which all the joints in the first floor have the  $M_c/M_b = 0.6$ , each time by decreasing the  $M_c/M_b$  ratio in one joint, as illustrated by Figure 6-4. In all cases, the  $M_c/M_b$  ratio in other joints in the model is equal to 1.2.

The collapse performance of these buildings, quantified by  $M_{col,50\%}$ , is plotted with respect to the average  $M_c/M_b$  ratio in the first floor, and shown in Figure 6-5. Like

Figure 6-3, Figure 6-5 shows that the collapse performance of the building increases as the average  $M_c/M_b$  ratio at the first floor level increases. Figure 6-5 also shows how the extent of the deficiency affects the collapse performance of the building, whereby increasing the extent of deficiency from zero joint to 6 joints with  $M_c/M_b = 0.6$ ,  $M_{col,50\%}$  decreases.

These results can also be used to show that the average of  $M_c/M_b$  in the critical story can be a suitable definition for this collapse indicator compared to the other possible definitions, such as minimum or maximum value of  $M_c/M_b$  in the critical floor, or a value based on the entire building. Figure 6-6 is similar to Figure 6-5, but on the x-axis, the average value of  $M_c/M_b$  of all of the joints at the first floor level is replaced with the value of the minimum  $M_c/M_b$  of all of the joints at the first floor level. Figure 6-6 shows that using an alternative definition for  $M_c/M_b$  collapse indicator, like the maximum or minimum  $M_c/M_b$  may not give us all the information about the building, because Figure 6-6 finds multiple collapse performance values for the same collapse indicator value.

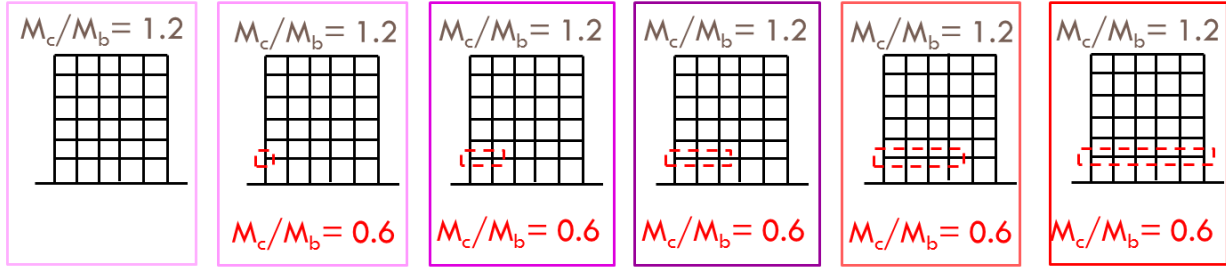


Figure 6-4. Schematic drawing of the gradual variation of  $M_c/M_b$  ratio of joints in the first floor.

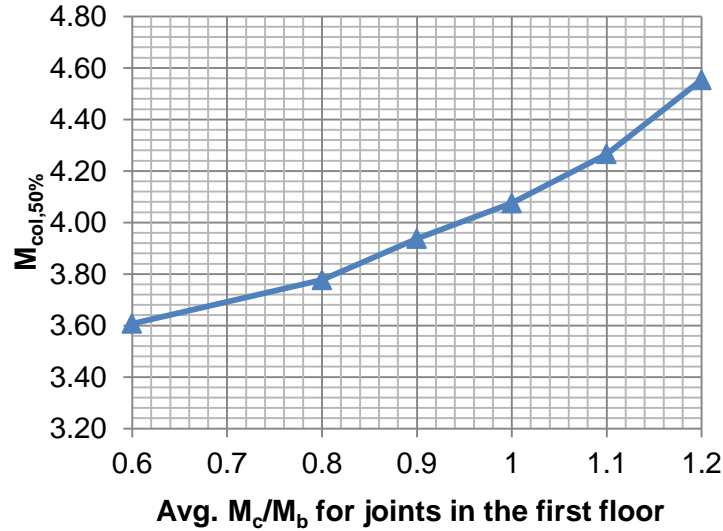


Figure 6-5. Variation of collapse performance of the case study building with respect to the variation of the average  $M_c/M_b$  ratio in the first story.

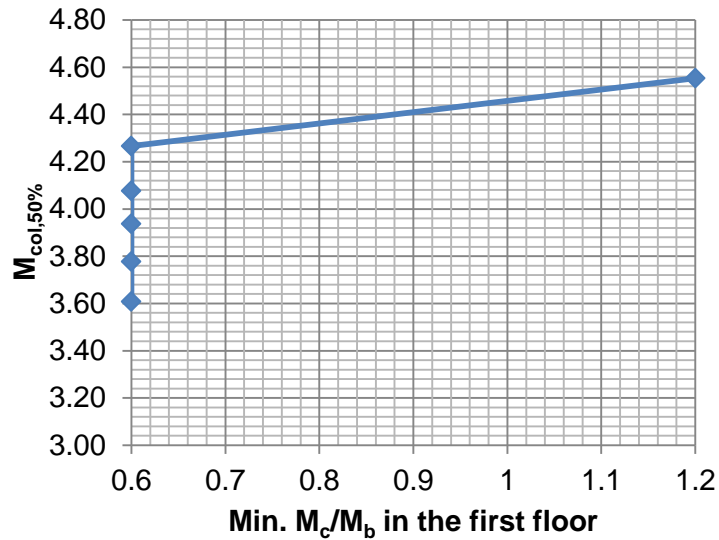


Figure 6-6. Variation of collapse performance of the case study building with respect to the variation of the minimum  $M_c/M_b$  ratio in the first floor.

To perform more investigation of the effect of extent of deficiency of  $M_c/M_b$ , and more specifically the effect of location of deficiency, three cases are considered here, as shown in Figure 6-7. For each pair of the models presented in Figure 6-7a and b, the average of  $M_c/M_b$  ratio in the first floor is the same, but the number of the highly deficient joints is different. In the other words, the distribution of the deficiency among the joints at the first floor is not the same for each pair of buildings.

The blue curve in Figure 6-8 is the same as the curve presented in Figure 6-5. Three points on this curve, with average  $M_c/M_b$  ratios of 0.8, 0.9, and 1.1, correspond to the models enclosed with the solid boxes in Figure 6-7a, b, and c, and are highlighted for comparison. The three additional (non-blue) points shown on Figure 6-8 correspond to the models shown in Figure 6-7a, b, and c in the dashed boxes. Comparing the collapse performance of each pair of the models in Figure 6-8, shows a maximum difference of 8% in the median collapse capacity. This difference is due to the fact that models that have some joints with  $M_c/M_b=1.2$ , *i.e.* more variability in the  $M_c/M_b$ , can experience more gradual failure as the worst joints fails first while the better joints are still intact. However, the collapse of the building with the uniform  $M_c/M_b$  ratio in the first floor is sudden, *i.e.* all joints fail at the same time. Since a building with truly uniform joint properties is highly unlikely, the differences between these two cases are judged to be small, and these results confirm that collapse performance of the building, *i.e.*  $M_{col,50\%}$  can be considered as a function of the average  $M_c/M_b$  ratio in the critical story with a good approximation.  $M_c/M_b$  is a parameter that defines how much damage distribution can occur in the structure before collapse. In case of existence of joints with different  $M_c/M_b$  ratios for joints in a single floor, the idea of averaging the  $M_c/M_b$  ratios in that floor tells us that, after the weaker joints reaches to their maximum strength, the force would redistribute among the stronger joints

in that floor, and stronger joints would compensate some of the deficiency in that floor. Moreover, these results show that the location of the deficiency  $M_c/M_b$  or in other words, the distribution of the deficiency  $M_c/M_b$  does not matter significantly for the collapse performance.

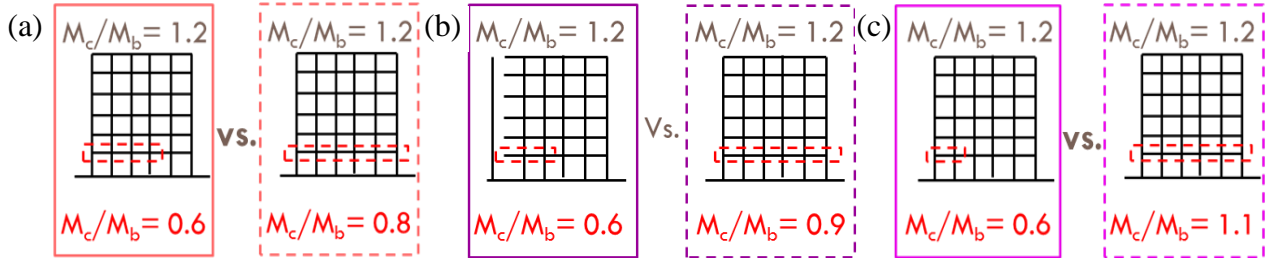


Figure 6-7. Schematic drawing of cases for studying the effect of the extent and location of deficiency  $M_c/M_b$  ratio in the first story with (a) average  $M_c/M_b = 0.8$ , (b) average  $M_c/M_b = 0.9$ , and (c) average  $M_c/M_b = 1.1$ .

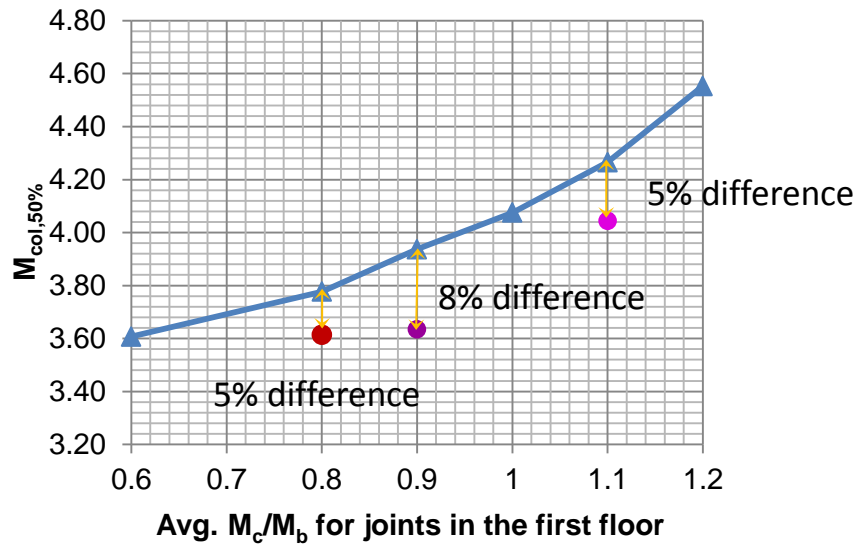


Figure 6-8. Comparison among three cases with the same average  $M_c/M_b$  ratio in the first floor, but with different distributions of the deficiency. The lower values correspond to the dashed boxes in Figure 6-8a, b, and c, wherein all of the joints at the first floor have the same  $M_c/M_b$  ratio.

All of the cases considered so far have examined a building with six column piers. To investigate the effect of number of piers, a new model composed of two frames in series connected with rigid links is tested, as shown in the green box in Figure 6-9. In this model, half of the joints in the first floor have the  $M_c/M_b$  ratio of 0.6 and half of the joints have the  $M_c/M_b$  ratio of 1.2, such that the average  $M_c/M_b$  in the first floor is 0.9. The collapse performance of this

model is compared with two other buildings with the same average  $M_c/M_b$  ratio, but with different distributions of  $M_c/M_b$ , and the results of this comparison are reported in Figure 6-10. The blue curve and the pink point are the same as the ones reported on Figure 6-8. The green point corresponds to the model with 12 piers and coincides almost exactly with the position of the blue curve, which represents the building in Figure 6-9. In this case, the results are exactly the same because in the two frame model half of the joints have  $M_c/M_b=0.6$  and the other half have  $M_c/M_b=1.2$ , which is exactly the same as the model in Figure 6-9a, except for the number of piers. This agreement between the results provides good indication that the definition of the collapse indicator  $M_c/M_b$  is independent of the number of piers in the critical story, and further supporting the concept of averaging of the  $M_c/M_b$ .

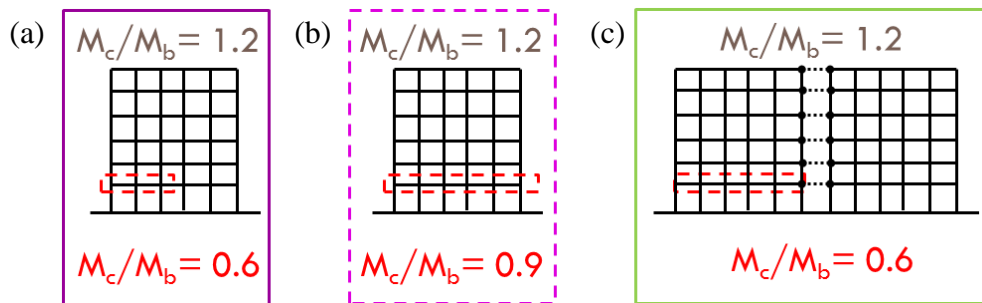


Figure 6-9. Schematic drawing of three cases to study the effect of the number of piers and the extent of deficiency  $M_c/M_b$  ratio in the first floor.

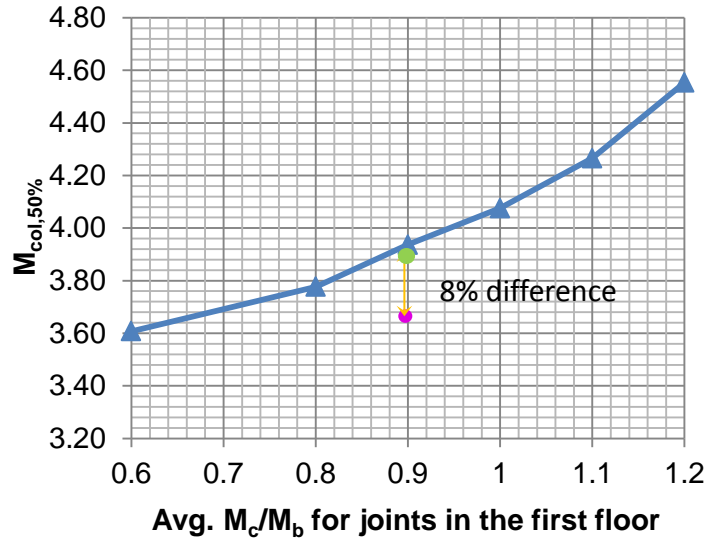


Figure 6-10. Comparison among three cases with the same average  $M_c/M_b$  ratio in the first floor, *i.e.* 0.9, but with different number of piers with low (deficient)  $M_c/M_b$ .

### 6.3.3 Variation of Adjacent Story Strength Ratio, $V_i/V_{i+1}$

#### 6.3.3.1 Context and $V_i/V_{i+1}$ Parameter Definition

Another common vertical irregularity in old concrete buildings is a discontinuity in story shear strength between two adjacent stories. This deficiency can lead to weak-story mechanisms, which are characterized by the failure of the building concentrating in one story. This deficiency may happen anywhere along the height of the structure, but is particularly common at the base of the building. It is clear that where there is a large discontinuity in strength between two stories, the collapse risk likely increases. The NIST Program Plan (NIST, 2010) defines  $V_i/V_{i+1}$  as the ratio of story shear strength for two adjacent stories.

This section of study considers the effect of the variation of  $V_i/V_{i+1}$  on the collapse performance of the building using, again, the flexural building models. Of particular interest is buildings with different frame lines which may have distinct  $V_i/V_{i+1}$  ratios. To study the effect of variation of  $V_i/V_{i+1}$  ratio, the first story is selected here as the critical story of the building, *i.e.* the

building fails consistently in the first story. The shear strength of each story is calculated as the summation of the strengths of all columns in that story, where the strength of each column in the models is defined as the summation of the end moment strengths, divided by the height of a column. The  $V_1/V_2$  ratio for the case study building is computed as 0.82, which has  $M_c/M_b = 1.0$  and  $V_p/V_n = 0.6$ .

### 6.3.3.2 Variation $V_i/V_{i+1}$ in Building with Non-Uniform Frame Lines

To study the effect of the deficiency  $V_1/V_2$  on the collapse performance of the case study building, a “flexural” model composed of two frame lines is selected, where the  $V_1/V_2$  ratio in the first frame is varied from 0.6 to 1.2 and  $V_1/V_2$  ratio in the second frame is kept constant as 1.2, as shown in Figure 6-11. To vary the  $V_1/V_2$  ratio, the moment strength of both the columns and beams in the first story and floor, respectively, is increased uniformly.

The collapse performance of these buildings, quantified by  $M_{col,50\%}$  is plotted with respect to the variation of average  $V_1/V_2$  ratio between two frames, and shown in Figure 6-12. This figure shows that the collapse performance of the building, *i.e.*  $M_{col,50\%}$  increases (improves) as the average  $V_1/V_2$  ratio increases. However, the rate of this increase is not constant and it is much higher for  $V_1/V_2 < 1.0$ , which is corresponding to the case where story 1 is weaker than story 2. For  $V_1/V_2 > 1.0$ , there is not much of the difference in the collapse performance of the building. Figure 6-12 also suggests that the critical value for the  $V_1/V_2$  ratio as 1.0, which is the kink point of the curve, but more data are needed to refine this estimate. We would expect that the blue curve in Figure 6-12 goes down for larger ratios of  $V_1/V_2$  based on the results of the similar study conducted by the author on a different case study building (ATC, 2011).

These results can be used to show that the average of  $V_i/V_{i+1}$  at the floor of interest can be a suitable definition for this collapse indicator compared to the other possible definitions. To

investigate more about the efficiency of the definition of  $V_i/V_{i+1}$ , another model composed of two frames in series with the  $V_1/V_2$  of 1.01 in both frames is developed and compared with the model with non-uniform distribution of  $V_1/V_2$ , but with the same average  $V_1/V_2$  of 1.01, as illustrated in Figure 6-13. Figure 6-14 compares the collapse performances of these two buildings. The  $M_{col,50\%}$  is the same for both models, regardless of the distribution of the  $V_1/V_2$  deficiency, which implies that average of  $V_i/V_{i+1}$  is an appropriate measure for the vertical strength irregularity. Averaging  $V_1/V_2$  in two frame lines tells us that although one frame may reach its maximum strength earlier due to having lower strength in the first story, the load would redistribute and the stronger frame would compensate the weakness of the system, such that the final collapse performance of the two systems shown in Figure 6-13 is the same.

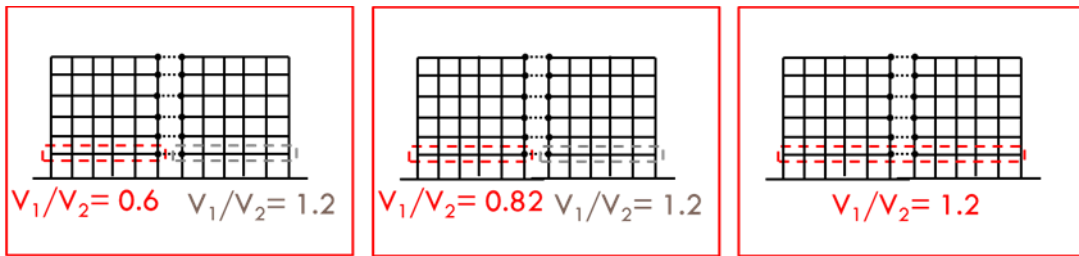


Figure 6-11. Schematic drawing for the variation of  $V_1/V_2$  ratio.

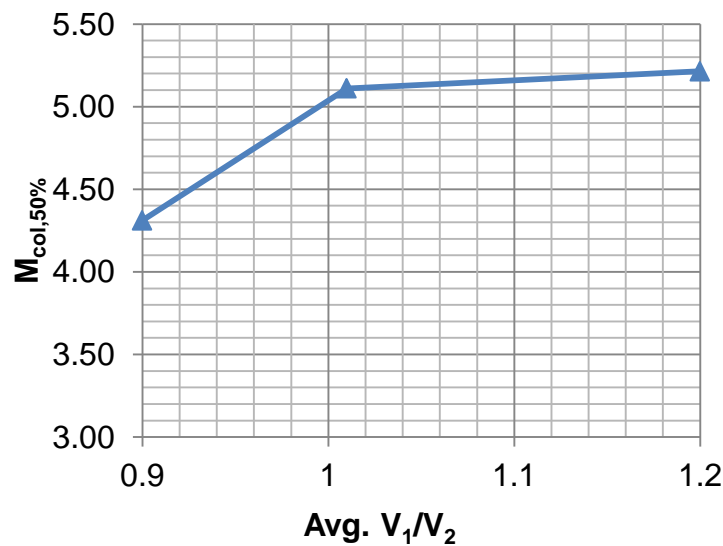


Figure 6-12. Variation of collapse performance of the two frames in series with respect to the variation of the average  $V_1/V_2$  ratio of the different frame lines.

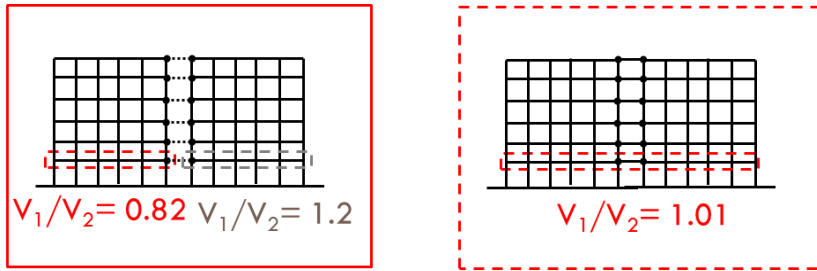


Figure 6-13. Schematic drawing for two cases with different distribution of  $V_1/V_2$  in order to study definition of deficiency  $V_i/V_{i+1}$ .

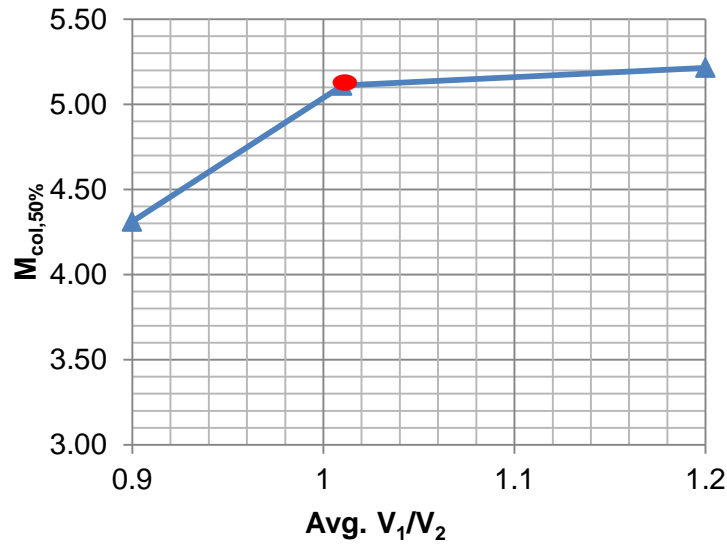


Figure 6-14. Comparison between two cases with the same average  $V_1/V_2$  ratio, i.e. 1.01, but with different distributions of the deficiency.

### 6.3.4 Variation of Column Flexural-Shear Strength Ratio, $V_p/V_n$

#### 6.3.4.1 Context and $V_p/V_n$ Parameter Definition

RC buildings built before the establishment of modern seismic regulations in 1970s may suffer from different deficiencies in design and detailing, such as wide transverse reinforcement spacing, 90 degree hooks, insufficient splice and development length, etc. Deficiencies such as wide transverse reinforcement spacing can make the columns more susceptible to shear or axial failure. These failure modes are more concerning than the flexural failure modes for columns because they occur more suddenly and in a brittle manner such that they cause a significant

strength reduction of the whole building in a short period of time. To measure this vulnerability, the NIST program plan (NIST, 2010) proposed the ratio of the flexural to shear strength ( $V_p/V_n$ ) as a collapse indicator.  $V_p$  is defined as the lateral strength corresponding to development of ultimate moment capacities at two ends of the column. It is computed as the summation of two end moments, as defined in *OpenSees* model, divided by height of the column.  $V_n$  is the nominal shear strength computed according to ASCE 41 Supplement 1 for low ductility demand (ASCE, 2006).  $V_p/V_n$  defines whether the response of a column/story is controlled by shear or flexure, as well as degree of shear/flexural criticality of a column. For instance if shear strength of a member is much lower than its flexural strength, *i.e.* large  $V_p/V_n$  ratio, the column may fail in shear much before it reaches its maximum flexural strength.

#### **6.3.4.2 Variation of $V_p/V_n$ in Building with Non-Uniform Columns**

To study the effect of the deficiency in terms of  $V_p/V_n$ , the  $V_p/V_n$  ratio in the first story is changed by introducing one, two, three, and six columns with  $V_p/V_n=1.20$ , while the rest of columns in the building have  $V_p/V_n=0.8$ , as shown in Figure 6-15. To vary the  $V_p/V_n$  ratio of the columns transverse reinforcement spacing is varied without any change to the stiffness or flexural strength of the columns. These analyses are all performed with the shear critical column model in the model with  $M_c/M_b = 1.0$ .

The collapse performance of these buildings, quantified by  $M_{col,50\%}$  is plotted with respect to the variation of average  $V_p/V_n$  ratio in the first story, and shown in Figure 6-16. This figure shows that the collapse performance of the building, *i.e.*  $M_{col,50\%}$  decreases as the average  $V_p/V_n$  ratio at the first story increases, indicating more shear criticality in the columns. Figure 6-16 also shows how increasing the extent of deficiency (*i.e.* number of shear critical columns) from zero to 6 columns with  $V_p/V_n = 1.2$ , decreases  $M_{col,50\%}$ .

To investigate the efficiency of other definitions of this collapse indicator, the same results as shown in Figure 6-16 is replotted in Figure 6-17 with a different x-axis, *i.e.* the maximum  $V_p/V_n$  of all of the columns in the first story. These results can be used to show that the average of  $V_p/V_n$  can be a suitable definition for this collapse indicator compared to the other possible definitions, because the maximum value of  $V_p/V_n$  in the critical story does not provide as much information.

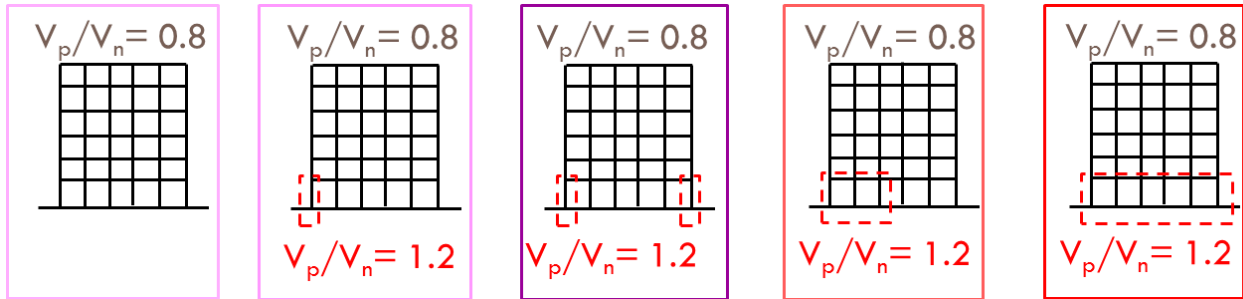


Figure 6-15. Schematic drawing for the variation of  $V_p/V_n$  ratio in the first story.

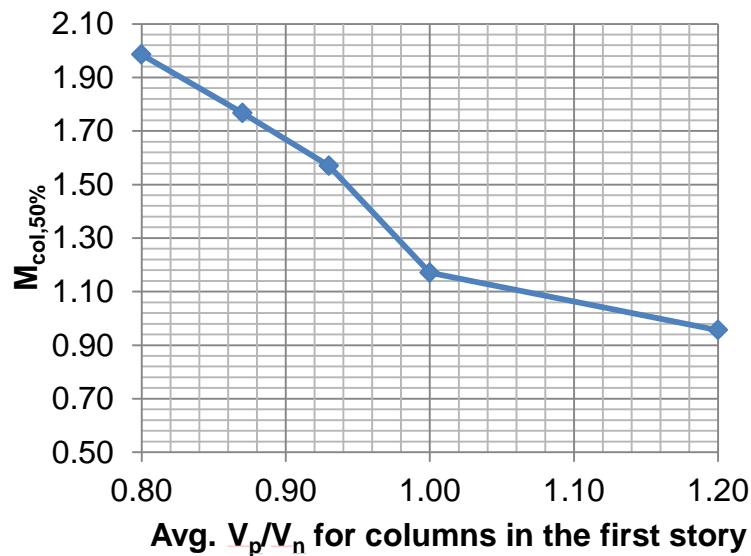


Figure 6-16. Variation of collapse performance of the case study building with respect to the variation of the average  $V_p/V_n$  ratio in the first story.

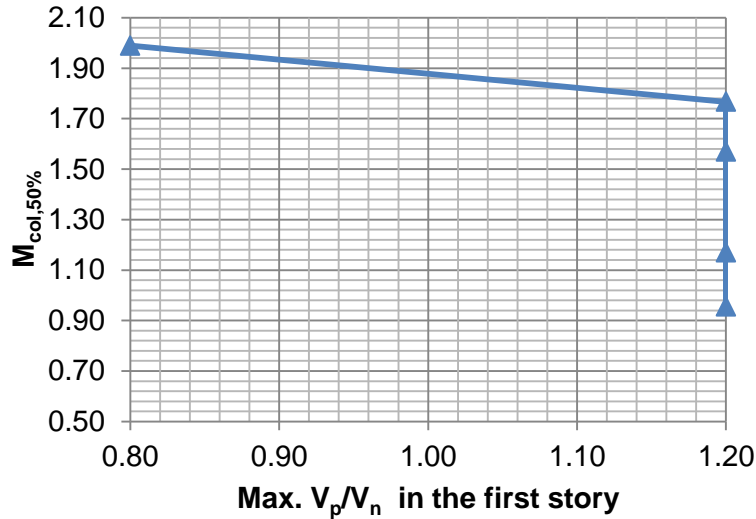


Figure 6-17. Variation of collapse performance of the case study building with respect to the variation of the maximum  $V_p/V_n$  ratio in the first story.

To perform more investigation on the effect of the extent of deficiency of  $V_p/V_n$ , and more specifically the efficiency of averaging  $V_p/V_n$  in the critical story, two cases are considered here, as shown in Figure 6-18. For both models presented in this figure, the average of  $V_p/V_n$  ratio in the first story is the same, but the number of the deficient columns, *i.e.* columns with  $V_p/V_n=1.2$ , is different. The blue curve in Figure 6-19 is the same as the curve presented in Figure 6-16. The red point on this figure with the  $V_p/V_n$  ratio of 1.0 is corresponding to the model enclosed with the red dashed box in Figure 6-18. Comparing the  $M_{col,50\%}$  of the red point with the blue curve in Figure 6-19, shows a difference of 20%. This difference is due to the fact that in these two models different columns fail. In the model with three bad columns, *i.e.* the model in the red box in Figure 6-18, the three bad columns fail axially or in shear. However, the dominant failure mechanism in the model with six columns with  $V_p/V_n = 1.0$  in the first story is the shear or axial failure of the interior columns.

The drift at which shear failure occurs in a column is a function of various parameters including transverse reinforcement ratio, axial load, and concrete compressive strength of the column (Elwood, 2004). The drift at axial failure is a function of the transverse reinforcement

ratio, axial load, and yield strength of the steel (Elwood, 2004). The dependency of the drift at shear and axial failure on various parameters makes the response prediction of shear critical stories very complicated. Even if all the columns in the critical story have the same cross sectional area and transverse reinforcement ratio, columns would fail at different drift levels due to the fact that the axial load in different piers are different and vary during the analysis. This axial load variation is observed more in the corner columns. These reasons indicate that the location of the deficiency may matter in the collapse performance of the building with different  $V_p/V_n$  ratios.

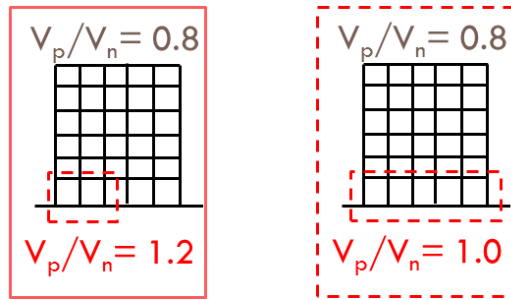


Figure 6-18. Schematic drawing for two cases with different distribution of  $V_p/V_n$  in order to study definition of deficiency  $V_p/V_n$ .

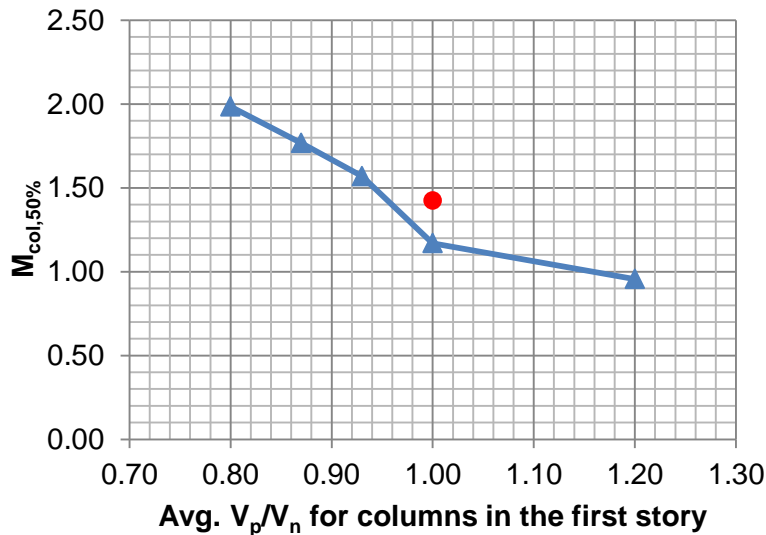


Figure 6-19. Comparison between two cases with the same average  $V_p/V_n$  ratio, i.e. 1.0, but with different distribution of deficiency.

In order to investigate the effect of the number of piers on the extent of the deficiency, a new model composed of two frames in series, connected with rigid links is tested, as shown in the green box in Figure 6-20. In this model, half of the columns in the first story have the  $V_p/V_n$  ratio of 0.8 and half of the joints have the  $V_p/V_n$  ratio of 1.2, such that the average  $V_p/V_n$  in the first story is 1.0. The collapse performance of this model is compared with two other buildings with the same average  $V_p/V_n$  ratio, but with a different distribution of the deficiency.

Figure 6-21 shows the results of this comparison. The blue curve and the red point are the same as the ones reported on Figure 6-19. The green point corresponds to the model with 12 piers, which has 8% difference with the blue curve. This difference could arise due to the same reasons explained above, related to variations in column shear and axial capacity, even in a uniform frame, and not due to the different number of piers.

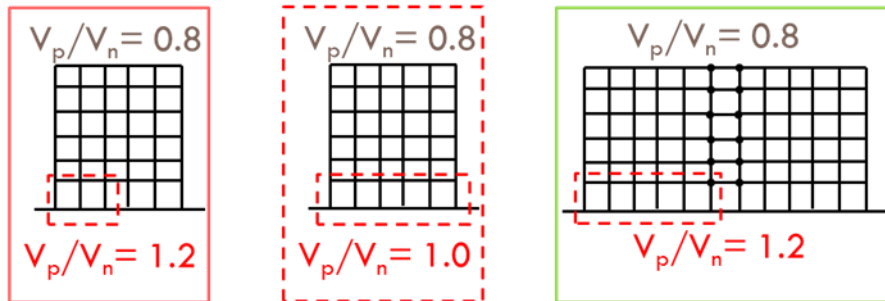


Figure 6-20. Schematic drawing for three cases to study the effect of the number of piers and the extent of deficiency  $V_p/V_n$  ratio in the first story.

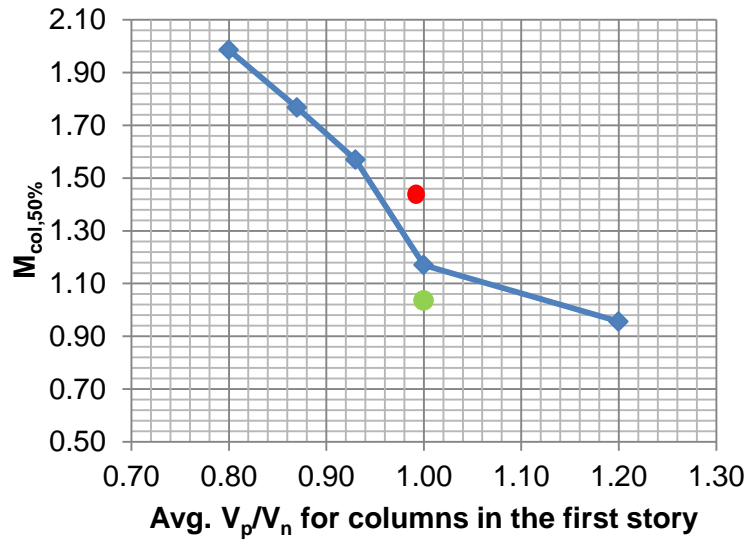


Figure 6-21. Comparison among three cases with the same average  $V_p/V_n$  ratio = 1.0, but with different distribution of deficiency and different pier numbers.

In order to perform more investigation on the effect of the location of deficiency  $V_p/V_n$ , two more models, with one and two deficient columns are tested, but with the different deficient column lines. Figure 6-22 illustrates the two sets of models compared here, where the orange dashed lines show the deficient columns in the new models and red dashed boxes show the deficient column lines in the previously presented models (the same as the models presented in Figure 6-15).

Figure 6-23 compares the collapse performance of these buildings. The blue curve in Figure 6-23 is the same as the curve presented in Figure 6-16. The pink and purple points on this figure are corresponding to the models enclosed with the pink and purple dashed lines Figure 6-22a and b. Comparing the collapse performance of each pair of the models in Figure 6-23 shows a big difference between each pair of models and, in particular, those models that have high shear criticality in the interior columns have worse collapse performance than those with high shear criticality in the exterior columns. This difference is due to the fact that after the interior columns fail in shear, the response is followed by immediately axial failure because of

the relatively high axial load (axial load ratio of 0.5). After the axial failure of one or more columns, the analysis cannot converge anymore even though only one or two columns has failed. As a result, the model cannot be excited to the intensity level in which collapse is formally identified by half of the columns failing either in shear or axially. As a result, this discrepancy can be considered as a modeling limitation.

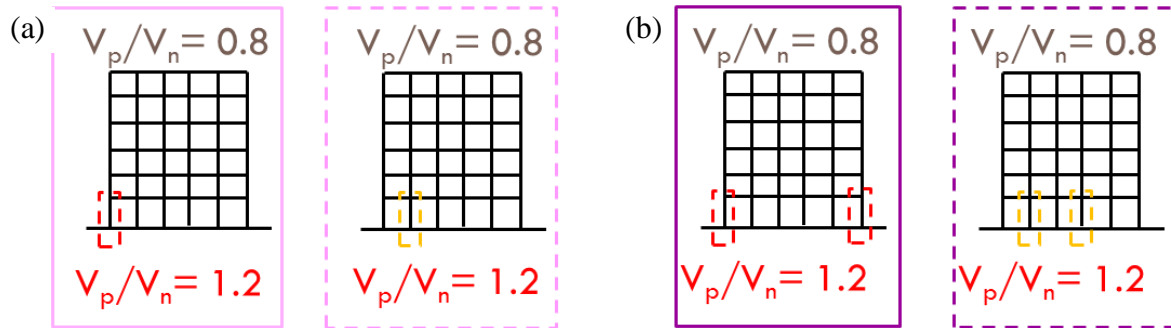


Figure 6-22. Schematic drawing for two pairs of models to study the effect of the location of deficiency  $V_p/V_n$  ratio in the first story.

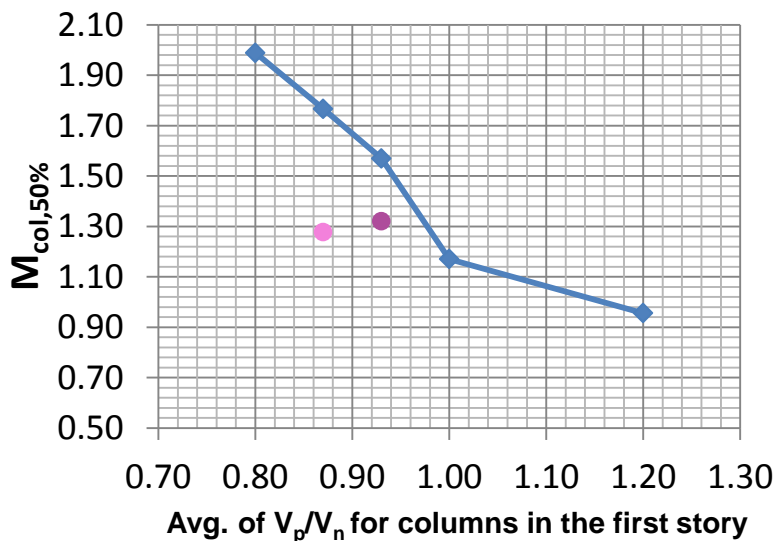


Figure 6-23. Comparison among four cases with the same number of deficient columns in the first story, but with different locations of the deficiency.

## 6.4 Conclusions

This chapter studied the effect of three different collapse indicators specifically,  $M_c/M_b$ ,  $V_i/V_{i+1}$ , and  $V_p/V_n$ , on the collapse performance of the uniform frame building. This study was

conducted in order to quantify the influence of these deficiencies on collapse performance, specifically investigating how the number and location of the deficient characteristic affect the collapse capacity. This study considered the variation of different collapse indicators in the critical story, *i.e.* the first story, so similar results are expected for buildings with different heights. However, further studies need to be conducted to confirm this statement.

The results of the study showed the expected decrease in collapse capacity as  $M_c/M_b$  ratio or number of columns with poor  $M_c/M_b$  ratios increased. These findings suggest that  $M_c/M_b$  collapse indicator can be defined as the average of the  $M_c/M_b$  ratio in all the joints in the floor of interest. The results of this study showed that the location of the deficiency  $M_c/M_b$ , as well as the number of piers in the case study building, does not matter significantly for the collapse performance.

Results of the study of the collapse indicator  $V_i/V_{i+1}$ , showed that the collapse performance of the building improves as the average  $V_1/V_2$  ratio increases. The critical value for the  $V_1/V_2$  ratio was estimated to be 1.0, which corresponds to the case that two adjacent stories have the same strength. Moreover, findings of this study showed that the average of  $V_i/V_{i+1}$  at the floor of interest is a suitable definition for this collapse indicator.

The investigation of the collapse indicator  $V_p/V_n$  was more challenging than the other two indicators. Results of the study on the collapse indicator  $V_p/V_n$  confirm that collapse performance of the building can be considered as a function of the average  $V_p/V_n$  ratio in the critical story for some buildings. However, for other buildings, averaging of  $V_p/V_n$  may bring a high approximation in the collapse performance assessment. This is mainly due to the fact that the location of the shear critical column, or in other words, the distribution of deficiency  $V_p/V_n$  matters for the collapse performance. However, this conclusion was made based on the results of

the current study which involves some modeling limitation and convergence issues after shear failure or axial failure occurs in the columns with high axial load. These results could be expected some changes following the improvement in the nonlinear modeling techniques.

## **7 Quantification of Modeling Uncertainties Based on the Blind Prediction Contest Submissions**

### **7.1 Overview**

In the assessment of the seismic performance of a building, two main sources of uncertainty are present: (a) uncertainty due to the selected ground motions used in the analysis, known as record-to-record uncertainty, and (b) uncertainty embedded in the simulation model, known as modeling uncertainty. Quantification and propagation of these sources of uncertainty through the assessment of seismic risk is one of the important aspects of the performance-based earthquake engineering (PBEE) framework. Uncertainty due to record-to-record (RTR) variability stems from variation in the response of the structure excited by different ground motions due to the specific characteristics of each record, such as frequency content. RTR uncertainty is incorporated in the PBEE framework through the development of robust techniques for ground motion selection and scaling whereby multiple ground motions, selected to represent the seismicity at the site of interest, are used in the assessment (Haselton et al., 2007). Modeling uncertainty stems from variation in the physical properties of the building components, as well as variation in the representation of these properties in an analysis model. Past research in the area of modeling uncertainty considered variation of different modeling parameters such as element strength, initial stiffness, hardening stiffness, plastic rotation capacity, and hysteretic energy dissipation capacity to quantify the significance of modeling uncertainty in seismic risk assessment (Ellingwood et al., 1980; Fardis and Biskinis, 2003; Haselton et al., 2007; Ibarra, 2003; Lee and Mosalam, 2005). Other researchers studied methods for propagating modeling uncertainties through seismic performance assessments using the first-order second-moment (FOSM) method (Haselton et al., 2007), or a response surface with Monte Carlo simulation (Liel et al., 2009).

State-of-the-art methods for seismic assessment have well-established methods for incorporating RTR variability. However, treatment of modeling uncertainty remains challenging. The term “modeling uncertainty”, as used here, reflects the uncertainty in the extent to which model represents the true structural response. This study evaluates the effect of modeling uncertainty using submissions to a blind prediction contest. In the recent years, different types of structures have been tested on shake tables for the purpose of evaluating seismic design criteria, investigating structural failure modes, or predicting structural response parameters. In some cases, before performing the experiment, teams are invited to predict the response of the structure in so-called “blind predictions”. Participants may predict the response using a variety of modeling techniques and analysis platforms, employing information from design drawings and material properties. The data submitted by participants provide a unique opportunity to study the uncertainty in the predicted response due to modeling.

This study quantifies the significance of modeling uncertainties in seismic performance assessment, using results of a blind prediction contest for a 7-story RC building at UCSD in 2006. These modeling uncertainties reflect differences in software platform, solution algorithm, element type, and model parameter calculation or selection. The effect of some of these sources of uncertainties has not been investigated previously, due to the fact that in most of the past studies, the nonlinear model is simulated using a single software package. After quantifying the modeling uncertainty, this source of uncertainty is combined with the RTR variability in order to investigate the total uncertainty in the results.

## **7.2 Methodology of Study**

This study employs the methodology for assessing the seismic performance of a building developed by the Pacific Earthquake Engineering Research Center, which provides a

probabilistic framework for relating ground motion intensity to structural response and performance, through nonlinear time-history simulation (Deierlein, 2004). Incremental Dynamic Analysis (IDA) is used to assess global performance as a function of ground motion intensity (Vamvatsikos and Cornell, 2002). IDA results show the relationship between ground motion intensity and building response parameters, such as the peak interstory drift ratio, in the structure. The final outcome of IDA is a set of fragility functions, which define the probability of exceeding a particular drift level or damage state, as a function of the ground motion intensity.

A key challenge in IDA is that the fragility curves so-developed reflect only one source of uncertainty, that coming from randomness of the selected ground motion records, and do not incorporate the uncertainty in the prediction of the drift level which is embedded in the modeling process. This limitation is significant because an analyst usually has only a single model of the structure of interest.

The proposed methodology used to quantify and incorporate modeling uncertainties in the analysis proceeds as follows. First, IDA is performed on a nonlinear model of the case study building for a set of earthquake records, and a set of IDA curves generated, as illustrated in Figure 7-1a. These IDA curves consider only the randomness due to the earthquake records and are called “IDA-RTR” curves. Modeling uncertainty is then quantified by the variability in drift results predicted by the participants in the blind prediction contest. Specifically, model predictions of building response submitted by blind test participants are used to quantify histograms of modeled interstory drifts for a particular spectral acceleration level. These histograms are used to fit probability distributions associated with modeling uncertainty.

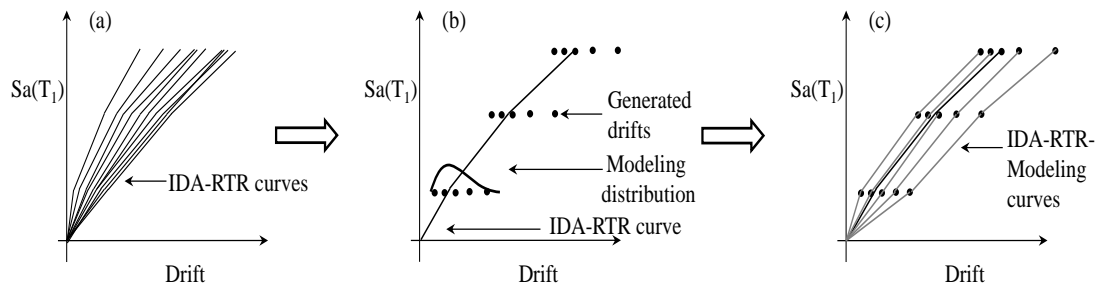


Figure 7-1. Schematic drawing illustrating the proposed methodology to consider (a) RTR uncertainty; (b) modeling uncertainty representing the blind prediction test data; and (c) IDA curves generated to represent the modeling uncertainty.

In the next step, modeling and RTR uncertainties are combined. For this purpose, each point on the IDA-RTR curve is replaced by a set of randomly generated points with the same spectral acceleration as the original curve, but a distribution of drifts representing modeling uncertainty. The drifts are generated such that they are probabilistically consistent with the distributions generated in the previous step, as shown in Figure 7-1b; the distribution used to generate the modeling drifts depends on the drift level. The generated random numbers at different excitation levels are then connected to generate a set of “IDA-RTR-Modeling” curves, as shown in Figure 7-1c. This set of IDA curves represents the effect of modeling uncertainty, for a given IDA-RTR curve. This process is repeated for all IDA-RTR curves, to generate a new set of IDA curves, known as “IDA-RTR-Modeling”, which incorporate the modeling uncertainty in addition to the RTR variability. This new set of IDA curves is used to compute the fragility curves associated with exceeding particular drift ratios of interest and the results are compared with those from the IDA-RTR curves.

### 7.3 Application of the Proposed Methodology

#### 7.3.1 Case Study Building

This chapter examines the blind predictions submitted for a full-scale 7-story RC wall building tested on the UCSD shaking table, shown in Figure 7-2. The tested structure represents

a slice of a 7-story load bearing wall building typical of Los Angeles construction. The building slice has a reinforced concrete “web” wall, which is the lateral force resisting system, with two transverse “flange” walls, and a post tensioned (PT) segmental precast pier, which provides torsional stability. The floor system is a flat slab supported with steel gravity columns (Panagiotou and Restrepo, 2011). The building was designed based on a displacement-based method, which led to smaller member sizes and less reinforcement than what is required by force-based approach (Panagiotou and Restrepo, 2011). The test was conducted to investigate the dynamic response of the building, including the interaction between wall, slab, and gravity system of the building (Panagiotou et al., 2011).

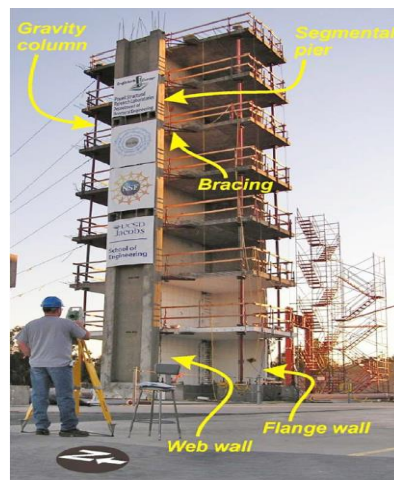


Figure 7-2. View of the building tested at UCSD (Moaveni et al., 2011).

In the experiment, four earthquake records were imposed on the building: 1) the longitudinal component of the 1971 San Fernando earthquake recorded at Van Nuys (EQ.1), which has  $S_a(T_1)$  of 0.32g, 2) the transverse component of the same Van Nuys record, which has  $S_a(T_1)$  of 0.75g, 3) the longitudinal component of the 1994 Northridge earthquake recorded at the Oxnard Boulevard station (EQ.3), which has  $S_a(T_1)$  of 0.60g, and 4) the 360° component of the 1994 Northridge earthquake recorded at the Sylmar station (EQ.4), which has  $S_a(T_1)$  of 1.38g (Moaveni et al., 2011).

### 7.3.2 Nonlinear Analysis of Building

In order to assess the building's seismic performance in this study, the nonlinear 2D model of the building developed by Martinelli and Filippou (2009), is analyzed under a set of earthquake records. In this model, the shear wall is simulated with distributed inelasticity force-based beam-columns (Spacone et al., 1996). The cross section is discretized in fibers that capture the interaction of the axial force and bending moment. The compressive behavior of concrete fibers is modeled with the modified Kent-Park material model (Kent and Park, 1971); tensile behavior is modeled with a bilinear behavior with a linear elastic branch followed by a linear softening branch. The volumetric confinement effect is taken into account by the modified Kent-Park model. The nonlinear Menegotto-Pinto material model, modified by Filippou et al. (1983) to include isotropic hardening effects, is used for steel fibers. Each story is modeled with a nonlinear beam-column element with three integration points representing each of the web and flange walls. The post-tensioned pier is modeled with linear elastic beam-columns. The connection between the flange and web wall are modeled with rigid end offsets. The mass is lumped at each floor. The footing under each wall is modeled with an elastic element. The period of the model is equal to 0.49s, very close to the experimental fundamental period of 0.52s. The ability of the model to predict the measured earthquake response of the 7-story RC shear wall specimen was demonstrated by the good agreement of the blind prediction results with the measured data, but it did not capture the lap-splice failure observed in the experiment (Martinelli and Filippou, 2009).

The model is analyzed using IDA to develop a fragility curve that accounts for the record-to-record variability. In IDA, the nonlinear structural model is subjected to a recorded ground motion, and dynamically analyzed to predict the structure's response. The time-history

analysis is repeated, each time increasing the scale factor on the input ground motion. This process is repeated for a large set of ground motion records. This study uses 35 of the 44 ground motions in the FEMA P-695 far-field set (FEMA, 2009). Nine of the 44 ground motions are recognized as the pulse-like ground motions excluded from this analysis (Champion and Liel, 2012). The IDA results of the nonlinear model for the selected ground motions are presented in Figure 7-4a. The use of the FEMA P-695 ground motion set is for illustration only; any set of ground motions selected according to established procedures could be used.

### **7.3.3 Description of Data**

The data set from the blind prediction test includes structural response predictions for the 7 story building submitted by 21 participant groups for 4 different ground motion time histories. Participants in the blind prediction competition were categorized in three groups: Engineering Practitioners (EP), Undergraduate Students (U), and Researcher Associates (RA). For each ground motion, participants predicted different response parameters of the building, such as maximum moment, maximum interstory drift ratio, maximum shear force, and maximum acceleration at each floor or story. A number of different software platforms were used by the participants including: Abaqus, OpenSees, SAP 2000, Adina, Ram Perform 3-D, and ETABS. The goal of this study is to quantify the modeling uncertainty in the blind prediction data and to assess its influence on the prediction of the ground motion intensity at which a structure experiences drift levels greater than a specified value. As a result, in this study, we focus on the uncertainty in model predictions of maximum interstory drift ratio, which are predicted for each story of the building for each time history. Interstory drift ratio is a dimensionless quantity computed as the difference in lateral deflection between floor  $i$  and floor  $i + 1$ , divided by the

height of the story. Aleatory uncertainty associated with material properties is assumed to be reduced because modelers were provided with measured material properties.

Table 7-1 reports the *IDR* values predicted by the practitioner groups for the first earthquake, *i.e.* EQ.1, as an example. The notation *IDR<sub>ij</sub>* in this table refers to the interstory drift ratio for the *i<sup>th</sup>* earthquake record at the *j<sup>th</sup>* story. Table 7-1 also reports the median and standard deviation of data submitted by all participants for EQ.1, and the experimentally measured drift ratio. Five out of 21 participant groups are considered to be outliers and dropped from the data set. The outliers are selected based on engineering judgment; specifically, groups reporting predictions of the average *IDR* over all stories that is 10 times greater or smaller than the experimental value for any earthquake record were excluded. The outliers so-identified are thought to have a significant error in the modeling processes, biasing the drift distribution associated with modeling uncertainties.

Table 7-1. Predicted (modeled) interstory drifts for the 7-story building for EQ.1.

<b>Participant Group</b>	<b>IDR11</b>	<b>IDR12</b>	<b>IDR13</b>	<b>IDR14</b>	<b>IDR15</b>	<b>IDR16</b>	<b>IDR17</b>
<b>EP1</b>	0.003	0.007	0.009	0.011	0.011	0.012	0.012
<b>EP3</b>	0.001	0.002	0.003	0.003	0.003	0.003	0.003
<b>EP4</b>	0.002	0.004	0.005	0.006	0.006	0.006	0.006
<b>EP5</b>	0.002	0.002	0.002	0.002	0.002	0.002	0.002
<b>EP6</b>	0.003	0.003	0.003	0.003	0.002	0.002	0.001
<b>EP7</b>	0.002	0.003	0.003	0.003	0.003	0.003	0.004
<b>EP8</b>	0.001	0.002	0.003	0.004	0.004	0.004	0.004
<b>Median of all groups</b>	0.002	0.003	0.003	0.003	0.003	0.003	0.004
<b>Standard deviation</b>	0.001	0.002	0.002	0.003	0.003	0.003	0.004
<b>Experimental results</b>	0.001	0.002	0.003	0.003	0.003	0.003	0.003

### 7.3.4 Probability Distributions of Modeled IDR

Uncertainty in the prediction of IDR is not expected to follow the same distribution at all drift ratios because of the increasing complexity with modeling larger drifts reflecting greater

nonlinearity in the structure. However, for a given drift level, we expect the distribution of modeled drifts to be similar, regardless of the story or earthquake record for which the drift was modeled and measured. To study the distribution of *IDR* obtained from blind predictions, 6 drift levels measured in the experiment corresponding to  $\Delta_{exp} = 0.003, 0.006, 0.009, 0.015, 0.018,$  and  $0.022$  are selected. (These values are rounded to the third decimal place.) Each experimental value is compared to the modeled drifts intended to predict that particular experimental value. In some cases this means that model predictions for different stories or earthquake records are combined, provided that all model values were intended to predict the same value of experimental drift,  $\Delta_{exp}$ . The experimental drift levels are selected based on two criteria: 1) for each value of drift, there are a significant number of corresponding modeling predictions reported by participants, and 2) there is enough separation between the selected drift ratios to consider the trend of variation in the modeling drift distribution with increasing *IDR*. Model predictions not corresponding to an experimental drift value in the list above were dropped from the data set. In total, more than 65% of the available data submitted by participants for the displacement field are used in this study. (The authors found that including the omitted in the analysis does not significantly change the findings.)

All modeled drift ratios corresponding to a particular experimental drift  $\Delta_{exp}$  are grouped together. For each drift level, two distributions are fitted. The first distribution is chosen as the best-fit distribution, using the Kolmogorov–Smirnov (K-S) test to measure goodness-of-fit (Massey 1951). Since the best-fit distribution may not be well known, a second distribution which satisfies the K-S test with the 95% confidence level, but is more commonly used (e.g. normal, lognormal, etc.) is also fitted. This second distribution is termed the “engineering fitted” distribution. Figure 7-3 illustrates the histograms and engineering fitted distributions for two

levels of  $\Delta_{exp}$  and the parameters defining these distributions for each drift level are reported in Table 7-2. The results suggest that the data grouped for  $\Delta_{exp}$  values of 0.015 and 0.018 follow a uniform distribution. This may be due to the limited number of data points at these drift ratios so data corresponding to these two drift levels are not considered in the subsequent analysis.

The data presented in Table 7-1, and similar model predictions made for the other earthquake records, show a difference or “bias” between the median of the modeling data and the measured value in the experiment. Table 7-2 reports the bias for each group of data, computed as the difference between the median of modeled value and the experimental value (Montgomery and Runger, 2010). This table shows that the models tend to under-predict drifts in comparison to the experiment. Table 7-2 also shows that the bias increases for larger experimental drifts, which correspond to higher levels of excitation. To study the distribution of drifts associated with modeling uncertainty, two cases are considered. In the first case, the “original” [uncorrected] data, as presented in Table 7-1, have been used to define the modeling *IDR* distribution directly. In the second case, the bias of data is removed by making the median of the modeling distribution the same as the experimental values, but the dispersion in the modeled data is preserved. This new set of data is called the “unbiased” [corrected] data set.

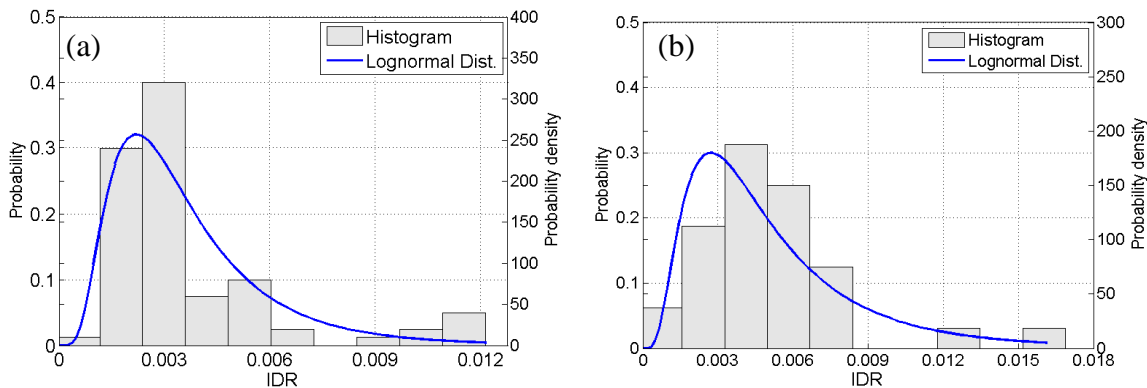


Figure 7-3. Histograms and engineering distributions for the “original” prediction data corresponding to (a)  $\Delta_{exp}=0.003$  and (b)  $\Delta_{exp}=0.006$ .

Table 7-2. Statistics of the predicted (modeled) drifts for different experimental drift values.

$\Delta_{exp}$	Best Fit Distribution	Engineering Fit Distribution	Median of Modeled IDR	$\sigma$ of Modeled IDR*	# of Modeled IDR data	Bias
0.003	Burr	Lognormal	0.003	0.003	80	-0.0002
0.006	Cauchy	Lognormal	0.005	0.003	32	-0.0017
0.009	Cauchy	Lognormal	0.007	0.004	95	-0.0022
0.015**	Gen. Pareto	Uniform	0.009	0.005	16	-0.0053
0.018**	Error	Uniform	0.012	0.007	16	-0.0062
0.022	Error	Lognormal	0.016	0.007	64	-0.0055

\* $\sigma$  is the standard deviation of the sample data \*\* Not considered in later analyses

## 7.4 Combination of Modeling Uncertainty With RTR Uncertainty

In this section, the modeling uncertainty quantified in the previous section is combined with the RTR uncertainty using the approach described above. The modeling uncertainty is represented by histograms or engineering fitted distributions of the modeled drift values. The effect of modeling uncertainty will be separately considered for the “original” and “unbiased” data sets, for a total of four distinct cases: 1) histograms of the original data; 2) engineering distributions of the original data; 3) histograms of the unbiased data; and 4) engineering distributions of the unbiased data.

### 7.4.1 Histograms With the Original Data

First, modeling uncertainty is quantified in the form of four histograms corresponding to the  $\Delta_{exp} = 0.003, 0.006, 0.009, 0.022$  and based on the original data. These histograms represent the modeling uncertainty associated with the prediction of a particular drift; each histogram is assumed to be valid for a specified range of drifts. For instance, the histograms corresponding to  $\Delta_{exp} = 0.003$ , is taken to represent the uncertainty in modeling drifts for drifts between zero and 0.0055. Similarly, the histograms corresponding to  $\Delta_{exp} = 0.006, 0.009$ , and 0.022 are taken as

the drift distribution for modeled drifts in the ranges of  $0.0055 < \Delta \leq 0.0085$ ,  $0.0085 < \Delta \leq 0.0155$ , and  $0.0155 < \Delta$ , respectively. Modeling uncertainty data are available up to a drift ratio of 0.022. The modeling drift distribution corresponding to  $\Delta_{exp} = 0.022$  is used for all drifts greater than 0.022.

For each IDA-RTR curve, the modeling uncertainty histograms are used to develop IDA-RTR-Modeling curves. These new IDA curves are generated using a Monte Carlo approach, such that for a given excitation level on the IDA-RTR curve, fifty alternative drifts that are consistent with the histogram for the modeled data are simulated.<sup>2</sup> For illustration purposes, ten IDA-RTR-Modeling curves generated for one IDA-RTR curve are shown in black in Figure 7-4b. This process is repeated for all of the IDA-RTR curves.

To evaluate the effect of propagating the modeling uncertainty through the analysis, a set of fragility curves are computed at different drift levels separately for the IDA-RTR results and IDA-RTR-Modeling results and compared in Figure 7-5. These fragility curves represent the probability of exceeding a particular drift level, given a specified ground motion intensity. Fragility curves are developed first by computing the empirical CDF of exceeding drift from IDA results and then fitting a lognormal distribution to the data using the maximum likelihood method. Figure 7-5 also reports the median and lognormal standard deviation of the lognormal fragility curves.

The incorporation of modeling uncertainty flattens the fragility curve (increasing the dispersion or standard deviation) and increases the median  $S_a$  value. The shift in the median indicates that not incorporating modeling uncertainty can be conservative at high excitation levels, *i.e.* for large  $S_a$  values. This conservatism occurs because the modeled drifts

---

<sup>2</sup> Since the histograms shown are for a single value of  $\Delta_{exp}$ , they are shifted if the IDA-RTR has a different value of  $\Delta_{exp}$ .

underestimate the true (experimental) drifts. The underestimation is likely due to the use of models that do not reflect the all sources of nonlinearity of the building. The results may also indicate that neglecting modeling uncertainty can be non-conservative at low excitation levels. This could be because of the lack of blind prediction data for drift ratios less than 0.003. Figure 7-5d shows that the significance of including the modeling variability decreases at the largest drift level (i.e. 0.02) and the relative difference between the dispersion of IDA-RTR and IDA-RTR-Modeling is smaller than at the other drift levels. This reduction of dispersion is observed because many of the IDA curves do not have data at this large of a drift. As shown in Table 7-2, the general trend is that the larger the drift, the greater the dispersion in modeled drift values, which increases the dispersion in the fragility curves. Due to the limited prediction data available at lower drift levels and difficulties in computing fragilities at higher drifts where IDA data are not available, we conclude that the fragility curves computed at drifts of 0.006 and 0.009 are the most representative of the effect of incorporating modeling uncertainty in the seismic assessment results.

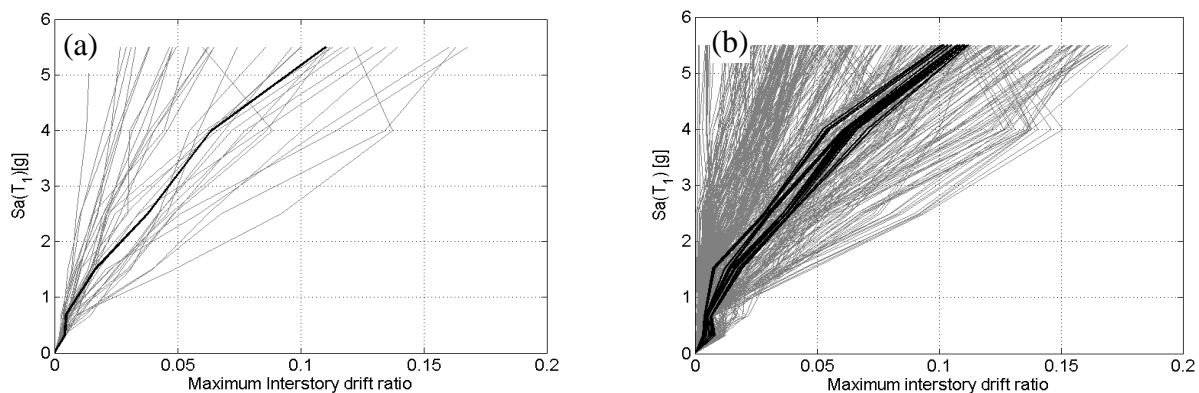


Figure 7-4. IDA results from nonlinear simulation of the 7-story building, representing: (a) RTR uncertainty, and (b) RTR and modeling uncertainty.

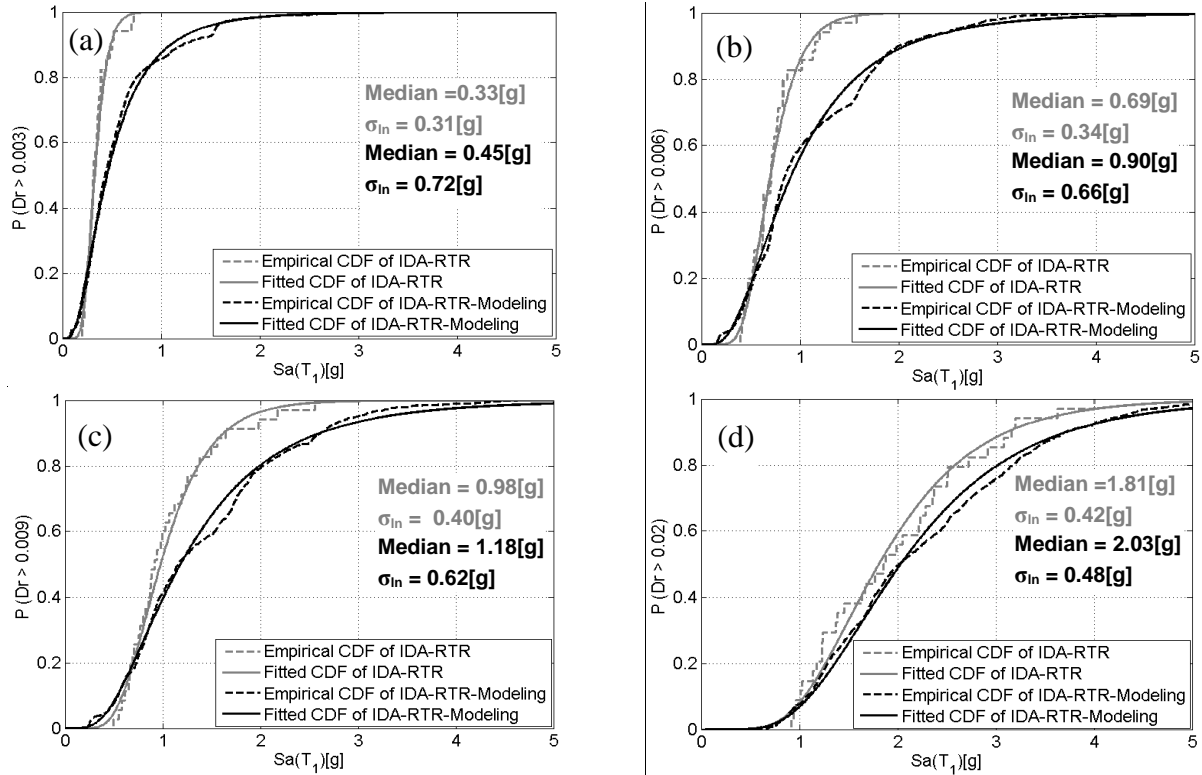


Figure 7-5. Comparison between fragility curves computed considering RTR variability only (gray lines) and RTR and modeling variability (black lines) for the original data. The fragility curves computed represent the probability of drifts exceeding a) 0.003, b) 0.006, c) 0.009, and d) 0.02.

## 7.4.2 Histograms With the Unbiased Data

In this section, the same procedure is repeated for the unbiased (corrected) data and the results are illustrated in Figure 7-6. This figure shows that removing the bias from the data virtually eliminates the shift in the median. However, the modeling fragility curve still has larger dispersion than the RTR-only curve because of the uncertainty in the drift prediction, even though on average, the modeled results give the true value.

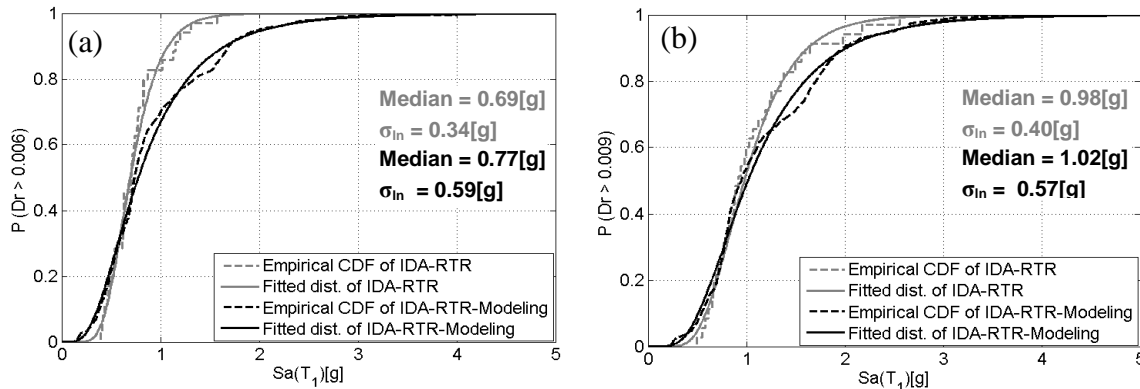


Figure 7-6. Comparison between fragility curves computed considering RTR variability only (gray lines) and RTR and modeling variability (black lines) for the unbiased data. The fragility curves computed represent the probability of drifts exceeding a) 0.006 and b) 0.009.

### 7.4.3 Fitted Distributions With the Original Data and Unbiased Data

In this section, the same procedure, as explained in the previous two sections, is repeated, except that the randomly generated model drifts are simulated using the engineering distributions, instead of the histograms. The process is repeated for the original and unbiased data, and the median and standard deviation of the fitted fragility curves are presented in Table 7-3. For comparison purposes, the median and standard deviation of the previous results (Figure 7-5 and Figure 7-6) are also summarized in Table 7-3. Comparison of the results shows that the distribution and histograms lead to very similar medians and standard deviation of the developed fragility curves. This finding implies that either of these two approaches can be implemented to incorporate the modeling uncertainty in seismic assessment process. However, using the engineering distribution is likely to be more straightforward in practice.

Table 7-3. Median and standard deviation of the fragility curves representing uncertainty in RTR and modeling, obtained from histogram and distribution approaches.

Drift	Histograms & Original data		Histograms & Unbiased data		Distributions & Original data		Distributions & Unbiased data	
	Median Sa(T <sub>1</sub> ) [g]	$\sigma_{ln}$ [g]	Median Sa(T <sub>1</sub> ) [g]	$\sigma_{ln}$ [g]	Median Sa(T <sub>1</sub> ) [g]	$\sigma_{ln}$ [g]	Median Sa(T <sub>1</sub> ) [g]	$\sigma_{ln}$ [g]
0.006	0.90	0.66	0.77	0.59	0.88	0.69	0.73	0.61
0.009	1.18	0.62	1.02	0.57	1.21	0.61	1.02	0.51

## 7.5 Conclusions and Recommendations

This study quantifies the effect of modeling uncertainty on seismic fragility assessments, using results of the 7-story RC building blind prediction contest at UCSD. The modeling uncertainty is presented in terms of drift distributions based on the modeled drift submitted by the contest participants. These drift distributions are defined by probability density functions or histograms of experiencing a specific drift ratio. These drift distributions are evaluated at different drift levels measured during the experiment. The modeling drift distributions are propagated through the results of the nonlinear time history analyses that consider only the record-to-record (RTR) variability. The resulting IDA curves are used to compute the fragility curves to represent the probability of exceeding a particular drift level as a function of ground motion intensity. The results showed that incorporating the modeling uncertainty to the RTR variability results leads to an increase in the median Sa level and increase the dispersion of the fragility curve by the average of 25% and 73%, respectively. The increase in the dispersion of the fragility curve, i.e. 73%, due to modeling uncertainty in this particular building is of the same order of magnitude as uncertainty associated with RTR variability.

The predicted increase in the dispersion is greater than that obtained by other methods for quantifying modeling uncertainty (e.g. Haselton et al. 2007), which predicted an increase in

the dispersion of about 55%. Analyses results showed that the main portion of the shift in the median is due to the bias existing in the modeled data for this test.

This study developed and tested the proposed methodology to incorporate the modeling uncertainty to the seismic assessment procedure based on blind prediction test data. The blind prediction test data represents a unique opportunity to quantify modeling uncertainties. The results of this study suggest that modeling uncertainties can be incorporated by introducing a drift distribution to represent the modeling uncertainty. However, the main challenge is understanding the modeling drift distributions, which involves more research to predict generalizable modeling drift distribution applicable to a wider range of buildings. The numbers and distributions presented in this study are valid only for this case study building. A remaining question is whether the level of underprediction in the contest submissions is typical.

## **8 Conclusion**

### **8.1 Summary and Findings**

Reinforced concrete (RC) frames with masonry infill walls were prevalent in high seismic areas in US as well as in other parts of the world and. This building type remains in practice in some countries including Mediterranean countries. These kinds of buildings pose a significant risk to occupants in terms of life safety and economic losses. Existing masonry infilled RC frames may suffer from the potential deficiencies in the concrete frame as well as the brittle behavior of the infill panel. The high number of existing masonry infilled frames induces the need to assess the seismic performance of these buildings. The main objective of this study is to develop a new modeling approach, known as multi-scale modeling approach here, to simulate the response of the masonry infilled frames in the PBEE framework, in order to quantify the collapse performance of existing masonry infilled RC frames in US and compare it with the bare frames. This modeling approach aims to preserve the accuracy in the prediction of the response of masonry infilled frames, while also ensuring modeling simplicity.

Chapter 2 reviewed the background study of the masonry infilled frames from the early studies conducted in this area in 1960s to the state of the art of modeling for this kind of buildings.

Chapter 3 and 4 proposed a multi-scale modeling approach to simulate the response of the masonry-infilled RC frames up to the point of earthquake-induced collapse. In the multi-scale model, the behavior of the macro (strut) model simulating the response of the infill wall is based on the infill response obtained from a micro model. Although extra effort is required to model the response of the RC frame building and infill at two scales, the macro model so-generated takes advantage of the accuracy of the micro modeling approach in predicting the masonry response, peak strength and expected failure modes depending on frame properties and the level

of gravity loading, while maintaining the computational efficiency of a macro model. These characteristics make the model suitable for assessments in which repeated nonlinear dynamic analyses are required, as in the performance-based earthquake engineering framework. The performance of the developed macro model is examined in this study, through comparison against experimental results for two infilled RC frame specimens. The good agreement of the numerical simulation with the experimental results under static monotonically increasing lateral loading demonstrates the capability of the integrated micro and macro modeling approach to capture the key characteristics of the wall response and wall-frame interaction.

Chapter 5 illustrated the implementation of the multi-scale modeling methodology through dynamic analysis of a case study building representative of 1920s era Los Angeles construction. The results showed that the presence of the infill panel in the frame decreases the collapse safety of the considered buildings. The results also showed that the developed macro-model model is able to simulate the dynamic response of the system under varying dynamic input until the point at which the frame loses its lateral load carrying capacity. Although validation of the dynamic response of the case study model results is impossible, comparison with a set of experimental results confirm the general trend observed in this study between the intensity of the excitation level and the structural response.

Chapter 6 focused on the collapse assessment of RC frames without masonry infill panel. This section is a subset of collaborative effort with the goal of developing an evaluation methodology for existing buildings. This chapter studied the effect of extent of three collapse indicators specifically,  $M_c/M_b$ ,  $V_i/V_{i+1}$ , and  $V_p/V_n$  on the collapse performance of the buildings. The results of Chapter 6 showed the expected decrease in collapse capacity as the extent of deficiency increases. These findings suggest that averaging of collapse indicator values in all

members (joints or columns) in the floor of interest may be an appropriate definition for some collapse indicators such as  $M_c/M_b$  and  $V_i/V_{i+1}$ , however, it may not be appropriate for other indicators such as  $V_p/V_n$ . Moreover, the results of this study showed that the location of some of the deficiencies such as  $M_c/M_b$  and  $V_i/V_{i+1}$  does not affect significantly the collapse performance, however it could be important for other collapse indicators such as  $V_p/V_n$ .

Chapter 7 developed and tested a methodology to quantify the effect of modeling uncertainty and incorporate the modeling uncertainty in the seismic assessment procedure based on results of the 7-story RC building blind prediction contest at UCSD. In this methodology the modeling uncertainty is introduced as a set of drift distributions. The results of this study showed that incorporating the modeling uncertainty to the RTR variability results leads to an increase in the median collapse capacity and dispersion of the fragility curve.

## **8.2 Future Research**

The current study recognized the need of several future research which help the goal of assessing the collapse performance of non-ductile concrete frames with and without masonry infill panels. These future research topics are grouped into two topics as follows.

### **8.2.1 Modeling of Masonry Infilled RC Frames**

More research is needed in order to have a better understanding of redistribution of lateral or vertical loads to the wall after the failure of the concrete columns. Having more knowledge about the force redistribution in the infilled frame would lead to improve proposed multi-scale modeling approach. In particular, improvements to the macro-model to more accurately consider the gravity-load capacity of the infill wall and degradation thereof under seismic loading are desired.

The proposed multi-scale modeling approach can be implemented for masonry infilled frames with openings followed by some modifications in strut orientation. More research is needed to find the relationship between in-plane and out-of-plane response of the masonry wall and how damages in one of these responses can affect the behavior of the wall in the other direction.

Existence of the masonry infill wall in a frame may change the response of the concrete columns in terms of the drift at which shear failure occurs and the shear capacity of the column. More numerical and experimental research is required to investigate the response of concrete columns in the infilled frames.

### **8.2.2 Quantification of Modeling Uncertainty**

The main challenge in the proposed methodology in this study is to understand the modeling drift distributions, which involves more research to predict generalizable modeling drift distribution applicable to a wider range of buildings.

## Bibliography

- Abrams, D.P., 1994. Proceedings from the NCEER workshop on seismic response of masonry infills. National Center for Earthquake Engineering Research.
- ACI, 2008. ACI 318: Building code requirements for reinforced concrete.
- Akin, L.A., 2006. Behavior of reinforced concrete frames with masonry infills in seismic regions. ETD Collection for Purdue University, 1–407.
- Al-Chaar, G., Issa, M., Sweeney, S., 2002. Behavior of masonry-infilled nonductile reinforced concrete frames. *Journal of Structural Engineering* 128, 1055–1063.
- Al-Chaar, G.L., Mehrabi, A., 2008. Constitutive models for nonlinear finite element analysis of masonry prisms and infill walls (No. ERDC/CERL TR- 08- 19), US Army Corps of Engineering.
- Almeida, J.C., Lourenco, P.B., Barros, J.A., 2002. Characterization of brick and brick–mortar interface under uniaxial tension, in: *Proceedings of 7th Int. Seminar on Structural Masonry*, Brazil: CEFET-MG. , 67–76.
- Amato, G., Cavaleri, L., Fossetti, M., 2008. Infilled frames: Influence of vertical load on the equivalent diagonal strut model. Presented at the 14 WCEE, Beijing, China.
- Anagnos, T., Comerio, M.C., Goulet, C., Steele, J., Stewart, J.P., 2010. Development of a concrete building inventory: Los Angeles case study for the analysis of collapse risk, in: *Proceedings of the 9th U.S. National and 10th Canadian Conference on Earthquake Engineering*, Toronto.
- Angel, R., Abrams, D.P., 1994. Out-of-plane strength evaluation of URM infill panels, *Proceedings from the NCEER workshop on seismic response of masonry infills*, in: *Technical Report*. Presented at the NCEER Workshop on Seismic Response of Masonry Infills, National Center for Earthquake Engineering Research, 9–14.
- Anil, Ö., Altin, S., 2007. An experimental study on reinforced concrete partially infilled Frames. *Engineering Structures* 29, 449–460.
- Applied Technology Council, 2009. Quantification of building seismic performance factors (FEMA P695).
- ASCE/SEI, 2006. *Seismic rehabilitation of existing buildings*. ASCE Publications.
- Aschheim, A.M., Moehle, J.P., 1992. Shear strength and deformation ability of RC bridge columns subjected to inelastic displacements. University of California, Berkeley, CA.
- Asteris, P.G., Antoniou, S.T., Sophianopoulos, D.S., Chrysostomou, C.Z., 2011. Mathematical macromodeling of infilled frames: State of the art. *Journal of Structural Engineering* 137, 1508–1517.

- ATC, 2010. Here today-here tomorrow: The road to earthquake resilience in San Francisco, ATC 52. Applied Technology Council, Redwood city, California.
- ATC, 2010. Community Action Plan for Seismic Safety (CAPSS) Project, ATC 52-2. Applied Technology Council, Redwood city, California.
- ATC, 2011. Evaluation of the methodology to select and prioritize collapse indicators. Applied Technology Council, Redwood city, California.
- ATC, 2012. Identification and mitigation of non-ductile concrete buildings. Applied Technology Council, Redwood city, California.
- Baradaran Shoraka, M., Elwood, K., 2013. Mechanical model for non-ductile reinforced concrete columns. *Journal of Earthquake Engineering*.
- Baradaran Shoraka, M., Yang, T.Y., Elwood, K.J., 2013. Seismic loss estimation of non-ductile reinforced concrete buildings. *Earthquake Engineering & Structural Dynamics* 42, 297–310.
- Bazant, Z.P., 1976. Instability, ductility, and size effect in strain-softening concrete. *Journal of the Engineering Mechanics Division* 102, 331–344.
- Bennett, R.M., Flanagan, R.D., Adham, S., Fischer, W.L., Tenbus, M.A., 1996. Evaluation and analysis of the performance of masonry infills during northridge earthquake. Oak Ridge, Tenn.
- Blackard, B., Willam, K., Mettupalayam, S., 2009. Experimental observations of masonry infilled RC frames with openings, in: Thomas TC Hsu Symposium on Shear and Torsion in Concrete Structures. pp. 199–222.
- Braga, F., Gigliotti, R., Laterza, M., D’Amato, M., Kunnath, S., 2012. Modified steel bar model incorporating bond-slip for seismic assessment of concrete structures. *Journal of Structural Engineering* 138, 1342–1350.
- Buonopane, S., White, R., 1999. Pseudodynamic testing of masonry infilled reinforced concrete frame. *Journal of Structural Engineering* 125, 578–589.
- Calvi, G.M., Bolognini, D., 2001. Seismic response of reinforced concrete frames infilled with weakly reinforced masonry panels. *Journal of Earthquake Engineering* 5, 153–185.
- Calvi, G.M., Bolognini, D., Penna, A., 2004. Seismic performance of masonry-infilled RC frames: benefits of slight reinforcement. Presented at the SÍSMICA 2004 - 6<sup>o</sup> Congresso Nacional de Sismologia e Engenharia Sísmica.
- Cavaleri, L., Fossetti, M., Papia, M., 2004. Effect of vertical loads on lateral response of infilled frames. Presented at the 13WCEE, Vancouver, B.C., Canada.
- Celarec, D., Ricci, P., Dolšek, M., 2012. The sensitivity of seismic response parameters to the

- uncertain modeling variables of masonry-infilled reinforced concrete frames. *Engineering Structures* 35, 165–177.
- Champion, C., Liel, A., 2012. The effect of near-fault directivity on building seismic collapse risk. *Earthquake Engineering & Structural Dynamics* 41, 1391–1409.
- Charleston, A., 2008. *Seismic design for architects: outwitting the quake*. Elsevier/Architectural Press, Amsterdam; Boston; London.
- Chrysostomou, C.Z., 1991. *Effects of degrading infill walls on the nonlinear seismic response of two-dimensional steel frames (Ph.D.)*. Cornell University, January 1991.
- Crisafulli, F.J., 1997. *Seismic behavior of reinforced concrete structures with masonry infills, (Ph.D.)*. University of Canterbury.
- Crisafulli, F.J., Carr, A.J., 2007. Proposed macro-model for the analysis of infilled frame structures. *Bulletin of the New Zealand Society for Earthquake Engineering* 40, 69–77.
- Crowley, H., Pinho, R., 2010. Revisiting Eurocode 8 formulae for periods of vibration and their employment in linear seismic analysis. *Earthquake Engineering & Structural Dynamics* 39, 223–235.
- Dawe, J.L., Seah, C.K., 1989. Out-of-plane resistance of concrete masonry infilled panels. *Canadian Journal of Civil Engineering* 16, 854–864.
- Deierlein, G.G., 2004. Overview of a comprehensive framework for earthquake performance assessment, in: *Performance-based seismic design concepts and implementation, Proceeding of an International workshop, PEER Rep. 2004/05*. Berkeley, CA, 15–26.
- Dhanasekhar, M., Page, A., 1986. The influence of brick masonry infill properties on the behavior of infilled frames. *ICE Proceedings* 81, 593–605.
- DIANA, 2011. *Finite element analysis*. TNO Building and Construction Research, Delft, The Netherlands.
- Dolsek, M., Fajfar, P., 2002. Mathematical modeling of an infilled RC frame structure based on the results of pseudo-dynamic tests. *Earthquake Engineering & Structural Dynamics* 31, 1215–1230.
- Dolsek, M., Fajfar, P., 2001. Soft storey effects in uniformly infilled reinforced concrete frames. *Journal of Earthquake Engineering* 5, 1–12.
- Dolšek, M., Fajfar, P., 2002. Mathematical modelling of an infilled RC frame structure based on the results of pseudo-dynamic tests. *Earthquake Engineering & Structural Dynamics* 31, 1215–1230.
- Dolšek, M., Fajfar, P., 2008. The effect of masonry infills on the seismic response of a four-storey reinforced concrete frame — a deterministic assessment. *Engineering Structures*

- 30, 1991–2001.
- Drysdale, R.G., Hamid, A.A., Baker, L.R., 1999. *Masonry structures: behavior and design*, 2nd ed. Prentice Hall, Boulder, Colorado, US.
- Dymiotis, C., Kappos, A.J., Chryssanthopoulos, M.K., 2001. Seismic reliability of masonry-infilled RC frames. *Journal of Structural Engineering* 127, 296–305.
- El-Dakhakhni, W.W., Elgaaly, M., Hamid, A.A., 2003. Three-strut model for concrete masonry-infilled steel frames. *Journal of Structural Engineering* 129, 177–185.
- Ellingwood, B., Galambos, T.V., MacGregor, J.G., Cornell, C.A., 1980. *Development of a probability-based load criterion for American National Standard A58*, National Bureau of Standards, Washington.
- Elwood, K.J., 2002. *Shake table tests and analytical studies on the gravity load collapse of reinforced concrete frames*. University of California.
- Elwood, K.J., 2004. Modeling failures in existing reinforced concrete columns. *Canadian Journal of Civil Engineering* 31, 846–859.
- Elwood, K.J., Moehle, J.P., 2005. Drift capacity of reinforced concrete columns with light transverse reinforcement. *Earthquake Spectra* 21, 71–89.
- Elwood, K.J., Moehle, J.P., 2008. Dynamic collapse analysis for a reinforced concrete frame sustaining shear and axial failures. *Earthquake Engineering & Structural Dynamics* 37, 991–1012.
- Faison, H., Comartin, C., Elwood, K., 2004. Reinforced concrete moment frame building without seismic details. *World Housing Encyclopedia*, [www.world-housing.net](http://www.world-housing.net).
- Fardis, M., 1997. Seismic design and response of bare and masonry-infilled reinforced concrete buildings. Part II: infilled structures. *Journal of Earthquake Engineering*.
- Fardis, M.N., Biskinis, D.E., 2003. Deformation capacity of RC members, as controlled by flexure or shear, in: *Otani Symposium*, 511–530.
- FEMA, 1998. *Evaluation of earthquake damaged concrete and masonry wall buildings*. Applied Technology Council, Redwood City, CA.
- FEMA, 2000. *Prestandard and commentary for the seismic rehabilitation of buildings*.
- FEMA, 2006. *Designing for earthquakes a manual for architects*, FEMA 454, Risk Management Series *Designing for Earthquakes*.
- FEMA, 2009. *Quantification of building seismic performance factors (FEMA P695)*. Applied Technology Council, Redwood City, CA.

- Filippou, F.C., Popov, E.P., Bertero, V.V., 1983. Effects of bond deterioration on hysteretic behavior of reinforced concrete joints, (NO. UCB/EERC-83/19). CA, Berkeley.
- Fiorato, A.E., Sozen, M.A., Gamble, W.L., 1970. Behavior of five-story reinforced concrete frames with filler walls, Interim report to the Department of Defense Office of Secretary of the Army, Office of Civil Defense, Urbana, Illinois (1970)..
- Fiorato, A.E., Sozen, M.A., Gamble, W.L., 1970. An investigation of the interaction of reinforced concrete frames with masonry filler walls ( No. UILU-ENG-70-100). Dept. of Civil Engineering, University of Illinois, Urbana- Champaign, IL.
- Flanagan, R.D., Bennett, R.M., 1999. Arching of masonry infilled frames: Comparison of analytical methods. Practice Periodical on Structural Design and Construction 4, 105–110.
- Gabrielsen, B.L., Kaplan, K., 1997. Arching in masonry walls subjected to out-of-plane forces. Earthquake Resistant Masonry Construction, NBS Building Science Series 106, 283–313.
- Galanis, P.H., Moehle, J.P., n.d. Development of collapse indicators for older-type reinforced concrete buildings.
- Gumaste, K.S., Nanjunda Rao, K.S., Venkatarama Reddy, B.V., Jagadish, K.S., 2006. Strength and elasticity of brick masonry prisms and wallettes under compression. Materials and Structures 40, 241–253.
- Hamburger, R.O., Meyer, J.D., 2006. The performance of steel-frame buildings with infill masonry walls in the 1906 San Francisco earthquake. Earthquake Spectra 22, 43–67.
- Haselton, C.B., Goulet, C.A., Mitrani-Reiser, J., Beck, J.L., Deierlein, G.G., Porter, K.A., 2007. An assessment to benchmark the seismic performance of a code-conforming reinforced concrete moment-frame building (No. PEER 2007/12).
- Haselton, C.B., Liel, A.B., Lange, S.T., Deierlein, G.G., 2008. Beam-column element model calibrated for predicting flexural response leading to global collapse of RC frame buildings (No. PEER 2007/03). CA, Berkeley.
- Hashemi, A., Mosalam, K., 2007. Seismic evaluation of reinforced concrete buildings including effects of masonry infill walls, PEER Technical Report. Pacific Earthquake Engineering Research Center.
- Hashemi, A., Mosalam, K.M., 2006. Shake-table experiment on reinforced concrete structure containing masonry infill wall. Earthquake Engineering & Structural Dynamics 35, 1827–1852.
- Holmes, M., 1961. Steel frame with brickwork and concrete infilling. ICE Proceedings 19, 473–478.
- Holmes, W., Mehra M., Moehle J., Somers P., 2013. Personal Communication.

- Ibarra, L., 2003. Global collapse of frame structures under seismic excitations (Ph.D.). Stanford University.
- Ibarra, L.F., Krawinkler, H., 2005. Global collapse of frame structures under seismic excitations. Pacific Earthquake Engineering Research Center.
- ICBO, 1927. Uniform Building Code. Long Beach, CA.
- ICBO, 1997. Uniform Building Code. Long Beach, CA.
- Kariotis, J., 1991. Determination of the compressive modulus of masonry by use of flat-jacks, San Pedro masonry infill evaluation. Los Angeles, CA.
- Kent, D.C., Park, R., 1971. Flexural members with confined concrete. *Journal of the Structural Division* 97, 1969–1990.
- Klingner, R.E., Bashandy, T.R., Sweeney, S.C., 1996. Evaluation and analytical verification of shaking table data from infilled frames. Part 2: Out-of-plane behavior, in: *Proc.*, 7th North American Masonry Conf. Notre Dame, 521–532.
- Klingner, R.E., Bertero, V.V., 1978. Earthquake Resistance of Infilled Frames. *Journal of the Structural Division* 104, 973–989.
- Kodur, V.K.R., Erki, M.A., Quenneville, J.H.P., 1995. Seismic design and analysis of masonry-infilled frames. *Can. J. Civ. Eng.* 22, 576–587.
- Koutromanos, I., Stavridis, A., Shing, P.B., Willam, K., 2011. Numerical modeling of masonry-infilled RC frames subjected to seismic loads. *Computers & Structures* 89, 1026–1037.
- Kyriakides, M., 2011. Seismic retrofit of unreinforced masonry infills in nonductile reinforced concrete frames using engineered cementitious composites. Stanford University.
- Lee, H. S., Woo, S.-W., 2002. Effect of masonry infills on seismic performance of a 3-storey R/C frame with non-seismic detailing. *Earthquake Engineering & Structural Dynamics* 31, 353–378.
- Lee, T. H., Mosalam, K.M., 2005. Seismic demand sensitivity of reinforced concrete shear-wall building using FOSM method. *Earthquake Engineering & Structural Dynamics* 34, 1719–1736.
- Lehman, D.E., Moehle, J.P., 1998. Seismic performance of well-confined concrete bridge columns ( No. PEER-98/01), Pacific Earthquake Engineering Research Center. University of California, Berkeley, Berkeley, CA.
- Li, X., Zhou, Z., Yu, H., Wen, R., Lu, D., Huang, M., Zhou, Y., Cu, J., 2008a. Strong motion observations and recordings from the great Wenchuan earthquake. *Earthquake Engineering and Engineering Vibration* 7, 235–246.

- Li, Y.-J., Zimmerman, T., 1998. Numerical evaluation of the rotating crack model. *Computers & Structures* 69, 487–497.
- Liel, A., 2008. Assessing the collapse risk of California's existing reinforced concrete frame structures: metrics for seismic safety decisions, (Ph.D. thesis). Stanford University.
- Liel, A.B., Haselton, C.B., Deierlein, G.G., 2011. Seismic collapse safety of reinforced concrete buildings. II: Comparative assessment of nonductile and ductile moment frames. *Journal of Structural Engineering* 137, 492–502.
- Liel, A.B., Haselton, C.B., Deierlein, G.G., Baker, J.W., 2009. Incorporating modeling uncertainties in the assessment of seismic collapse risk of buildings. *Structural Safety* 31, 197–211.
- Liel, A.B., Lynch, K.P., 2012. Vulnerability of reinforced-concrete-frame buildings and their occupants in the 2009 L'Aquila, Italy, earthquake. *Natural Hazards Review* 13, 11–23.
- Linares, J.G., 2007. Adaptive reuse of existing structures. *Structure Magazine* 26–27.
- Lotfi, H.R., Shing, P.B., 1991. An appraisal of smeared crack models for masonry shear wall analysis. *Computers & Structures* 41, 413–425.
- Lotfi, H.R., Shing, P.B., 1994. Interface model applied to fracture of masonry structures. *Journal of Structural Engineering* 120, 63–80.
- Lourenco, P.B., Rots, J.G., 1997. Multisurface interface model for analysis of masonry structures. *Journal of Engineering Mechanics* 123, 660–668.
- Lourenco, P.B., 1996. Computational strategies for masonry structures. Universidade do Porto, Portugal.
- Lourenço, P.B., Zucchini, A., Milani, G., Tralli, A., 2006. Homogenisation approaches for structural analysis of masonry buildings, in: *structural analysis of historical constructions*, New Delhi 59-75.
- Luco, N., Ellingwood, B.R., Hamburger, R.O., Hooper, J.D., Kimball, J.K., Kircher, C.A., 2007. Risk-targeted versus current seismic design maps for the conterminous United States, *Structural Engineers Association of California 2007 Convention Proceedings*, 163–175.
- Mack, R.C., Speweik, J.S., 1998. Repointing mortar joints in historic masonry buildings. Washington D.C.
- Madan, A., Hashmi, A.K., 2008. Analytical prediction of the seismic performance of masonry infilled reinforced concrete frames subjected to near-field earthquakes. *Journal of Structural Engineering* 134, 1569–1581.
- Madan, A., Reinhorn, A., Mander, J., Valles, R., 1997. Modeling of masonry infill panels for structural analysis. *Journal of Structural Engineering* 123, 1295–1302.

- Mainstone, R.J., 1971. On The stiffness and strengths of infilled frames. ICE Proceedings, 230.
- Mainstone, R.J., Weeks, G.A., 1970. The influence of a bounding frame on the racking stiffness and strengths of brick walls. SIBMAC Proceeding. Presented at the Second International Brick Masonry Conference, Building Research Station, England.
- Mallick, D.V., Severn, R.T., 1968. Dynamic characteristics of infilled frames. ICE Proceedings 39, 261–287.
- Manzouri, T., 1995. Repair and Retrofit of Unreinforced Masonry Walls: Experimental evaluation and finite element analysis. Department of Civil, Environmental & Architectural Engineering (Ph.D. thesis). University of Colorado.
- Massey, F.J., 1951. The Kolmogorov-Smirnov test for goodness of fit. Journal of the American Statistical Association 46, 68–78.
- Mehrabi, A., 1994. Behavior of Masonry-infilled reinforced concrete frames subjected to lateral loading (Ph.D. Thesis). University of Colorado-Boulder.
- Mehrabi, A., Shing, P., 1997. Finite element modeling of masonry-infilled RC frames. Journal of Structural Engineering 123, 604–613.
- Mehrabi, A.B., Benson Shing, P., Schuller, M.P., Noland, J.L., 1996. Experimental evaluation of masonry-infilled RC frames. Journal of Structural Engineering 122, 228–237.
- Moaveni, B., He, X., Conte, J.P., Restrepo, J.I., Panagiotou, M., 2011. System identification study of a 7-Story full-scale building slice tested on the UCSD-NEES shake table. Journal of Structural Engineering 137, 705–717.
- Moehle, J.P., Ghannoum, W., Bozorgnia, Y., 2006. Collapse of lightly confined reinforced concrete frames during earthquakes, in: Wasti, S.T., Ozcebe, G. (Eds.), Advances in Earthquake Engineering for Urban Risk Reduction, Nato Science Series: IV: Earth and Environmental Sciences. Springer Netherlands, pp. 317–332.
- Montgomery, D.C., Runger, G.C., 2010. Applied statistics and probability for engineers, 5th ed. Wiley.
- Nakamura, H., Higai, T., 2001. Compressive fracture energy and fracture zone length of concrete, in: modeling of inelastic behavior of RC structures under seismic loads, ASCE. pp. 471–487.
- Negro, P., Taylor, C.A., 1996. Effect of infills on the global seismic behavior of rc frames: results of pseudo dynamic. Presented at the Eleventh world conference on earthquake engineering.
- NIST, 2010. Program plan for the development of collapse assessment and mitigation strategies for existing reinforced concrete buildings ( No. NIST GCR 10-917-7). NEHRP Consultants Joint Venture.

- Oliveira, D.V., Lourenco, P.B., 2004. Implementation and validation of a constitutive model for the cyclic behaviour of interface elements. *Computers & structures* 82, 1451–1461.
- Panagiotou, M., Restrepo, J.I., 2011. Displacement-based method of analysis for regular reinforced-concrete wall buildings: application to a full-scale 7-story building slice tested at UC–San Diego. *Journal of Structural Engineering* 137, 677–690.
- Panagiotou, M., Restrepo, J.I., Conte, J.P., 2011. Shake-table test of a full-scale 7-story building slice. phase I: rectangular wall. *Journal of Structural Engineering* 137, 691–704.
- PEER, 2010. OpenSees, Pacific Earthquake Engineering Research Center. University of California, Berkeley.
- Pincheira, J., Dotiwala, F.S., D’Souza, J.T., 1999. Seismic analysis of older reinforced concrete columns. *Earthquake Spectra* 15, 245–272.
- Polyakov, S.V., 1960. On the interaction between masonry filler walls and enclosing frame when loaded in the plane of the wall, in: *construction in seismic regions*. translation in *Earthquake Engineering*, Earthquake Engineering Research Institute, Moscow, 36–42.
- Priestley, M.J.N., Verma, R., Xiao, Y., 1994a. Seismic shear strength of reinforced concrete columns. *Journal of Structural Engineering* 120, 2310–2329.
- Rao, G.A., 2001. Generalization of Abrams’ law for cement mortars. *Cement and Concrete Research* 31, 495–502.
- Sachanski, S., 1960. Analysis of the earthquake resistance of frame buildings taking into consideration the carrying capacity of the filling masonry, in: *Proc. 2nd World Conf. on Earthquake*, 2127–41.
- Saneinejad, A., Hobbs, B., 1995. Inelastic design of infilled frames. *Journal of Structural Engineering* 121, 634–650.
- Sattar, S., Liel, A.B., 2010. Seismic performance of reinforced concrete frame structures with and without masonry infill walls, in: *9th US national and 10th Canadian Conference on Earthquake Engineering*, Toronto, Canada.
- Schmid, B., Kariotis, J., Schwartz, E., 1978. Tentative Los Angeles ordinance and testing program for unreinforced masonry buildings. South Lake Tahoe.
- Sezen, H., 2002. Seismic behavior and modeling of reinforced concrete building columns. University of California, Berkeley, Berkeley, CA.
- Sezen, H., Moehle, J., 2004. Shear strength model for lightly reinforced concrete columns. *Journal of Structural Engineering* 130, 1692–1703.
- Sezen, H., Whittaker, A.S., Elwood, K.J., Mosalam, K.M., 2003. Performance of reinforced concrete buildings during the August 17, 1999 Kocaeli, Turkey earthquake, and seismic

- design and construction practice in Turkey. *Engineering Structures* 25, 103–114.
- Shing, P., Stavridis, A., Koutromanos, I., Willam, K., Blackard, B., Kyriakides, M., Billington, S., Arnold, S., 2009. Seismic Performance of Non-Ductile RC Frames with Brick Infill, in: *Improving the Seismic Performance of Existing Buildings and Other Structures*. American Society of Civil Engineers, pp. 1117–1128.
- Shing, P.B., 2013. Collapse simulation of masonry-infilled RC frames. Presented at the ATC-95 workshop, San Francisco, CA.
- Smith, B.S., 1962. Lateral stiffness of infilled frames. *Journal of the Structural Division, ASCE* 88, 183–199.
- Spacone, E., Filippou, F.C., Taucer, F.F., 1996. Fibre beam–column model for non-linear analysis of R/C frames: part I. formulation. *Earthquake Engineering & Structural Dynamics* 25, 711–725.
- Stafford Smith, B., Carter, C., 1969. A method of analysis for infilled frames. *ICE Proceedings* 44, 31–48.
- Stafford-Smith, B., 1962. Lateral stiffness of infilled frames. *Journal of Structural Division* 88, 183–199.
- Stang, A.H., Parsons, D.E., McBurney, J.W., 1929. Compressive strength of clay brick wall. *Bureau of Standards Journal of Research* 3, 507–571.
- Stavridis, A., 2009. Analytical and experimental study of seismic performance of reinforced concrete frames infilled with masonry walls., (Ph.D. thesis). University of California San Diego.
- Stavridis, A., Koutromanos, I., Shing, P.B., 2012. Shake-table tests of a three-story reinforced concrete frame with masonry infill walls. *Earthquake Engineering & Structural Dynamics* 41, 1089–1108.
- Stavridis, A., Kyriakides, M.A., Willam, K., Blackard, B., Koutromanos, I., Shing, P.B., Arnold, S., Billington, S.L., n.d. Seismic performance of non-ductile RC frames with brick infill, in: *improving the seismic performance of existing buildings and other structures*. American Society of Civil Engineers, pp. 1117–1128.
- Stavridis, A., Shing, P., 2010. Finite-element modeling of nonlinear behavior of masonry-infilled RC frames. *Journal of Structural Engineering* 136, 285–296.
- Syrmakizis, C.A., Vratsanou, V.Y., 1986. Influence of infill walls to RC frames Response, in: *Proc., 8th European Conf. on Earthquake Engineering*, European Association for Earthquake Engineering (EAE). Istanbul, Turkey, pp. 47–53.
- Taylor, R.L., 1987. FEAP finite element analysis program. Univeristy of California- Berkeley, Berkeley, California.

- Te-Chang, L., Kwok-Hung, K., 1984a. Nonlinear behavior of non-integral infilled frames. *Computers & Structures* 18, 551–560.
- Terzaghi, K., 1996. *Soil mechanics in engineering practice*. John Wiley & Sons.
- Thomas, F.G., 1953. The strength of brickwork, in: *The Struct. Engr.* London.
- Tothong, P., Luco, N., 2007. Probabilistic seismic demand analysis using advanced ground motion intensity measures. *Earthquake Engineering & Structural Dynamics* 36, 1837–1860.
- Turneure, F.E., Maurer, E.R., 1914. *Principles of reinforced concrete construction*, 2nd. ed. John Wiley & Sons, Inc., New York.
- Vamvatsikos, D., Cornell, C.A., 2002. Incremental dynamic analysis. *Earthquake Engineering & Structural Dynamics* 31, 491–514.
- Van der Pluijm, R., 1992. Material properties of masonry and its components under tension and shear, in: *Proceedings of the 6<sup>th</sup> Canadian Masonry Symposium*. Saskatoon, Saskatchewan: University of Saskatchewan.
- Vecchio, F.J., Collins, M.P., 1986. The modified compression-field theory for reinforced concrete elements subjected to shear. *ACI J.* 83, 219–231.
- Zarnic, R., Gostic, S., 1997. Masonry infilled frames as an effective structural sub-assembly, *Seismic Design Methodologies for the Next Generation of Codes: Proceedings of the International Workshop*. Bled, Slovenia.
- Zarnic, R., Tomazevic, M., 1988. An experimentally obtained method for evaluation of the behavior of masonry infilled RC frames, in: *Proceedings of the 9th World Conference on Earthquake Engineering*. pp. 163–168.